Estimate of Geopressures using Conformal Mapping in Eccentric Wells

Uyara F. Silva, Manoel I. Q. Júnior, Santiago Lemos, Alan. F. Silva, Geovanne P. Furriel, Nikholas Segatti and Wesley P. Calixto

***Abstract*—The purpose of this work is to calculate Surge and Swab pressures in eccentric wells. Analysis of the phenomenon, in which fluid is confined between two eccentric cylinders, are made. Conformal mapping calculations is used to lead the original eccentric domain into equivalent concentric domain, since usual models only make calculation for concentric geometries. The results of this study, using the proposed methodology, are presented and discussed.**

***Index Terms*— annulus geometry, conformal mapping, surge pressure, swab pressure, yield power law drilling fluid.**

I. INTRODUCTION

The usual methodology for pressure calculation, during drilling of wells, assumes that the drill string and well work concentrically. However, the rotary movement of the drill makes the set (drill and well) works eccentrically with the well. Therefore, the calculations obtained through the usual methodologies have errors because they do not consider the effect of the eccentricity.

Surge and Swab pressures are problems that can happen during the drilling of oil wells [1]. The prediction of these pressures is essential to determine the appropriate speeds and accelerations for introduction and withdrawal of the drill string in the wellbore [2].

Surge pressure is the increase in wellbore pressure, that goes beyond the maximum supported by walls. It can fracture the rock formation and causes fluid loss [3]. Swab pressure occurs when pressure inside the wellbore is below the pore pressure, causing fluid penetration from the rock into the wellbore (kick effect). If not controlled, the kick effect can become blowout, which means uncontrolled flow from the hole to surface [2]. To avoid the blowout, it is necessary to control and to manage the pressures, ensuring that they are within desired limits [3].

Calculations of Surge and Swab pressures have extreme importance to avoid kick effect and subsequent blowout. Kick effect can occur when the hydrostatic pressure is lower than the pore pressure, fracturing the formation and thus the pore fluid invades the well. The absence of control of the kick effect can results in blowout, fluid inside the well reaches surface uncontrollably and can cause explosions and dump of oil into the environment.

The usual methodology to calculate the Surge and Swab pressures assumes that the casing string and drill work concentrically [4]. However, the rotational movement of the drill causes the geometry of the well to be eccentric. Calculations obtained by usual methods do not consider the effect of eccentricity [5].

In order to reduce errors due to the eccentricity it can be used conformal mapping, that takes a domain into another, preserving the angles and physical quantities [6]. The purpose of this work is use conformal mapping to calculate the value of Surge and Swab pressures taking into account the effect of eccentricity between the casing string and the wellbore.

Conformal mapping are domain transformations and represent complex analytic functions, so this work assumes that conformal mapping are capable to lead eccentrics geometries into concentric geometries. Therefore, the value of the pressures can be calculated at any time of the drilling dynamics. The model is developed for power law drilling fluids under isothermal conditions, considering a constant fluid density. The model can be used in vertical wells, both terrestrial and marine. This work is focused on the problems caused by Surge and Swab pressures.

II. WELL DRILLING PROCESS

For drilling wells, the drill column with the drill in the tip is introduced into the formation, making the well [7]. The process of well drilling is made by steps, each step is drilled a given depth and thickness [8]. Introduction and withdrawing the drill string is called maneuver [9].

For each maneuver is introduced a new column set with new thickness down to a certain depth. During drilling, a hydrostatic fluid is injected through the drill bit into the well with the purpose of carrying gravels out of the wellbore. Hydrostatic fluid is also used to lubricate the drill bit and give more support to the wellbore walls. After drilling part of the well, the drill column is removed and then is introduced a casing string into the hole, a metal pipe used to support the wellbore wall which has just been bored, preventing landslides [10].

Surge pressure, Fig. 1 (a), occurs when the hydrostatic pressure of the fluid is above pores pressure at the time of introduction of the drill string with speed V_p

higher than adequate. Surge can also occurs when drilling fluid is injected more than necessary, increasing pressure on the rock [11]. Hydrostatic pressure becomes greater than the fracture pressure (the rock strength) and can cause loss of drilling fluid. When this occurs, cementing of the well is required, to fill the space where the wellbore was fractured [12].

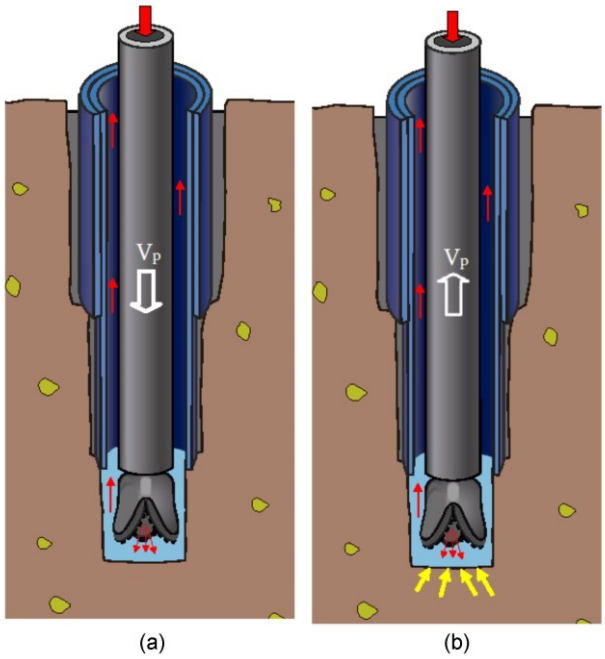

Fig. 1: Geopressures: (a) Surge and (b) Swab.

The Swab pressure, Fig. 1 (b), happens in the column withdrawal operation with speed V_p generating pressure drop by drag of the fluid along the tube walls [13]. When withdrawing the drill, vacuum can be generated causing hydrostatic pressure decrease, thus making pore pressure to become greater than hydrostatic pressure in the well and the kick effect to occur [12].

A. Pressures inside the well

The concept of pressure within wells is associated with the fluids contained within the rocks, and the result of the loading, which reacts equally in all directions.

1) Pore pressure: In rock formation, only part of the total volume is occupied by solid particles, which settle to form the structure. The remaining volume is often called voids, or pores, and is occupied by fluids. Pore pressure, often referred as formation pressure or static pressure, is the pressure of fluids contained in porous spaces of the rock. It is a function of the specific mass of the formation fluid and the loads it is bearing. In petroleum areas, the fluid filling a formation can be water, oil or gas [2].

2) Hydrostatic pressure: Hydrostatic pressure is exerted by the weight of the hydrostatic column of fluid, being function of the height of the column and the specific mass of this fluid. The drilling fluid has as one of its main objectives to keep the well safe and stable. The pressure provided by the drilling fluid varies if it is inside the drill string or in the annulus. This difference occurs because when the fluid is returning through the annular space, it carry the dirty made by drilling process. The weight of suspended gravels increases the specific mass of the drilling fluid by providing higher pressure at the bottom of the well. Another variable that interferes with the hydrostatic pressure generated by the drilling fluid is that the fluid be static or moving [2].

B. Kick and Blowout Effects

The pressure inside the well must be between the minimum and maximum boundary (operating window), for this to occur, the amount of fluid injected into the well must be analyzed according to the structure of the formation. The operating window must be determined and respected during maneuvering to prevent the well wall from fracturing, by excessive hydrostatic pressure or by lack of weight to contain the pore pressure. The speed of the maneuver should also be well calculated before the introduction of the drill string.

According to the type of formation being drilled, the imbalance between the pressure inside the well and the pore pressure can have different consequences. If the pore pressure becomes larger than the pressure inside the well, the formation fluid may invade the well. This typical undesired occurrence is called kick and can lead to loss of time during drilling. If kick occurs, it should be controlled by a higher injection of hydrostatic fluid through the drill string. In more severe and uncontrolled cases, the kick may hit the surface, resulting in blowout, uncontrolled flow of fluid coming out of the well due to some failure in the pressure control system, which can have disastrous consequences such as total destruction of the platform and the death of workers or damage to the environment. On the other hand, pressures inside the well greater than the fracture pressure, resistance of the formation, can lead to the invasion of the well fluid to the formation, being possible the collapse of the well [2].

C. Operating window

The operating window determines the allowable pressure variation exerted by drilling fluid inside the well, in order to maintain the integrity of the well, respecting the pore, fracture and collapse pressures. This window should determine the minimum and maximum fluid weight that can be used inside the well. The operating window is used to prevent kick and blowout effects or landslide [2]. Fig. 2 illustrates an operating window example where the fluid weight limits should be between the fracture pressure and the pore pressure.

If the weight of the fluid is less than the pore pressure, there may be a kick effect, if the weight of the fluid is greater than the fracture pressure, there will be loss of fluid for formation and possible landslide [15].

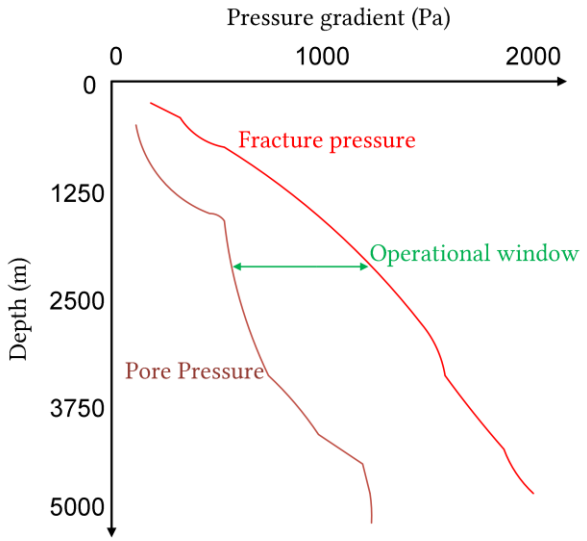

Fig. 2: Operational Window

III. CONFORMAL MAPPING

A deep-sea navigator can be guided by the stars and the angle that his course makes between the latitude and longitude lines. Since the Middle Ages, navigators have realized that it was possible to have spherical surface angles conserved on plane maps. When the angles between the curves on Earth are equal to the corresponding angles in the plane map, the map is called conform map [1].

The idea of a map conforming to the Earth was developed by the Belgian mathematician, geographer and cartographer Gerardo Mercator in 1569, known as Mercator projection. Although this projection presented distortions in proportions, it revolutionized cartography of the time. The points of the sphere, except the poles, are projected on a cylinder in which the sphere is inscribed, Fig. 3, the parallels are parallel straight horizontal lines, where the distance between successive parallels is proportional to their proximity to the Equator line, that is, the closer they are to the Equator, the smaller the distance between them. Meridians are projected in equidistant vertical parallel straight lines [1].

Advances in conforming map theory were performed by other scientists, Euler in 1777 (sphere in plan), and Lagrange in 1779 to obtain all the conforming representations of a part of the Earth's surface in a plane where all circles of longitudes and latitudes are represented by circular arcs in the plane. All of these authors, including Lambert with conforming conics, used complex numbers, but Lagrange's presentation is the clearest and most general.

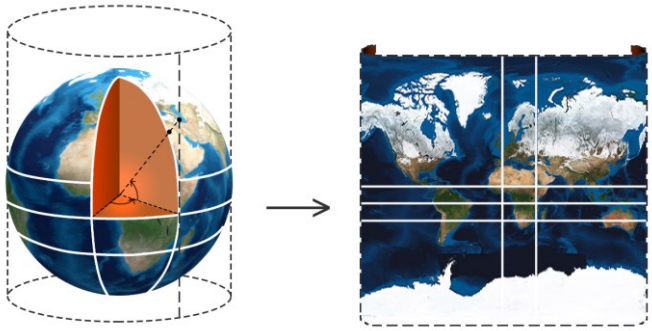

Fig. 3: Mercator Projection.

The discovery came in 1851 when Riemann gave the fundamental result, known as the Riemann's theorem, which was the starting point for all further developments in conformal mapping theory.

To prove this theorem, Riemann assumed that the variational problem, now known as the Dirichlet problem, has a solution. Fifty years later, in 1901, Hilbert demonstrated the existence of the solution of the Dirichlet problem. The validity of Riemann's result was rigorously established by Schwarz in 1890, using number of theorems coming from the logarithmic potential theory. At the end of the century XIX and the beginning of the century XX Cauchy, Riemann, Schwarz, Christoffel, Bieberbach, Carathéodory, Goursat, Koebe and others have established theoretical aspects about the theory of functions with complex variables

A. Conformal Mapping Definition

Conformal mapping are analytical functions, w=f(z), that carry the points of the domain D in points of the domain I maintaining the property of the angles, capable of converting mathematical problem of difficult solution into a simpler one without changing the physical characteristics of the system. The function has domain and range in the complex plane. Under some restrictive conditions, the mapping function can be defined [6]:

$$w = f(x) = f(x + yi) = u(x; y) + v(x; y)i, \quad (1)$$

where

$$z = x + yi \quad (2)$$

and

$$v = u + vi. \quad (3)$$

Considering w = f(z) the complex function that takes points from the plane z in points of the plane w, so f(z) is a geometric transformation, since curves in the plane

z has as images, curves in the plane w. The curve C_0 in the complex plane z has the curve S_0 in the complex plane w as its image, Fig. 4.

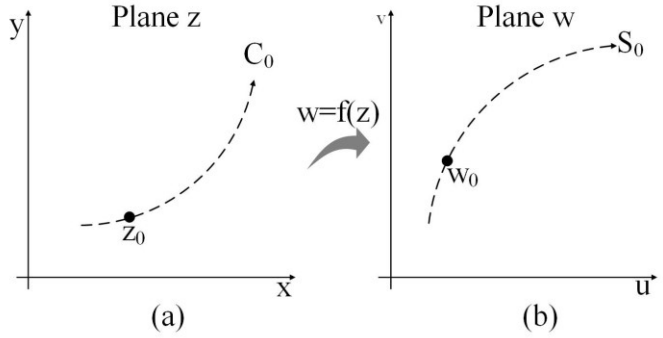

Fig. 4: Curve in z Plane and its Image in w Plane.

Considering positive direction of the course along C_0, the corresponding positive direction over S_0 is determined by the transforming function f. Taking the point z_0 in C_0, its image in w is $w_0 = f(z_0)$ over S_0, as shown in Fig. 4. Considering also the $z_0+\Delta z$ over C_0 in the positive sense from z_0, the limit of the argument of Δz when it tends to zero is the angle of inclination α of the tangent line to C_0 in z_0, Fig. 5 (a).

If $w_0+\Delta w$ is the image of $z_0+\Delta z$, then the argument of Δw tends towards the inclination angle β from the tangent to S_0 in w_0, when Δw tends to zero, with orientation according to Fig.5 (b).

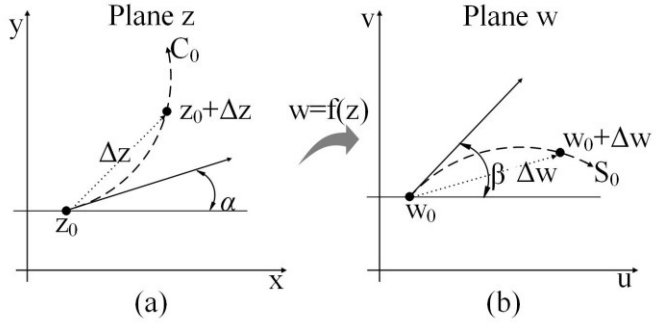

Fig. 5: Slope angle (a) α in Plane z and (b) β in Plane w.

IV. METHODOLOGY

A. *Conformal Mapping*

The problem in calculation of pressures consists in obtaining an equivalence between the eccentric and concentric plans. Fig. 6 illustrates the transverse section in the annulus formed between the wellbore and the column, by two coaxial cylinders with radii r_1 for external cylinder and r_2 for internal cylinder in the eccentric plane. The external plate is the well while inner plate is the column (drill).

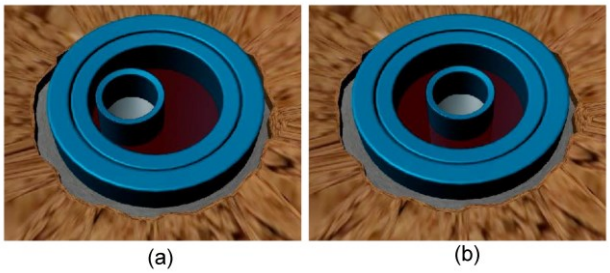

Fig. 6: Plan (a) eccentric in the domain D and plan (b) concentric in the domain I.

Assuming that the plates are circular in the total length and $\psi \neq 0$ is the eccentricity of the circles, there is in the Fig. 6 (a) the real problem. There is some difficulty to calculate the pressures in devices with this geometry. However, a new geometry that makes possible the pressures calculation can be found.

Using algebraic manipulation [14], it is possible to develop a conformal mapping, given by (4), that leads two eccentric circles with radii r_1 (external cylinder) and r_2 (internal cylinder) into two concentric circles Fig. 6 (b).

$$w(z) = t.\frac{r_1}{r_2}e^{i\theta}.\frac{d(z-z_a)-s(z_b-z_a)}{d(z-z_a)-t(z_b-z_a)}, \tag{4}$$

where θ, s and t are real, z_a are the points of the external plate and z_b, the points of the inner plate [6], s and t are the roots of the expression (4), given by:

$$\begin{aligned} s.t &= r_1^2 \\ (d-s).(d-t) &= r_2^2. \end{aligned} \tag{5}$$

In (4), $d = |z_a - z_b| = \psi > 0$ and z_a, z_b, r_1, r_2 , R_1, $R_2 > 0$ and $z_a \neq z_b$ [14], this equation can still write as:

$$\frac{r_2}{r_1}.\frac{t}{(d-t)} = \frac{R_2}{R_1},$$

$$-\frac{-d^2-r_1^2+r_2^2+\sqrt{-4d^2r_1^2+(d^2+r_1^2-r_2^2)^2}}{2d} = t, \tag{6}$$

$$-\frac{-d^2-r_1^2+r_2^2-\sqrt{-4d^2r_1^2+(d^2+r_1^2-r_2^2)^2}}{2d} = s.$$

Thus, in this new geometry, circles are concentric and the relationship between the domains D and I can be done.

B. *Rheological Parameters*

Fluids are classified according to their rheology, for this reason three parameters are considered: shear stress, shear rate and viscosity [15].

Shear stress τ is defined as the force F that, applied to an area A, the interface between the moving surface and

the liquid, causes flow in the first layer of liquid and the first layer causes flow in the second layer of liquid and so on. This moving surface is the drill string which moves when performing the maneuver.

Shear rate can be defined as variation of flow velocity with the variation of the distance between the drill string and walls of the well [15].

The viscosity is the ratio between shear stress and shear rate, and is the measure of the fluid resistance.

To calculate the shear stress over the shear rate in the well, the Hershell model is used. It is also known as Yield Power Law Fluid model, whose relationship of the three parameters is given by:

$$\tau = K\gamma^n + \tau_0, \quad (7)$$

where, τ is the shear stress and γ is the shear rate, τ_0 is the yield stress, K is the consistency index that indicates the degree of fluid resistance against the flow and n, named behavior index, indicates the distance of the Newtonian fluid model [15].

In the ratio $\gamma \times \tau$, for yield power law fluids, when the shear rate is $\gamma = 0$, the shear stress is the yield stress τ_0. The yield stress is the minimum stress necessary for the fluid to start leaking [15].

C. Mathematical Model for Surge and Swab Calculation

In order to determine Surge and Swab pressure in concentric plan is necessary to determine the input values for the annular geometry and the rheology of the fluid used in the drilling of the well.

For the rheology of the fluid, there are considered three parameters: shear stress, shear rate and viscosity. The shear stress τ is defined as the force F that, applied on an area A of the interface between the moving surface and the liquid, causes flowing in the first liquid layer, which in turn causes, in the second, the second in the third, and so on.

This moving surface is the drill string which moves during the performing maneuver. Shear rate can be defined as variation in flow rate with the height variation (distance from the surface causing the shear) [15].

The viscosity is the ratio between shear stress and shear rate, and is a measure of resistance to fluid flow.

The annular geometry, Fig. 7, is the height H, which is the distance between the surface of the drill string and the well, the diameter of the well $d_h = 2R_1$, the diameter of the drill string $d_p = 2R_2$, and the velocity V_p of descent or ascent of the drill string. Since the used methodology for calculating the pressures considers the concentricity between the well and the drill string, $H=R_1 - R_2$.

The rheological parameters are: the consistency index K, the fluid behavior index n and the initial shear stress required for the flow called yield stress τ_0 [12].

The values of Surge and Swab pressure are calculated by [3]:

$$P_{su} = \frac{P_e^n}{\left(\frac{n}{n+1}\right)^n \left(\frac{H}{V_p}\right)^n \left(\frac{H}{K}\right)} . L, \quad (8)$$

where L is the total length of the drill string and P_e is the specific pressure obtained from the ratio of the well geometry and the rheological parameters of the fluid.

The difference between Surge and Swab is that the Surge is the increased pressure on the well when the drill string down, and the Swab is the decrease of pressure in the well when the drill column rises.

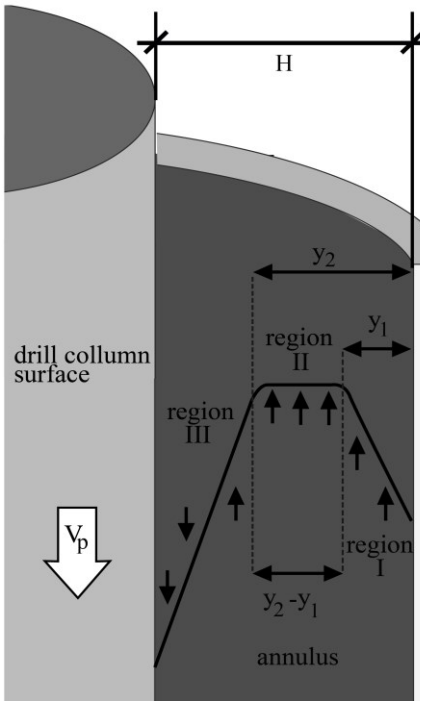

Fig. 7: Annulus geometry.

For the calculation of (8) is necessary to find expressions that define the speeds in the three regions of Fig. 7. The model for calculating the speed was developed by Crespo and Ahmed [12], for yield power law fluids.

Vector y assumes values between 0 and H, and is given in meters. For each value of y, there is a value for the velocity of the flow, indicated by the vertical arrows.

The constant y_1 is the size of region I and y_2 is the sum of region I and region II. Region II is within the limits $y_1 \leq y \leq y_2$ and has constant speed, the region I is within the limits $0 \leq y \leq y_1$ and region III is within the limits $y_2 \leq y \leq H$. The velocities in the region I and in the region III

vary according to vector y [12].

For the velocity profiles in the regions of the mathematical model of Crespo, dimensionless variables for speed are used as (9):

$$V_i' = \frac{V_i}{V_p}, i = 1, 2, 3. \quad (9)$$

This variables are dimensionless because of the division between two quantities with the same unit of measurement.

The same is true for the values of widths y_1 and y_2, as (10):

$$y_i' = \frac{y_i}{H}, i = 1, 2. \quad (10)$$

Values of y'_i, are always between 0 and 1 because they are the results of the divisions between points in y and their maximum value, H. So, these values are dimensionless.

The velocity profile in the region I is given by:

$$V_1' = P[(y_1' - y')^b - (y_1')^b], \quad (11)$$

where $0 \leq y' \leq y'_1$.

The velocity profile in the region II is given by:

$$V_2' = 1 - P(1 - y_2')^b, \quad (12)$$

where $y'_1 \leq y' \leq y'_2$.

The velocity profile in the region III is given by:

$$V_3' = 1 - P[(1 - y_2')^b - (y' - y_2')^b], \quad (13)$$

where $y'_2 \leq y' \leq 1$.

The values y'_1 and y'_2 are the widths shown in Fig. 7 and are associated with regions of different velocity profiles of fluid. The exponent b used in (11), (12) and (13) takes account the fluid behavior index:

In (11), (12) and (13) the value of the dimensionless pressure P is given by:

$$P = \left(\frac{n}{n+1}\right)\left(\frac{H}{V_p}\right)\left(\frac{\Delta P}{L}\frac{H}{K}\right)^{1n}. \quad (14)$$

Expression (12) is related to the pressure variation ΔP in the total length L of the drill string, P is a dimensionless vector.

The total flow rate is the sum of the flow rate of the three regions given by [3]:

$$q_t' = \int \left(\int V_1' \, dy_1' + \int V_2' \, dy_1' + \int V_3' \, dy_1' \right) dx'. \quad (15)$$

Solving the integral in (15), is obtained:

$$q_t' = -P\left[\left(\frac{b}{b+1}\right) y_1'^{b+1}\right] - [P(1 - y_1' - \chi)^b - 1]$$
$$(1 - y_1' - \chi) + P\left(\frac{b}{b+1}\right)$$
$$(1 - y_1' - \chi)^{b+1} - P y_1' \chi \quad (16)$$

Where:

$$\chi = \frac{\frac{2\tau_0}{H}}{\frac{\Delta P}{L}}, \quad (17)$$

and

$$(1 - y_1' - \chi)^b - (y_1')^b - \frac{1}{P} = 0. \quad (18)$$

In (18), the value of y'_1 is obtained by iteration by Newton-Raphson method.

Relating the geometry of the well and the drill string (geometry of the annulus), it is possible to calculate the specific flow rate using [3]:

$$q_e' = \frac{-1}{\left(\frac{R_1}{R_2}\right)^2 - 1}. \quad (19)$$

Reconnecting the rheology of the fluid with the geometry of the annular space ($P \times q'_t$), the interpolating polynomial is obtained:

$$f(q_t') = P_e. \quad (20)$$

With interpolating polynomial (20) and (19), is possible to find the value of P for the value of $q'_t = q'_e$, that is, $P(q'_e)$.

P_e is the specific pressure that will be used in (8).

The variables V'_1, V'_2, V'_3, y', y'_1, y'_2, y'_3 and q'_t are dimensionless.

D. Algorithm

To obtain the values of P_{su} the following algorithm is used: i) The bilinear transformation given by the expression (4) is used to obtain the equivalent concentric plane and thus the constant value of H is obtained; ii) with the input parameters, rheological and geometric, the value of P is obtained from (14), for each given value of ΔP; iii) with P, the value of y'_1 in (18) is calculated for the combination of the input values ΔP and V_p; iv) the value of y'_1 is replaced in (16), so, the value of the total flow q'_t is obtained for each value of L; v) soon, q'_e is obtained from (19); vi) The graph relating P and q'_t is generated, it presents the relation between the geometry of the annular space and the rheology of the fluid. This graph represents the relation between the geometry of the annular space and the rheology of the fluid. From this relation the interpolating polynomial is created (20) and the value of P_e is obtained, (q'_e, P_e) is the point on the graph (q'_t P) and vii) with the value of P_e the values of the pressures Surge and Swab, P_{su}, can be obtained using (4). The Fig. 8 shows the flowchart produced.

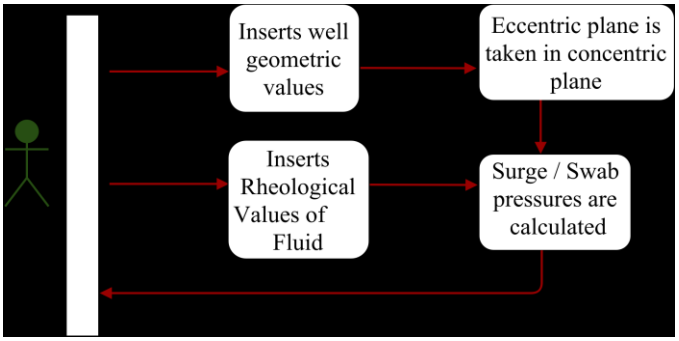

Fig. 8: Algorithm.

V. RESULTS

As results, it is presented the calculation of the Surge pressure in a dummy well using the usual methodology and the proposed methodology. A comparison was made between the values obtained for each methodology. A study was performed on the relationship between eccentricity and pressures values. The maximum eccentricity for the well geometry was calculated.

A. Case Study 1: Eccentricity × Geopressions

To relate the eccentricity to the geopressures it is necessary to have the input parameters. However, the thickness H, in the usual models is not uniform throughout the circumference of the coating column (there is eccentricity). In this way, it is proposed that the drilling of the well be monitored, and at each interval of time Δt, determined by the user, the concentric geometry equivalent is obtained.

All case studies use data from Crespo, which are: i) geometry, considering the well being drilled by drilling column with length L=36 m, diameter d_2=0.254 m and diameter of the coating column d_1=0.508 m and ii) rheological, yield power law fluid with n=0.48, K = 0.74 Pa.s^n e τ_0 = 3.11 N/m^2.

1) Calculation of Geopressure Considering Traditional Methodology: In order to carry out this case study, it is considered the drilling of the well whose radius of the coating column and the radius of the drilling column form concentric geometry. For calculation of the Surge pressure, generated in the descent of the column with constant speed V_p=0.1524 m.s^{-1}, the usual methodology ignores the value of eccentricity. Then the thickness H of the annular space is only the subtraction of the radius of the coating column by the radius of the drilling column H = r_1-r_2 = 0.127m.

Assuming, for all studies, ΔP = 1.38×10^{7}Pa, equivalent to 2000 psi at the bottom of the well, it is possible to obtain the vector P using (14), relating well geometry to fluid rheology. With vector P, it is possible to obtain the vector of the flow rate q'_t.

Using (19), it is possible to obtain q_e=-0.33 and having the interpolating polynomial (20), it is possible to obtain P_e=3.68. Substituting the P_e value in (4), obtains the Surge pressure value, P_{su}=1.84×10^{5}Pa, equivalent to 26,78 psi.

In the real well drilling system, the drill string and casing column do not work concentrically. If there is a maximum eccentricity, when the drill string abuts the casing column, they can stick together, damaging drilling the well.

TABLE I provides the input and output values for the usual model, which does not consider the value of the eccentricity in the calculations.

TABLE I
RESULT CONSIDERING THE USUAL METHODOLOGY

Symbol	Quantity	Value
ψ	eccentricity	0.1257 m
n	behavior index	0.48
K	consistency index	0.74 Pa.s^n
τ_0	yield stress	3.11 N/m^2
r_1	radius of the coating column	0.254 m
r_2	radius of the drilling column	0.127m
P_{su}	Surge	1.84 × 10^{5}Pa

2) Calculation of Geopressure with Eccentric Geometry: To use the geometry of the previous case considering the eccentricity, before using the mathematical model of Crespo, the equivalent concentric geometry must be calculated. The values of R_1 e R_2 of the concentric

plane, are the new rays of the coating column and drilling column, respectively. As the conformal mapping do not change the magnitudes of the system, the values of ΔP remain the same for both eccentric and concentric geometry.

For the geometry under study, there is maximum eccentricity ψ_{max} = 0.1257 m. From this eccentricity, the value of the Surge geopressure can be calculated using the conformal mapping in (4), Which carries the eccentric plane of Fig. 9 (a) in the concentric plane of Fig. 9 (b). The new radius of the concentric plane are R_1 = 0.2806 m for coating column and R_{2m}= 0.2539 m for drill string. From this conformal mapping H = 0.0267 m is obtained.

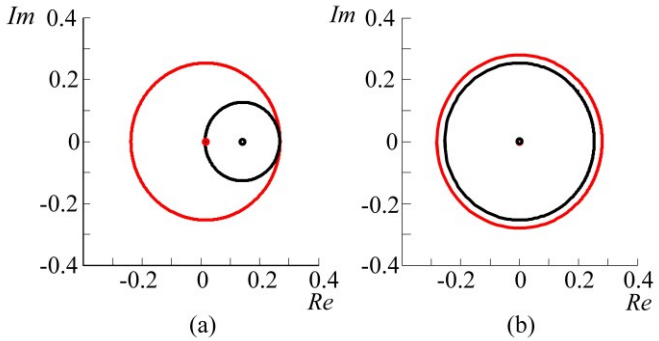

Fig. 9: Real System Transformation (a) Eccentric Plane e (b) Concentric Plane.

Applying the calculations of the mathematical model of the annular space in the new concentric plane, Fig. 9 (b), it is possible to get the value of Surge geopressure of 1.56×10^6 Pa, equivalent to 226.63 psi.

Using the usual methodology, the value of P_{su}=1.84 $\times10^5$ Pa or P_{su}=26.78 psi. Using the proposed methodology and taking into account the eccentricity, it is possible to obtain the value of P_{su} = 226.63 psi. The proposed methodology finds, in this case, a value of approximately 8.46 times higher than the value found by the traditional methodology. A fact that occurs by not considering the eccentricity, which could cause serious problems at the moment of the maneuver.

The TABLE II provides the input and output values for the case study considering the eccentricity and using the proposed methodology.

TABLE II
RESULT CONSIDERING CONSTANT ECCENTRICITY

Symbol	Quantity	Value
ψ	eccentricity	0.1257 m
n	behavior index	0.48
K	consistency index	0.74 Pa.s^n
τ_0	yield stress	3.11 N/m^2
r_1	radius of the coating column	0.254 m
r_2	radius of the drilling column	0.127 m
R_1	radius of the coating column after conformal mapping	0.2806 m
R_2	radius of the drilling column after conformal mapping	0.2539 m
P_{su}	Surge	1.56×10^6Pa

Considering the same input parameters, but with ψ = 0.062 m, the new geometry is calculated. The equivalent concentric plane, has R_1 = 0.4664 m and R_2 = 0.2539 m for the coating column and the drilling column, respectively, as illustrated in Fig. 10.

Applying the calculations of the mathematical model in the new concentric plane, Fig. 10 (b), it is possible to reach the value of P_{su} = 8.642 $\times10^4$ Pa equivalent to P_{su} = 12.51 psi.

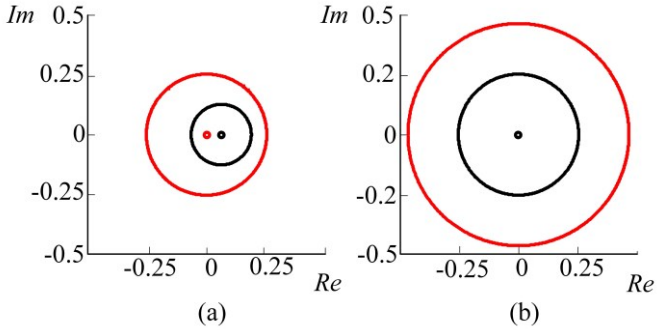

Fig. 10: Real System Transformation (a) Eccentric Plane and (b) Concentric Plane.

This result shows the dynamics of the effect of the eccentricity on the pressures at the bottom of the wells, since all the configurations were maintained, varying only the eccentricity. For average eccentricity, P_{su}= 12.51 psi, 2.14 times lower than the value obtained using the traditional methodology.

The TABLE III provides the input and output values for the case study with ψ = 0.062 m and considering the eccentricity and using the proposed methodology.

TABLE III
RESULT CONSIDERING CONSTANT ECCENTRICITY

Symbol	Quantity	Value
ψ	eccentricity	0. 062 m
n	behavior index	0.48
K	consistency index	0.74 Pa.s^n
τ_0	yield stress	3.11 N/m^2
r_1	radius of the coating column	0.254 m
r_2	radius of the drilling column	0.127 m
R_1	radius of the coating column after conformal mapping	0.4664 m
R_2	radius of the drilling column after conformal mapping	0.2539 m
P_{su}	Surge	8.642×10^4Pa

B. Case Study 2: Calculation of Geopressures with Variation in Eccentricity

Considering also the situation in which the rotary movement of the drill descending into the well causes the drill string and the casing column to generate different eccentric geometries for each depth, that is, ψ is different for each value of $\Delta P/\Delta L$, it is possible to calculate the Surge geopressure in each section of the well. In this case, it is also considered the speed of descent varying in time, speed increases with depth. For this case it varies from $V_p = 0$ to $V_p = 0.1524$ m.s^{-1}.

For this case, the pressure ΔP varies from $\Delta P = 1.37\times10^6$ Pa, on the surface until $\Delta P = 1.38\times10^7$ Pa, at the well bottom.

It is observed that there is variation in the value of the eccentricity because the system is dynamic, and the eccentricity varies in time, so it is possible, using the conformal mapping and considering the variation of the eccentricity $0 < \psi < 0.1257$m, calculate the new H values for the eccentricity vector.

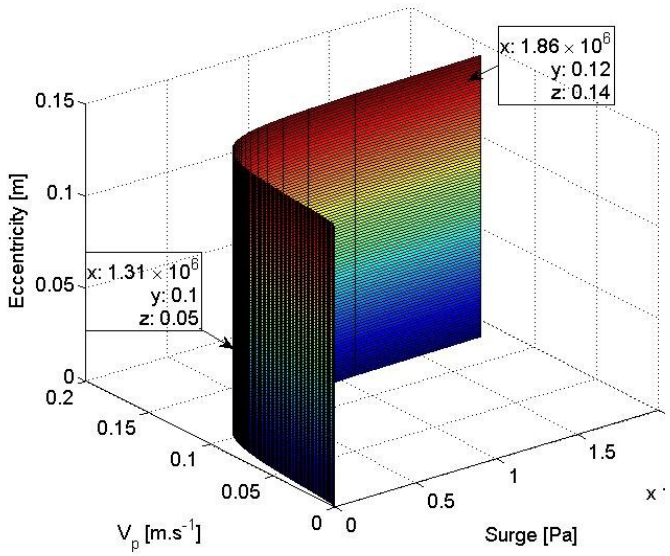

Fig. 11: $P_{su} \times V_p \times \psi$

It is possible to produce the surface that relates the eccentricity, the Surge geopressure and the descent speed of the drill, as shown in Fig. 11.

It is observed in Fig. 11, that higher the descent speed V_p, greater the increase in surge pressure, in this case it would be feasible to establish the maximum velocity of 0.1 m/s, from this point Surge pressure begins to grow exponentially. In the same way, another surface can be produced that relates ψ, Surge and ΔP, as shown in Fig. 12.

Fig. 12 shows that the higher the pressure ΔP inside the well, the higher the Surge pressure. Fig. 12 indicates whether the injected fluid levels are suitable for well geometry.

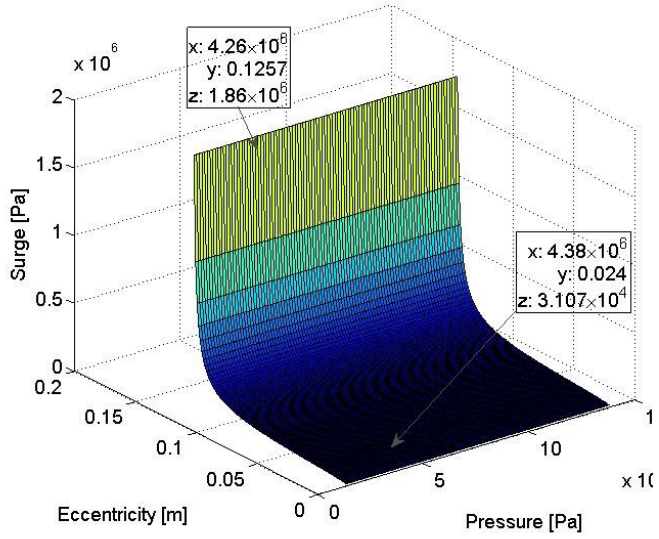

Fig. 12: $\psi \times \Delta P \times P_{su}$

The traditional method and the proposed method start from the same point when there is concentricity. However, for the input data presented (geometry and rheology) and considering variations in eccentricity values and ΔP, it can be observed that the values of Surge for the traditional method are higher than for the proposed method until a certain value. Fig. 13 illustrates the comparison between the traditional method and the proposed method, which considers eccentricity.

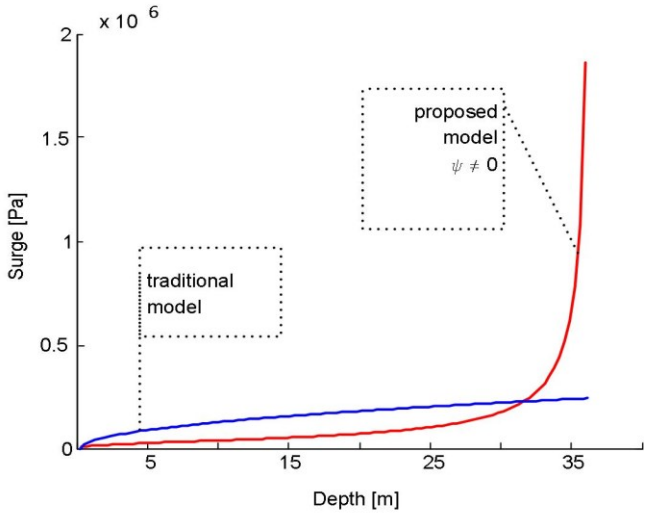

Fig. 13: Comparison between Surge Values Obtained

If the value of Surge pressure is greater than the real one, can cause damage to the formation, therefore, the operating window that contains the pressures and speeds, ideal for safe operation of the maneuvers, has maximum and minimum boundary. If the calculated pressure value is incorrect, hydrostatic fluid will be injected erroneously. The pore pressure may be greater than the rock fracture pressure, and may cause the kick effect. Therefore, it is important to know the operating window, the velocity values that the well supports and the actual geopressure values.

VI. CONCLUSIONS

It is possible to observe that the eccentricity produces incoherence between the adopted model and the real system. With the proposed methodology it is possible to calculate the maximum and minimum pressures, related to the maximum and minimum eccentricities that alter the values of H in the well drilling. The flow depends on pressure range, length of the drill string, well and drill string radius. In turbulent flows the speed of the drilling column and hydrostatic fluid is of great importance for the calculation of the variation of pressure in the bottom of the well. Pressure change increases exponentially with increasing drilling column speed. The increase in pressure also depends on the depth of the well. Pressure variation also depends on annular space, flow rate increases with increasing thickness H. To reduce pressure changes it is important to monitor speed and eccentricity between columns as well as amount of hydrostatic fluid injected into the well. The proposed method is able to calculate the Surge and Swab geopressures for non Newtonian fluids at the bottom of the well, considering the variation of the eccentricity of the same.

REFERENCES

[1] U. F. Silva, M. I. Q. Júnior, G. P. Furriel, A. H. F. *Silva, A. J. Alves,* and W. P. Calixto, "Application of conformal mapping in the calculation of geological pressures," Chilecon, 2015.

[2] L. A. S. Rocha and C. T. Azevedo, Geopressures and Settlement Coatings columns (in Portuguese); 2 edition. Interciência, 2009.

[3] F. Crespo and R. Ahmed, Experimental Study and Modeling of Surge and Swab Pressures for Yield-power-law Drilling Fluids. PhD thesis, University of Oklahoma, 2011.

[4] O. N. Mbee, "Prediction of surge and swab pressure profile for flow of yield power law drilling fluid model through eccentric annuli," Master's thesis, African University of Science and Technology, 2013.

[5] Z. Bing, Z. Kaiji, and Z. Ginghua, "Theoretical study of steady-state surge and swab pressure in eccentricc annulus [j]," Journal of Southwest - China Petroleum Institute, vol. 1, 1995.

[6] W. Calixto, "Application mapping as at the carter factor calculation (in portuguese)," Master's thesis, Federal University of Goias, 2008.

[7] W. F. Rogers, "Compostion and properties of oil well drilling fluids, "Gulf Publishing Co., Houston, TX, 1948.

[8] W. C. Frison, "Apparatus and method for treatment of wells," May 9 1989. US Patent 4,828,033.

[9] D. Amorim Júnior and W. Iramina, "Maneuvers for exchanging drills in *oil wells (in portuguese)," TN Petróleo, vol. 61, pp. 190–194, 2008.*

[10] R. Caenn and G. R. Gray, "Drilling fluid and completion; 6 edition (in portuguese)," Editora Elsevier, pp. 1–5, 2014.

[11] A. G. Karlsen, "Surge and swab pressure calculation: Calculation of surge and swab pressure changes in laminar and turbulent flow while circulating mud and pumping," Institutt for petroleumsteknologi og anvendt geofysikk, 2014.

[12] F. Crespo and R. Ahmed, "A simplified surge and swab pressure model for yield power law fluids," Journal of Petroleum Science and Engineering, vol. 101, pp. 12–20, 2013.

[13] W. P. Calixto, B. Alvarenga, J. C. da Mota, L. d. C. Brito, M. Wu, A. J. Alves, L. M. Neto, and C. F. Antunes, "Electromagnetic problems solvng by conformal mapping: A mathematical operator for optimization (in portuguese)," Mathematical Problems in Engineering, 2011.

[14] H. Kober, Dictionary of Conformal Representations, vol. 2. Dover New York, 1957.

[15] J. C. V. Machado, Rheology and Fluid Flow - Emphasis on Oil Industry (in Portuguese); 2 edition. Editora Interciência, 2002.

Calculation of Grounding Grids Parameter at Arbitrary Geometry

Carlos L. B. Silva, Thyago G. Pires, Wesley P. Calixto, Diogo N. Oliveira, Luis A. P. Souza and Antonio M. Silva Filho

***Abstract*—This paper deals with the computation of ground resistance, surface voltage, touch voltage and step voltage, to mesh with horizontal wires arranged in different angles. The computer program implemented used in the mathematical modeling is based on the method proposed by Heppe, which allows obtaining the grounding parameters for homogeneous soil and soil stratified in two layers. The results obtained with the proposed method will be compared with other methods in literature. Also will be presented the results of a grounding grid using wires at various angles.**

***Index Terms*— Grounding grids parameters, Heppe, soil stratified in two layers.**

I. INTRODUCTION

THE study and analysis of grounding grids brings great concern to engineers, as is the initial step in the process of building a substation. The main purpose of the grounding grid design is to keep the step voltages, touch and electrical resistance to earth within tolerable limits [1].

The classic method of grounding grid design [2] is a method that does not require computing resources and its intended to be easy to use. However, it has some limitations for heterogeneous soil, to the analysis of potential on the ground's surface and the geometry of the ground grid. It can only be used in cases where the wires are equidistant and in grounding grids with the following shapes: square, rectangular, L-shape and T-shape.

The geometry of the grounding grid depends on the area of the substation [3] and several studies prove a greater effectiveness of the unequally spaced grounding grids as regards the trend the touch voltages [4].

The methodology used in this paper to obtain the ground resistance and the potential on the soil surface is based on Heppe [5] using the method of images and the average potential method. The examples shown in [5] used only grids containing conductors placed in parallel and perpendicular to each other, deployed on homogeneous soil. However, our method enables the use of meshes in any relative positions with conductors placed in soil stratified in two layers.

The computer program was developed to implement the mathematical model and allows the calculation of the grounding potential rise, the potential on the soil surface and the ground resistance. The touch voltages and the step voltages obtained from de surface potential.

Some results of grounding grids will be presented in standard formats, which are compared with traditional methods. Results of a ground grid of unconventional geometry are also presented.

II. METHODOLOGY

The grid conductors are conceptually divided in rectilinear segments in order to discretize the system. The accuracy of the modeling is associated with the number of segments used. The greater the number of segments, the more precise is the modeling.

In each segment, it is considered that the distribution of leakage current is constant throughout its length, but distinct from segment to segment. It is assumed that all segments have the same voltage, which is equal to the ground potential rise (GPR).

After the division, the leakage current of each segment and GPR are calculated. Then, the leakage current is used to calculate the ground resistance and the voltage at the ground surface at any desired point. To find the leakage current (i) in each segment the linear equation shown in (1) must be solved. Where m is the number of segments.

$$\begin{aligned} &R_{11}\cdot i_1 + R_{12}\cdot i_2 + R_{13}\cdot i_3 + \cdots + R_{1m}\cdot i_m = v_1 \\ &R_{21}\cdot i_1 + R_{22}\cdot i_2 + R_{23}\cdot i_3 + \cdots + R_{2m}\cdot i_m = v_2 \\ &R_{31}\cdot i_1 + R_{32}\cdot i_2 + R_{33}\cdot i_3 + \cdots + R_{3m}\cdot i_m = v_3 \\ &\vdots \\ &R_{m1}\cdot i_1 + R_{m2}\cdot i_2 + R_{m3}\cdot i_3 + \cdots + R_{mm}\cdot i_m = v_m \end{aligned} \tag{1}$$

The above system can be written in matrix form as:

$$\begin{bmatrix} R_{11} & R_{12} & R_{13} & \cdots & R_{1m} \\ R_{21} & R_{22} & R_{23} & \cdots & R_{2m} \\ R_{31} & R_{32} & R_{33} & \cdots & R_{3m} \\ \vdots & \vdots & \vdots & \ddots & \vdots \\ R_{m1} & R_{m2} & R_{m3} & \cdots & R_{mm} \end{bmatrix} \cdot \begin{bmatrix} i_1 \\ i_2 \\ i_3 \\ \vdots \\ i_m \end{bmatrix} = \begin{bmatrix} v_1 \\ v_2 \\ v_3 \\ \vdots \\ v_m \end{bmatrix} \tag{2}$$

The total current injected into the grid (i_g) is equal to the sum of leakage current of all segments, as shown in (3).

$$\sum_{k=1}^{m} i_k = i_g \tag{3}$$

Appending (3) in (2), we have:

$$\begin{bmatrix} R_{11} & R_{12} & R_{13} & \cdots & R_{1m} & -1 \\ R_{21} & R_{22} & R_{23} & \cdots & R_{2m} & -1 \\ R_{31} & R_{32} & R_{33} & \cdots & R_{3m} & -1 \\ \vdots & \vdots & \vdots & \ddots & \vdots & \vdots \\ R_{m1} & R_{m2} & R_{m3} & \cdots & R_{mm} & -1 \\ 1 & 1 & 1 & \cdots & 1 & 0 \end{bmatrix} \cdot \begin{bmatrix} i_1 \\ i_2 \\ i_3 \\ \vdots \\ i_m \\ GPR \end{bmatrix} = \begin{bmatrix} 0 \\ 0 \\ 0 \\ \vdots \\ 0 \\ i_g \end{bmatrix} \tag{4}$$

Thus the GPR becomes a system variable, because the total current injected into the grid is usually a project information and not the potential of electrodes.

Next, computation of mutual and self-resistance of (4), the ground resistance and voltages will be explained. All terms are calculated for each individually segment, without any symmetry of the grid as used in [5]. To calculate the mutual resistance and the voltage at the ground surface the method of images is used.

A. Mutual Resistance

The mutual resistance (R_{jk}) is the ratio of the voltage produced on the segment k by leakage current of segment j. The symmetry of mutual resistance allows. The self-resistance (R_{jj}) is the ratio between the voltages produced on the segment by its own leakage current.

Considering a soil composed of two layers with the upper layer having resistivity ρ_1 and depth H, and lower layer having resistivity ρ_2 and extending to a great depth. The mutual resistance between a segment j and a segment k, and their images, buried at the same depth (D) in the upper layer of soil is given by (5) and in the bottom layer is given by (6).

Considering a soil composed of two layers with the upper layer having resistivity ρ_1 and depth H, and lower layer having resistivity ρ_2 and extending to a great depth. The mutual resistance between a segment j and a segment k, and their images, buried at the same depth (D) in the upper layer of soil is given by (5) and in the bottom layer is given by (6).

Fig. 1 is the corresponding diagram to the terms of (8) and (9). The images of segment are in different planes. The point C is in the same plane of segment AB and point G is in the same plane of segment EF.

$$R_{jk} = \frac{\rho_1}{4 \cdot \pi \cdot L_j \cdot L_k} \cdot \left\{ \sum_{n=0}^{\infty} K^n \cdot [M(2 \cdot n \cdot H) + M(2 \cdot n \cdot H + 2 \cdot D)] + \sum_{n=1}^{\infty} K^n \cdot [M(2 \cdot n \cdot H) + M(2 \cdot n \cdot H - 2 \cdot D)] \right\} \tag{5}$$

$$R_{jk} = \frac{\rho_2}{4 \cdot \pi \cdot L_j \cdot L_k} \cdot \left[M(0) - K \cdot M(2 \cdot H - 2 \cdot D) + (1 - K^2) \cdot \sum_{n=0}^{\infty} K^n \cdot M(2 \cdot n \cdot H + 2 \cdot D) \right] \tag{6}$$

Where K is the reflection factor.

$$K = \frac{\rho_2 - \rho_1}{\rho_2 + \rho_1} \tag{7}$$

The term M is given by (8), for $0 \le \theta \le \pi$.

$$M(CG) = \underline{CB} \cdot \ln\left(\frac{BF + \underline{B'F}}{BE + \underline{B'E}}\right) - \underline{CA} \cdot \ln\left(\frac{AF + \underline{A'F}}{AE + \underline{A'E}}\right) + \underline{GF} \cdot \ln\left(\frac{BF + \underline{F'B}}{AF + \underline{F'A}}\right) - \underline{GE} \cdot \ln\left(\frac{BE + \underline{E'B}}{AE' + \underline{E'A}}\right) - \frac{CG \cdot \delta}{\sin\theta} \tag{8}$$

The term δ is the following equation:

$$\delta = \tan^{-1}\left(\frac{CG}{BF \cdot \tan\theta} + \frac{\underline{CB}}{CG} \cdot \frac{\underline{GF} \cdot \sin\theta}{BF}\right) - \tan^{-1}\left(\frac{CG}{BE \cdot \tan\theta} + \frac{\underline{CB}}{CG} \cdot \frac{\underline{GE} \cdot \sin\theta}{BE}\right) - \tan^{-1}\left(\frac{CG}{AF \cdot \tan\theta} + \frac{\underline{CA}}{CG} \cdot \frac{\underline{GF} \cdot \sin\theta}{AF}\right) + \tan^{-1}\left(\frac{CG}{AE \cdot \tan\theta} + \frac{\underline{CA}}{CG} \cdot \frac{\underline{GE} \cdot \sin\theta}{AE}\right) \tag{9}$$

In the case of parallel segments, when θ decrease towards zero, the term $CG.\Omega /sin\ \theta$ approaches $BE+AF-BF-AE$.

To compute the self-resistance a hypothetical segment parallel and identical to the original segment separated by a distance equal to the radius of the conductor is considered.

B. Ground Resistance

The ground resistance (R_g) is the ratio between the GPR, computation with (4), and the total current injected into the grid.

$$R_g = GPR / i_t \tag{10}$$

C. Voltage on Soil Surface

Once the leakage currents in each segment is found, the voltage at a point on the soil surface due to the contribution of a leakage current of a segment located in a upper layer is

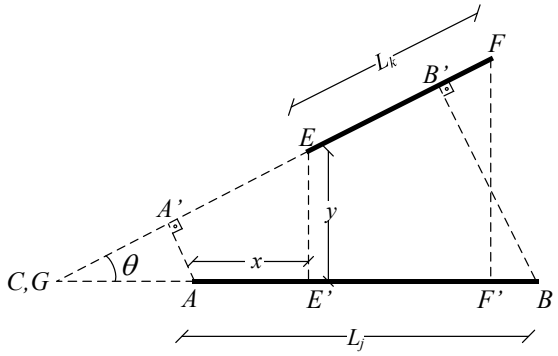

Fig. 1. Angled segments.

calculated by (11) and of a segment located in a bottom layer is calculated by (12).

$$V = \frac{i \cdot \rho_1}{2 \cdot \pi \cdot L} \cdot \left\{ \ln\left(\frac{\sqrt{x^2 + y^2 + D^2} + x}{\sqrt{(x-L)^2 + y^2 + D^2} + x - L} \right) + \sum_{n=1}^{\infty} K^n \cdot \left[\ln\left(\frac{\sqrt{x^2 + y^2 + (2 \cdot n \cdot H + D)^2} + x}{\sqrt{(x-L)^2 + y^2 + (2 \cdot n \cdot H + D)^2} + x - L} \right) + \ln\left(\frac{\sqrt{x^2 + y^2 + (2 \cdot n \cdot H - D)^2} + x}{\sqrt{(x-L)^2 + y^2 + (2 \cdot n \cdot H - D)^2} + x - L} \right) \right] \right\} \quad (11)$$

$$V = \frac{\rho_1 \cdot i \cdot (1+K)}{2 \cdot \pi \cdot L} \cdot \left\{ \ln\left(\frac{\sqrt{(x_p - L)^2 + y_p^2 + D^2} + L - x_p}{\sqrt{x_p^2 + y_p^2 + D^2} - x_p} \right) + \sum_{n=1}^{\infty} K^n \cdot \left[\ln\left(\frac{\sqrt{(x_p - L)^2 + y_p^2 + (2 \cdot n \cdot H + D)^2} + L - x_p}{\sqrt{x_p^2 + y_p^2 + (2 \cdot n \cdot H + D)^2} - x_p} \right) \right] \right\} \quad (12)$$

Therefore, the voltage at a point on the soil surface is calculated by superposition, by the sum of the contribution of all segments.

D. Touch, Mesh and Step Voltages

With the surface voltages, the other voltages can be determined. The touch voltages is the potential difference between the GPR of a ground grid and the surface potential at the point where a person could be standing while at the same time having a hand in contact with a grounded structure. Furthermore, the mesh voltage is the maximum touch voltage within a mesh of ground grid. Moreover, the step voltage is the difference in surface potential that could be experienced by a person a distance of 1m with the feet without contacting any grounded object.

III. RESULTS

Three case studies are presented. The case studies 1 and 2 perform the validation of the proposed method by comparing VCM with traditional methods. Case study 1 compare the values of the ground resistance of the grids with square mesh by other methods. Case study 2 compare the ground resistance, mesh voltage and step voltage with the design procedure in [6]. Finally, case study 3 show the results for an unconventional grid.

A. Case Study 1

Table I shows the ground resistance values for a square grid (20m x 20m) and a rectangular grid (40m x 10m) in homogeneous soil. The ground resistance values are calculated using the simplified calculations provided in the ANSI-IEEE Std. 80/2013: Dwight [7], Laurent and Nieman [6], Sverak [8] and Schwarz [9]. In addition to the calculations presented by Nahman [10] and Chow [11]. The BEM method (Boundary Element Method) is obtained from [12] and VCM is computed with the method presented in this paper. The values in parentheses are the percentage differences from the values calculated by VCM [15].

The grounding grid features used as program inputs are:

d = 0.01 m (diameter of the conductor)
D = 0.5 m (depth of burial)
ρ = 100 Ωm (soil resistivity)

TABLE I
GROUND RESISTANCE

Method	Square (20mx20m)		Rectangular (40mx10m)	
	4 meshes	*16 meshes*	*4 meshes*	*16 meshes*
Dwight	2.2156 (15.9%)	2.2156 (6.4%)	2.2156 (6.8%)	2.2156 (3.2%)
Laurent	3.0489 (15.7%)	2.7156 (14.7%)	2.9848 (25.5%)	2.6918 (25.4%)
Sverak	2.9570 (12.2%)	2.6236 (10.8%)	2.8929 (21.6%)	2.5998 (21.1%)
Schwarz	2.8084 (6.6%)	2.6035 (10.0%)	2.4690 (3.8%)	2.3211 (8.15%)
Nahman	3.6367 (38.1%)	3.1491 (33.0%)	-	-
Chow	4.8017 (82.3%)	3.2621 (37.8%)	-	-
BEM	2.6269 (0.3%)	2.3631 (0.2%)	2.2734 (4.4%)	2.0795 (3.1%)
VCM	2.6343	2.3669	2.3784	2.1461

B. Case Study 2

This case study compares VCM with traditional method [6] for two grids in a soil stratified in two layers, rectangular grid and L-shape grid. To calculate the classic method was used the methodology of [13] to find the apparent resistivity. The features of the soil and of two ground grids used as program inputs are:

ρ_1 = 200 Ωm (upper layer resistivity)
ρ_2 = 400 Ωm (bottom layer resistivity)
H = 8 m (depth of the upper layer)
D = 0.5 m (depth of burial of ground grid)
d = 5 mm (wire diameter)
ΔL = 5 m (distance between parallel conductors)
i_g = 1000 A (total current injected into the grid)

Fig. 2 show a rectangular grid with dimensions 35m x 20m containing 28 meshes. The apparent resistivity seen by grid is 253.33Ωm. For the classic method the ground resistance was 4.87Ω, the mesh voltage (V_m) was 1019.95V and the step voltage (V_s) was 687.77V. With VCM the ground resistance was 4.66 Ω, the mesh voltage was 927.92V in the corners, the maximum step voltage within the grid was 250.32V and the step voltage in the corners was 509.82V.

Assuming a T-shaped grid as show in Fig. 3 with 18 meshes and dimensions 30m x 25m, the apparent resistivity seen by grid is 246.67Ωm. According IEEE Std. 80-2013 [6], the ground resistance was 6.00 Ω, the mesh voltage was 1278.20V and the step voltage was 830.82V. Calculating by VCM the

ground resistance was 5.40 Ω, the mesh voltage was 1168.56V and the step voltage was 330.63V within the grid and 639.80V in the top corners.

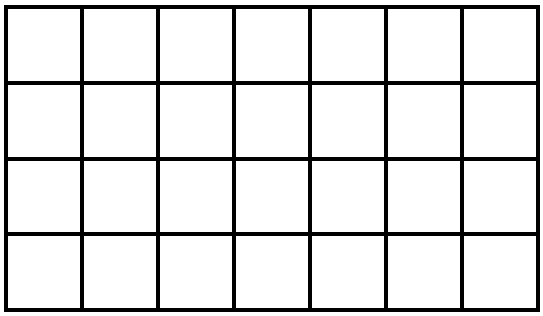

Fig. 2. Rectangular grid – 35m x 20m.

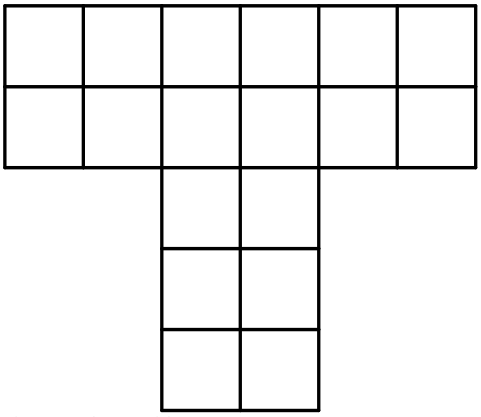

Fig. 3 T-shape grid – 30m x 25m.

Table II show the results found to the grids above with the difference of VCM to ANSI-IEEE Std. 80/2013.

TABLE II
PARAMETERS WITH IEEE STD. 80 AND VCM

Grid	Data	Method		Difference
		Std. 80	*VCM*	
Rectangular 35mx20m	R_g (Ω)	4.87	4.66	4.31%
	V_m (V)	1019.95	927.92	9.02%
	V_s (V)	687.77	509.82	25.87%
T-Shape 30mx25m	R_g (Ω)	6.00	5.40	10.00%
	V_m (V)	1278.20	1168.56	8.58%
	V_s (V)	830.82	639.80	22.99%

C. *Case Study 3*

Figure 7 show a grounding grid of 120m x 80m, with variable spacing between the conductor. The profiles of the potential at the soil surface in the lines indicated by A,B,C and D obtained by the method proposed in this work are compared with the results of Huang [1]. The following input data used:

ρ_a = 200 Ωm (apparent ground resistivity)
D = 0.6 m (depth of burial of ground grid)
d = 8.75 mm (wire diameter)
i_g = 10000 A (total current injected into the grid)

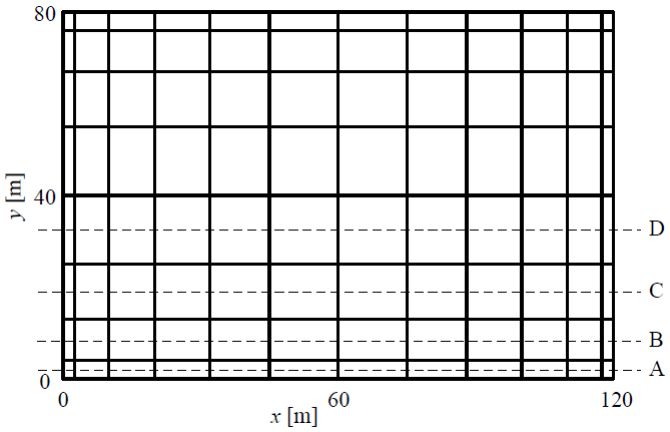

Fig. 7 Grounding grid with different spacing.

Figure 8 shows the potential on the soil surface profile obtained.

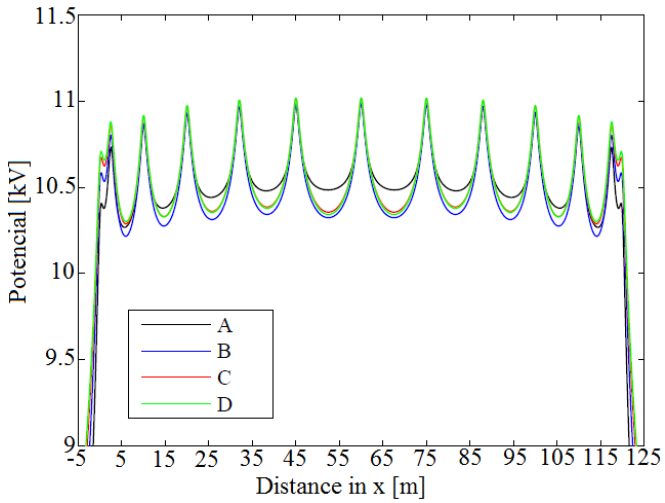

Fig. 8 Profiles on the soil surface, results obtained by the proposed method.

The potential on the soil surface with geographic location of coordinates x = 1.25m and y = 2.0m, obtained in the work of Huang [1] is 10.37kV while by the proposed method is 10.40kV. The result obtained for the soil surface potential with geographic location of coordinates x = 52.5m and y = 32.5m in the work of Huang [1] is 10.23kV and by the proposed method is 10.34kV.

Figure 9 shows the distribution of the equipotential through isolines. Potential peaks observed at the intersections of the electrodes, except at the border of the grid where potential reduction occurs. The maximum potential at the soil surface occurs in coordinate x = 60m and y = 40m, with a value of 11.33kV.

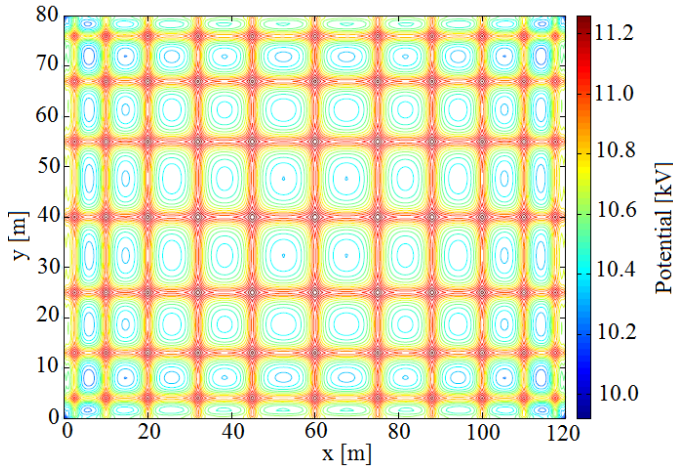

Fig. 9 Equipotential distributed on the soil surface.

The maximum surface potential obtained at the central point of the grid due to the symmetrical distribution of the electrodes around the point.

Case Study 4

It presented a grid composed of conductors at different angles and different lengths as show in the Fig. 10. The grid has 16 meters in the x-axis and 17 meters in the y-axis [14]. The following input data were used:

ρ_1 = 200 Ωm (upper layer resistivity)
ρ_2 = 400 Ωm (bottom layer resistivity)
H = 8 m (depth of the upper layer)
D = 0.5 m (depth of burial of ground grid)
d = 5 mm (wire diameter)
i_g = 1200 A (total current injected into the grid)

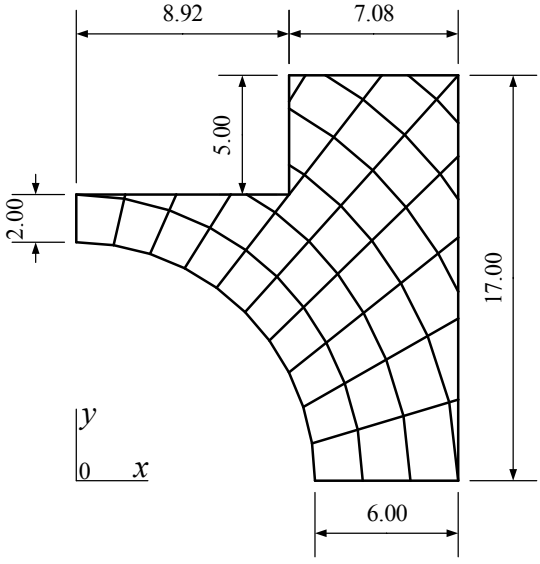

Fig. 10 Unconventional grid.

Fig. 11 shows the voltage profile in three dimensions and contour of the soil surface potential inside the perimeter of the ground grid.

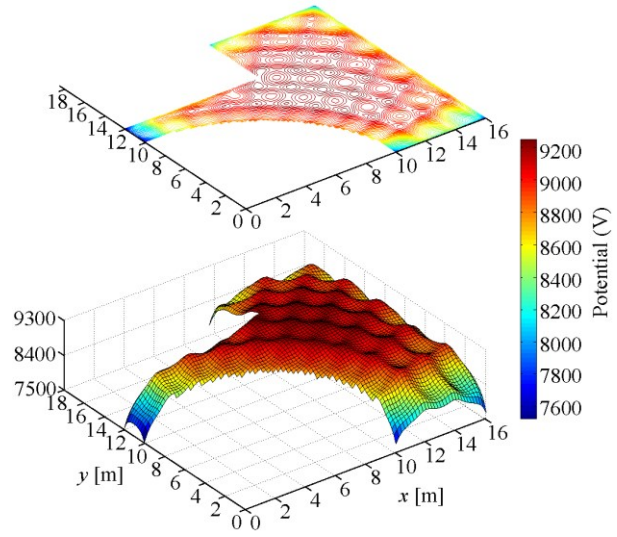

Fig. 11 Surface Potential.

All voltages calculated for points on the surface located within the perimeter of the mesh. The value obtained for the ground resistance was 8.0Ω, for mesh voltage was 2075.98V at the coordinates x = 0m and y = 10m; and the maximum step voltage was 925.04V between the point of coordinates x_1 = 16m and y_1 = 17m, and the point of coordinates x_2 = 15.36m and y_2 = 16.23m. The GPR was 9595.60V and the maximum surface voltage (V_{surf}) is 9245.45V at the coordinates x = 9.8m e y = 10.0m.

D. Study Case 5

The study case presented to verify the influence of the depth of the grounding grid, the ground grid used shown in Figure 10, and the depth varied from 0.5m to 3.5m. The potential profiles on the surface were obtained from the cut at y = 11m in the grounding grid shown in Figure 10. Table III show the values obtained for the resistance of the grounding grid, GPR, the maximum potential at the ground surface, the touch voltage and the maximum step voltage for different depths of the ground grid. The following input data used:

ρ_1 = 200 Ωm (upper layer resistivity)
ρ_2 = 400 Ωm (bottom layer resistivity)
H = 2 m (depth of the upper layer)
D = 0.5m – 3.5m (depth of burial of ground grid)
d = 5 mm (wire diameter)
i_g = 1200 A (total current injected into the grid)

The Table IV show the coordinate maximum of the surface potential and step voltage.

Fig.12 and Fig.13 shows the elevation of the ground resistance values and the GPR of the ground grid, which are directly proportional.

TABLE III
GROUNDING GRID PARAMETERS AT DIFFERENT DEPTHS

D(m)	R_g (Ω)	GPR(V)	V_s (V)	V_{touch} (V)	V_{step} (V)
0.5	9.93	11916.08	11626.38	2377.19	1103.1
1.0	9.64	11565.18	11223.86	2771.30	984.57
1.5	9.48	11371.17	10984.02	3040.44	847.52
1.6	9.46	11350.29	10948.32	3094.98	826.73
1.7	9.45	11337.78	10917.37	3154.29	808.28
1.8	9.45	11337.74	10892.96	3223.90	792.26
1.9	9.47	11363.41	10881.04	3320.62	779.05
2.0	9.68	11620.32	10965.79	3687.02	773.77
2.1	16.89	20270.30	11231.81	12577.11	762.37
2.2	16.85	20219.40	11140.67	12611.32	739.89
2.3	16.78	20138.91	11047.19	12610.62	718.45
2.4	16.71	20050.57	10953.58	12598.41	698.02
2.5	16.63	19960.81	10860.20	12581.82	678.55
3.0	16.29	19549.73	10396.24	12501.50	593.77
3.5	16.02	19224.64	9937.84	12459.86	525.35

TABLE IV
COORDINATE MAXIMUM OF THE SURFACE POTENTIAL AND STEP VOLTAGE.

Parameter	Coordinates
V_{step}	x = 16.0m and y = 17.0m x = 12.4m and y = 16.3m
V_s	x = 0m and y = 20m

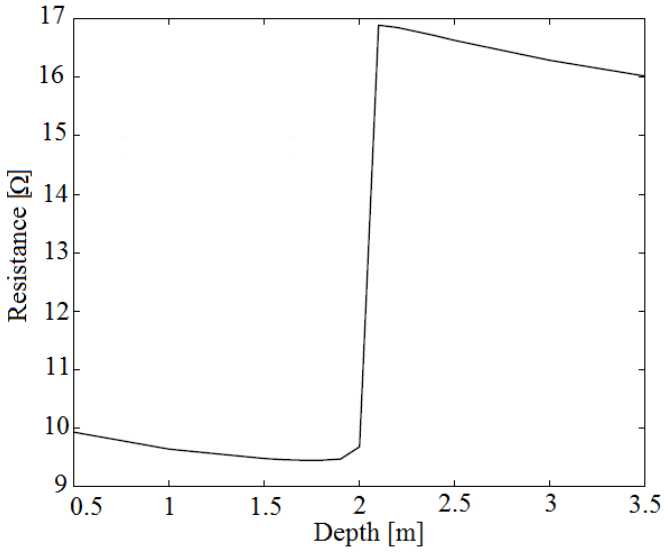

Fig. 12 Resistance (R_g) versus depth (D).

The boundary between the first and second soil layers occurs exactly in D = 2m. The potential on the soil surface increases in the depths just below to this border (Figure 14).

Figure 15 shows the increase of the touch voltage near the boundary between the soil layers, since the grounding grid when positioned in the second soil layer, which has a higher resistivity (400Ω.m) in relation to the first layer that has lower resistivity (200Ω.m), produces higher touch potential.

Figure 16 shows that the pitch voltage decreases smoothly with increasing depth, having a level in the depths near the boundary between the layers.

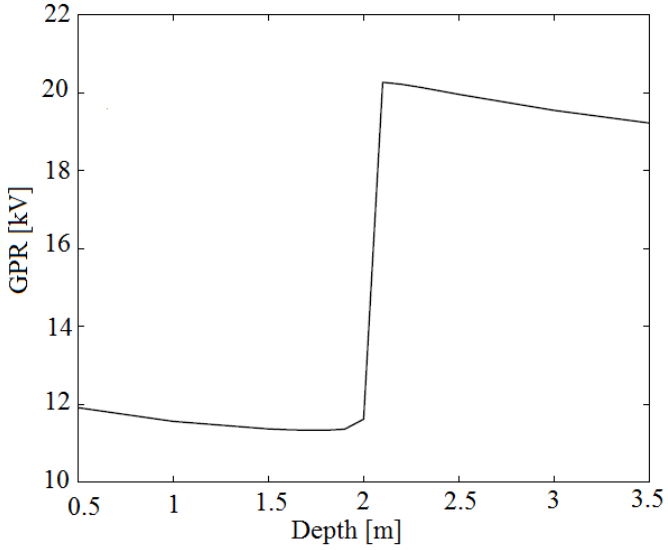

Fig. 13 GPR versus depth (D).

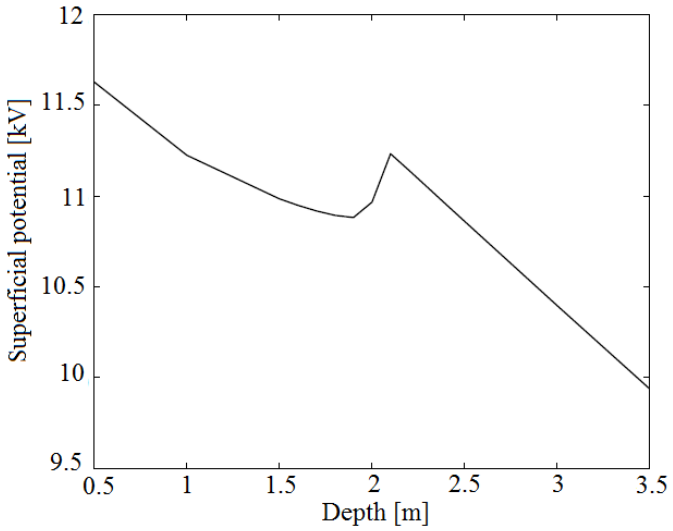

Fig. 14 Superficial potential (V_s) versus depth (D).

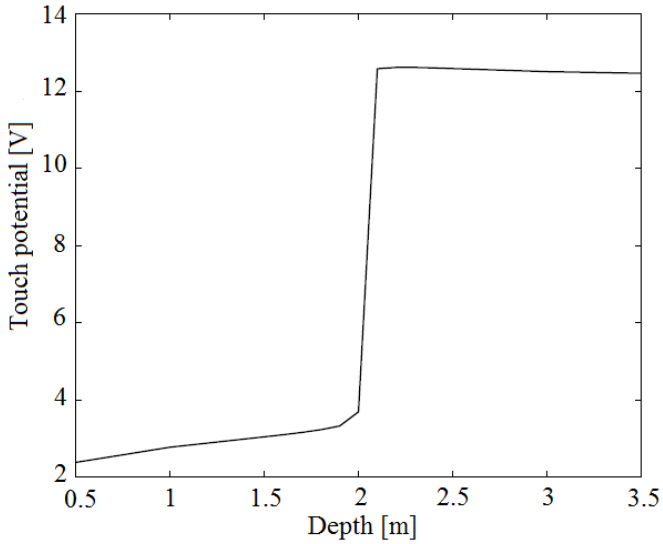

Fig. 15 Touch potential (V_t) versus depth (D).

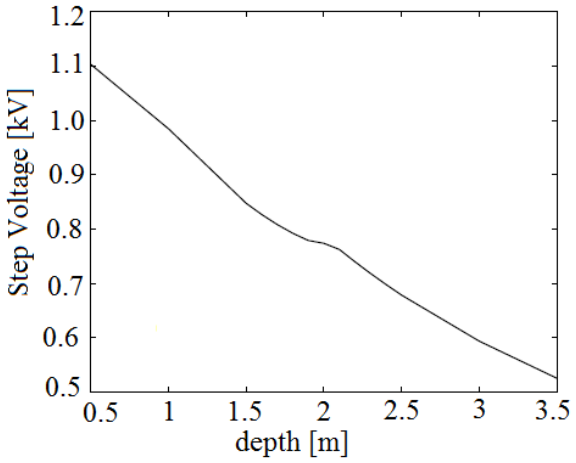

Fig. 16 Surface Potential.

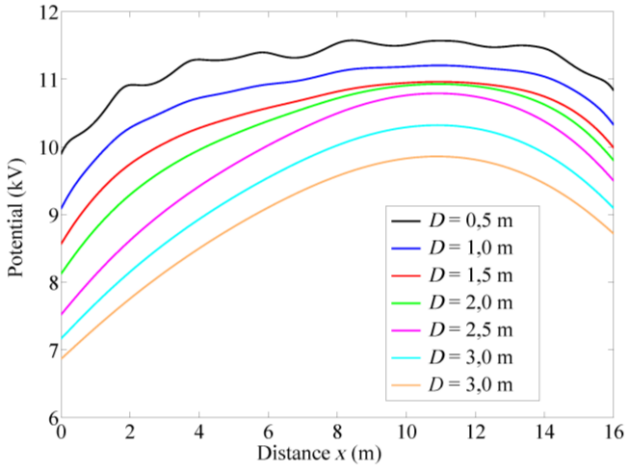

Fig. 17 Surface Potential.

Figure 17 illustrates the potential profiles at the soil surface at y = 11 m for the different depths of the grounding grid, where it is observed, reduction of potential with the increase of the depth of the grounding grid, reduction in the number of peaks along the distance.

IV. Conclusion

The method implemented in this paper allows the computation of the ground resistance, grid voltage and step voltage of grids composed by horizontal wire electrodes in shapes that are more complex. Wire segments can have any position or displacement among them.

The difference between the results obtained with this method and those of the ANSI-IEEE Std. 80/2013 for the grounding resistance was up to 25.5%. For grid voltage was up to 16.6% and 41.9% for step voltage. The individual calculation of the leakage current for each segment leads to a greater precision of the method.

This method also proves to be useful for allowing a precise analysis of the voltage on the soil surface, it is possible to calculate the voltage at any desired point. Also, the detailed study of any grounding grid at any depth in the soil is possible.

V. Acknowledgement

The authors thank the National Counsel of Technological and Scientific Development (CNPq), Coordination for the Improvement of Higher Level Personnel (CAPES) and the Research Support Foundation for the State of Goias (FAPEG) for financial assistance to this research.

References

[1] L. Huang, X. Chen, and H. Yan, "Study of unequally spaced grounding grids," *Power Delivery, IEEE Transactions on,* vol. 10, pp. 716-722, 1995.

[2] IEEE, "Guide for Safety in AC Substation Grounding," in IEEE Std 80 (Revision of IEEE Std 80-2000/ Incorporates IEEE Std 80-2013/Cor 1-2015), ed, 2015.

[3] B. Thapar, V. Gerez, A. Balakrishnan, and D. A. Blank, "Simplified equations for mesh and step voltages in an AC substation," *Power Delivery, IEEE Transactions on,* vol. 6, pp. 601-607, 1991.

[4] A. Covitti, G. Delvecchio, A. Fusco, F. Lerario, and F. Neri, "Two Cascade Genetic Algorithms to Optimize Unequally Spaced Grounding Grids with Rods," in *Computer as a Tool, 2005. EUROCON 2005.The International Conference on*, 2005, pp. 1533-1536.

[5] A. J. Heppe, "Computation of Potential at Surface Above an Energized Grid or Other Electrode, Allowing for Non-Uniform Current Distribution," *Power Apparatus and Systems, IEEE Transactions on,* vol. PAS-98, pp. 1978-1989, 1979.

[6] "IEEE Guide for Safety in AC Substation Grounding," IEEE Std 80-2013 (Revision of IEEE Std 80-2000/ Incorporates IEEE Std 80-2013/Cor 1-2015), pp. 1-226, 2015.

[7] H. B. Dwight, "Calculation of Resistances to Ground," *American Institute of Electrical Engineers, Transactions of the,* vol. 55, pp. 1319-1328, 1936.

[8] J. G. Sverak, "Sizing of Ground Conductors Against Fusing," *Power Apparatus and Systems, IEEE Transactions on,* vol. PAS-100, pp. 51-59, 1981.

[9] S. J. Schwarz, "Analytical Expressions for the Resistance of Grounding Systems [includes discussion]," *Power Apparatus and Systems, Part III. Transactions of the American Institute of Electrical Engineers,* vol. 73, 1954.

[10] J. Nahman and S. Skuletich, "Irregularity Correction Factors for Mesh and Step Voltages of Grounding Grids," *Power Apparatus and Systems, IEEE Transactions on,* vol. PAS-99, pp. 174-180, 1980.

[11] Y. L. Chow and M. M. A. Salama, "A simplified method for calculating the substation grounding grid resistance," *Power Delivery, IEEE Transactions on,* vol. 9, pp. 736-742, 1994.

[12] S. S. M. Ghoneim, "Optimization of grounding grids design with evolutionary strategies," Thesis (PhD), Faculty of Enginnering Sciences, Univeristät Duisburg-Essen, Duisburg, Germany, 2007.

[13] J. Endrenyi, "Evaluation or Resistivity Tests for Design of Station Grounds in Nonunirorm Soil," *Power Apparatus and Systems, IEEE Transactions on,* vol. 82, pp. 966-970, 1963.

[14] Pires, Thyago G. ; Nerys, Jose W. L. ; Silva, Carlos L. B. ; Oliveira, Diogo N. ; Filho, Antonio M. Silva ; Calixto, Wesley P. ; Alves, Aylton J., Computation of resistance and potential of grounding grids in any geometry. In: 2016 IEEE 16th International Conference on Environment and Electrical Engineering (EEEIC), 2016, Florence. 2016 IEEE 16th International Conference on Environment and Electrical Engineering (EEEIC), 2016.

[15] Pires, Thyago G. ; Silva, Carlos L. B. ; Oliveira, Diogo N. ;Nerys, Jose W. L. ; Alves, Aylton J.; Calixto, Wesley P. Computation of grounding grids parameter on unconventional geometry. In: 2015 CHILEAN Conference on Electrical, Electronics Engineering, Information and Communication Technologies (CHILECON), 2015, Santiago. 2015.

Model predictive for Mobile robot control

Alireza Rezaee

***Abstract*—This paper proposes a Model Predictive Controller (MPC) for control of a P2AT mobile robot. MPC refers to a group of controllers that employ a distinctly identical model of process to predict its future behavior over an extended prediction horizon. The design of a MPC is formulated as an optimal control problem. Then this problem is considered as linear quadratic equation (LQR) and is solved by making use of Ricatti equation. To show the effectiveness of the proposed method this controller is implemented on a real robot. The comparison between a PID controller, adaptive controller, and the MPC illustrates advantage of the designed controller and its ability for exact control of the robot on a specified guide path.**

***Index Terms*—robot, control, model, prediction.**

I. Introduction

Model Predictive Controllers (MPC) are widely adopted in industry as effective tools for dealing with large scale multi-variable and multi-constrained control problems (Guang et al,2005; Camacho and Bordons, 1999; Nagy et al, 2005). The main idea of MPC lies in online construction of the system model, predicting its future states and generating the required control actions by repetitive solution of an optimal control problem. Issues may arise for guaranteeing closed-loop stability, model uncertainty handling and reducing the on-line computations.

There are three kinds of MPC controller schemes that use different methods for system modeling but are similar to each other in control process (Likar et al, 2007) :

1- MAC: uses impulse response for system modeling,
2- GPC : uses transfer function for system modeling,
3- DMC: uses step response for system modeling.

These controllers optimize a cost function that depends on the control law (Hauge et al, 2002).

Although DMC is primarily developed for control of chemical processes (Camacho and Bordons, 1999; Garcia et al., 1989; Limon et al, 2005), it has been extended successfully to other applications such as motorway traffic systems (Bellemans et al, 2006), switching max-plus-linear discrete event systems and simplified model of biped walking models(van et al, 2006; Azevedo et al, 2002) . However implementation of this control scheme in robotics has been less reported and seems to be in still in its infancy (Limon et al, 2005; Kouvaritakis et al, 2006). In this work we concentrate on application of MPC/DMC controllers in position control of robotic systems.

The rest of this paper is organized as follows: The next section presents the idea of MPC controller, section 3 describes P2AT robot, section 4 discusses the effect of variation of DMC parameters on speed error, section 5 discusses results of the experimental implementation of MPC/DMC on a real robot, and finally the last section contains the conclusions.

Assistant Professor of Department of system and Mechatronics Engineering, *Faculty of New Sciences and Technologies*, University of Tehran, Tehran, Iran, arrezaee@ut.ac.ir.

II. Model Predictive controller

The main strategy of a model predictive controller is illustrated in Figure 1. In a typical MPC algorithm the system outputs are predicted for a certain interval of time (prediction horizon) by making use of a proper system model which is constructed based on the information (inputs and outputs) gathered from the system past as well as future control signals that have to be determined properly. As shown in the figure the control signal is a sequence of step functions with variable amplitude. Amplitudes of these inputs are obtained by solving an optimization problem that tries to keep the system output close to the reference set point. Objective function of this problem is usually a quadratic function of the difference between the predicted output signals and the reference trajectory.

All the MPC algorithms using a linear model have similar behavior. Here we demonstrate how DMC works.

$$Y = A\Delta u + Y_0 \tag{1}$$

Where A includes the step response, Y is the predicted output, Y0 is past output, and u is the control law (Azevedo et al, 2002, Shridhar and Cooper, 1997).

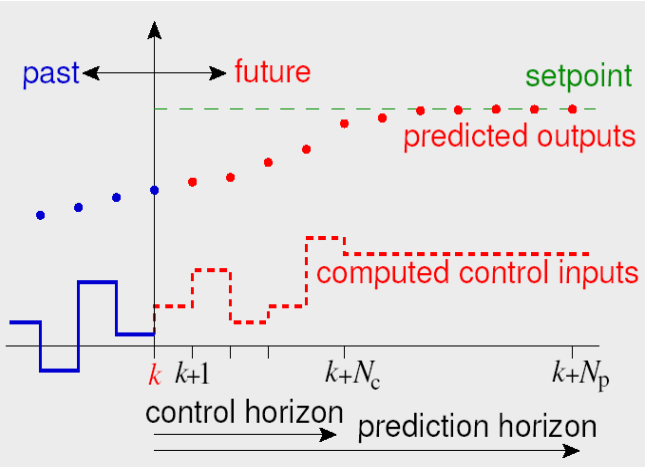

Fig.1. Methodology of MPC.

Due to uncertainities of the model it is very hard to achieve the exact value of A to satisfy the desired bahavior. To compansate for this problem an error term is added to the system output:

$$correction = y_n^p - y_n \tag{2}$$

$$\hat{Y} = A\Delta u + Y_0 + \begin{bmatrix} y_1^p - y_1 \\ \dots \\ y_n^p - y_n \end{bmatrix} = A\Delta u + Y_0 + E_f \tag{3}$$

Where the correction term represents the difference between the current plant actual output and the output extracted from the model. The error vector over prediction horizon is then written as

$$E = R - \hat{Y} = R - A\Delta u - Y_0 - E_0 \tag{4}$$

Using the above expression a quadratic cost function, J, can be defined which is minimized to obtain the optimal controller

$$\min_{\Delta u} J = E^T W_1 E + \Delta u^T W_2 \Delta u \tag{5}$$

where W1 and W2 are constants. The modified control law is obtained as:

$$\Delta u = (A^T W_1 A + W_2)^{-1} A^T W_1 E' \equiv K_c E' \tag{6}$$

Fig. 2 shows the structure of a model predictive controller. In this configuration the block labeled as "Model" contains the model of the robot that predicts the behavior of the robot over a certain time horizon. The Future Inputs (u(t+k|t)) are calculated under constrains and by optimizing a cost function. This process continues until the end of the trajectory.

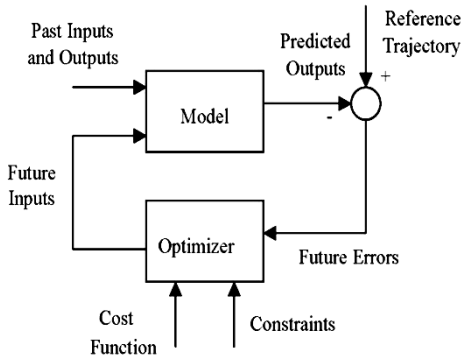

Fig. 2. The structure of a MPC.

A. *The Algorithm of a DMC controller*

The algorithm of a DMC controller is as follows:

1- Obtain model of the robot to be controlled.

2- Use the model to predict behavior of the robot over a certain time horizon.

3- Calculated the E from equation (4).

4- Determine the control action by optimizing a performance index, which typically is the error between the outputs predicted from the model and the desired output over the time horizon.

5- Apply the optimal control actions and then measure robot outputs over the time horizon. The measured values at the final stage will be used as initial conditions of the model in the next iteration.

6- Repeat steps 2 to 5 until the end of the trajectory.

III. ROBOT CONTROL

For robot control with MPC controller we need to have the model equation of the robot (Fig. 3). The robot under consideration in this study is a four wheel P2AT robot in which wheels of the robot are controlled independently.

Fig. 3. P2AT robot.

In order to obtain the system model and design the proper controller for it, a sound appreciation of dynamic behavior of

the system is needed. To do that a simple sketch of the robot is shown if Fig. 4, it is assumed that the distance between each wheel is constant and four wheels have the same radius. Kinematic model of the robot is described by

$$x(k+1)=\begin{bmatrix}x(k+1)\\ y(k+1)\\ \theta(k+1)\end{bmatrix}$$
$$=\begin{bmatrix}x(k)+\vartheta(k)\Delta t\cos(\theta(k))\cos(\alpha(k))\\ y(k)+\vartheta(k)\Delta t\sin(\theta(k))\cos(\alpha(k))\\ \theta(k)++\vartheta(k)\Delta t\sin(\alpha(k))/L\end{bmatrix}=F[z(k)]=F[x_m(k),u(k)]$$

$$S_i=\frac{(\dot{X}-a\dot{\cos}\theta)}{\cos\theta}-\frac{L}{2}w\dot{\theta}$$

$$S_o=\frac{(\dot{X}-a\dot{\cos}\theta)}{\cos\theta}+\frac{L}{2}w\dot{\theta} \quad (7)$$

Where $u(k)=[\vartheta(k),\alpha(k)]^T$ is the control vector for motion tracking,Δt is the sample period and S_i and S_o denote speed of the left and right wheels respectively and the distance between wheels is shown by L and w. Moreover, a is the distance between reference point of the robot and the wheels. Additionally, the position of the robot in global reference frame is specified by coordinates X and Y. The angular difference between the global and local reference frames is given by θ.

Such a non-linear system is open loop controllable, which can be linearised in order to use traditional linear feedback control to regulate the robot. But if the robot operates over a large range in its state space, especially when the robot turns around corners, the linearization of the kinematics will lead to the loss of controllability. Since the MPC's models are based on linear regressions.

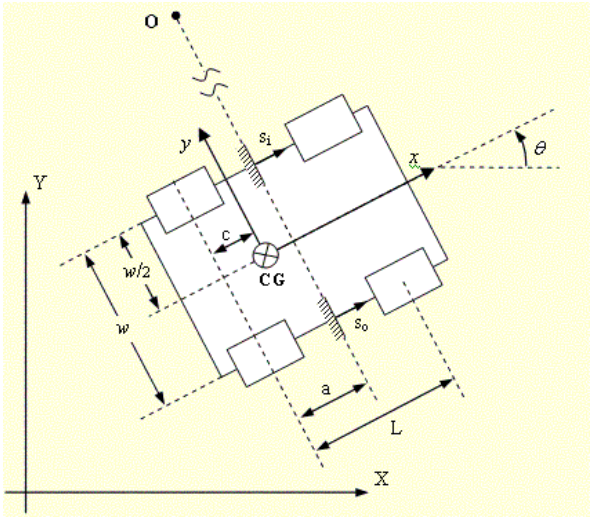

Fig. 4. Schematic of the P2AT robot.

IV. The Effect of DMC Parameters on Controller Performance

Due to the simple nature of the linear mathematical models (Mayne et al, 2000; Axehill, 2004; Axehila, 2004) most of the MPCs including impulse and step response models and the transfer function model are based on this type of model description (Dougherty and cooper, 2004; Gilbert and Tan., 1991). Thus, the first step in controller design is to linearize the model equations and then calculate the control laws. Figure 5 shows the schematic of the MPC controller that is connected to the system (robot). Rest of this paper is devoted to study effect of different parameters of the model on the controller performance. To do that a series of experiments were conducted on a simple straight path and speed of robot was measured for different instances (Figs. 6-13).

MPC controller is to optimize a cost index J(x(k),u(k))) under the constraints of formula 7:

$$\min_{u(k)}J(x(k),u(k)) \quad (8)$$

The current control vector is chosen to minimise thee state errors and control energy over several steps in future so that the path tracking of the robot is smooth aand stable. Therfore, the cost index can be expressed as

$$J=\frac{1}{2}\sum_{i=N_1}^{N_2}\|x_r(k+i)-x(k+i)\|^2+\frac{1}{2}\sum_{i=1}^{N_\mu}\lambda_i\|\Delta u(k+i-d)\|^2 \quad (9)$$

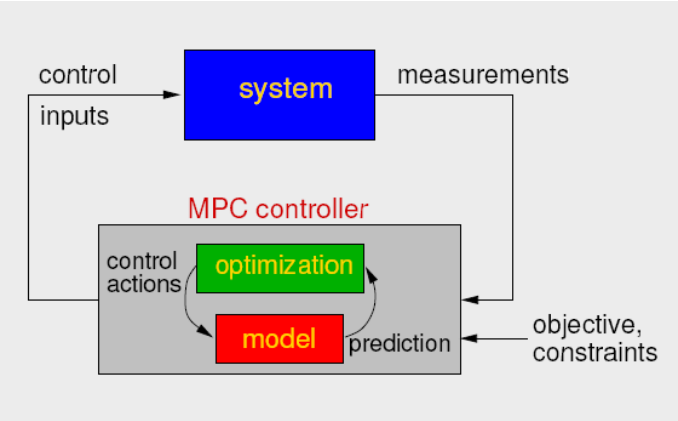

Fig. 5. Connection between MPC controller and the system (robot).

A. *Effect of M (control horizon)*

Figures 6, 7 show the effect of control horizon parameter, M, on the control output and control law respectively. It is observed that by increasing value of M the settling time is decreased and the control effort is increased. This also increases the computational complexity. According to the experimental results the optimal value of m selected as 2.

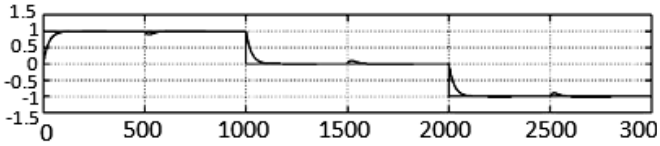

M=1, N=20, P=5, α=0.5, W2=0.

(a)

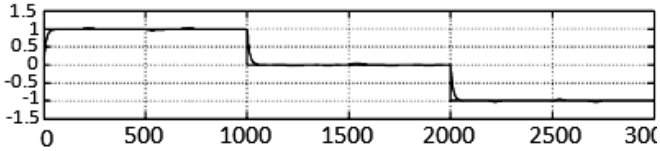

M=2, N=20, P=5, α=0.5, W2=0.

(b)

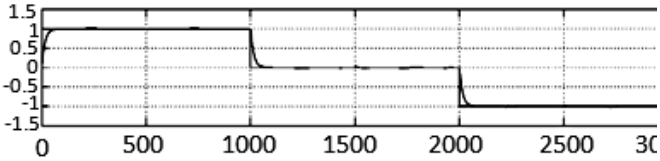

M=4, N=20, P=5, α =0.5, W2=0.

(c)

Fig .6. output.

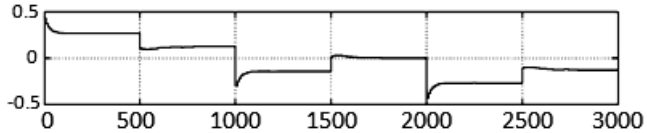

M=1, N=20, P=5, α =0.5, W2=0.

(a)

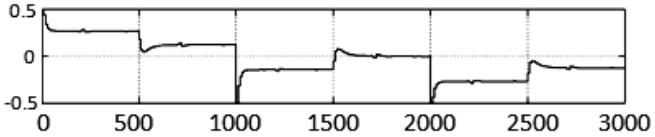

M=2, N=20, P=5, α =0.5, W2=0.

(b)

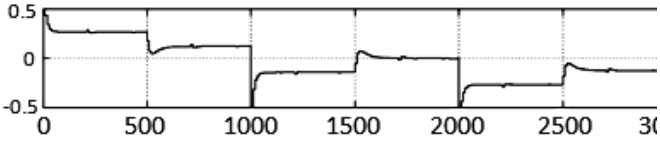

M=4, N=20, P=5, α =0.5, W2=0.

(c)

Fig.7.control law

B. *Effect of P (prediction horizon)*

Figures 8, 9 show the system output and control law for two different values of parameter P respectively. It can be seen that by increasing value of P the settling time is decreased and the control effort is increased and the computational complexity is increased simultaneously.

.

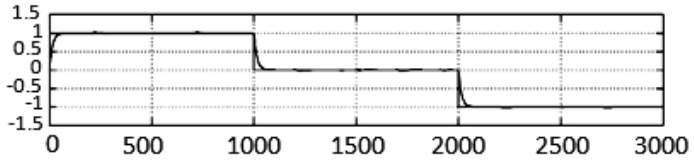

M=2, N=20, P=3, α =0.5, W2=0.

(a)

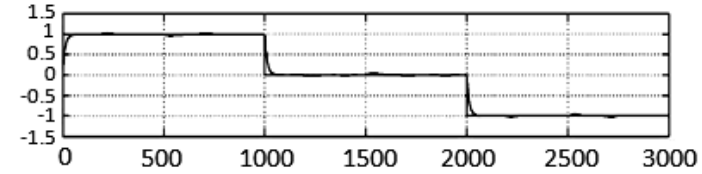

M=2, N=20, P=10, α =0.5, W2=0.

(b)

Fig. 8. output

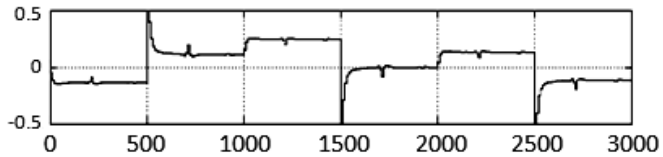

M=2, N=20, P=3, α =0.5, W2=0.

(a)

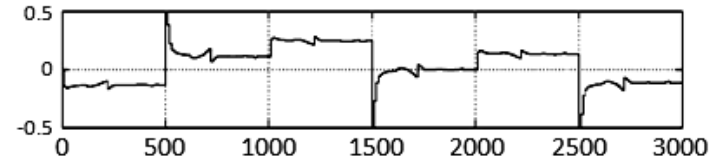

M=2, N=20, P=10, α =0.5, W2=0.

(b)

Fig. 9. control law.

C. *Effect of W2*

Figures 10, 11 show the effect of changing weight factor W2 (See Eq. 5) on the system output and the control law. It is seen that by increasing the value of W2 increases the settling time while the control effort is decreased and computational complexity is not changed.

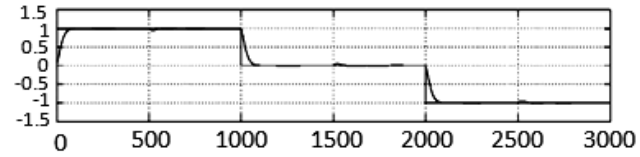

M=2, N=20, P=5, α =0.5, W2=0.1.

(a)

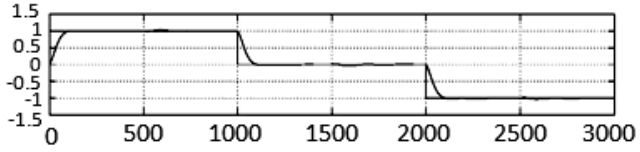

M=2, N=20, P=5, α =0.5, W2=1.

(b)

Fig.10. output.

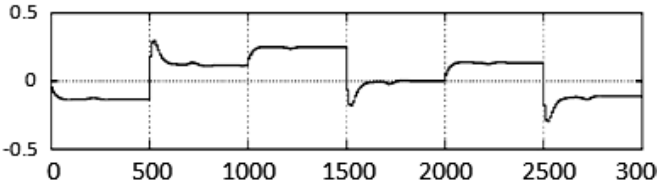

M=2, N=20, P=5, α =0.5, W2=0.1.

(a)

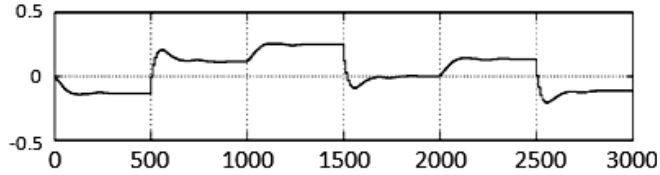

M=2, N=20, P=5, α =0.5, W2=1.

(b)

Fig.11. control law.

D. Effect of α

Figures 12 and 13 show the effect of variation of α used in the input signal filter band and applied on the control output and control law respectively. According to these figure increasing the value of α, increases the settling time and decreases the control effort. However the computational complexity is not changed.

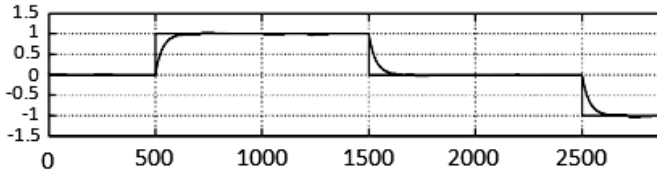

M=2, N=20, P=5, α =0.7, W2=0.

(a)

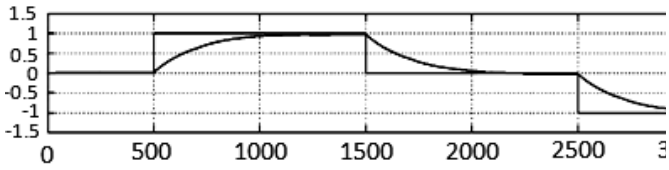

M=2, N=20, P=5, α =0.9, W2=0.

(b)

Fig. 12. Output.

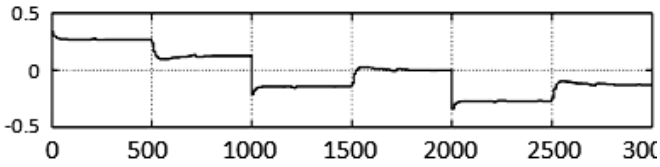

M=2, N=20, P=5, α =0.7, W2=0.

(a)

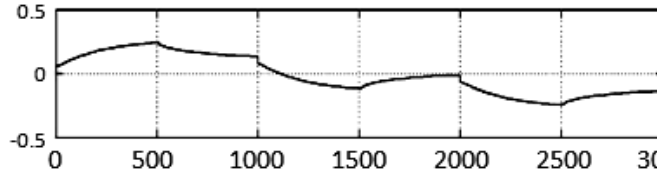

M=2, N=20, P=5, α =0.9, W2=0.

(b)

Fig.13control law.

V. COMPARISON OF MPC WITH OTHER CONTROL MODELS

To show the effectiveness of the MPC controller three different controllers (MPC, PID and adaptive) are implemented on P2AT mobile robot and the system is tested in an elliptical path (Fig. 14).

PID control tuning is described at (Gu et al,1997)

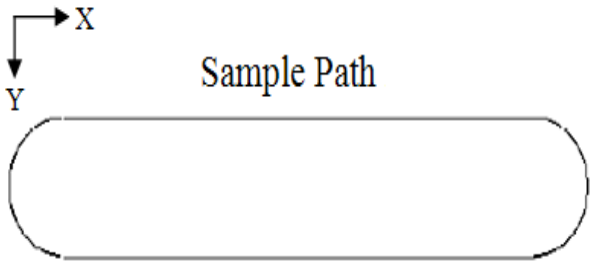

Fig.14.elliptical path.

Figures 15-17 show the error and its first derivative for different controllers. Moreover the real path moved by the robot is given in the subplots. As figure 17 shows, the MPC controller has a lower error compared to the other control methods and can track the path more precisely.

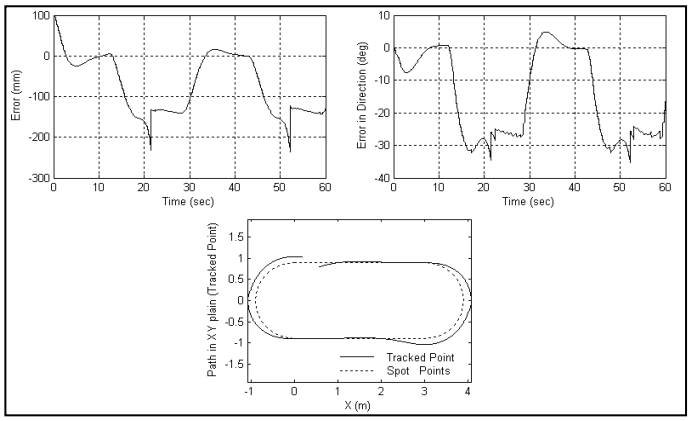

Fig.15.Robot path with PID controller.

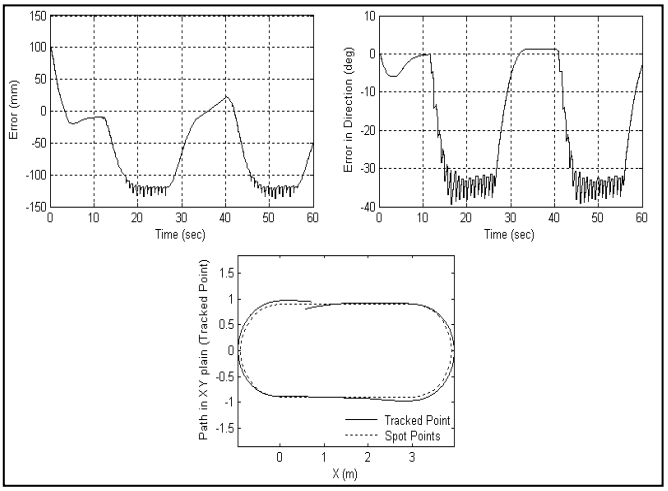

Fig. 16. Robot path with adaptive controller.

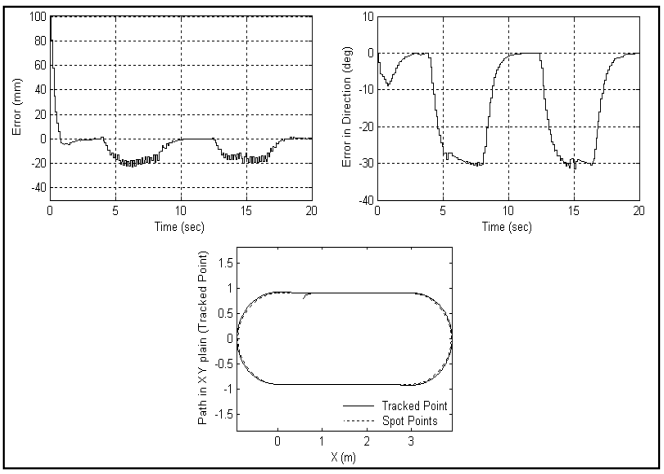

Fig.17. Robot path with MPC controller.

VI. CONCLUSION

In this paper implementation of MPC controller on P2AT robot was explained. The conducted experiments show effectiveness of the proposed method on control of the mobile robot. Furthermore the effects of the model parameters such as control horizon, prediction horizon, weighting factor and signal filter band on the controller performance were studied. Finally, a comparison between the designed MPC controller and PID and adaptive controllers was presented demonstrating superior performance of the Model Predictive Controllers.

REFERENCES

[1] Guang, Li., Lennox, B., Zhengtao, Ding., 2005, Infinite horizon model predictive control for tracking problems,

[2] Control and Automation,. ICCA '05. International Conference on, pages 516 – 521.

[3] Camacho, E.F., Bordons, C., 1999. Model Predictive Control , Springer-Verlag 2 edition.

[4] Nagy, Z. , Franke, R., Mahn, B., Allg , ower, F., 2005, Real-time implementation of nonlinear model predictive control of inite time processes in an industrial,framework. In International Workshop on Assessment and Future Directions of Nonlinear Model Predictive Control, Germany, pages 483-490.

[5] Likar, B., Kocijan, J., 2007, Predictive control of a gas-liquid separation plant based on a Gaussian process model. Computers & Chemical Engineering, 31(1):142–152.

[6] Hauge, T.A., Slora, R. and Lie, B., Model Predictive Control of a Norske Skog , Preliminary Study, in proceedings of Control Systems,2002, June 3-5, Stockholm, Sweden, pages 75-79.

[7] Garcia, C.E., Prett, D.M, Morari, M., 1989. Model Predictive Control: Theory and Practice, A Survey. Automatica, 25(3):335-348.

[8] Limon, D., Álamo, T., Camacho, E.F., 2005. Enlarging the domain of attraction of MPC controllers, Automatica.

[9] Kouvaritakis, B., Cannon, M., Couchman, P., 2006, MPC as a tool for sustainable development integrated policy assessment. IEEE Transactions on Automatic Control, 51(145–149).

[10] Bellemans, B., Schutter, D., De Moor, B., 2006, Model predictive control for ramp metering of motorway traffic: A case study, Control Engineering Practice, 14(7): 757-767.

[11] van den Boom, T.J.J., De Schutter, B., 2006. MPC of implicit switching max-plus-linear discrete event systems - Timing aspects, Proceedings of the 8th International Workshop on Discrete Event Systems (WODES'06), Ann Arbor, Michigan, pages 457-462.

[12] Azevedo, C., Poignet, P., Espiau, B., 2002. Moving horizon control for biped robots without reference trajectory. In IEEE International Conference on Robotics and Automation, pages 2762–2767.

[13] Shridhar, R., Cooper, J., 1997. A Tuning Strategy for Unconstrained SISO Model Predictive Control. England: Chem..

[14] Mayne, D.Q., Rawlings, J.B, Rao, C.V., Scokaert, P., 2000. Constrained model predictive control: Stability and optimality. Automatica, 36:789-814.

[15] Axehill D., 2004. A Preprocessing Algorithm with Applications to MPC, 43th IEEE Conference on Decision and Control.

[16] Axehila, D., 2004. A Preprocessing Algorithm with Applications to MPC , Fifth Conference on Computer Science and Systems Engineering, Norrköping, Sweden, October 21.

[17] Dougherty D., Cooper, D., 2004. A practical multiple model adaptive strategy for single- loop MPC.

[18] Gilbert, E. G., Tan., 1991. K., Linear system with state and control constraints: The theory and application of maximal output admissible sets. IEEE Transactions on Automatic Control, 36:1008-1020.

[18]D. Gu, H. Hu, M. Brady, F. Li,1997, Navigation System for Autonomous Mobile Robots at Oxford, *Proceedings of International Workshop on Recent Advances in Mobile Robots, Leicester, U.K.*, , 1-2: 24-33.

Alireza Rezaee received his B.Sc. degree in Control Engineering from Sharif University of Technology, Iran 2002 and M.Sc and Ph.D degree in Electrical Engineering from Amirkabir University of Technology, Iran (2005 and 2011 respectively). From 2013 till now he is an assistance professor in department of system and mechatronics engineering in new sciences and technology faculty at university of Tehran. His research interest are in intelligent robotics, mobile robot, navigation, machine learning, bayesian networks, cognitive science

Hybrid Optimization Process Applied to Tuning of Dynamic Matrix Control: Study Case with DC Motor

Douglas Freire de Carvalho, Cleber Asmar Ganzaroli, Luiz Alberto do Couto, Rafael Nunes Hidalgo Monteiro Dias, Wesley Pacheco Calixto

***Abstract*—This paper presents study about Dynamic Matrix Control (DMC) controller applied to speed control of DC motor. DMC controller parameters (prediction horizon, control horizon and damping rate of reference) are obtained through optimization methods employing heuristic, deterministic and hybrid strategies. The use of advanced control technique combined with using of optimization methods aims to achieve highly efficient control, reducing the transient state period and variations in steady state. These methods were applied on a simulation model in order to verify which one provides better control results.**

***Index Terms*—Predictive Control, Deterministic Optimization, Heuristic Optimization, Hybrid Optimization, DC motor.**

I. Introduction

DIRECT current (DC) motors are used in various situations ranging from residential applications to purposes of industrial scale. Utilization of DC motors implies, often, in its speed control. Aiming to do a high quality speed control of DC machines several number of techniques has been developed [1].

Control systems techniques are employed seeking to promote proper implementation of processes, generally, controlling manipulated system variables to obtain desired values for output system variables [2]. Control systems techniques are often applied to control speed of DC machines aiming to promote proper implementation of processes.

Model based Predictive Control (MPC) refers to determinate class of control algorithms that seek to obtain optimal control signal minimizing certain objective function, explicitly using process model. By calculating series of actions of manipulated variables, the MPC seeks, overall, that the system output reaches its reference trajectory. MPC have been developed seeking to solve problems of process control in industrial environment, particularly in oil industry, being initially proposed by Richalet at 1978, proposing the Model Predictive Heuristic Control (MPHC) and by Cutler & Remaker at 1980, proposing the Dynamic Matrix Control (DMC) [3]. MPC are employed in various areas being widely accepted by industry and academia, applicable to various systems (multivariable, nonlinear, with high dead time, constrained variables, etc.).

Currently DMC is the most popular MPC algorithm, widely used for control of chemical processes and with good results in several other applications. DMC become widely popular in industry for present intuitive operation and provide significant results [4]. DMC is based on use of step response finite model of the system to be controlled and its control strategy is presented in time domain, being more intuitive than systems modeled in state space. Applications of DMC controller for linear systems without restrictions present analytical solutions for objective function minimization problem, reducing computational costs. However, nonlinear systems or with dead time and imposition of restrictions to system are met clearly and efficiently by DMC controller [5].

Given the complexity of some problems and the search for efficient and robust controllers, controllers' optimization is presented as interesting proposal. Implementation of controllers' optimization process, generally, seeks to define optimized values for controller variables, aiming to reduce the error between reference proposed and output of controlled system [6].

The literature presents various optimization methods that can be divided into two distinct groups: i) deterministic and ii) heuristic methods. Deterministic methods follow fixed sequence from a defined starting point, returning always the same output value if the starting point is maintained. Heuristic methods seek optimal solution promoting stochastic variations from possible solutions sets, this strategy results in unpredictable sequences and return different optimal values each run, even keeping the initial conditions [6].

Both optimization methods, deterministic and heuristic, present advantages, being not possible determinate the best method for all cases. In general, heuristic methods present better results when looking for solutions in large search spaces. Deterministic methods present better performance in smaller search spaces, close to starting point.

Aiming to combine features of different methods, hybrid optimization methods are implemented seeking for better solutions that any of individuals methods could present. Hybrid optimization methods combines two or more other

Authors thank the National Counsel of Technological and Scientific Development (CNPq), the Research Support Foundation for the State of Goiás (FAPEG) and the Coordination for the Improvement of Higher Education Personnel (CAPES) for financial assistance to this research.

optimization methods to solve problems. Hybrid methods could either choosing one method depending on the data, or switching between them over the course of algorithm. The hybrid optimization methods combining heuristic and deterministic methods are widely presented in literature. In general, these hybrid methods combines the amplitude and reliability of heuristic methods with accuracy of deterministic methods [9].

II. METHODOLOGY

A. Modeling and simulation of direct current motors

The DC motor has mathematical models known in the literature, [8]. Generally, models are composed of two parts: the electrical and mechanical. In equating of electrical part, the parameters are resistance Ra and inductance La of armature. In equating of mechanical part, we have the moment of inertia J and viscous friction coefficient B. The relation between the two parties is realized through constants of torque Kt and back EMF Kb. The mathematical model of DC motor can be represented, in frequency domain, by the block diagram of Fig. 1.

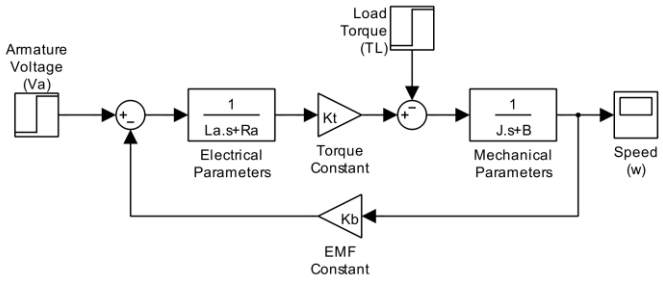

Figure 1. DC motor block diagram

Based on diagram shown in Fig. 1 and on the multiple systems reduction theory, became possible to obtain two transfer functions. In (1) the speed ω against the armature voltage Va and in (2) the speed ω against the load torque TL.

$$\frac{\omega(s)}{V_a(s)} = \frac{K_t}{\alpha s^2 + (\beta + \gamma)s + \delta + K_t K_b} \qquad (1)$$

$$\frac{\omega(s)}{T_L(s)} = \frac{-L_a \cdot s - R_a}{\alpha s^2 + (\beta + \gamma)s + \delta + K_t K_b} \qquad (2)$$

where: α = La · J, β = La · B, γ = Ra · J e δ = Ra · B.

B. Dynamic Matrix Control

Dynamic Matrix Control (DMC) controller enables inclusion of restrictions imposed by system to its basic structure making its application more efficient. The inclusion of restrictions in control law enable the DMC controller to perform actions on the system boundary, really close the restrictions. In systems such as speed control of DC motors, where the breakdown of machine restrictions causes serious injury, the use of DMC controller is highly suggested [5].

DMC controller implements the classic strategy of predictive controllers. Classical MPC strategy seeks to select the best possible set of control signals, within predetermined horizon, making explicit use of controlled process model. This application of DMC use the DC motor step response model to predict speed of the DC motor.

Another important part of classical MPC strategy is the implementation of moving horizon. The use of previous data indicates the current state of the process. In this application the past speed of DC motor and armature voltage are used in controller to increase its accuracy.

Beyond use of past data, moving horizon strategy limit the application of control signal proposed. This limitation occurs in order to update the data for increased accuracy. Repetition of steps mentioned at each sampling instant results in an increase in computational cost and an increase in controller accuracy.

Moving horizon strategy is completed by updating the data and proposing a new set of control signals at each sampling instant. Great care must be taken to enable the controller to perform all operations within the sampling period.

Fig. 2 illustrates the configuration of MPC algorithm. Parts of controller are illustrated, clearing the DMC strategy applied.

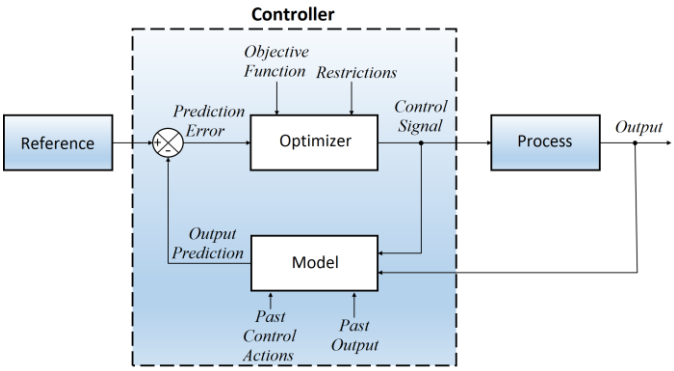

Figure 2. MPC controller block diagram

Restrictions of peak current Ip [A] and nominal armature voltage VN [V] aimed at ensuring proper functioning of DC motor. The non-compliance of these restrictions cause bad engine operation and may cause irreversible damage to the machine. Insertion of these restrictions in DMC control law enables the controller to safely operate, close to the limits of machine, providing improved speed control performance.

The parameters of DMC controller to be optimized are: Prediction horizon R, Control horizon L and damping rate of reference signal α

C. Controllers Optimization

Controllers' optimization aims, by choosing of values to controller's optimizable variables, minimize error between output of controlled system and proposed reference [6]. Deterministic, heuristic hybrid optimization methods are implemented to DMC controller applied to speed control of DC motor in order to compare them and establish which

method provides best results. The best optimization method will provide the controller with less transient period and greater stability in steady state.

The deterministic method to be applied will be the Quasi-Newton (QN) method, the heuristic method will be the Genetic Algorithm (GA). The hybrid method will combine the capacity to cover wide range of values from GA and accuracy of QN [9].

Given the fact that optimization methods seek to minimize defined fitness function, having no deep knowledge of system that pretends optimize, such optimization methods may suggest configurations that will bring damage to DC motor. Seeking to prevent that optimization methods propose gains to controllers that will bring damage to DC motor some penalties have been imposed to fitness function. These penalties are defined by maximum limits for armature voltage and current to the DC motor to be controlled.

The evaluation function to be used by all controllers' optimizators is the Integral of Absolute Error (IAE), calculated basing on error between speed reference and speed developed by DC motor IAEω. Taking penalties and evaluation function cited the fitness function is given by:

$$f(x) = IAE\omega \cdot (\kappa + \nu) \qquad (3)$$

where: $\kappa = Ia_{max} - I_p$ and $\nu = Va_{max} - V_N$, to $\kappa > 0$ and $\nu > 0$

The results given by (3) qualifies the controllers optimized. The best optimization method delivery the process with less error between proposed reference and speed developed by DC motor. The penalties have great influence, taking care of safety operation of DC motor. At end, the best optimization method delivery the process with minor errors, i.e., minor fitness function value.

III. Results

A. Modeling and simulation of direct current motors

To perform the simulation, real parameters obtained from a commercial DC motor was used. These parameters are shown in Tab. I.

Table I
DC motor parameters

$J = 0.032000167\ Kgm^2$	$L_a = 0.027089\ H$
$B = 0.0022069\ Nms/rad$	$R_a = 6.898\ \Omega$
$K_t = 1.073\ Nm/A$	$K_b = 1.073\ V/rad/s$
$V_a = 230.0\ V$	$I_p = 33.38\ A$

Applying the DC motor parameters obtained in (1), becomes possible to verify that the system has two real and distinct poles. Then, it is expected that the system response to input of step type is of over-dumped type as illustrated in Fig. 3.

The Fig. 3 present the speed developed by DC motor referred throughout experiment, being the input of the unit step type. The existing variation in instant t = 10 s is caused due to load torque insert with numerical value of 2% of system reference value, being equal to TL = 0.02 N · m for reference of 1.0 rad/s.

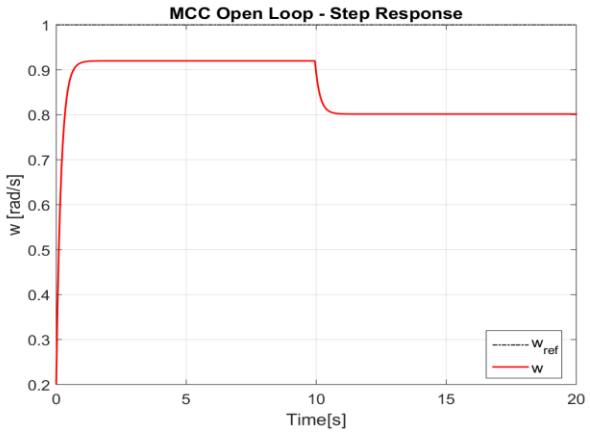

Figure 3. Step response of DC motor

B. Controllers Optimization

The optimizable parameters of DMC controller, R, L and α, should respect the restrictions of MPC controllers, being 1) prediction horizon R: positive integer value, less than or equal to model horizon N; 2) control horizon L: positive integer value, less than or equal to prediction horizon R and being 3) damping rate reference α: real value between 0 and 1.

These restrictions are related to the optimization process, representing constructive restrictions of control technique and being not related to the highlighted restrictions in the system to be controlled.

The fitness function presented in (3) is implemented for all optimization methods. Taking the parameters of the commercial DC motor presented in Tab. I the restrictions are defined as $V_N = 230.0V$ to armature voltage and $I_p = 33.38A$ to armature current.

C. Study Case 1: Deterministic Optimization of DMC

Using the deterministic method, the optimization of DMC controller was realized starting from initial stochastic parameters. Fig. 4 present values of speed, armature current and armature voltage developed by DC motor controlled by DMC with parameters values obtained by Quasi-Newton method. It considered the set-point speed at 100 rad/s and inserted load of 2.0 N · m applied at time t = 10 s.

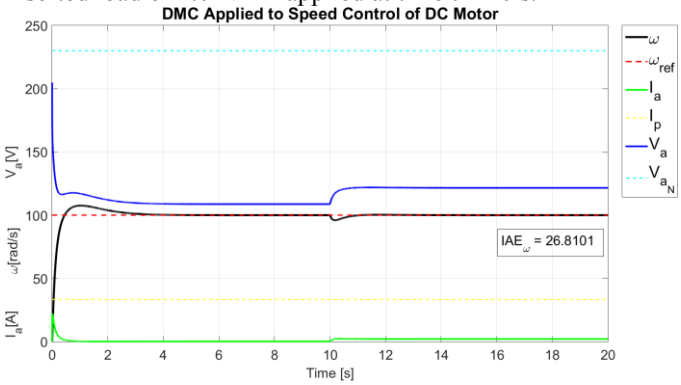

Figure 4. DC motor controlled by DMC tuned by deterministic method (ωref =100 rad/s).

Analyzing Fig. 4 is noted higher values for armature voltage and armature current in early moments of the experiment, DC motor starting. Is noted also that with the stabilization of speed developed by DC motor in speed reference both the armature voltage and the armature current remain stable. In instant t = 10 s the insertion of load with value 2.0 N causes disturbance to system slowing DC motor speed developed and making it necessary the increase of armature voltage and armature current values to that the speed developed reaches reference speed. Again, with stabilization of DC motor speed in speed reference both the armature voltage as the armature current remains stable. Fig. 4 yet present the integral of absolute error between reference speed and speed developed by DC motor being IAEω = 26.8101.

Fig. 5 present values of speed, armature current and armature voltage developed by DC motor controlled by DMC with parameters values obtained by Quasi-Newton method. It considered the set-point speed at 50 rad/s and inserted load of 1.0 N · m applied at time t = 10 s.

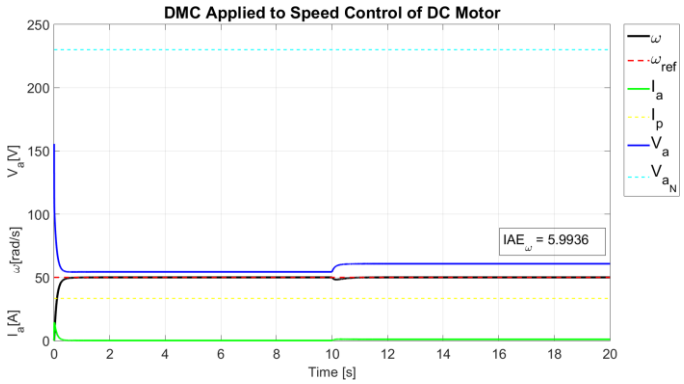

Figure 5. DC motor controlled by DMC tuned by deterministic method (ωref = 50 rad/s).

Analyzing Fig. 5 is noted similarity to Fig. 4. Is noted higher values for armature voltage and armature current in early moments of the experiment and stabilization of these values with the stabilization of motor speed. Is noted the perturbation of system due to insertion of load with value of 1.0 N at time t = 10 s, similar to the previous experiment, it is evident the increase of armature voltage and armature current values aiming to return and the stabilization of speed developed by DC motor to reference speed. Fig. 5 yet present the integral of absolute error between reference speed and speed developed by DC motor being IAEω = 5.9936.

Tab. II presents the total error found during the experiments and the optimal values for parameters of DMC controller obtained using the deterministic Quasi-Newton method.

Table II
RESULTS OF DMC CONTROLLER OPTIMIZED BY QUASI-NEWTON METHOD

ω_{ref}	$f(x^*)$	R	L	α
100	26.81014	15	9	0.00378
50	5.99360	12	10	0.00366

DMC controller tuning by deterministic (Quasi-Newton) method promote adequate performance of DC motor speed control. Note that with different set-point values different parameter are obtained. Another observation is that, with lower set-point values smaller fitness function values are obtained; this fact occurs, mainly, because the evaluation parameter is the Integral of Absolute Error of Speed IAEω and with the reduction of set-point the error area is reduced in same percentage.

D. Study Case 2: Heuristic Optimization of DMC

Genetic Algorithm (GA) was implemented with an initial population of 20 individuals. Mutation and crossover rates were defined from linear variation where the mutation rate is 30% in the initial generation and 90% in the final generation and the crossover rate of 90% in the initial generation and 30% in the final generation. Selection method used was the tournament. The maximum number of generations Gmax was set at 100 generations.

Fig. 6 present values of speed, armature current and armature voltage developed by DC motor controlled by DMC with parameters values obtained by Genetic Algorithm method. It considered the set-point speed at 100 rad/s and inserted load of 2.0 N · m applied at time t = 10 s.

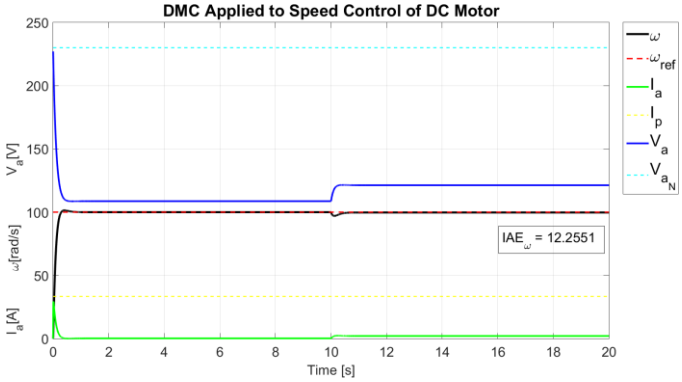

Figure 6. Speed of DC motor controlled by DMC tuned by heuristic method (ωref = 100 rad/s).

Analyzing Fig. 6 is noted higher values for armature voltage and armature current in early moments of the experiment, DC motor starting. Is noted also that with the stabilization of speed developed by DC motor in speed reference both the armature voltage and the armature current remain stable. In instant t = 10 s the insertion of load with value 2.0 N causes disturbance to system slowing DC motor speed developed and making it necessary the increase of armature voltage and armature current values to that the speed developed reaches reference speed. Again, with stabilization of DC motor speed in speed reference both the armature voltage as the armature current remains stable. Fig. 6 yet present the integral of absolute error between reference speed and speed developed by DC motor being IAEω = 12.2551.

Fig. 7 present values of speed, armature current and armature voltage developed by DC motor controlled by DMC with parameters values obtained by Genetic Algorithm method. It considered the set-point speed at 50 rad/s and inserted load of 1.0 N · m applied at time t = 10 s.

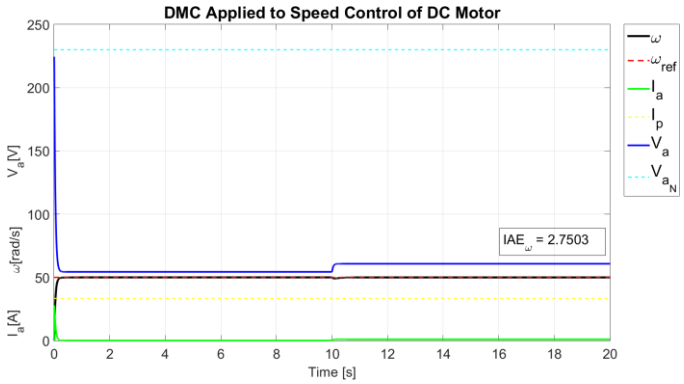

Figure 7. DC motor controlled by DMC tuned by heuristic method (ωref = 50 rad/s).

Analyzing Fig. 7 is noted similarity to Fig. 6. Is noted higher values for armature voltage and armature current in early moments of the experiment and stabilization of these values with the stabilization of speed. Is noted the perturbation of system due to insertion of load with value of 1.0 N at time t = 10 s, similar to the previous experiment, it is evident the increase of armature voltage and armature current values aiming to return and the stabilization of speed developed by DC motor to reference speed. Fig. 7 yet present the integral of absolute error between reference speed and speed developed by DC motor being IAEω = 2.7503.

With the results obtained using the heuristic method, it is possible to observe the improvement in curves presented in relation to deterministic method. Tab. III presents the total error found during the experiments and the optimal values for parameters of DMC controller obtained using the heuristic Genetic Algorithm method.

Table III
OPTIMIZATION OF GAINS USING THE HEURISTIC METHOD.

ω_{ref}	$f(x^*)$	R	L	α
100	12.25510	9	5	0.00321
50	2.75025	7	7	0.00299

The optimization using the heuristic method allowed the improvement of the performance of DMC controller in response time and also in the annulment of the error in permanent regime. Fitness function values were reduced significantly in relation to values presented by implementation of deterministic method. Reduction of fitness function values represent better control of speed developed by DC motor.

E. Study Case 3: Hybrid Optimization of DMC

The implemented hybrid optimization initiates the search for optimized values realizing wide search within the set of possible solutions. To develop wide search hybrid optimization implements genetic algorithm. GA implemented at beginning of hybrid optimization repeats the characteristics of GA implemented isolated presented in *III.D*.

After wide search performed the hybrid optimization implemented seeks greater precision for solution presented until then. The hybrid optimization implements Quasi-Newton algorithm for refinement of the solution presented in the first step. The QN algorithm implemented in the hybrid optimization presents repeats the characteristics of QN implemented isolated presented in *III.C*.

Fig. 8 present values of speed, armature current and armature voltage developed by DC motor controlled by DMC with parameters values obtained by Hybrid method. It considered the set-point speed at 100 rad/s and inserted load of 2.0 N · m applied at time t = 10 s.

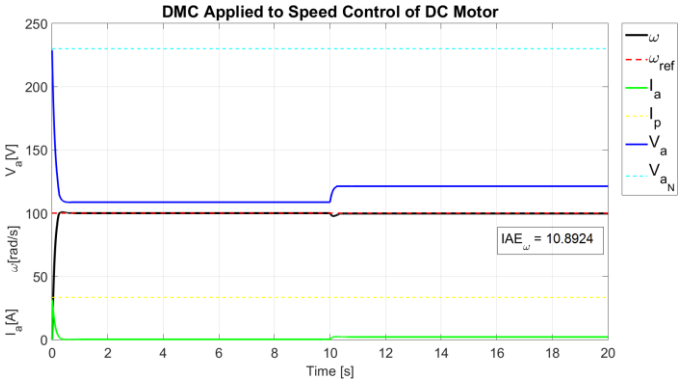

Figure 8. DC motor controlled by DMC tuned by hybrid method (ωref = 100 rad/s).

Operation of DC motor controlled by DMC tuned by hybrid optimization method, Fig. 8, is similar to operation presented with optimization by heuristic method, Fig. 6. In speed developed by DC motor could be noted reduction of overshoot before speed stabilization. Note also, reduction in speed decrease caused by insertion of load with value 2.0 N at t = 10s. Characteristics evidenced in Fig. 8 illustrate reduction in integral of absolute error between reference speed and speed developed by DC motor, resulting in IAEw = 10.8909.

Fig. 9 present values of speed, armature current and armature voltage developed by DC motor controlled by DMC with parameters values obtained by Hybrid method. It considered the set-point speed at 50 rad/s and inserted load of 1.0 N · m applied at time t = 10 s.

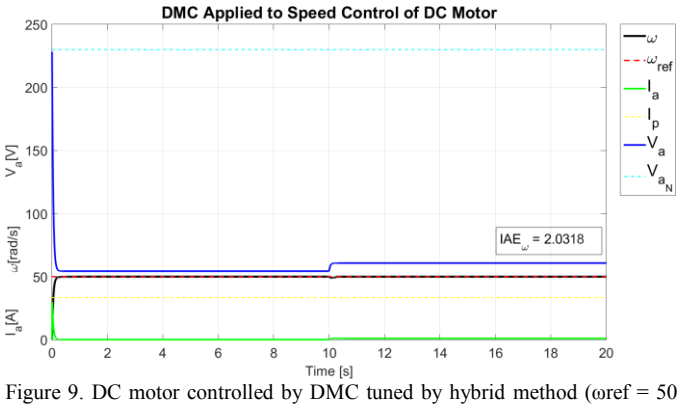

Figure 9. DC motor controlled by DMC tuned by hybrid method (ωref = 50 rad/s).

Fig. 9 presenting operation of DC motor controlled by DMC tune by hybrid optimization method details operation

similar to Fig. 8. Could be noted that even with a reduction of set-point the armature voltage and current still near of safety operation points at DC motor startup. Direct relation of armature voltage and current with speed developed by DC motor request high values of these parameters at DC motor startup. High armature voltage and current values at DC motor startup quickly drive speed to desired reference. Short period for high values of armature current and voltage guarantees absence of overshoots at speed developed by DC motor. Fig. 9 yet present the integral of absolute error between reference speed and speed developed by DC motor being IAEω = 2.031.

With the results obtained using the hybrid method, it is possible to observe the improvement in curves presented in relation to heuristic method. Tab. IV presents the total error found during the experiments and the optimal values for parameters of DMC controller obtained using the heuristic Genetic Algorithm method.

Table IV
OPTIMIZATION OF GAINS USING THE HEURISTIC METHOD.

ω_{ref}	$f(x^*)$	R	L	α
100	10.89239	7	2	0.00191
50	2.03181	7	1	0.00170

Reduction presented in fitness function $f(x)$ values reflects the improvement of DMC controller with parameters tuned by hybrid optimization method in relation of tuning by other optimization methods. The improvement characterize minor error between speed reference and speed developed by DC motor.

F. Comparison Between Optimization Methods

Tab. V presents final values observed after execution of experiments where DC motor speed control was carried out by DMC controller tuned by deterministic method (Quasi-Newton), by heuristic method (Genetic Algorithm) and by hybrid method (Genetic Algorithm/Quasi-Newton).

Table V
DC MOTOR PARAMETERS FINAL VALUE

Optimizator	Set-point	*IAEω*	*Iamax*	*Vamax*
QN	100	26.8101	22.2045	204.8631
	50	5.9936	14.5460	155.5752
GA	100	12.2551	29.4314	227.0795
	50	2.7503	27.8424	224.4494
Hybrid	100	10.8923	32.6256	229.2125
	50	2.5033	29.7023	226.2568

In Tab. V IAEω values present the integral of absolute error between speed reference and speed developed by DC motor controlled by DMC tuned by different optimization methods. For smaller values of IAEω smaller are errors occurred in the experiment consequently better is the proposed DMC parameters and better is the optimization method for the analyzed system.

For a speed set-point equal to 100 rad/s the controller tuned by hybrid method presents the lowest value of IAEω, characterizing itself as the best method for this system. The value of IAEω presented by the system optimized by hybrid method is 11.12% smaller than the value presented when implemented heuristic method and 56.37% smaller when implemented deterministic method.

Similarly, for set-point equal to 50rad/s, the implementation of hybrid method presents better performance. The value of IAEω presented by the system optimized by hybrid method is 8.98% smaller than the value presented when implemented heuristic method and 58.23% smaller when implemented deterministic method.

Yet analyzing the data presented in Tab. V, for all the experiments, using parameters obtained from simulations, the armature voltage limits Va = VN = 230.0V and armature current Ia = Ip = 33.38A were respected.

In this article, the set of gains R, L and α obtained through system optimization with speed set-point equal to 50rad/s cannot be implemented when it is intended to operate the same plant with speed set-point equal to 100rad/s. To this operating characterizes, the DC motor restrictions, as peak current Ip = 33.38 and armature voltage VN = 230.0, are not respected, as shown in the figure below.

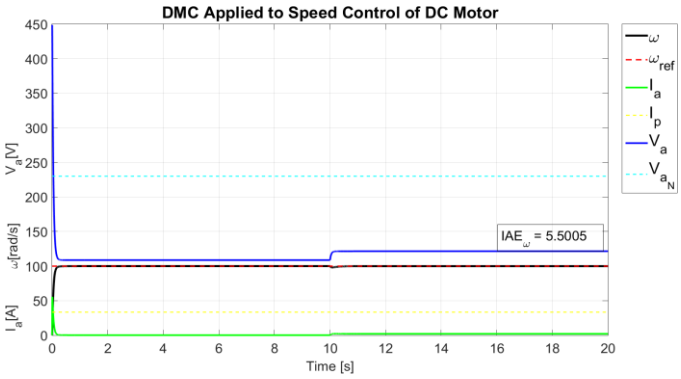

Figure 10. DC motor speed for system controlled by DMC tuned by AG for set-point ωref = 50 rad/s applied for set-point ωref = 100 rad/s.

Yet analyzing Fig. 10, evidence the impossibility of applying the parameters obtained by optimization methods for the DMC controller with reference equal to 50 rad/s on the same controller with the reference equal to 100 rad/s. It note peak current applied to the DC motor exceeding the threshold value, reaching Iamax = 55.6820A and armature voltage applied to the DC motor exceeding the limit value, reaching Vamax = 448.8387V.

IV. CONCLUSION

Held up the implementation of predictive DMC controller to speed control of DC motor, being employed to tune the controller, optimization techniques deterministic (Quasi-Newton), heuristic (Genetic Algorithm) and hybrid (Genetic Algorithm/Quasi-Newton). The proposed optimized

controllers were simulated for the same DC motor speed control in order to compare which optimization method obtain the most efficient controller, searching for reduction of the transient period and variations in continuous operation. To analyze the efficiency of the control developed was used as main criterion the Integral of Absolute Error of speed, presenting the existing error between the speed developed by DC motor and reference speed. Analysis of results shows a better performance of DMC controller optimized with hybrid method. Attentive to the fact that optimization for a given operating point does not guarantee safe operation of the controller in all parts of the system. Note that the tuning of the controller set-point of 50 rad/s afford gains that would outweigh the engine safety restrictions if the same gains are implemented in the same DMC controller, but seeking to reach set-point of 100 rad/s. Finally, conclude that the implementation of DMC controller combined with the optimization parameters through the heuristic optimizer using genetic algorithm results in approach that shows promising results, enabling optimized DMC controller to be implemented in systems where search is control with high performance.

ACKNOWLEDGMENT

Authors thank the National Counsel of Technological and Scientific Development (CNPq), the Research Support Foundation for the State of Goiás (FAPEG) and the Coordination for the Improvement of Higher Education Personnel (CAPES) for financial assistance to this research.

REFERENCES

[1] W. Goncalves da Silva, “Speed control of electric drives in the presence of load disturbances,” Ph.D. dissertation, University of Newcastle upon Tyne, 1999.

[2] N. Nise, Control Systems Engineering. John Wiley & Sons, 2007.

[3] C. R. Cutler and B. L. Ramaker, “Dynamic matrix control?? A computer control algorithm,” in joint automatic control conference, no. 17, 1980, p. 72.

[4] S. J. Qin and T. A. Badgwell, “A survey of industrial model predictive control technology,” Control engineering practice, vol. 11, no. 7, pp. 733– 764, 2003.

[5] E. F. Camacho and C. B. Alba, Model predictive control. Springer Science & Business Media, 2013.

[6] W. P. Calixto, T. M. Pereira, J. Mota, A. Alves, E. Domingues, J. Domingos, A. Coimbra, and B. Alvarenga, “Development of mathematical operator to heuristic optimization algorithms applied to problem of geoprospection, In Portuguese,” TEMA (São Carlos), vol. 15, no. 2, pp. 177–194, 2014.

[7] C. A. e. a. Ganzaroli, “Heuristic and deterministic strategies applied on a cascade pi controller tuning for speed control of a dc motor,” IEEE Control Systems Magazine, 2015.

[8] S. Chapman, Electric machinery fundamentals. Tata McGraw-Hill Education, 2005.

[9] Vasant, Pandian M., Meta-Heuristics Optimization Algorithms in Engineering, Business, Economics, and Finance, IGI Global, 2012.

Analysis and monitoring of electrical grounding grid encapsulated with concrete: case study using simulation in finite element method

Thiago Martins Pereira, Rodrigo Alves Lima, Viviane Margarida Gomes, Wesley Pacheco Calixto, Aylton José Alves

***Abstract*— This work study the influence of concrete, plaster, clay and others buried structures in grounding systems. Comparison of soil characteristics between dry and rainy seasons on different grounding systems. The study includes comparison of six different grounding system on dry season and wet season. Simulations in finite element method was performed for tree layer stratified soil and the electrostatic equipotential surfaces were mapped into the region of interest.**

***Index Terms*— Grounding Systems, finite elements method.**

I. Introduction

HERBERT G. Ufer was in charge of the facilities from Davis Montana military base, one of the tasks was to protect the bombs warehouse from atmospheric discharge [1] He utilized structural system to reinforce the grounding efficiency from the traditional grounding rod system [2]. Subsequent inspections of the installations showed that combined grounding systems presented lower resistance and greater consistency in high electrical resistance soils than grounding systems without concrete structures[3]. Concrete is a hygroscopic substance and therefore, absorbs water more easily than lost. For that reason, concrete presence in soil helps to keep soil humidity levels and grants a lower resistance to soil [1].

Grounding systems are used for many different functions, from noise reduction for better functioning of electronic equipment to security applications, power systems and substations grounding is important to maintain stable and secure systems for equipment and users [4].

This work starts from the hypothesis that the electrical behavior of soil is altered by climate seasonality [5]. The grounding grid efficiency was studied during the rainy season and during dry season in combined and non-combined systems.

Concrete used in construction basically consists of a mixture of cement, water and crushed stone. Buried concrete block has equivalent behavior to a semiconductor element with resistivity between 30Ω and 90 Ω as IEEE indicates their standardizations [3] [6].

Grounding probes were build using different types of material.in monitoring the current on dry soil and moist soil studying behavior of materials on different humidity.

Concrete hygroscopic feature helps both concrete and soil to remain moist, lowering soil resistance [2]. This moisture is present between the solid particles of the soil, so it consists basically water, organic minerals and dissolved inorganic [7]. Utilization of the structural columns was also mentioned to reinforce the grid in its function [8].

In the 70's it was indicated the use the enclosed electrodes in concrete, with a view to improve grounding grid performance. The lack of standardization in telecommunications wiring was a concern among operators and only in 1991 there was standardization and regulation, facilitating the use of ground [11].

Among the main functions of grounding Because the grounding system importance, are highlighted four most common applications. Protection systems and security function to living beings and protection to equipment [11]. Thus, grounding installation purposes includes personal safety in the handling and maintenance of equipment, avoiding dangerous tensions. Grounding systems are also capable of providing overvoltage protection, limiting noise and crosstalk in transmission systems and serve as return path for DC circuits. Additionally, they serve as protection in case of lightning [12].

Grounding probes were built using different types of composition from clay to concrete with salt. The different hygroscopy from materials makes different electric current drained.

II. METHODOLOGY

A. Data Acquisition

To verify the influence of concrete efficiency of grounding systems built two-ground grid. These structures were installed on same topographical area and have same number of rods, differentiated only by the presence of one of concrete in mesh. Data acquisition made at two-week intervals to monitor the effect of climate seasonality in meshes checking the humidity, temperature and grounding resistance.

The Wenner method is a method for measuring resistivity of homogeneous soil which four rods are inserted into equally spaced ground like Figure 1.

The central terminals are used to determine the voltage side terminals are for power insertion into the ground.

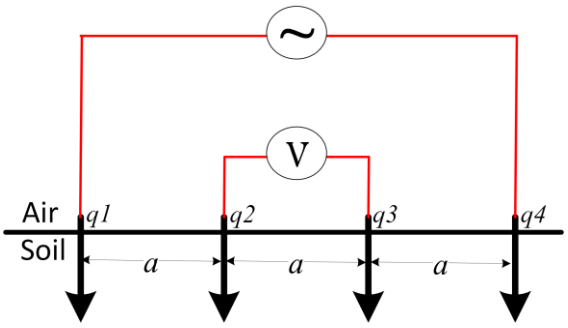

Fig. 1. Simplified disposition in soil of six different grounding grids

Current flowing between the rods produce a potential in voltage measuring rods, with voltage and current values, Wenner show a correlation between soil resistivity and measured resistance. Increasingly the rods distance, more current will penetrate into soil and a deeper soil resistivity will be measured.

Another six grounds grid were built and installed on another place on same topographical area. This six was inserted on soil

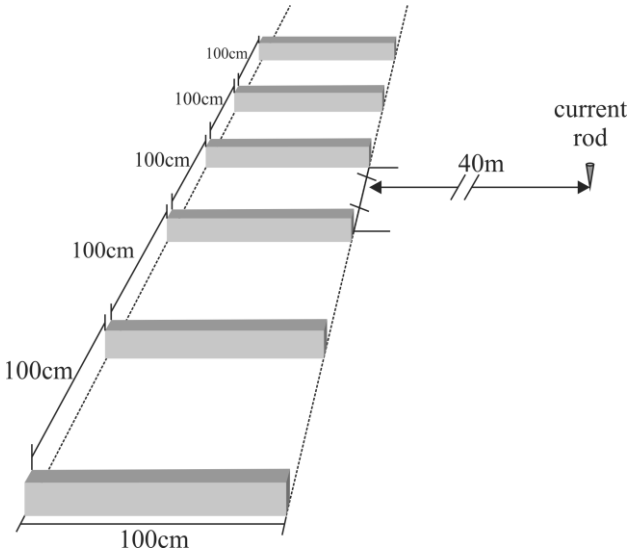

Fig. 2. Simplified disposition in soil of six different grounding grids

has different constitution using the same 50mm conductor. The difference on constitution display how de grounding

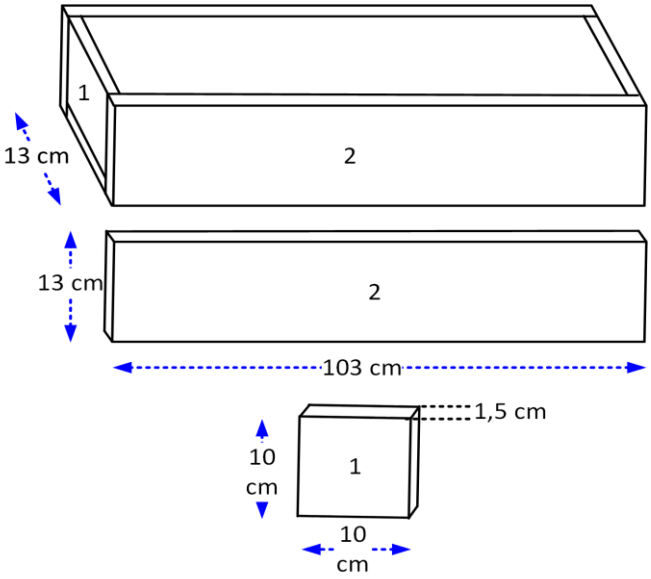

Fig.3. Grounding system mold

resistance changes in different soil. The Figure 2 displays how was disposed and measured the grounding resistance.

The first on left has concrete, gravel and salt, second concrete and gravel, third only concrete, fourth plaster, fifth clay and last on right has only conductor buried on soil.

The mold used to build grounding system guarantees size of grounding systems. Grounding systems has 100cm length, 10cm depth and 10cm of width. The mold used is described on Figure 3.

The fall-of-potential method was used to obtain curve that represents the locations of grounding resistance. [17] This method consists the equipment called megohmmeter that generates a know current, between earth electrode and the outer stake, while the drop voltage potential is measured between the earth stake and the outer current stake. [18] The distance used between earth stake and current stake was 40m like NBR 15749 says. The potential stake is moved every 5 meters from earth stake to current stake. There is seven different values measured on these grounding systems. According the measured values, is drawn a graphic that shows grounding resistance. The expected graphic on Figure 4 shows resistance with distance and the influence of earth stake and current stake on measure. The linearity region distance between earth stake and current stake changes according different soil types. Regularly the linearity region is 37,5% to 62,5% between the roads. In case of the curve don't present the linearity level some mistake may have occurred on rods or cable connections.

B. Simulation Software

Finite element method (FEM) allows to simulate and validate data obtained from soil stratifications [13]. Performance of ground and influence of neighboring structures to ground grid

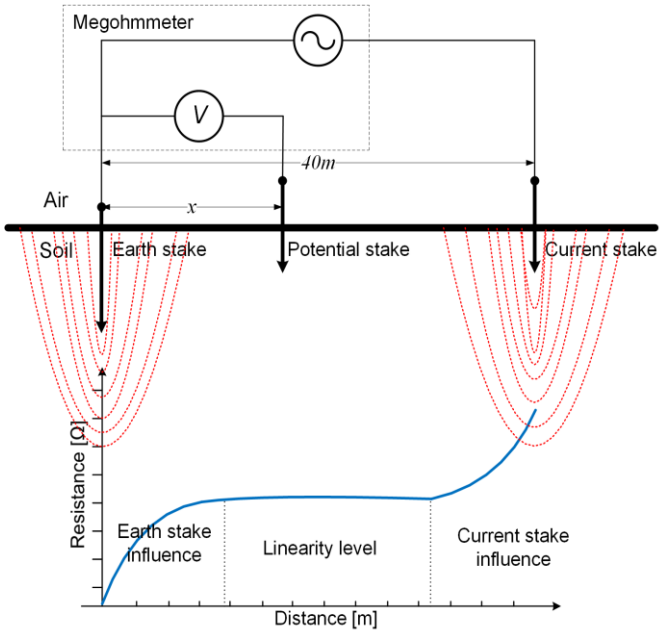

Fig. 4. The fall of potential method

are observed for solution of potential surfaces in plane and on edge of layers. Simulation allows observing dissipation of electric current and influence of aggregate structures to ground grid [14].

Finite element method consists of a mathematical analysis based on discretization of a continuous environment into small elements while maintaining the same characteristics of the original environment. All elements are described in differential equations and then they are solved using mathematical models. The accuracy and performance of method depends on number of elements and nodes. Smaller elements and consequently greater amount thereof and greater number of nodes in mesh greater will be precision of resolution of problem. Even when dealing with an approximation method, increasing amount of elements size tends to zero and so the amount of us tend to infinity. When this occurs the problem solution tends to an exact solution, i.e., the smaller the size of the largest elements accuracy of the analysis results.

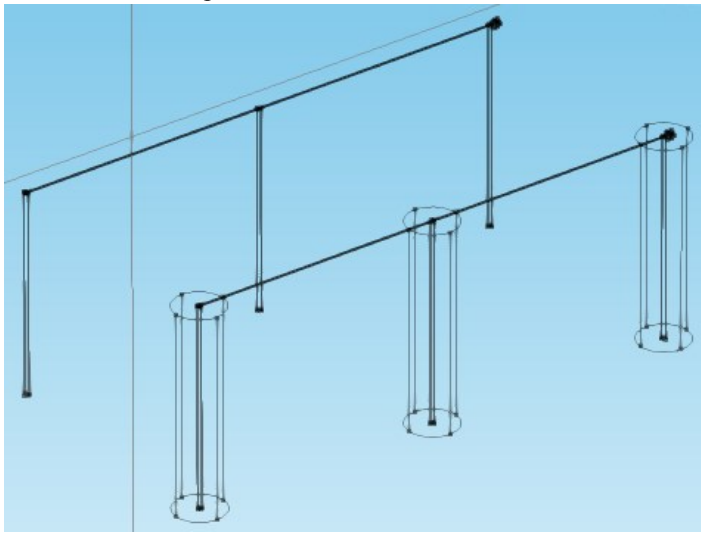

Fig. 5. Construction in FEM software of ground grid.

Modeling involves the reproduction of main geometric and electrical aspects of ground grid [15]. Figure 5 presents the soil modeling of details in detail. It illustrated three interconnected rods without concrete and three interconnected concreted rods. Soil characteristics, resistivity and depth are calculated and used in simulator in stratified three-tier model and forty meter radius.

Mesh construction detail is shown in Figure 5. Rods are made of copper with 5/8 inch in diameter and 2.4 meters long, on right its shown rods combined with concrete, being enclosure is 30 cm radius and 2.40 meters long. Distance between rods is 4,5 meters, distance between ground mesh is 3 meters. Simulations were done by inserting 200V and 2000V in each grounding system.

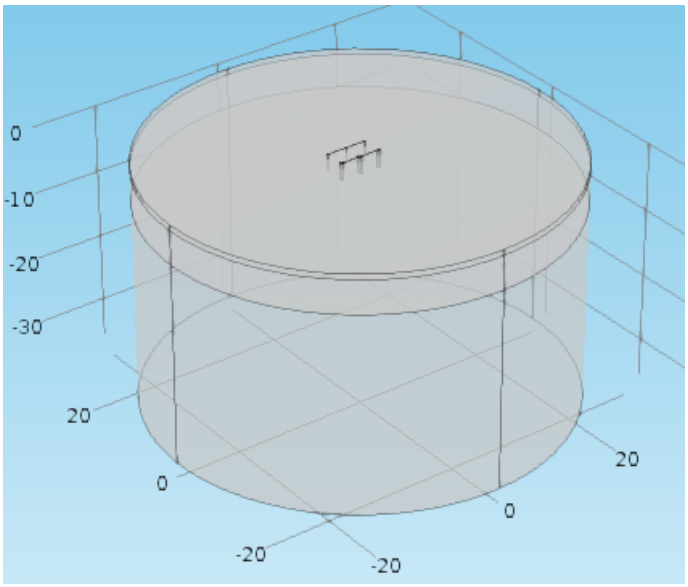

Fig. 6. Building of the soil in FEM simulation software on the grid and their properties.

Considering the distance on fall-off-potential 40m between grounding system and current road was used this size to build the model like Figure 6.

III. Results

A. Data Acquisition

The Table 1 shows characteristics of soil collected in the field during the rainy season and dry season. These data allow the comparison between soil resistance and response by the absorption and retention of water [16]. Second column corresponds to soil characteristics in dry season and third column corresponds to rainy season.

Figure 7 shows the resistance curves depending on the positioning of electrodes for same periods of year. The red line represents values obtained using three points in mesh without concrete and blue curve is the response of ground with concrete.

TABLE I
DATA COLLECTION BEFORE THE RAINY SEASON.

Feature	*Drought*	*Rainy*
Soil Moisture	*25.0 %*	*70.0 %*
Soil Temperature	*32.2 ℃*	*26.3 ℃*
Humidity	*27.0 %*	*59.0 %*
Ambient Temperature	*31.0 ℃*	*28.4 ℃*
Resistance Grounding Concrete	*275.7 Ω*	*165.3 Ω*
Grounding Resistance Standard	*537.0 Ω*	*361.7 Ω*
Precipitation	*0,0 mm*	*45.0 mm*

Figure 8 shows the ground due to the spacing of the rods resistance curve showing the increase of efficiency of the mesh after the concrete insertion along the rods. How much moisture in the soil after rain considerably alters response of soil resistivity, improving ground resistance. Blue line is no concrete ground resistance before the rain, and red line is the grounding strength concrete after rain.

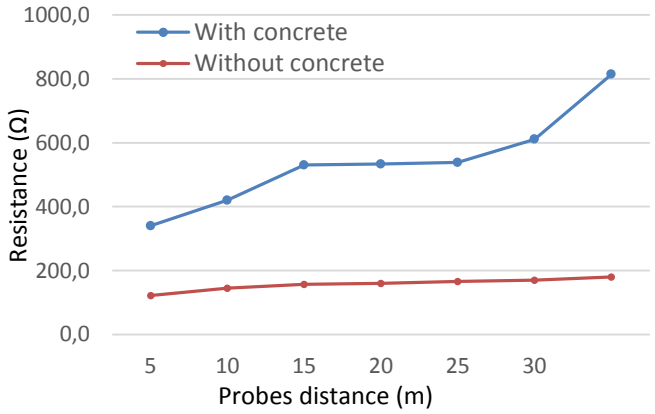

Fig. 7. Chart show grounding resistance at end of dry season in relation to distance from stems using Werner method.

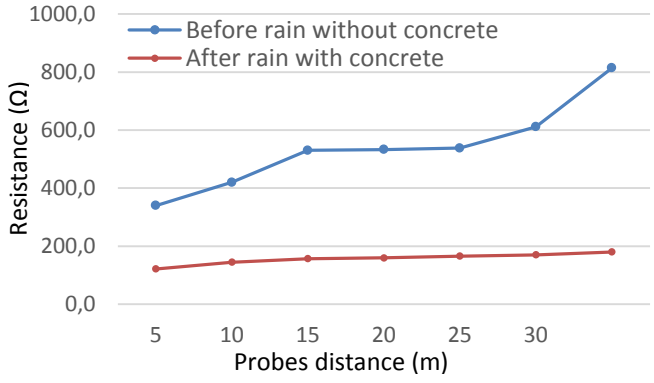

Fig. 8. Comparing ground not concretes rain and concreted after rain.

Wenner method used to measure soil resistivity, this method related to the amount of soil resistivity and the resistance measured. Wenner's method used in the 4 rods equally spaced ground straight. Two side rods used for the insertion of electrical current in the ground, since central rods used to determine tension. Wenner method considers the homogeneous ground and if it departs from rods is considered value of resistivity of same depth as distance between the rods [12]. The Table 2 shows acquired values were sampled only 4 values starting with 1 meter to 6 meters, because the space was short and the distance of 6 meters between rods already requires an area of length of 18 meters, and the length available for measurement was 20 meters.

TABLE II
WENNER METHOD

Distance	*Drought*	*Rainy*
1 m	*125.0 Ω*	*815.3 Ω*
2 m	*160.0 Ω*	*2030.2 Ω*
4 m	*110.0 Ω*	*2771.4 Ω*
6 m	*160.0 Ω*	*2113.5 Ω*

Table 3 shows resistivity of soil layers over a longer period presenting lower humidity 3/10/2013 and higher humidity 04/20/2014, according to values shown in Table 3. Was built Figure 9 with depths of layers having the thicknesses changing according to the moisture retained by the soil.

TABLE III
SOIL RESISTIVITY

Layer	*10/03/2013*	*10/17/2013*	*12/04/2013*	*04/20/2014*
1	*352.93 Ω*	*1033.88 Ω*	*749.92 Ω*	*469.44 Ω*
2	*1411.61 Ω*	*10062.9 Ω*	*3591.83 Ω*	*1663.14 Ω*
3	*2795.98 Ω*	*623.3 Ω*	*404.78 Ω*	*1071.28 Ω*

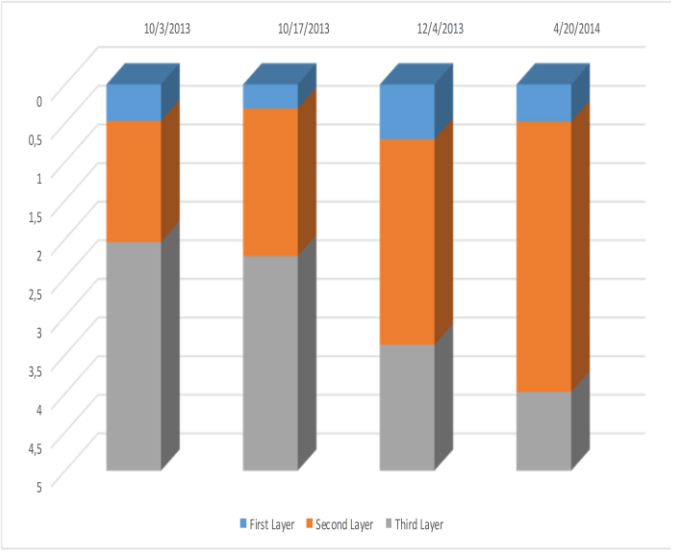

Fig. 9. Chart the depths of soil layers

The six grounding probes was tested in different soil moisture, on Figure 10 has shown de worst and better grounding resistance curve. The first probe made by concrete, gravel and salt, has the betters results on dry season and wet season.

Table IV shows de difference of grounding resistance between dry and raining season measured in Ohms. The first ground shows that concrete is better than any another grounding on wet season or dry season. The biggest difference

TABLE IV
GROUNDING RESISTANCE

	Gnd 1	*Gnd 2*	*Gnd 3*	*Gnd4*	*Gnd 5*	*Gnd 6*
Dry	*524*	*798*	*730*	*643*	*708*	*1769*
Wet	*213*	*367*	*477*	*451*	*603*	*1111*

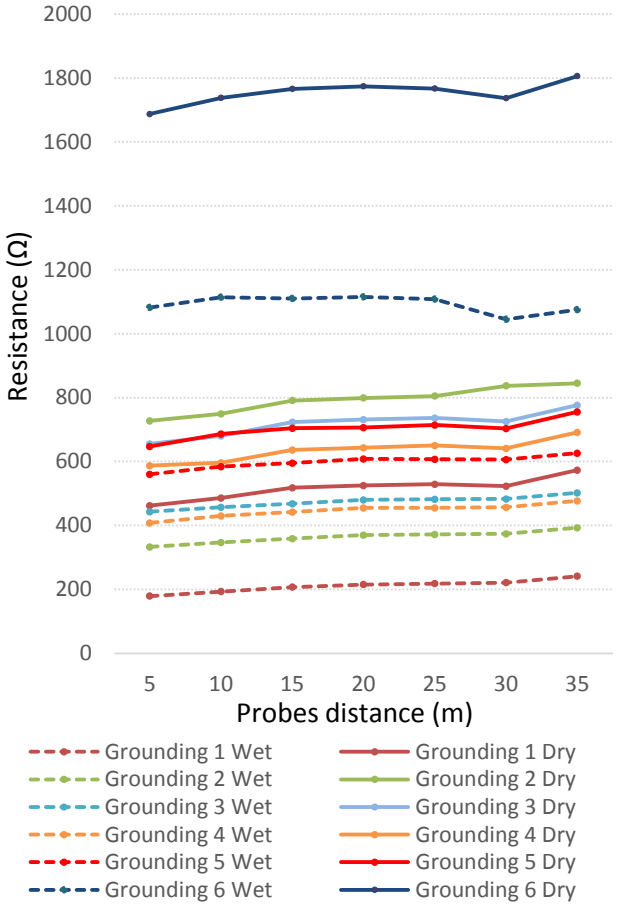

Fig. 10. Grounding Resistance Curves

on dry season was 337% and on dry season 521%.

B. Computational Method

Figure 11 shows the equipotential lines form insert 200 V

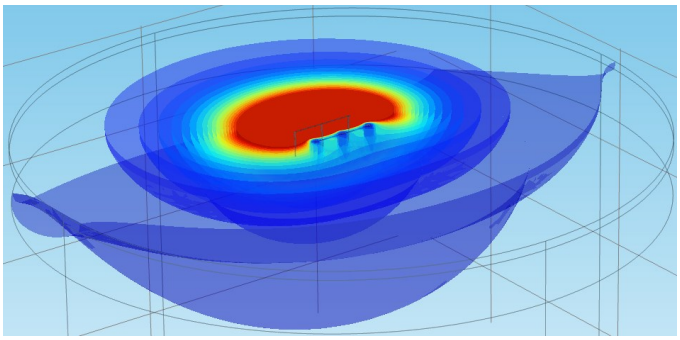

Fig. 11. Shows equipotential surfaces in soil and interaction between two grounds studied with inclusion of 200 V.

on rods of ground grid. Interaction with rods concreted ground grid. The outer loop ensures that there is a higher voltage drop, maximizing the absorption of electrical current through the ground grid.

Simulation of charge distribution in ground by inserting a

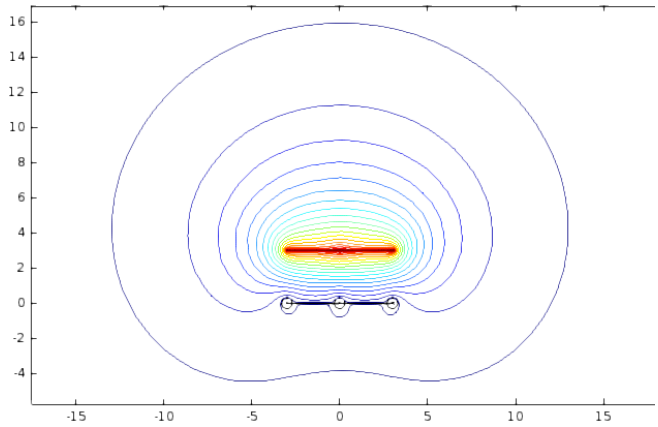

Fig. 12. Simulation of equipotential lines in plane parallel to surface of soil.

2000 V voltage can see in Figure 12.

IV. CONCLUSIONS

As first measurements and studies in experimental ground on the dates of September 7 and October 3, 2013 has considerable difference in resistance of grounds with and without concrete after a long period of drought and after rain During dry season grounding with the rods wrapped in concrete already had a degree of improved efficiency that grounding without concrete. The concreted loop resistance was 275.7 Ω and without concrete showed resistance 537.0 Ω a difference of almost 200%. Difference is accentuated by concrete characteristics such as moisture, its resistivity is smaller than ground contact area with ground is increased, which helps the current distribution in soil.

A study can be done is influence of meshes creating interaction between them, when there injection voltage in a mesh, there is the scattering voltage at this soil. Due to the proximity of ground grid, note change in the lines of equipotential caused the second ground grid. Figure 5 illustrates the difference in grounding resistance level in mesh without concrete before the rain and the mesh concreted after rain. Use of FEM to determine equipotential surfaces due to scattering of current through soil and its mesh with next ground with these images it is possible to study and see what electrical interaction between layers and substances buried in ground make to ground. Differences in responses are already expected between two meshes, we can put data in a computer simulator for verification of equipotential surfaces and consequently ground to ground response.

Several aspects to be analyzed, since strength of concrete in ground, moisture retention of concrete in relation to retention of moisture from soil.

REFERENCES

[1] O. Vicente, "Study on the electrical behavior of concrete used in structural grounding systems," 2010.

[2] A. Nadler and H. Frenkel, "Determination of soil solution electrical conductivity from bulk soil electrical conductivity measurements by the four-electrode method," *Soil Science Society of America Journal*,
vol. 44, no. 6, pp. 1216–1221, 1980.

[3] P. W. Rowland, "Industrial system grounding for power, static, lightning and instrumentation, practical applications," in *Textile, Fiber and Film Industry Technical Conference, 1995., IEEE 1995 Annual*. IEEE, 1995,
pp. 1–6.

[4] L. Cong-Li and P. Minfang, "A new approach for monitoring grounding grid of electrical power system," in *Electronic Measurement and Instruments, 2007. ICEMI'07. 8th International Conference on*. IEEE,
2007, pp. 4–419.

[5] W. P. Calixto, "Mathematical and computational methods applied to geoelectric prospecting with three-dimensional stratification," In portuguese Ph.D. dissertation,
2012.

[6] J. B. J. Pereira, "Modeling of uncertainties in electrical grounding systems" In portuguese 2008.

[7] W. P. Calixto, L. M. Neto, M. Wu, H. J. Kliemann, S. S. de Castro, and K. Yamanaka, "Calculation of soil electrical conductivity using a genetic algorithm," *Computers and Electronics in Agriculture*, vol. 71, no. 1, pp. 1–6, 2010.

[8] E. J. Fagan and R. H. Lee, "The use of concrete-enclosed reinforcing rods as grounding electrodes," *Industry and General Applications, IEEE Transactions on*, no. 4, pp. 337–348, 1970.

[9] J. Preminger, "Evaluation of concrete-encased electrodes," *Industry Applications, IEEE Transactions on*, no. 6, pp. 664–668, 1975.

[10] T. R. Brinner, J. D. Atkins, and M. O. Durham, "Electric submersible pump grounding," *Industry Applications, IEEE Transactions on*, vol. 40, no. 5, pp. 1418–1426, 2004.

[11] M. Santos, W. Cunha, and A. Nascimento, *"Infrastructure in systems of Communication Technology"*, vol. 1, no. 1, 2010.

[12] G. Kindermann and J. M. Campagnolo, *"*Grounding Systems*"* In portuguese. *Sagra- DC Luzzatto*, 1992.

[13] J. Paknahad, K. Sheshyekani, F. Rachidi, and M. Paolone, "Lightning electromagnetic fields and their induced currents on buried cables. Part ii: The effect of a horizontally stratified ground," *IEEE Transactions on Electromagnetic Compatibility*, vol. 56, no. 5, pp. 1146–1154, Oct 2014.

[14] Y. Wang, R. Chen, S. Lin, J. Tian, J. Li, and M. Chen, "Calculation and analysis of the current carrying capability of electric cable based on finite element method," in *Electrical Insulation and Dielectric Phenomena, 2009. CEIDP '09. IEEE Conference on*, Oct 2009, pp. 307–310.

[15] J. A. Guemes and F. E. Hernando, "Method for calculating the ground resistance of grounding grids using fem," *IEEE Transactions on Power Delivery*, vol. 19, no. 2, pp. 595–600, April 2004.

[16] A. Habjanic and M. Trlep, "The simulation of the soil ionization phenomenon around the grounding system by the finite element method," *IEEE Transactions on Magnetics*, vol. 42, no. 4, pp. 867–870, April

[17] MA, Jinxi; DAWALIBI, Farid P. Extended analysis of ground impedance measurement using the fall-of-potential method. *IEEE Transactions on Power Delivery*, v. 17, n. 4, p. 881-885, 2002.

[18] MA, Jinxi; DAWALIBI, Farid P. Influence of inductive coupling between leads on ground impedance measurements using the fall-of-potential method. *IEEE Transactions on Power Delivery*, v. 16, n. 4, p. 739-743, 2001.

Geoelectric method applied in correlation between physical characteristics and electrical properties of the soil

Antonio Marcelino Silva Filho, Carlos Leandro Borges Silva, Marco Antonio Assfalk Oliveira, Thyago Gumeratto Pires, Aylton José Alves, Wesley Pacheco Calixto, Marcelo Gonçalves Narciso

Federal University of Goias, Brazil

***Abstract*—This paper presents the study of the relationship between electrical properties and physical characteristics of the soil. Measures of apparent electrical resistivity of the soil were made for different types of soil, varying moisture content gradually while maintaining a constant compaction, and then varying the compaction and relating it to a constant humidity. Development of a correlation surface is proposed in order to identify granulometry of the soil from moisture and compaction measurements. For the study of spatial variability, two areas were chosen to allow the change of moisture content and compaction in order to verify the measurement capacity of apparent electrical resistivity of the soil as methodology to identify change in soil dynamics. Results obtained show correlations among apparent electrical resistivity of the soil, moisture, soil compaction and clay content.**

***Index Terms*— Geoelectric prospecting, apparent electrical resistivity, soil compaction, moisture content.**

I. Introduction

SOIL can be considered as an electrical conductor having a tortuous path or a large number of conduction paths with variable lengths and cross sections. Soil property to conduct electric current is called apparent electrical conductivity of the soil σ_a, which can be calculated from measurements of the voltage V collected in field, after applying a current I to the soil.

Methods used in precision agriculture require fast and accurate answers to map the potential productivity of a given area [1]. One of the principles of precision agriculture is based on the property of soil to vary the apparent electrical conductivity according to variation of its physical and chemical properties such as texture, moisture, compaction, hydraulic potential, organic matter content, etc. For these reasons, apparent electrical conductivity of the soil has attracted the attention of researchers and investors for being a fast, noninvasive and inexpensive method [2]. In addition, investigations related to σ_a can aid in the measurement of clay and water content [10].

On a plot, areas with homogeneous physical and chemical characteristics can be identified with the mapping of σ_a. With these values mapped geographically within land, it is possible to divide the regions in management areas and then proceed to collect some samples for analysis and, depending on their physical and chemical properties, make decisions on how to intervene with the inputs, pesticides and irrigation. The mapping of σ_a is becoming an effective tool in the investigation of physical and chemical behavior and spatial variability of the soil, allowing to identify areas with similar properties and easily define management zones [3].

This paper strives to present the development of methodology to correlate soil electrical conductivity, soil moisture content (w), clay content (δ) and soil compaction (C).

The development of theoretical and experimental mechanism allowing abacus production for identification of soil granulometry from moisture and compaction measurements also comprises a goal of this paper.

II. METHODOLOGY

Electric conductivity is an intrinsic property of the whole electric current conductive material. In Geoelectric Prospecting, the conductor is the soil in which the electric current flows through the presence of free salts in the soil solution (liquid phase) and also due to the exchangeable ions in the particle surface [6].

However, unlike what happens with a wire conductor of electricity, the electric current in the ground can cycle through several ways, as illustrated in Fig. 1. In moist soils, the current conduction occurs mainly through the salt content in the soil water which occupies the largest pores, region 1 in Fig. 1. However, there are also solid phase contribution to the electrical conductivity in moist soils mainly by exchangeable cations associated with the clay mineral, region 2 in Fig. 1. A third path for electric current in the soil exists through particles in direct and continuous contact with each other, region 3 in Fig. 1. These three paths of current flow contribute to the overall electrical conductivity of the soil known as apparent electrical conductivity of the soil σ_a [5].

Apparent electrical resistivity of the soil ρ_a (which is the inverse of σ_a) is obtained through field measurements using geoelectric prospecting methods, the Wenner method [7].

The calculation of soil electrical resistivity is performed by an instrument which measures soil electrical resistance R_m [8]. This instrument has four terminals, T_1, T_2, T_3, T_4, connected to four rods spiked at depth P at the points q_1, q_2, q_3, q_4, aligned and separated by the same distance a. Electric current I is injected into the terminal T_1 (q_1) and collected in the terminal T_4 (q_4), which produces electric potential V at points q_2 and q_3. With I and potential difference V between q_2 and q_3, resistance R_m can be calculated. Thus, apparent electrical resistivity of the soil ρ_a [Ωm] is given by [4]:

$$\rho_a(a) = \frac{4\pi a R_m}{1 + \frac{2a}{\sqrt{a^2 + (2P)^2}} - \frac{2a}{\sqrt{(2a)^2 + (2P)^2}}} \quad (1)$$

This value ρ_a varies with distance a, since the soils are heterogeneous. Thus, the magnitude happens to be called apparent electrical resistivity $\rho_a(a)$ where the resistivity values are a function of a [11].

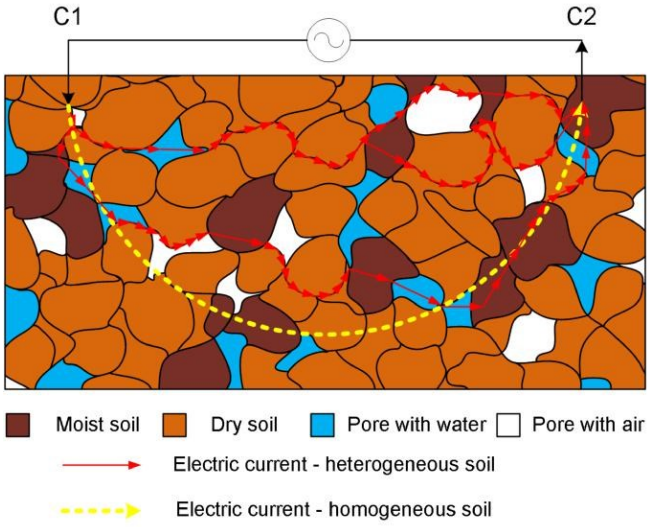

Fig. 1. Path of electric current in the soil.

A. Lateral Profiling

Lateral Profiling method is the geoelectric investigation technique used in the horizontal mapping, which consists of the relocation of electrodes in the following points at each measurement, keeping a fixed distance among the rods [9]. Wenner array is used for the application of this technique, where apparent electrical conductivity of the soil σ_a is determined at midpoint of the arrangement between potential electrodes. Entire area can be mapped by identifying these midpoints, delimiting different conductivity regions.

Fig. 2 illustrates the technique for research. In this case, the method applies in column 1 at A1, B1, C1 and D1. In this example the Wenner method is used to apply the Lateral Profiling. The horizontal mapping of apparent electrical conductivity is determined by performing electrical pathway of columns 2, 3 and 4.

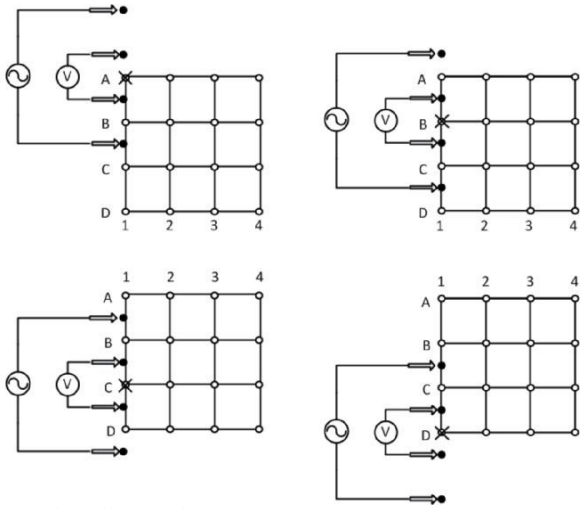

Fig. 2. Lateral Profiling Method.

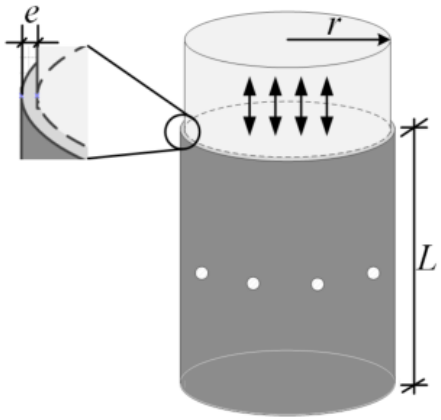

Fig. 3. PVC cell.

B. Experimental procedure - Laboratory Study

For the application of the proposed methodology, a PVC container (cell) is built in order to contain the soil samples. Constructed cell has r = 37,5mm internal radius, L = 80mm height, wall thickness of e = 4mm and 4 holes for insertion of current and potential electrodes for the application of Wenner arrangement, as illustrated in Fig. 3.

1) Sample Preparation

Sample preparation consists in doping the same with known amounts of clay. From the sandy soil, samples are prepared with different proportions of clay, varying the texture of each sample.

Each portion (sample) must contain the same mass. In each portion, withdraws certain amount of soil and inserts the same amount of clay, in order to obtain samples with a known clay content. For example, to prepare the sample with clay content of 20%, it is weighed initially the full portion of collected soil

TABLE I
GRANULOMETRIC CLASSIFICATION OF THE SAMPLES

Clay [%]	Granulometric Classification
0	Sand
20	Sandy Loam
40	Sandy Clay Loam
60	Sandy Clay
80	Sandy Clay
100	Clay

and withdraws the equivalent of 20% of its weight, inserting in place the same amount of clay, in order to obtain the sample doped with 20% clay.

This methodology is adopted in order to obtain samples with a gradual variation in granulometric classification of the soils. After this doping step, samples were sent to laboratory for analyze granulometric classification of the same. The Tab I provides the classification results.

2) Relation among electrical resistance (R_m), soil moisture (w) and clay content (δ)

Relationship among electrical resistance of the soil R_m, soil moisture w and the clay content δ consists of performing R_m measures in soils with different clay content, gradually varying the moisture content, keeping the compaction C constant.

The R_m values are obtained from geoelectrical prospection methods which detect effects produced by the flow of electric current in the soil. Method of geoelectric prospection utilizes Wenner arrangement for data collection, where electric current is injected and captured in the soil by current electrodes, and voltage is measured at two points of surrounding region by potential electrodes.

Soil samples are first taken to the oven (heater) in order to reduce moisture levels to values close to 0%. After passing through the desiccator cooling process, it is gradually added portions of water equivalent to 5% of the mass of the dry sample. At each increment of water portion to the sample, the corresponding value of electrical resistance R_m is measured by the electrical resistivity meter as illustrated in Fig. 4(a). For each sample, the compaction load is constant.

3) Relation among electrical resistance (R_m), soil compaction (C) and clay content (δ)

The practical experiment to relate R_m, C and δ consists of performing R_m measurements in soils with different clay content, gradually varying the compaction C keeping moisture content w constant.

Soil samples are taken to the oven (heater) and cooled in desiccator. After passing through the cooling process, all samples are gradually moistened until they have constant moisture, $w \approx 20\%$.

At each increase in compaction values, the corresponding value R_m is measured by the electrical resistivity meter. Apparatus of Fig. 4(b) is designed in order to apply pressure on the sample that is within the PVC cell. Under the PVC cell, it places the scale to measure the force exerted on the sample. R_m is measured at each increment of 1 kg in compaction.

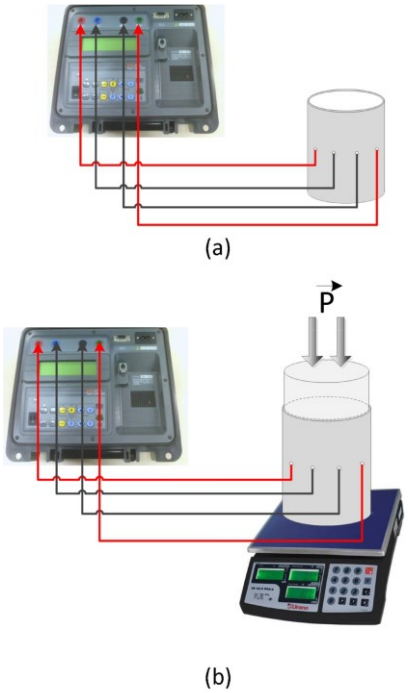

Fig. 4. PVC cell connected to electrical resistivity meter: (a) R_m *x* w *x* δ and (b) R_m *x* C *x* δ.

C. Experimental procedure - Field Study

Two areas are chosen to enable the change of moisture content and compaction, in order to verify the measurement capability of ρ_a to identify changes in soil dynamics. Wenner method is used along with Lateral Profiling method for determining ρ_a. The entire area is mapped in the state it is in. One sub-region within the area should be chosen, where water should be added (sub-region with different color in Fig. 5), modifying the moisture. Again, the survey of ρ_a is performed in the same region. This same methodology can be applied to the mapping of the soil penetration resistance by simply, instead of adding water to modify the dynamics of the system, change the soil compaction.

III. RESULTS

The soil for laboratory analysis was classified as Gleysol and collected in location *S*1346'14.5" *W*5048'16.1".

A. Relation among electrical resistance (R_m), soil moisture (w) and clay content (δ)

Fig. 6 illustrates equipment and connections used to analyze the correlation R_m *x* w *x* δ, where red cables are electrical current injection electrodes and black cables are electrical potential electrodes. Initially, the humidity of each sample is measured by moisture meter, in order to verify whether soil samples are with humidity values near 0%. Then, the mass of

each dry sample is measured in order to calculate the mass of water corresponding to be inserted gradually in the sample.

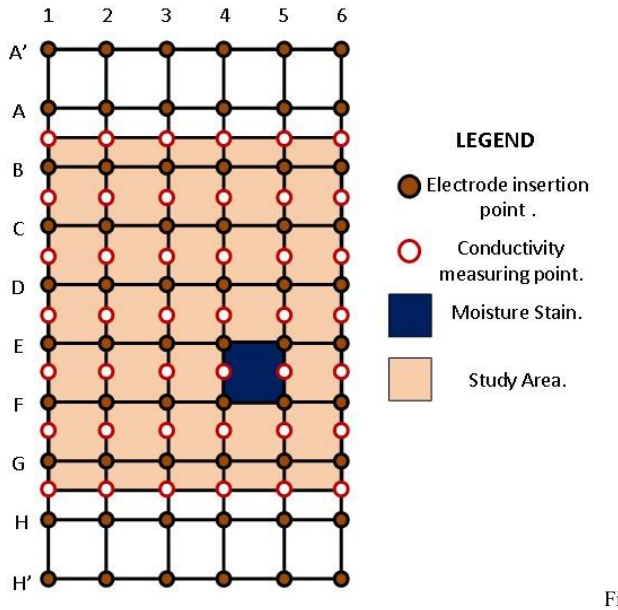

Fig. 5. Delimited area for the application of Lateral Profiling method.

Fig. 6. Equipment for the analysis of correlation R_m x w x δ.

At each insert 5% water portion, resistance R_m is measured with electrical resistivity meter, for each one of the 6 samples.

In any sample could be obtained value of R_m for dry soil, therefore, for this situation the resistance value is greater than the set full scale. Values of R_m were obtained for moisture contents above w = 10%, except for Gleysol sample. This type of soil allows to obtain resistance values at lower moisture levels by their sandy granulometry, which, due to its porosity, facilitates the circulation of electric current through the liquid phase located in the larger pores.

Fig. 7(a) shows the curves of 6 soil types under study in order to evaluate the effect of moisture w and clay content in R_m values.

Resistance R_m varies considerably with the change of soil moisture content w and clay content δ (Fig. 7(a)). Maintaining constant compaction, electrical resistance R_m decreases with increasing moisture and clay content. Due to the grain size, the sandy sample (0% clay) has a higher pore area than the other samples. With increased moisture content, these spaces occupied by air become occupied by water allowing smaller values of R_m with increasing humidity, resulting in high percentage value in the reduction of electrical resistance R_m.

B. Relation among electrical resistance (R_m), soil compaction (C) and clay content (δ)

Apparatus of Fig.8 was developed to apply pressure on the samples for the experiment of correlation R_m x C x δ. A scale placed below the cell performed measurements of the force applied on the sample. It changed gradually the pressure, in order to perform measurements R_m at each 1 kg of applied load. Pressure applied to the soil sample is calculated through the value read on the scale. Red cables in Fig.8 are electrical current injection electrodes and black cables are electrical potential electrodes.

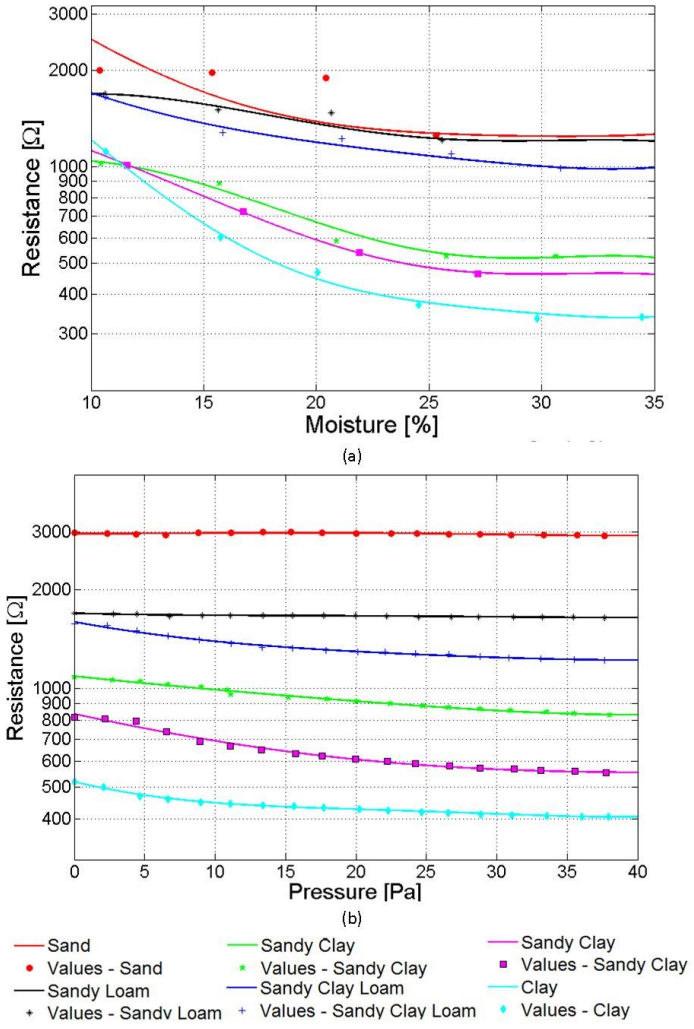

Fig. 7. Correlation Curves: (a) R_m x w x δ and (b) R_m x C x δ

Fig. 7(b) shows the curves of the 6 soil types under study in order to verify the effect of compaction C and clay content δ in R_m values. Each 1 kg load applied, the resistance R_m is

measured by earth meter for each of the 6 samples. For all of them, humidity is approximately constant $w \approx 20\%$.

Resistance decreases with increasing clay content and the increase in the levels of soil compaction, particularly on soils with greater presence of clay fractions in its constitution. For samples of sandy soil and sandy loam soil, where there is a predominance of sand fractions, the influence of compaction on R_m values was lower when compared to samples with higher clay content, indicating R_m behaves differently for sandy and clay soils.

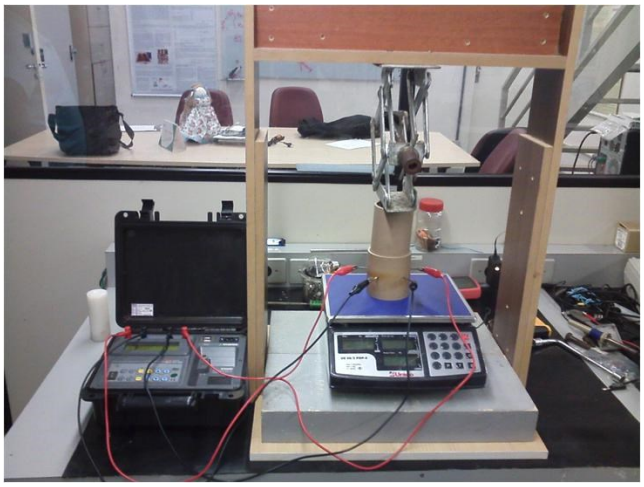

Fig. 8. Apparatus developed for the analysis of correlation R_m x C x δ.

C. Correlation Surface

With the data of Fig. 7, correlations can be established among resistance R_m, moisture, soil compaction and clay content in order to facilitate the identification of soil granulometry from moisture and compaction measurements. Fig. 9 shows the correlation surface R_m x C x w x δ, where the plane x,y represents the relationships R_m x w and R_m x C and the z axis represents the clay content. On this surface, the data used were the saturation, or the average moisture of w = 28,99% and average compaction of C = 37,78kPa. The color grading in the figure corresponds to granulometric variation of soil.

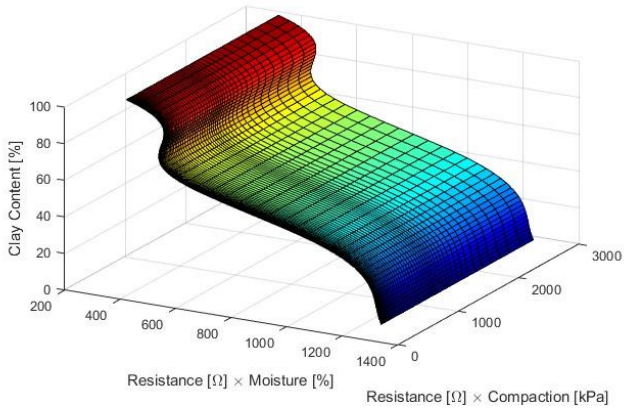

Fig. 9. Correlation Surface.

From the saturation data of R_m in Fig. 7, clay content can be determined through the correlation surface. For example, in the case of moisture saturation was obtained R_m = 1252Ω (Fig. 7(a)), while for the case of compaction saturation was obtained R_m = 2930Ω (Fig. 7(b)). With these two points in the x,y plane, clay content in z axis can be obtained from correlation surface (Fig. 9). Note that the value found is δ = 0%, or sandy soil. Thus, for the case of an argisoil with moisture content w ≈ 28% and compaction $C \approx 37kPa$, granulometry of the soil can be identified on the correlation surface. For this, the use of Tab I is required, which defines the intervals: 0% ≈ 20% sand soil; 20% ≈ 40% sandy loam soil; 40% ≈ 60% sandy clay loam soil; 60% ≈ 100% sandy clay soil and equal to 100% clay soil.

D. Identification of soil moisture stains through Lateral Profiling method.

The region defined for the study has 5 meters long and 5 meters wide. Lateral Profiling was used with spacing $a = 1m$ and $P = 20cm$ depth. With data of R_m and through equation 1, the apparent resistivity matrices before and after the insertion of water are produced, Fig. 10(a) and Fig. 10(b) respectively.

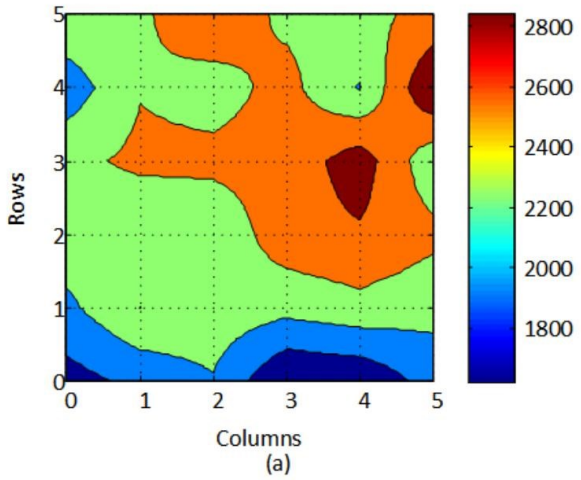

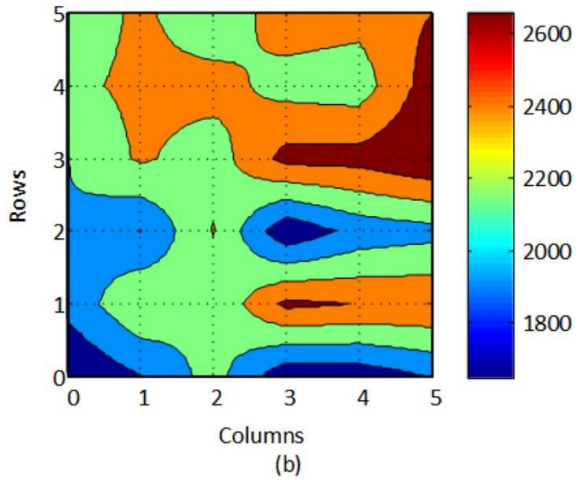

Fig. 10. Moisture stains mapping through Lateral Profiling method (ρ_a).

The colors of Fig. 10(a) and Fig. 10(b) represent areas with homogeneous physical and chemical characteristics. Each of these 5 color shades are associated to soil portion with same properties. To map the soil of this region, for example, would be required to collect 5 soil samples to be analyzed in laboratory, perform soil mapping and, based on their physical and chemical properties, make decisions about management of inputs, pesticides and irrigation.

Fig. 11(a) demonstrates the dynamics occurred in the system, obtained by subtracting of matrices from Fig. 10(a) and Fig. 10(b). Formation of isolines are observed in region where water was added, showing that proposed method has sensitivity to detect differences in apparent electrical resistivity of the soil, mapping its dynamics.

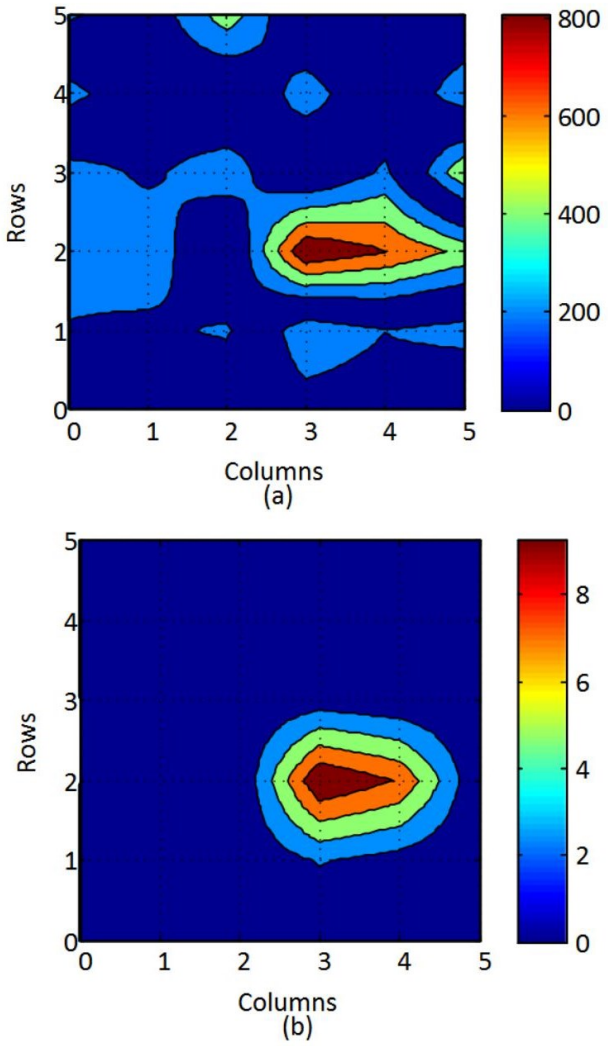

Fig. 11. Moisture stains mapping: (a) proposed method and (b) moisture meter TDR.

In this same area and at the same time it was used a Time-Domain Reflectometer (TDR) to measure the soil moisture content in order to compare the results found in the proposed method.

Fig. 11(b) shows the result obtained by TDR, after subtraction of data measured before and after insertion of the water.

The proposed method, Fig. 11(a), obtains more details than TDR, Fig. 11(b), indicating the proposed method is more sensitive than TDR.

E. Identification of soil compaction stains through Lateral Profiling method.

In another region, soil compaction is changed, using the same proposal, producing matrices before and after compaction. Fig. 12(a) represents apparent electrical resistivity data collected for original soil conditions and Fig. 12(b) represents measured values for soil after compaction.

As in Section III-D, each of 5 colors shades are associated to soil portion with same properties allowing, analogously, the mapping of spatial variability of the soil.

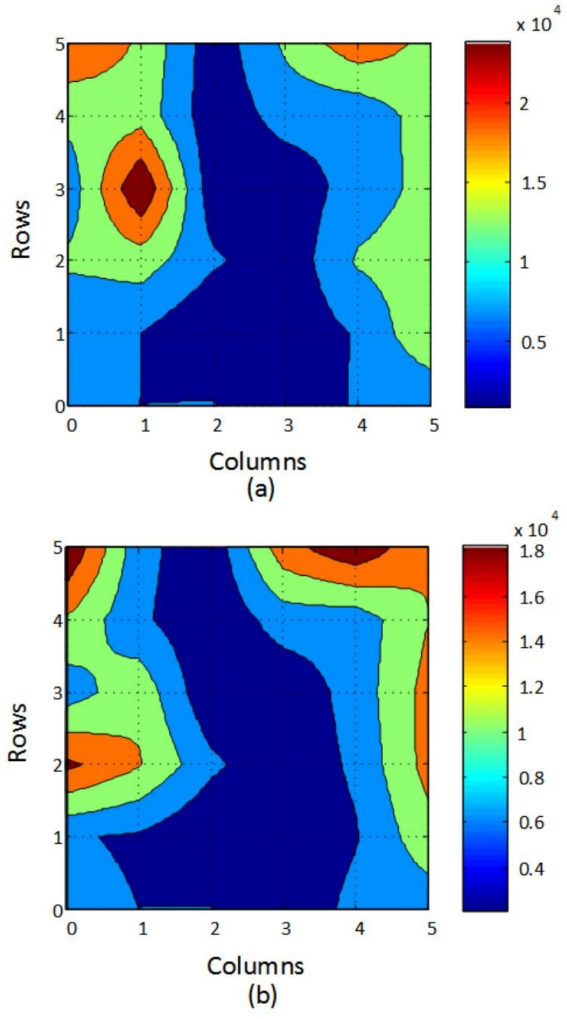

Fig. 12. Compaction stains mapping through Lateral Profiling method (ρ_a).

Fig. 13(a) shows the result of the difference between the matrices before (Fig. 12(a)) and after (Fig. 12(b)) compaction in subregion of study area. Hot colors of Fig. 13(a) represents the differences occurred in dynamics of the area where soil was compacted, showing that stain

compaction was detected by measuring of apparent electrical resistivity of the soil.

In this same area and at the same time a digital penetrometer was used to measure soil compaction in order to compare the results found by the proposed method. Thus, using the digital penetrometer, soil compaction was measured before and after the change of the dynamic, generating two matrices. Fig. 13(b) shows result of the subtraction of these two matrices. Again, it is observed that proposed method has isolines with greater precision details, see relationship between the curves of Fig. 13(a) and (b).

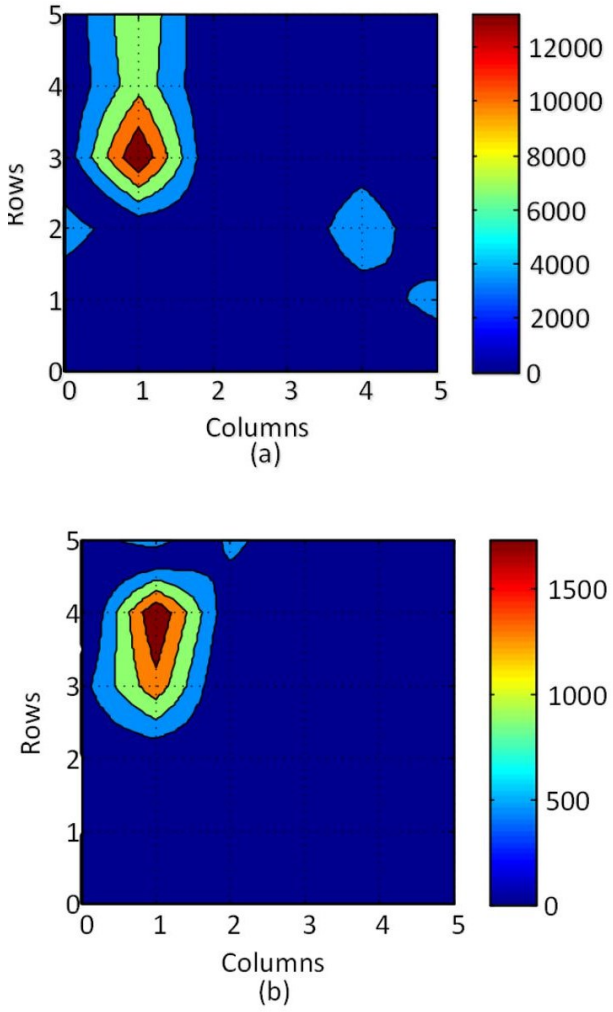

Fig. 13. Compaction stains mapping: (a) proposed method and (b) penetrometer.

IV. Conclusions

The main purpose of this work was to develop methodology for correlating water content in soil, clay content and compaction with electrical properties of the soil, measured by geoelectrical prospecting methods. Resistance R_m varies considerably with the change in moisture content of the soil w. R_m also decreases with increasing w and the measured resistance decreases with increasing clay content. Clay soils conduct better than sandy soils. The compaction C influences the values of R_m, especially for samples with higher clay content, but at a lower degree than the moisture w. Through the Correlation Surface (Fig. 9) it is possible to correlate electrical resistance of the soil, moisture, soil compaction and clay content in order to identify the granulometry of the soil.

Field experiments indicate that Lateral Profiling method is appropriate for measuring regions with same characteristics. These experiments were able to accurately measure the change in soil dynamic produced intentionally. The proposed method is more accurate both in detecting moisture as in detection of soil compaction. The Lateral Profiling method is more sensitive to plot curves and, from correlation abacus, humidity values and compaction can be inferred directly on readings of apparent electrical resistivity of the soil.

Another observation subject of argumentation is related to different color shades of Fig. 10 and Fig. 12. Each tonality is associated to specific soil area with different physical and chemical characteristics. In possession of this georeferenced surface it is possible to proceed data collect on the regions of different shades and utilizing the consideration that the same tonalities has the same physical and chemical characteristics, considerably reduce the amount of sample collection and the number of laboratory analysis. Thus, Lateral Profiling is a noninvasive, fast and low cost method for mapping spatial variability of the soil, supporting decision making on how and when to intervene with inputs, pesticides and irrigation.

Acknowledgment

The authors would like to thank Coordination for the Improvement of Higher Education Personnel (CAPES), the National Counsel of Technological and Scientific Development (CNPq) and Research Support Foundation of Goias State (FAPEG) for financial support research and scholarships.

References

[1] E.D. Lund, P.E. Colin, D. Christy, and P.E. Drummond. Applying Soil Electrical Conductivity Technology to Precision Agriculture. Saint Paul: Proceedings ASA/CSSA/SSSA, 1998.

[2] A. Tabbagh, M. Dabas, A. Hesse, and C. Panissod. Soil resistivity: A Non-invasive Tool to Map Soil Structure Horizontal. Geoderma, vol.97, p. 393-404, 2000.

[3] E.L. Eisenreich. Electrical Conductivity Mapping for Precision Agriculture. Proceedings. Montpellier, Ecole National Superiure Agronomique: European Conference on Precision Agriculture, v. 3, 2001.

[4] A.M. Silva Filho, G.P. Furriel, W.P. Calixto, A.J. Alves, F.A. Profeta, J.L. Domingos, E.G. Domingues, and M.G. NARCISO. Methodology to Correlate the Humidity, Compaction and Soil Apparent Electrical Conductivity. IEEE Congreso Chileno de Ingenieria Electrica, Electronica, Tecnologias de la Informacion y Comunicaciones (IEEE CHILECON 2015), 2015, Santiago. ACTAS de IEEE Chilecon 2015, Universidad Central de Chile, p. 1-7, 2015.

[5] D.L. Corwin and S.M. Lesch. Application of soil electrical conductivity to Precision Agriculture:Theory, Principles, and Guidelines. Agronomy Journal, v.95, n.3, 2003.

[6] S. P. Friedman. Soil properties influencing apparent electrical conductivity: a review. Computers and electronics in agriculture, 2005.

[7] W.M. Telford, L.P. Geldart, and R.E. Sheriff. Applied Geophysics, Cambridge University Press, 1990.

[8] J.D. Rhoades, and R.D. Ingvalson. Determining Salinity in Soils with Soil Resistance Measurements. Soil Science of American Proceedings, vol.35, 1971.

[9] O. Banton, M.K. Seguin, and M.A. Cimon. Mapping Field-Scale Physical Properties of Soil with Electrical Resistivity. Soil Science Societies American Journal, vol.61, 1a. ed. SSSAJ, 1997.

[10] B.G. Williams, and D. Hoey. The use of electromagnetic Induction to Detect the Spatial Variability of the Salt and Clay Content of Soil. Australian Journal of Research, v.25, n.1, p.21-7, Melbourne, 1987.

[11] W.P. Calixto, A.P. Coimbra, B. Alvarenga, J.P. Molin, A. Cardoso, and L. Martins Neto. 3-D Soil Stratification Methodology for Geoelectrical Prospection. IEEE Transactions on Power Delivery, v. 27, p. 1636-1643, 2012.

Simulation and analysis of an isolated full-bridge DC/DC boost converter operating with a modified perturb and observe maximum power point tracking algorithm

Calebe A. Matias
Giordani Pacífico Medeiros
Pedro H. F. Moraes
Bruno de A. Fernandes
Aylton J. Alves
Experimental and Technological Research and Study Group (NExT)
Federal Institute of Goias (IFG), Goiânia, Brazil
Email: calebeabrenhosa@gmail.com

Wesley P. Calixto
Geovanne P. Furriel
School of Electrical, Mechanical and Computer Engineering
Federal University of Goiás (UFG), Goiânia, Brazil
Email: w.p.calixto@ieee.org

***Abstract*— the purpose of the present study is to simulate and analyze an isolated full-bridge DC/DC boost converter, for photovoltaic panels, running a modified perturb and observe maximum power point tracking method. The zero voltage switching technique was used in order to minimize the losses of the converter for a wide range of solar operation. The efficiency of the power transfer is higher than 90% for large solar operating points. The panel enhancement due to the maximum power point tracking algorithm is 5.06%.**

***Index Terms*—energy efficiency, geometric Brownian motion, Monte Carlo simulation, performance measurement and verification, solar water heating.**

I. INTRODUCTION

HE concern to produce clean energy is relevant in Tview of the global warming and pollution. The search for new technologies to improve power conversion of renewable energy sources is the focus of studies and discussions in many academics centers and industries across the globe [1].

Photovoltaic (PV) panels are made of photosensitive semi- conductors. Their semiconductor cells are hit by solar radiation and produce a difference of potential. The problem is that panels cannot deliver the maximum power by their own considering the impedance matching principle. That is the main reason for using a power converter running a maximum power point tracking (MPPT) algorithm [2].

DC/DC converters are used to change the impedance seen by any source, due to control of the trigger circuit of these switches [3]. A DC/DC converter is needed when speaking at tracking the maximum power of an energy source, as a photovoltaic panel [4].

The analysis of the behavior and power transfer ratios of a converter can determine its efficacy on deliver the maximum power to the load. A computer simulation provides lots of information about these characteristics. This can be used to help the development of a real converter [5].

This paper aims to analyze the power transfer ratios and the modified perturb and observe (P&O) MPPT performance of an isolated full-bridge DC/DC boost converter considering the power loss on its components in order to verify the feasibility of the development of a real device [6], [7].

In order to minimize the losses on the switches of the converter the zero voltage switching technique was applied to trigger the MOSFETs.

To perform the analysis of the results and approach of the electrical model of a photovoltaic panel was made for generating its characteristic curve. Later, there were made an analysis of the operation of the DC-DC converter and observations on the MPPT technique.

II. METHODOLOGY

A simulation was performed aiming to analyze the power transfer ratio for a wide range of solar operation and the MPPT method.

A. Materials

The selected PV panel was KC200GT from KYOCERA, with 54 cells. Its main electrical performance under standard test conditions (irradiance 1000W/m², AM 1.5 spectrum and module temperature at 25ºC) data are shown in Table I. The simulation was performed with SPICE software (Simulation Program with Integrated Circuits Emphasis).

TABLE I
ELECTRICAL PERFORMANCE UNDER STANDARD TEST CONDITIONS

Maximum Power	200W (+10% / -5%)
Maximum Power Voltage	26.3V
Maximum Power Current	7.61A
Open circuit Voltage	32.9V
Short circuit Current	8.21A
Max System Voltage	600V
Temperature Coefficiente of VOC	$-1.23x10^{-1}V/°C$
Temperature Coefficient of ISC	$3.18x10^{-3}A/°C$
Area	$1.41m^2$

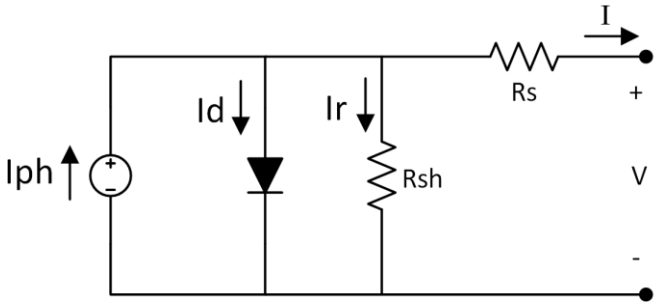

Fig. 1. Single-diode model of the photovoltaic module.

B. Electrical model of a photovoltaic panel

There are several electrical models that describe the behavior of a photovoltaic panel, among them stands out the model with one diode, one series resistance and one resistor in parallel [8], [9], as shown in Fig. 1.

Applying Kirchhoff's law on the circuit, the equation of the load current is obtained as in (1).

$$I = I_{ph} - I_d - I_r \tag{1}$$

Where I_{ph} is the current generated by the photovoltaic effect, I_d is the current in the diode and I_r is the current in R_{sh}.

The I_{ph} current is dependent on the solar radiation and temperature as (2).

$$I_{ph} = \left[I_{ph,stc} + Ki(T - T_{stc})\right]\frac{G}{G_{stc}} \tag{2}$$

Where $I_{ph,c}$ is the current generated by the photovoltaic effect under standard conditions, K_i is the temperature coefficient of the short circuit current, T_{stc} is the temperature at standard conditions (25°C), G_{stc} is the radiation at standard conditions ($1000W/m^2$).

The current in the diode (I_d) has a non-linear characteristic and is dependent on such factors as the saturation current (I_0), the Boltzmann constant (k), the electron charge (q), the ideality factor (a_1) and the number of cells in series (n_s) as (3).

$$I_D = I_0\left\{exp\left[\frac{q \times (V + I \times R_s)}{n_s \times k \times T \times a_1}\right] - 1\right\} \tag{3}$$

The calculation of the saturation current considers the temperature coefficient of open circuit voltage (K_v), temperature coefficient of short circuit current (K_i), the short circuit current I_{sc} under standard conditions ($I_{S,stc}$) and the open circuit voltage under standard conditions ($V_{OC,stc}$) as (4).

$$I_0 = \frac{I_{S,stc} + ki(T - T_{stc})}{exp\left[\frac{q\left(V_{OC,stc} + kv(T - T_{stc})\right)}{(n_s \times K \times T)}\right] - 1} \tag{4}$$

The current through the resistor in parallel is as (5).

$$I_R = \frac{V + I \times R_s}{R_{sh}} \tag{5}$$

There are two other important parameters needed to be calculated: the value of R_{sh} and R_s. These values lead the calculated maximum power point match the experimental maximum power point ($V_{mp} \times I_{mp}$). An iteration algorithm, under PyLab environment, that increases the value of R_s to estimate the $I_{ph,c}$, I_{ph} and R_{sh} values as (2), (6) and (7).

$$I_{ph,stc} = \frac{R_{sh} + R_s}{R_{sh}} I_{sc,stc} \tag{6}$$

$$R_{sh} = \frac{V_{mp}(V_{mp} + I_{mp} \times R_s)}{\left[V_{mp} + I_{ph} - I_d - P_{max,E}\right]} \tag{7}$$

The characteristic curve of the photovoltaic panel was obtained using a computational algorithm. The following values of parallel (R_{sh}) and series (R_s) resistances used on simulation were:

$$R_{sh} = 158.66\Omega$$

$$R_s = 0.0053\Omega$$

C. *Modified perturb and observe MPPT method*

This method was proposed by [7]. The classical P&O MPPT algorithm considers that the PV power variation is caused by only the PV voltage perturbation. In fact the PV power is influenced by both the converter and the environ- mental conditions, such as irradiance and temperature.

During rapidly irradiance changing period, on conventional P&O method, there is a wrong control signal due to simple observation of the PV power and voltage reference. Fig. 2 represents the PV power curve at irradiance I_1 and irradiance I_2. Considering that the conventional P&O algorithm is running from point A to point B, trying to reach point D, at irradiance I_1, so the control signal must increase the voltage from V_1 to a short period of time (Δt) and soon back to irradiance I_1, the converter might read the power at point C and the next control signal must decrease power, for with the increasing voltage and the power reduction the algorithm will try to reach the maximum power point running the opposite way of the real condition, point D. So the conventional perturb and observe method fails to track the maximum power point [7].

To fix this issue a modified P&O MPPT algorithm is needed. This method consists in distinguish the power variation caused by the MPPT control and the irradiance. This can be done by adding a PV power measurement between of control period. The diagram in Fig. 3 illustrates the process. Where $dP_{0.5}$, shown in (8), is the power difference between the middle-point ($dP_{k-0.5}$) and the starting point (dP_{k-1}), which contains the power of both solar radiation and MPPT control; dP_1, shown in (9), contains the power caused by only the irradiance variation and dP , shown in (10), is the power caused by only the MPPT control [10] [7].

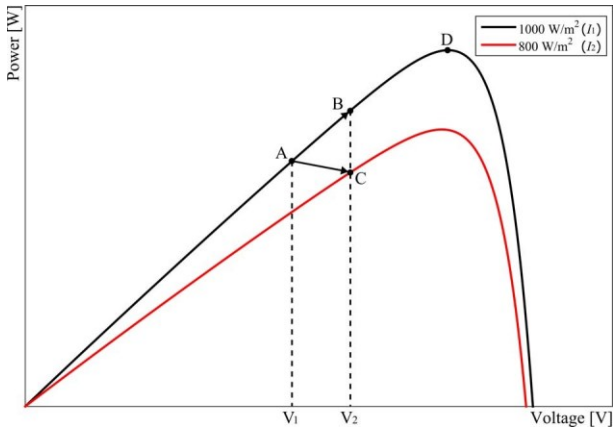

Fig. 2: Control signal analysis of the conventional P&O.

$$dP_{0.5} = P(k-0.5) - P(k-1) \quad (8)$$

$$dP_1 = P(k) - P(k-0.5) \quad (9)$$

$$dP = dP_{0.5} - dP_1 \quad (10)$$

So the algorithm uses the power variation caused by only the MPPT control signal to track the maximum power point. This fixes the problem of the conventional P&O method.

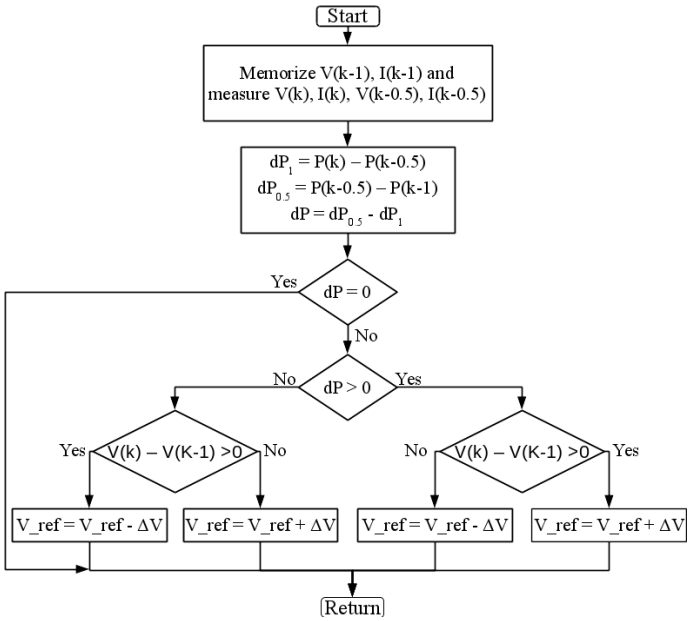

Fig. 3: Modified P&O algorithm method.

III. Simulation and Results

Using SPICE software a simulation was performed to determine the voltage and current values of each component.

The schematic in Fig. 4 represents the circuit used in the simulation. An algorithm running the mathematic model of the solar panel provides the voltage V_{PV} to DC-DC converter.

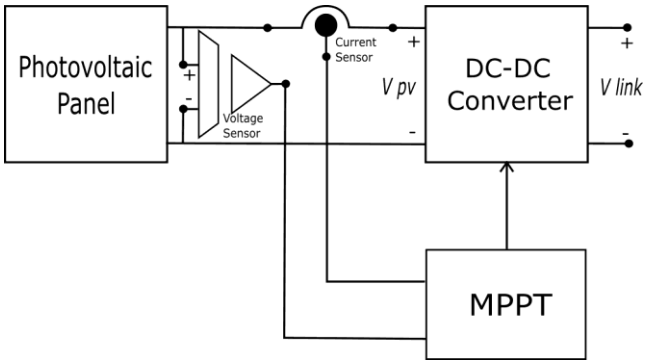

Fig. 4: Schematic of the circuit used in simulation.

A. Operating mode of full-bridge DC/DC boost converter

The isolated full-bridge DC/DC converter, depicted in Fig. 5, working as a step-up or boost converter. V_{PV} is the operating voltage of the photovoltaic panel, which can be varied until the open circuit voltage limit (V_{oc}). The use of C_{PV} decoupling capacitor is recommended to prevent the effects of high frequency current ripple generated by the converter, in the photovoltaic panel.

The MOSFETs are used to generate an alternating waveform in the primary of the transformer with a duty

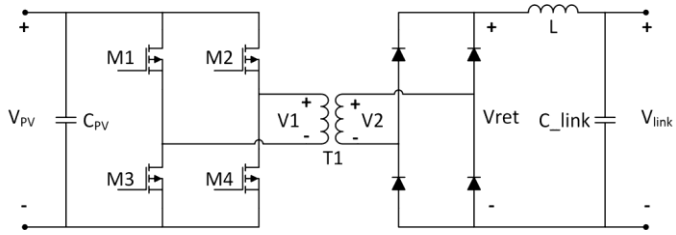

Fig. 5: DC-DC Isolated Full Bridge Power Converter Circuit.

cycle frequency equals 110 kHz. Fig. 6 shows the actuation cycle of the MOSFETs and the waveform generated in the primary of the transformer (V1). A charge/discharge time on the MOSFETs generate losses for there is voltage and current over them at the same time. To minimize these losses a Zero Voltage Switching (ZVS) technique is used. Therefore a time period in which the voltage at the primary of the transformer (V1) remains zero due to the use of this technique, so the switching time of the MOSFETs are different, depicted in Fig. 6.

The transformer amplifies the voltage at a ratio of n. The next stage is rectifying this voltage and then filters the current e voltage ripple through the inductor L and the capacitor C_Link.

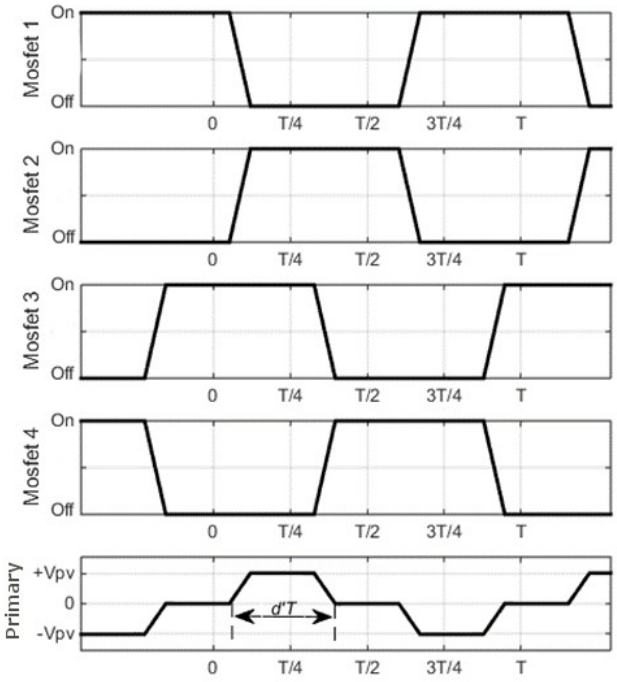

Fig. 6: MOSFETs waveform of the converter.

The DC link voltage is:

$$V_{link} = n \times V_{PV} \times 2d' \qquad (11)$$

The duty cycle of the MOSFETs switching is equal D, where D = 2.d'. The voltage blanking time (voltage equals zero) in the primary of the transformer (V1) is changed by the duty cycle of effective work d' = D/2, as depicted in Fig 6.

The simulation was performed under standard conditions, so the commercial electronic components are specified for its limits values. A load resistance was attached at the DC-DC converter, so measurements can be made. The voltage and current values were observed on each component; therefore the list of commercial components is determined, seen in Table II.

The performance analysis of the DC/DC converter is performed using the specification of the components of the Table II. A 1:18 transformer ratio was used to elevate the voltage to the desired level.

After running a new simulation, varying the solar radiation, the values on the Table III was obtained. This information shows that the converter works properly under wide range of solar operation points and it keeps the efficiency higher than 90% for operation points above 5%. When the solar panel is operating under low solar radiation the converter loses the efficiency and the MPPT algorithm does not work effectively.

Fig. 7 represents the output power of the panel due to suddenly irradiance variation. When the irradiance gets from $1000Wm^2$ to $800W/m^2$ the output power decreases. The implemented modified P&O MPPT has a batter dynamic response than the classic.

B. Modified P&O MPPT analysis

The modified P&O MPPT method was proposed to correct the MPPT control signal during rapidly solar radiation changing. During steady state both methods work properly, but when the irradiance changes suddenly the recovery time on the modified algorithm is faster than the classic.

TABLE II
COMPONENTS USED IN THE SIMULATION

Component	Specification
Panel KC200GT	200W
C_{in}	330uF
Mosfets	$Rson$ = 0.07Ω, 16 A, 60V
Diodes	1000V, 2A
L	12mH, 5Ω
Transformer	1: 18
C_link	$30uF, 450V$
C_{out}	$1000nF, 275\ Vac$

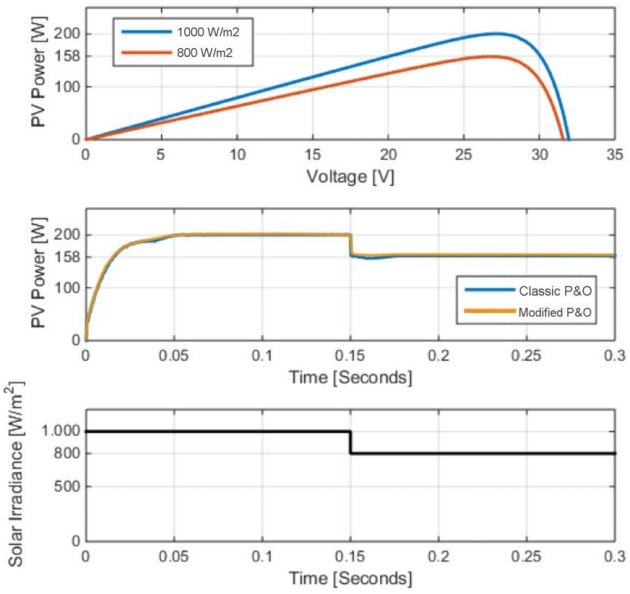

Fig. 7: Modified P&O MPPT response.

The efficiency of the panel, η, can be evaluated as:

$$\eta = \frac{\int_0^T p(t)dt}{A_c \int_0^T G(t)dt} \quad (12)$$

where $p(t)$ is the power output of the panel, G(t) is the solar radiation and A_c is the area of the panel.

A comparison between the panel efficiency under the conditions depicted in Fig. 7 using both algorithms gives that the conventional and the modified P&O efficiency is respectively 12.24% and 12,86%. So the enhancement on panel efficiency, using the modified P&O method, was 5.06%, compared to classical method.

The efficiency of the panel considers the integration on time interval [0, T], which means as more irradiance variation over the panel, during the time, higher is its efficiency gain, for the time recovering of the power is lower than conventional P&O.

TABLE III
SIMULATION RESULTS OF THE DC-DC CONVERTER.

PV Operation Point	5% (10W)	25% (50W)	50% (100W)	100% (200W)
PV voltage: Medium voltage [V]	24.55	27.35	26.11	26.15
PV current: Average current [A]	0.4304	1.73	3.83	7.65
PV power [W]	10.56	47.42	100.04	200
Duty Cycle [%]	8.17	15.96	24.81	35.48
DC Link voltage: Medium voltage [V]	67.73	146.72	212.66	298.79
DC link current: Average current [A]	0.1354	0.29345	0.424533	0.59759
Power DC Link [V]	9.17	43.05	90.45	179.33
Equivalent load resistance [Ω]	500.22	499.98	499.99	499.99
Efficiency [%]	87	91	90	90

IV. CONCLUSION

The performed simulations with the commercial specified components shows that the isolated full-bridge DC/DC boost converter is efficient because it keeps its efficiency above 90% almost in the entire operation range.

The modified P&O MPPT improved the power conversion compared to the classic method. The panel efficiency enhancement was 5.06%. The results could be better for a real condition of solar radiation, in view of the quick irradiance variation on time due to shadows caused by clouds.

The result shows that the physical implementation of the device is feasible.

ACKNOWLEDGMENT

The authors would like to thank Coordination for the Improvement of Higher Education Personnel (Capes), the National Counsel of Technological and Science Development (CNPq) and Research Support Foundation of Goias State (FAPEG) for financial support research and scholarships.

REFERENCES

[1] M. I. Hofferta et al., "Advanced technology paths to global climate stability: Energy for a greenhouse planet," Science, vol. 298, pp. 981– 987, 01 Nov 2002.

[2] B. Parida, S. Iniyanb, and R. Goic, "A review of solar photovoltaic technologies," *Renewable and Sustainable Energy Reviews*, vol. 15, pp. 1625–1636, 2011.

[3] M. H. Rashid, *Power electronics handbook*, third edition ed. Butterworth-Heinemann, 2010.

[4] N. Femia, G. Petrone, G. Spagnuolo, and M. Vitelli, *Power Electronics and Control Techniques for Maximum Energy Harvesting in Photo- voltaic Systems*. CRC Press, 2013.

[5] M. G. Villalva, M. F. Espindola, T. G. de Siqueira, and E. Ruppert, "Modeling and control of a three-phase isolated grid-connected converter for photovoltaic applications," *Revista Controle & Automação*, vol. 22, no. 3, pp. 215–228, 2011.

[6] S. B. Kjær, "Design and control of an inverter for photovoltaic applications," Ph.D. dissertation, Fac. of Eng. and Science, Aalborg University, Denmark, Aalborg, Jan. 2005.

[7] B. Yu, "An improved dynamic maximum power point tracking method for pv application," *IEICE Electronics Express*, vol. 11, no. 2, pp. 1–10, 2014.

[8] M. G. Villalva, J. R. Gazoli, and E. R. Filho, "Comprehensive approach to modeling and simulation of photovoltaic arrays," *IEEE Transactions on Power Eletronics*, vol. 24, no. 5, pp. 1198–1208, 2009.

[9] G.P. Medeiros, "Analysis and simulation of the p&o mppt algorithm using a linearized pv array model," *10th Brazilian Power Electronics Conference* (COBEP), 2009.

[10] L. Piegari, R. Rizzo, I. Spina, and P. Tricoli, "Optimized adaptive perturb and observe maximum power point tracking control for photovoltaic generation," *Energies 2015*, vol. 8, pp. 3418–3436, 2015.

Proposal of heuristic regression method applied in descriptive data analysis: case studies

Flávio A. Gomes, Alfredo de O. Assis, Márcio R. da C. Reis, Viviane M. Gomes, Sóstenes G. M. Oliveira, Wanderson R. H. de Araujo, Wesley P. Calixto

***Abstract*—The purpose of this paper is to use the hybridized optimization method in order to find mathematical structures for analysis of experimental data. The heuristic optimization method will be hybridized with deterministic optimization method in order to that structures found require not knowledge about data generated experimentally. Five case studies are proposed and discussed to validate the results. The proposed method has viable solution for the analysis of experimental data and extrapolation, with mathematical expression reduced.**

***Index Terms* - regression, heuristic, modeling, optimization.**

I. Introduction

This paper is an extended version of our paper published in 2016 IEEE 16th International Conference on Environment and Electrical Engineering [1]. Traditionally, researches show the need to express the variable behavior through functions that represent experimental data. In several areas, regression methods are used to establish the relationship between variables, such as in the image processing [2], analysis of concrete structures [3] [4], extraction of tone of voice [5], health area [6] and waste flow forecasting [7].

To [8], the regression analysis consists in the study of the dependence between variables, verifying the relationship of the explanatory variables towards the dependent variable to perform forecasts and previews. This study is necessary due the existent lack of knowledge of the algebraic expression that rules the system being analyzed.

The absence of the function that describes the behavior of the system implies in simulations or experiments performing in order to define the outputs, every time the inputs are changed. Several times, this requires time and effort, which can make the process of study the system unpractical. The experiments (real or simulated) provide, as output, discrete data, however, in most cases, there is needed a function that describes the data in a continuous way [9].

Once the function that defines the system is found, many analyses can be performed, such as data prediction, which tries to obtain an output for a certain correspondent input beyond the predefined interval [10]. In case of forecasting of natural resources demand, the efficient use can be obtained based on the performed predictions.

In many situations, even simulations take a considerable amount of time, making the system analysis process difficult. In order to solve this problem, we use regression to replace part of the system by an expression that represents it, decreasing the simulation time. In [1], a regression of collected data on a test bench of controlled rectifiers was performed.

Regression methods use techniques that seek flexibility and predictive capacity. Many studies base themselves on polynomials and trigonometric functions for approximating data. However, regressions by hybrid functions, polynomial and trigonometric, present themselves more representative that each of them apart, overcoming limitations as the periodicity for polynomial or prediction for trigonometric series [11]. Other methods are used for prediction and curve fitting, such as Artificial Neural Networks in [3] and [4], which got better results that quadratic regressions and additives models in [7], which are compared to *cubic smoothing splines*.

Researches about regression seek effective parametrization methods, in order to improve the curve fitting. In [12] is used *Darwinian Particle Swarm Optimization*, *P-Spline* method in [13], regularized algorithm of Levinson-Galerkin in [6], the least squares method to parametrize trigonometric series in [5] and in [14] has the solving of compound optimization criterion through weighted polynomial regression models.

The purpose of this work is to present a methodology to determine mathematical expressions that represent the systems with the least number of possible terms. The main contribution is to reduce the edge effect due to the reduced number of terms. Besides that, it contributes to the recognition of systems from the experimental data and also in assertive extrapolation at considerable intervals.

The proposed methodology is based on the generalization of the power and trigonometric series and the application of optimization methods. Section II presents the theoretical background, Section III brings the proposed methodology and the results achieved are presented in Section IV.

II. Background

According to [15], a bounded-input, bounded-output system (BIBO) is stable when it is limited in respect of the space's norm in which it is defined ($L_2,\ L_\infty$). Using the space:

$$L_2(\Omega) = \{f(t) \mid ||f(t)||_2 < \infty\}, \tag{1}$$

The norm of (1) is defined by $||f(t)||_2 = \sqrt{\int_\Omega |f(t)|^2 dt}$, where Ω is a subinterval in the real numbers and $f(t)$ is a square-integrable function in Ω. By analyzing the experimental data $f_{ex}(x)$ of a BIBO system, we have according to [16] that the collected data are represented by:

$$f_{ex}(x) = f_{op}(x) + \epsilon, \tag{2}$$

Since $f_{op}(x)$ represents the regression and ϵ is the random additive error of the process that does not depend on "x" and satisfies the homoscedasticity criterion, which is, that the variance of ϵ is constant. In this sense it is said that $f_{op}(x)$ is the regression that represents the system if the mean square error (MSE) is as minimal as possible. Therefore, the following optimization problem is generated:

$$f_{op}(x) = \min_{x \in \Omega}\{||\epsilon||_2^2\}, \tag{3}$$

where $f_{op}(x)$ depends on the used base for data interpolation.

For the representation of these events, there is a wide collection of interpolation and extrapolation theories, being the polynomial approximation of Weierstrass the main interpolation theorem. In this, it is shown that in the space of the continuous functions $C_{[a,b]} \subset L_2[a,b]$ any function $f \in C_{[a,b]}$, where $a,\ b \in \mathbf{R}$, can be approximated by a polynomial function [17]. Extending its definition to the space of the analytic functions $f \in C_{(-\infty,\infty)}$, any function can be expressed as a power Series.

The standard methods vary from polynomial to trigonometric representations, using the base β_1 for the power series or polynomial, given by (4), and the base β_2 for the trigonometric series, given by (5).

$$\beta_1 = \{1, x, \cdots, x^n, \cdots\} \tag{4}$$

and

$$\begin{aligned}\beta_2 = \{1, \sin(\frac{\pi x}{p}), \sin(\frac{2\cdot\pi x}{p}), \cdots \sin(\frac{n\pi x}{p}), \cdots \\ \cos(\frac{\pi x}{p}), \cos(\frac{2\cdot\pi x}{p}), \cdots \cos(\frac{n\pi x}{p}) \cdots\}\end{aligned} \tag{5}$$

The obtained approximations verify trends and represent data by means of functions [18]. Thus, the regression methods are chosen depending on the characteristics of the problem. The bases β_1 and β_2 have properties of representation in the space of continuous functions in the interval $[a,b]$. When there is some kind of frequent oscillation, the base β_1 is insufficient to extrapolate the polynomial regression interval, since to represent the trigonometric frequencies, there is the need to transform the polynomial regression into a series. However, the extrapolation problem is also present in the base β_2, since it has limitations for data prediction for Non-periodic functions [11] [5].

III. Metodology

The proposed methodology will use hybridized optimization method (heuristic and deterministic) to determine parameters of predefined structures. Based on experimental data, the optimization process will return the mathematical expression that will represent the dynamics of the system, as Fig. 1.

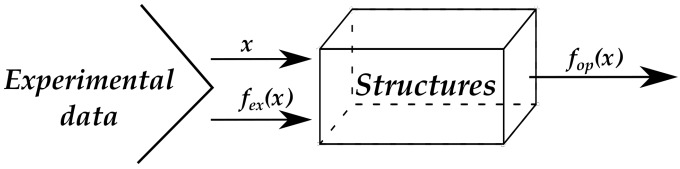

Figure 1. Flow of optimization process.

These structures, based on polynomial, trigonometric, and exponential functions, enable to represent a significant amount of curves. Regression will be performed by comparing the curve defined by the experimental data f_{ex} with the curve generated by structures, called optimized curve f_{op}. Structures that generalize the power and trigonometric series given by f_{op_1}, f_{op_2} and f_{op_3} will be proposed in order to meet the different curve profiles. These structures are presented in expressions (6), (7) and (8), respectively.

$$f_{op_1} = a_0 + \sum_{i=1}^{n} a_i \cdot x^{b_i} \tag{6}$$

$$f_{op_2} = a_0 + \sum_{i=1}^{n} a_i \cdot x^{b_i} \cdot \cos(c_i \cdot x + d_i) \tag{7}$$

$$f_{op_3} = a_0 + \sum_{i=1}^{n} a_i \cdot x^{b_i} \cdot \cos(c_i \cdot x + d_i) \cdot \exp(e_i \cdot x) \tag{8}$$

where: $a_0, a_i, b_i, c_i, d_i, e_i \in \mathbf{R}$.

Unlike other methods [11] [14], the parameters of f_{op} will assume values belonging to the set of real numbers. Therefore, polynomials of the β_1 base from the power series will be generalized to rational functions, well as trigonometric functions with fixed frequencies of the β_2 base will be generalized to any real frequency. Thus, it will be possible to express experimental data with smaller structures, compared to other regression methods, maintaining the power of prediction.

Based on the characteristics of experimental curve f_{ex}, the proposed methodology will select the structure that have greater proximity between the optimized curve f_{op} and the experimental f_{ex}. Thus, the optimization process will be applied following the expression (3), but due to the fact of working with discrete signals of finite duration in the optimization process, the calculus of approximation error or evaluation function F_{aval} will be given by:

$$F_{aval} = \sqrt{\sum_{i=1}^{n}(f_{ex_i} - f_{op_i})^2} \tag{9}$$

where: n will be the number of f_{ex} points.

Before performing the regression, data set will be processed in order to select the characteristic intervals I_k to assist in the optimization process, that will express the orderly domain J of the f_{ex} curve in

$$J = I_1 \cup I_2 \cup \cdots \cup I_k \tag{10}$$

where: k will be the number of intervals.

The first regression interval will be the one that contains the initial point of f_{ex} curve. The method will be applied successively by the union of subsequent intervals given by expression (10). In order to define the intervals, experimental curve will be divided into parts, based on inflection points and variation at the ordinates axis.

The inflection point is the main factor for choosing the structure and also the optimization method. This occurs because this concept is related to the change in the function's variation rate, being characterized by the point at which the derivative of the function changes from increasing to decreasing and vice versa.

This feature influences both at the choice of structure and the improvement of the optimization process. Due to the fact that structures with several inflection points tend to be more oscillatory, this parameter directly influences the choice of structure that best fits the data. If we analyze the optimization aspect, by dividing the interval based on inflection points reduces the possibility of stopping the process in some local optimum point. In this sense, the way of choosing the structures from the simple characteristic of the experimental data is defined.

The amount of inflection points will be the base parameter to define those intervals. If there are until 2 inflection points, it will mean that data set have no oscillatory characteristic. Therefore, data set will be divided into 10 equal parts and the intervals will be chosen based on variation at ordinate axis on these parts. The highest variation will be chosen as reference and the set of intervals (J) of (10) will be compound by only those that will achieve variation higher than 30% in relation to the chosen reference.

If there are 3 or more inflection points, it will mean that data set presents sinuosity and its analysis will be based on these oscillations. Thus, the highest variation at ordinates axis for all set will be chosen as reference. The subinterval between first 3 inflection points will be chosen to check the higher variation at ordinates axis present in this subset. If this variation exceeds 5% of reference variation, then this subinterval will be selected as the set of interval (J) of (10) for analysis in the optimization process. If this variation does not overcome that percentage, the subinterval will be grouped with other more relevant. The following inflection points will continue being analyzed in search of variations that meet this restriction.

These intervals will be passed for the optimization routine that hybridizes the heuristic methods, Genetic Algorithm, and deterministic, Nelder-Mead, in order to find the optimized parameters [19]. At the end, the result will be the values of structures parameters proposed and their respective evaluation functions F_{aval} of data set. The best result will selected and the parameter values will be replaced at the corresponding structure with the view to mount the function that describes the set of experimental data.

IV. Results

In order to generate the set of experimental data, known and used functions have been used to evaluate regression processes in mathematics and statistics. These functions do not represent physical systems and still present problems of mapping by both interpolating polynomials and extrapolations. These functions were used as case studies as well as data collected from a test bench of controlled rectifiers. This choice was done due to: i) the possibility to perform extrapolation of original set, ii) the approximation error with the results obtained at the initial simulation can be measured, and iii) the success of optimization process can be verified.

A. Case Study 1

The generating function of experimental data chosen for this first case study was given by:

$$f_{ex} = \frac{1}{1+x^2} \tag{11}$$

This function was chosen because of presenting oscillation problem near the edges of interval analyzed using polynomial interpolation with polynomials of high order. This problem is known as Runge phenomenon like cited in [20]. In the expression (11), x assumes 1000 values in the range $1 \leq x \leq 100$. The smallest error was got by the structure that contains only polynomials derived from (6) and the eleven terms of final expression was given by:

$$\begin{aligned} f_{op} = & -6.08 \cdot 10^{-5} + 1.30 \cdot x^{-2.07} \\ & + 5.62 \cdot 10^{-5} \cdot x^{-1.52} - 0.81 \cdot x^{-2.89} \\ & - 9.54 \cdot 10^{-4} \cdot x^{-0.77} + 6.21 \cdot 10^{-4} \cdot x^{-0.40}. \end{aligned} \tag{12}$$

Fig. 2 illustrates experimental and optimized curves obtained with $F_{aval} = 1.25 \cdot 10^{-2}$. In the same figure there is a cut at the point 75 showing the difference between both curves with instantaneous error of about 10^{-4}.

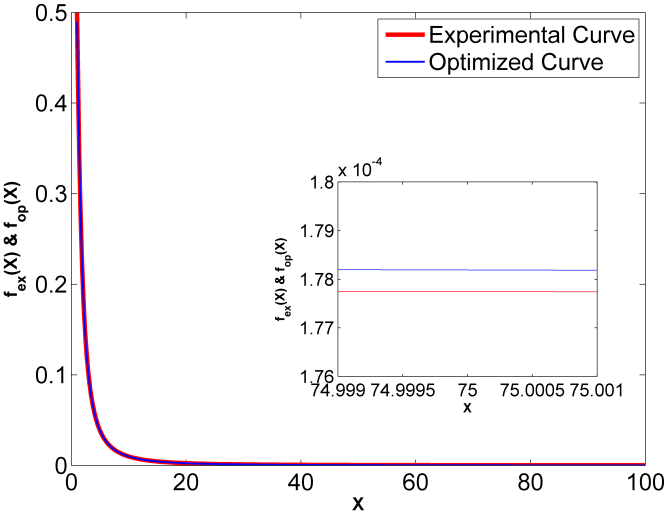

Figure 2. Case study 1.

B. Case Study 2

For the second case study, the generating function of the chosen experimental data was given by:

$$f_{ex} = \sin(2 \cdot x + 3) \cdot \exp(-0.5 \cdot x) \tag{13}$$

This function was chosen because of presenting a difficult behavior to be mapped by the structures (6) and (7). It presents also different oscillations throughout data set analyzed. In the expression (13), x assumes 1000 values in the range $0 \leq x \leq 40$. The smallest error was got by the most complete structure that contains polynomials, cosine, and natural exponential derived from (8). The eleven terms found of final expression was given by:

$$\begin{aligned} f_{op} &= 2.18 \cdot 10^{-9} - 1.00 \cdot x^{4.27 \cdot 10^{-7}} \\ &\cdot \cos(1.99 \cdot x - 1.71) \cdot \exp(-0.50 \cdot x) \\ &- 4.61 \cdot 10^{-12} \cdot x^{1.12} \cdot \cos(-0.39 \cdot x + 1.48) \\ &\cdot \exp(0.14 \cdot x). \end{aligned} \tag{14}$$

Fig. 3 illustrates experimental and optimized curves obtained with $F_{aval} = 0.14$. In the same figure there is a cut at the point 30 showing the difference between both curves with instantaneous error of about 10^{-8}.

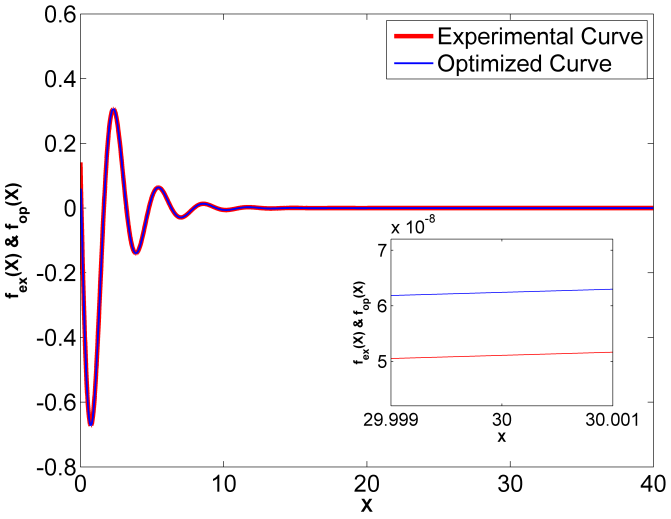

Figure 3. Case study 2.

C. Case Study 3

The chosen generating function of the experimental data for this third case study was given by:

$$f_{ex} = x + \frac{1}{\tan(x)} \tag{15}$$

This function was chosen because it presents output data with negative values, increasing oscillation and also in order to compare with polynomial interpolation methods. In (15), x assumes 20 values in the interval $1 \leq x \leq 20$. The smallest error was obtained by the structure that has polynomials and cosines (7) and the 25 terms of the final expression was given by (16).

$$\begin{aligned} f_{op} &= 19.16 + 44.95 \cdot x^{-0.11} \cdot cos(6.31 \cdot x + 10.42) \\ &+ 11.32 \cdot x^{-0.79} \cdot cos(2.15 \cdot x + 3.10) \\ &+ 2.96 \cdot 10^{-6} \cdot x^{4.73} \cdot cos(2.17 \cdot x + 8.90) \\ &- 5.85 \cdot 10^{-6} \cdot x^{3.72} \cdot cos(4.31 \cdot 10^{-3} \cdot x - 3.51 \cdot 10^{-3}) \\ &+ 6.47 \cdot 10^{-3} \cdot x^{1.90} \cdot cos(-0.22 \cdot x - 1.22) \\ &- 5.19 \cdot 10^{-5} \cdot x^{2.97} \cdot cos(0.71 \cdot x + 19.87). \end{aligned} \tag{16}$$

Fig. 4 illustrates the experimental and optimized curves obtained with $F_{aval} = 1.97 \cdot 10^{-1}$. Within the same figure, there is a cut at the point $x = 3$, which illustrates the difference between both curves, with the order of the distance between them of approximately 10^{-2}.

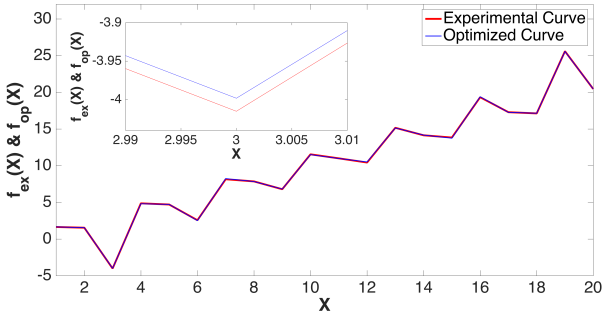

Figure 4. Case study 3.

Polynomial interpolations were also performed to the same generating function in (15) in order to compare the proposed method and this technique of curve fitting. Two polynomials were found, one being 20 degree in (17) and the other nine degree in (18).

$$\begin{aligned} f_{pol20} &= 3.01 \cdot 10^{-13} \cdot x^{19} - 6.29 \cdot 10^{-11} \cdot x^{18} \\ &+ 6.10 \cdot 10^{-9} \cdot x^{17} - 3.65 \cdot 10^{-7} \cdot x^{16} \\ &+ 1.51 \cdot 10^{-5} \cdot x^{15} - 4.57 \cdot 10^{-4} \cdot x^{14} \\ &+ 1.05 \cdot 10^{-2} \cdot x^{13} - 1.87 \cdot 10^{-1} \cdot x^{12} \\ &+ 2.61 \cdot x^{11} - 28.80 \cdot x^{10} + 2.52 \cdot 10^{2} \cdot x^{9} \\ &- 1.74 \cdot 10^{3} \cdot x^{8} + 9.43 \cdot 10^{3} \cdot x^{7} - 3.96 \cdot 10^{4} \cdot x^{6} \\ &+ 1.27 \cdot 10^{5} \cdot x^{5} - 3.01 \cdot 10^{5} \cdot x^{4} + 5.07 \cdot 10^{5} \cdot x^{3} \\ &- 5.67 \cdot 10^{5} \cdot x^{2} + 3.73 \cdot 10^{5} \cdot x - 1.06 \cdot 10^{5}. \end{aligned} \tag{17}$$

$$\begin{aligned} f_{pol9} &= -2.09 \cdot 10^{-7} \cdot x^{9} + 1.84 \cdot 10^{-5} \cdot x^{8} \\ &- 6.80 \cdot 10^{-4} \cdot x^{7} + 1.38 \cdot 10^{-2} \cdot x^{6} \\ &- 1.69 \cdot 10^{-1} \cdot x^{5} + 1.30 \cdot x^{4} - 6.25 \cdot x^{3} \\ &+ 18.52 \cdot x^{2} - 29.4 \cdot x + 18.01. \end{aligned} \tag{18}$$

Fig. 5 illustrates the experimental and optimized curves by the proposed method and by the polynomials in (17) and (18).

The approximation error of the proposed method was $F_{aval} = 1.97 \cdot 10^{-1}$, whereas using the polynomial of 20 degree the error was $F_{aval} = 2.03 \cdot 10^{1}$ and the polynomial of nine degree with error of $F_{aval} = 4.67 \cdot 10^{2}$.

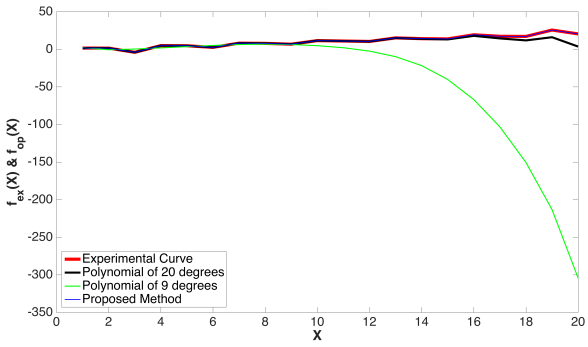

Figure 5. Proposed method and polynomial interpolation comparison.

D. Case Study 4

In this case study, the errors of extrapolations made for the previous case studies were calculated in order to verify the efficiency of the proposed method. In addition to reduction of terms of the expressions found, the extrapolations showed that the curve fitting captured the essence of the systems studied. The case study of section IV-A was extrapolated until point 300 in order to show the curve fitting after the original interval. Fig. 6 illustrates the experimental and optimized curves. The measured error for the new interval was $F_{aval} = 1.13 \cdot 10^{-2}$ and within the same Fig. 6 there is a cut at the point $x = 280$, which illustrates the difference between both curves with the order of the distance between them being approximately 10^{-5}.

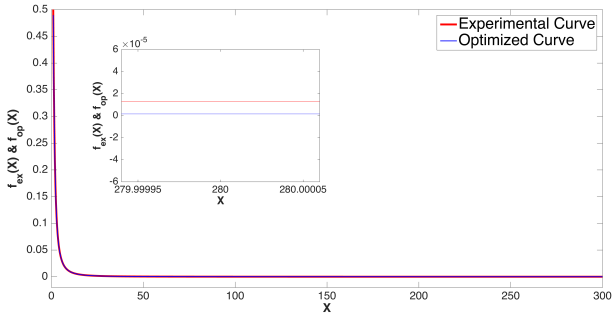

Figure 6. Extrapolation of the case study 1.

For the case study of section IV-B, the extrapolation was performed both before and after the initial interval. In Fig. 7, the explanatory variable x takes on values in the new interval $-15 \leq x \leq 60$ and again, it can be noticed that (14) follows the behavior of the experimental data curve. The measured error for the new interval was $F_{aval} = 2.36 \cdot 10^{-2}$ and within the same Fig. 7, there is a cut close to the point $x = -11.84$, which illustrates the difference between the two curves, being the order of distance between them approximately 10^{-3}.

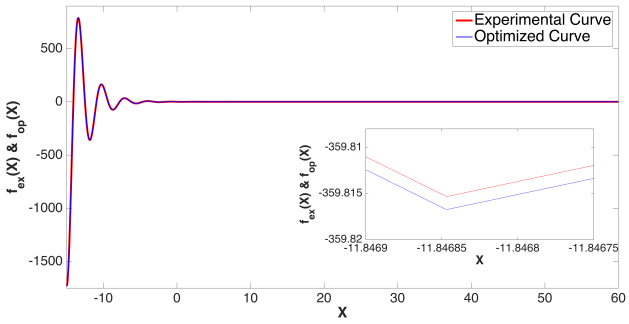

Figure 7. Extrapolation of the case study 2.

For the case study of section IV-C, the extrapolation was performed a little after the initial interval, since the approximation error of the curves by the methods becomes difficult to be perceived graphically. The nine degree polynomial in (18) was unable to adjust the curve in the original interval, remaining in the extrapolation process. The 20 degree polynomial in (17) obtained a suitable approximation in the analyzed interval and diverged abruptly when the extrapolation occurred shortly after the original interval due to the edge effect or Runge's phenomenon [20] which is noticed in polynomial interpolations.

In Fig. 8, there are presented the experimental and optimized curves by the proposed method and by the interpolating polynomials. The explanatory variable x assumes values in the new range $5 \leq x \leq 21$ and again, it can be noted that (16) follows the behavior of the experimental data, whereas the interpolating polynomials lose their ability of approaching. For the new interval, the measured errors by using the proposed method and (17) and (18) were $F_{aval} = 7.27 \cdot 10^{-1}$, $F_{aval} = 6.68 \cdot 10^{2}$ and $F_{aval} = 6.41 \cdot 10^{2}$, respectively.

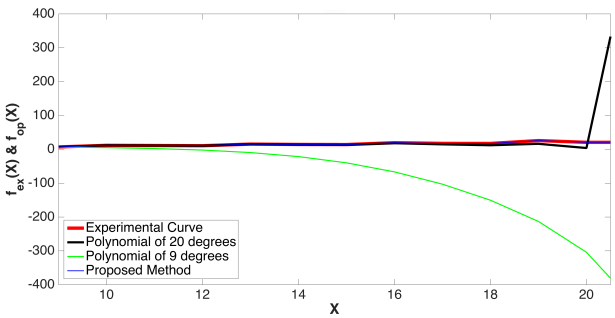

Figure 8. Extrapolation of the case study 3.

E. Case Study 5

At the fifth case study were analyzed data collected at a test bench for studies of controlled rectifiers. These rectifiers provide DC voltage of variable output as from a fixed AC voltage. Due to its ability to provide DC voltage continuously variable, the controlled rectifiers revolutionized the modern industrial control equipments. This converter was shown in Fig. 9.

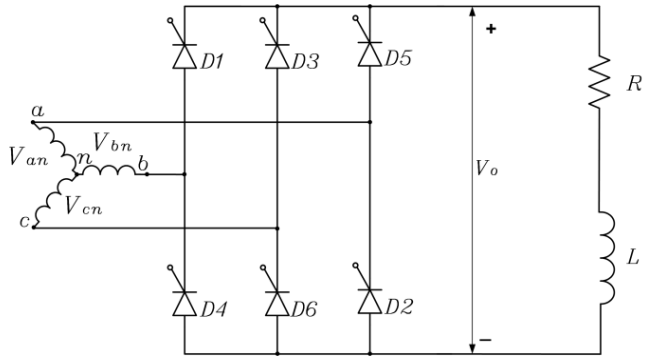

Figure 9. Power converter circuit with RL load.

In order to obtain the instantaneous value of voltage controlled output V_o, the literature has the solutions given by (19) according to [21].

$$V_o = \begin{cases} \beta\sqrt{2}\ V_{ab} & \texttt{if } \omega t \leq \frac{\pi}{6} \\ \beta\ \sin\left(\omega t + \frac{\pi}{6}\right) & \texttt{if } \frac{\pi}{6} + \alpha \leq \omega t \leq \frac{\pi}{2} + \alpha, \\ \beta\ \sin \omega t' & \texttt{if } \frac{\pi}{3} + \alpha \leq \omega t' \leq \frac{2\pi}{3} + \alpha, \end{cases} \quad (19)$$

where: $\omega t' = \omega t + \frac{\pi}{6}$ and V_{ab} is the voltage (effective) of input line and β is the extinction angle of electric current described in [22].

A test bench has been developed for obtaining experimental data of the converter output voltage and the firing angles of keys. The collected data set was interpolated in order to also contain 1000 values, and then was applied the proposed method to obtain analytical expression that represent the voltage as a function just of the firing angle α. The smallest error was obtained by the structure of polynomials and cosines derived from (7) and the 21 terms of found expression was given by (20):

$$\begin{aligned} f_{op} = 263 + \ & 40.9 \cdot x^{0.98} \cdot \cos(3.78 \cdot 10^{-4} \cdot x + 1.57) \\ & + 3.67 \cdot x^{0.16} \cdot \cos(8.20 \cdot 10^{-2} \cdot x + 3.01) \\ & - 2.84 \cdot 10^{-4} \cdot x^{2.62} \cdot \cos(-3.96 \cdot 10^{-2} \cdot x + 3.67) \\ & - 0.15 \cdot x^{0.93} \cdot \cos(0.10 \cdot x - 61.3) \\ & - 0.46 \cdot x^{3.57 \cdot 10^{-5}} \cdot \cos(0.22 \cdot x + 3.92 \cdot 10^{-2}). \end{aligned} \quad (20)$$

Fig. 10 presents the characteristic experimental curve of voltage of converter controlled three phase operating with load RL (resistor-inductor) and the optimized curve obtained. The approximation error found was $F_{aval} = 37.6$. The set of terms was analysed to identify the importance of each of them in the composition of encountered error. It was noticed that removing the last term in expression (20) the new value was $F_{aval} = 42.7$, that is, with 17 terms it still maintain an acceptable approximation error.

V. Conclusion

This work presented the hybrid optimization method to be applied in the development of descriptive analysis data

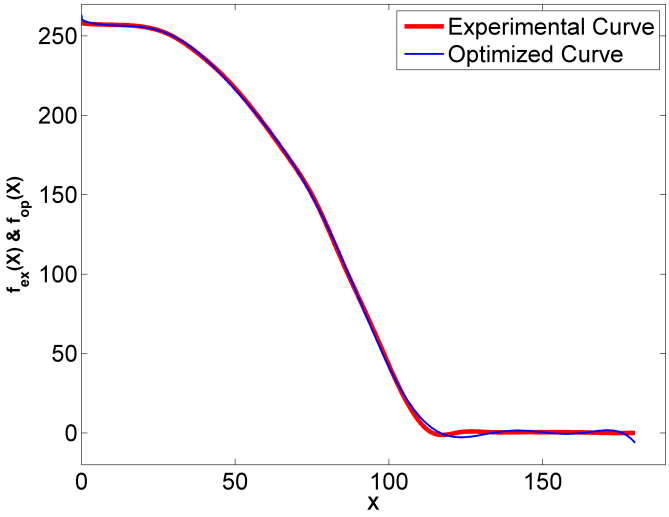

Figure 10. Case study 5.

structure. The study results indicate that the proposed method is able to formulate mathematical expressions, in the form of regression, allowing to explore the relationship between the dependent and independent or explanatory variables. The proposal finds values in the set of real numbers for the coefficients, exponents and frequency of structures that generalize the power and trigonometric series, in an attempt to minimize errors. This proposed method is able to find a continuous function expression that represents a set of experimental data described by a discrete function expression. Another advantage is the extrapolation performed in an assertive form at first and second case studies without observe problems like Runge phenomenon at the edges of analyzed sets. Researches are still being developed in order to compare the proposed method with the traditional methods of regression.

Acknowledgment

The authors would like to thank Coordination for the Improvement of Higher Education Personnel (CAPES), the National Counsel of Technological and Scientific Development (CNPq) and Research Support Foundation of Goiás State (FAPEG) for financial support research and scholarships.

References

[1] F. A. Gomes, V. M. Gomes, A. d. O. Assis, M. R. d. C. Reis, G. da Cruz, and W. P. Calixto, "Heuristic regression method for descriptive data analysis," 2016.

[2] E. Garcia, R. Arora, and M. R. Gupta, "Optimized regression for efficient function evaluation," 2012.

[3] W. H. Chien, L. Chen, C. C. Wei, H. H. Hsu, and T. S. Wang, "Modeling slump flow of high-performance concrete using a back-propagation network," 2010.

[4] I.-C. Yeh, "Modeling slump flow of concrete using second-order regressions and artificial neural networks," 2007.

[5] K. Steiglitz, G. Winham, and J. Petzinger, "Pitch extraction by trigonometric curve fitting," 1975.

[6] T. Strohmer, "A levinson–galerkin algorithm for regularized trigonometric approximation," 2000.

[7] A. Antoniadis, I. Gijbels, and A. Verhasselt, "Variable selection in additive models using p-splines," 2012.

[8] D. Gujarati and D. Porter, "Econometria básica - 5.ed.:," 2011.
[9] L. A. Aguirre, "Introdução à identificação de sistemas–técnicas lineares e não-lineares aplicadas a sistemas reais," 2004.
[10] M. K. Goyal, "Monthly rainfall prediction using wavelet regression and neural network: an analysis of 1901–2002 data, assam, india," 2014.
[11] R. L. Eubank and P. Speckman, "Curve fitting by polynomial-trigonometric regression," 1990.
[12] M. S. Couceiro, D. Portugal, N. Gonçalves, R. Rocha, J. M. A. Luz, C. M. Figueiredo, and G. Dias, "A methodology for detection and estimation in the analysis of golf putting," 2013.
[13] B. U. Park, E. Mammen, Y. K. Lee, and E. R. Lee, "Varying coefficient regression models: a review and new developments," 2015.
[14] H. Dette, G. Haller, *et al.*, "Optimal designs for the identification of the order of a fourier regression," 1998.
[15] P. T. Chen G, "Introduction to fuzzy sets, fuzzy logic, and fuzzy control systems," 2000.
[16] G. Broniatowski, Michel; Celant, "Interpolation and extrapolation optimal designs. 1, polynomial regression and approximation theory," 2016.
[17] R. Glowinski, K. Atkinson, and W. Han, "Theoretical numerical analysis: A functional analysis framework," 2003.
[18] H. A. Schilling and S. L. Harris, "Applied numerical methods for engineers using matlab," 1999.
[19] W. P. Calixto, A. Paulo Coimbra, J. C. d. Mota, M. Wu, W. G. Silva, B. Alvarenga, L. d. C. Brito, A. J. Alves, E. G. Domingues, and D. P. Neto, "Troubleshooting in geoelectrical prospecting using real-coded genetic algorithm with chromosomal extrapolation," 2015.
[20] L. Trefethen, *Approximation Theory and Approximation Practice*. Society for Industrial and Applied Mathematics, 2013.
[21] M. Rashid, "Eletrônica de potência: circuitos, dispositivos e aplicações," 1999.
[22] M. R. C. Reis, "Comparative analysis of optimization methods applied of tuning PI controller," 2014.

An Effective Implementation of Internet of Things for Agile Demand Response

M. Babar*†, J. Grela*, A. Ozadowicz*, P.H. Nguyen†, Z. Hanzelka* and I.G. Kamphuis†
*Faculty of Electrical Engineering, Automatics, Computer Science and Biomedical Engineering
AGH University of Science and Technology, Krakow, Poland
†Electrical Energy Systems Group, Department of Electrical Engineering,
Eindhoven University of Technology, Eindhoven, The Netherlands
Email: m.babar@tue.nl

***Abstract*—Transactive based control mechanism (TCM) needs the IoT environment to fully explore flexibility potential from the end-users to offer to involved actors of the smart energy system. On the other hand, many IoT based energy management systems are already available to a market. This paper presents an approach to connect the current demand-driven (top-down) energy management system (EMS) with a market-driven (bottom-up) demand response program. To this end, this paper considers multi-agent system (MAS) to realize the approach and introduces the concept and standardize design of Agilometer. It is described as an elemental agent of the approach. Proposed by authors Agilometer consists of three different functional blocks, which are formulated as an IoT platform according to the LonWorks standard. Moreover, the paper also performs an evaluation study in order to validate the proposed concept and design.**

***Index Terms*—demand response; energy management system; Internet of Things; Transactive based control mechanism ; smart metering;**

I. Introduction

In general, Transactive based control mechanism (TCM) requires the integration of advanced information and communication technology to dynamically manage power supply and demand. One of the most popular control methodologies to enable TCM is Multi-agent System (MAS) for integrating demand response and home energy management systems [1].

Multi-agent system comprises two or more intelligent control units (i.e. referred as agents). Agents are capable of interacting with each other in a controlled environment, as well as they can be organized in multiple ways such that a global objective of the system should be distributed among all agents into a set of smaller tasks. In context of energy management system (EMS), every agent has the ability to monitor energy usage, primary process parameters (e.g., occupancy, comfort level), and control signals during an operation [2]. Agent is also equipped with communication module for sharing of data and information with other agents.

During the last decade, MAS has been widely considered in many different power system applications and pilot projects. For example, the PowerMatcher developed by the Netherlands Organization for Applied Scientific Research (TNO) is a demand response that balances demand and supply over local basis. The project present bidding mechanism to manage the loads with more precision and efficiency. The devices inside the PowerMatcher are represented by agents, where they are organized in co-tree fashion. Each agent talks to upper-stream agent and expresses its willingness to consume or produce energy in the form of a simple bid (a demand or supply relationship). Based on the bids the upstream agent (namely concentrator) decides what any device should produce or consume in order to keep the system balance [3].

The energy department of Flemish Institute for Technological Research (VITO) also developed a similar product based on the same MAS organization, it was initially referred as Intelligator. Later, VITO focused on the development of a software library contains advanced algorithms, which enhance the intelligence of agents. In particular, the algorithms consider local electronic auction to regulate the system where participants of auction send their requested power in form of bid to an upstream-agent (namely auctioneer). The auctioneer finds a balance between production and consumption by adding all bids from agents. Then it responds to the participants with a demand schedule over day-ahead basis [4].

There are also some technological applications like PowerRouter by NEDAP or Intelliweb by Mastervolt, which perform an intelligent control of solar energy at home in order to increase power injection to the grid. These applications provides access to data via their data server to acquire and control in real-time [5], [6].

Furthermore, there are projects that use MAS based EMS to improve quality and control of power system, like ForskEL in Denmark [7]. Moreover, an ongoing EU project "Multi-agent systems and secured coupling of Telecom and EnErgy gRIds for Next Generation smart grid services" is aimed at developing IoT platform for the monitoring and optimal management of low-voltage distribution grids by integrating last mile connectivity solutions with distributed optimization technologies, while enhancing the security of increased bi-directional communications [8].

In short, all existing applications and research provide enough study to perform demand in power system. However, current evidence is either anecdotal or insufficient to provide generalize principles. Moreover, different research communities tried to tackle the issue of demand response integration in EMS within their own expertise, at the cost of precision in respective domain. Hence the studies lack representativity,

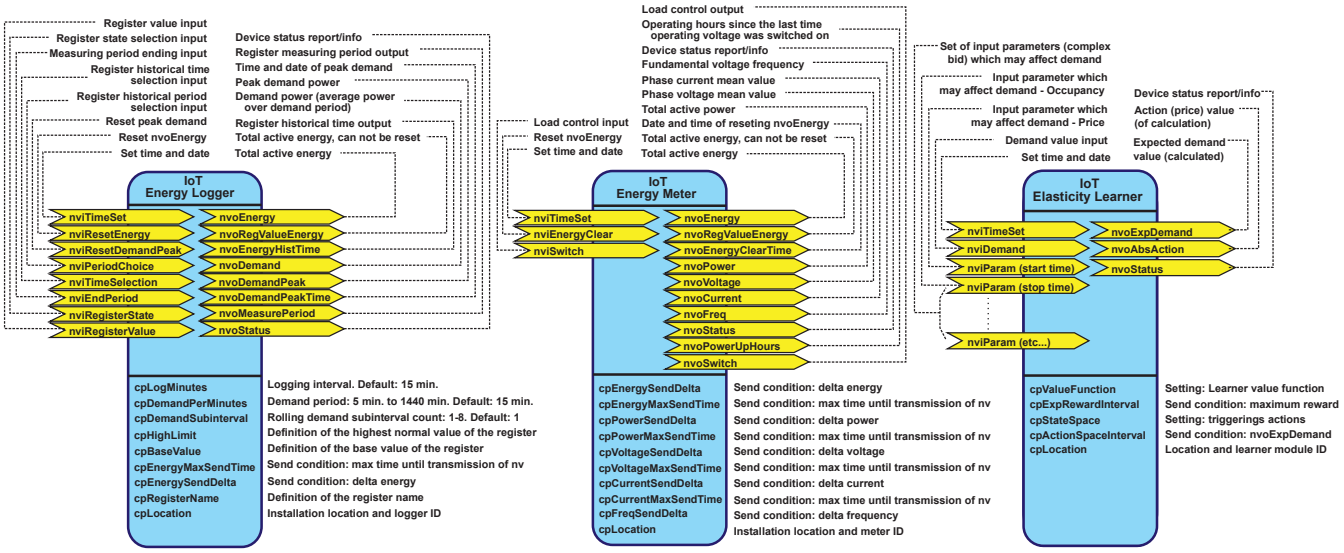

Fig. 1. A developed Agilometer functional blocks.

which is taken into consideration in this paper. The paper proposes "Agilometer" as a key element to achieve the concept of agile demand response, presented in [9], [10].

There are six key features that should be defined in the Flexometer.

- Abstract and standardized design for information sharing
- Availability of data for training
- Ability to work iteratively and deliver incrementally
- Self-adaptability
- Use of communication technology
- Delivery of demand flexibility on demand

This paper addresses mentioned features of the Flexometer as follows. Section II discusses the abstract and standardized design and concept for information sharing. It further explains in detail the features of data availability training, iterative processing and self-adaptability in form of three different functional blocks of Flexometer. Section III presents how Flexometer is implemented in the context of TCM by using simple and low-tech communication methods. Section IV focuses on the evaluation and validation of real-time operation of Flexometer. Finally, some conclusions are drawn in Section V.

II. Design and Concept of Flexometer

In order to implement Flexometer in EMS, the IzoT platform, introduced by Echelon Corp., has been selected. It is offered as next generation of the LonWorks standard technology dedicated for Building Automation and Control Systems (BACS), with capability to use IP-all-the-way to the end device. The IzoT platform has already provided a development environment with chips, stacks, communication, application interfaces (API) and management software. Interoperability between IzoT network devices is provided by functional profiles, in accordance with the LonWorks standard.

Based on this platform, a standardized design of the Flexometer is proposed in this section. Flexometer supports three main functions: (1) an Energy Meter, (2) an Energy Logger and (3) an Elasticity Learner, as shown in Fig. 1. In the functional profile there are defined network variables (NVs) and configuration properties (CPs), which are included in functional blocks as per algorithm requirement. Herein, the paper designs the functional blocks in such a fashion that they are collectively able to express all kind of primary process parameters and customer preferences. However, the details explanation of each network variables (NVs) and configuration properties (CPs) within each block are presented in [11], [12].

A. Energy Meter

Changes within the device and its primary process parameters are acquired by energy meter on real-time basis. The energy meter also captures changes that may occur due to customer preferences (e.g. user implicitly controlled or EMS explicitly controlled the device) or may occur naturally due to environmental change (e.g. room temperature). Then energy meter stores the current primary process parameters and customer preferences as a table with columns for all network variable and configuration properties respectively.

B. Energy Logger

Once the energy meter has acquired agent state (i.e.primary process parameters and customer preferences), energy logger then separates it into events. Each event denotes an instance with respect to the state and a control action that was being performed. Then the pair of action and state is logged into the logger.

To apply learning algorithm, the state must be mapped to a Markov decision process (MDP) consisting of a data tuple (state, action, transition probability, reward). State x_k of an agent includes all possible network variables and configuration properties. Action u_k captures the control action to an agent (e.g. turn on/off lamp). Transitional probability is a vector

describing the transition of a agent from current state to a new state for a given action. Reward r_k herein is simply a marginal energy cost incurred by an agent for the given state x_k and action u_k, as follows:

$$\lambda_k = \Gamma_k \times (1 + \frac{1}{\epsilon_k}) \tag{1}$$

where $\Lambda \doteq [\lambda_1, \ldots, \lambda_K]$ represents the vector of marginal cost which is expected to incurred by Flexometer. Γ_k represents price during k^{th} interval. ϵ_k is a price elasticity of demand.

C. Energy Elasticity Learner

This functional block has an objective to forecast a state of an agent for an expected action by using the concept of price elasticity of demand. It has been found in [13] that price elasticity of demand can be successfully use for estimating agent's value-proposition (i.e. bid). If K represents the number of intervals through out the day, then the price elasticity of demand or demand elasticity is defined as the change in demand δD_k due to the change in the electricity price $\delta\lambda_k$ during an interval. Moreover, the effect of current price over demand is called self-elasticity and the effect of prices during other intervals over current demand is called cross elasticity. Combing cross-elasticity and self-elasticity in a matrix, as shown in (2) is called price elasticity matrix (PEM).

$$\epsilon = \begin{bmatrix} \epsilon_{p,p} & \epsilon_{f,p} \\ \epsilon_{p,f} & \epsilon_{f,f} \end{bmatrix} \tag{2}$$

where $\epsilon_{p,f}$ represents the map from past input to future output. It is usually referred as postponing cross-elasticity which contains all necessary information about the past behavior of the consumer. In particular it contains the information of the past states of an agent that may influence the future states. In the literature, this notion is often called as Markov property. $\epsilon_{f,p}$ represents the map of expected future input to past output. It is usually referred as advancing cross-elasticity which contains the prediction of future behavior of an agent.

Network variables (i.e. nvParam) in the functional block of energy elasticity learner are associated with customer preferences. Every nvParam is updated by a customer before the activation of an agent. The most common temporal preferences could be start time and stop time to the agent, which means during a day the agent can start from the given time and must complete its task before the identified time. In this way, it can be inferred that nvParam has a direct influence on PEM.

As the behavior of a reinforcement learning agent is determined by its reward function (given in (1)) and algorithm parameters, these must be designed to enable and strengthen the kinds of behaviors desired from the agent. Herein, Q-learning is considered in order to learn the behavior of an agent. The objective of a reinforcement learning agent is determined an optimal actions such that its reward function (given in (1)) is maximized. Learning starts from an arbitrary initial Q-function Q_0 and updates it without requiring a model, using instead observed state, transitions and rewards, i.e. (x_k, u_k, x_{k+1}, r_k). After each transition, Q-function is updated using such a data tuple (x_k, u_k, x_{k+1}, r_k), as follows:

$$Q_{k+1}(x_k, u_k) = (1 - \alpha_k)Q_k(x_k, u_k) + \alpha_k \left[r_k + \max_{u'} Q_k(x_{k+1}, u') \right] \tag{3}$$

where $\alpha_k \in (0, 1]$ is the learning rate. The term between square brackets is the temporal difference, i.e., the difference between the updated estimate $r_k + \max_{u'} Q_k(x_{k+1}, u')$ of the optimal Q-value of (x_k, u_k), and the current estimate $Q_k(x_k, u_k)$. As the number of transitions approaches infinity, Q-learning asymptotically converges to Q provided the state and action spaces are discrete and finite.

The agent also has to exploit its current knowledge in order to obtain good performance, e.g., by selecting greedy actions in the current Q-function. This is a typical illustration of the exploration-exploitation trade-off in online RL. A classical way to balance exploration with exploitation in Q-learning is ε-greedy exploration, which selects actions according to:

$$u_k = \begin{cases} u \in \underset{u'}{\text{argmax}} Q_k(x_k, u') & \text{with probability } 1 - \varepsilon_k \\ \text{a random action} & \text{with probability } \varepsilon_k \end{cases} \tag{4}$$

III. Physical Implementation

The proposed functional blocks were implemented in autonomic IzoT automation network node. IzoT device stack were based on Raspberry Pi 2 Model B Boards, with 900MHz quad-core ARM processors and 1GB of memory, with an integrated power measurement circuit.

A. Measurement system design

The measurement system was developed by using two analog-to-digital converters (ADC) CS5460 manufactured by CIRRUS LOGIC. It was designed to accurately measure and calculate: Real (True) Energy, Instantaneous Power, current (IRMS), and voltage (VRMS) for single phase 2- or 3-wire power metering applications. In the application it was connected with Raspberry Pi microcontroller by its GPIO (general purpose input/output) pins with SDI, SDO, CLK, GND, CS signals. A schematic diagram of the connections in the mentioned system is presented in Fig. 2. Moreover, authors discussed the details of the measurement design in [14].

B. Finite State Machine

In the phase of logical implementation, a software application has been developed for the Flexometer, implemented in Raspberry Pi with the IzoT platform stack. The software application provides and supports: (1) communication between CS5460 IC and Raspberry Pi via SPI interface, (2) reading of specific data from the CS5460 , and (3) an application code for control and learning was written in C programming language [11], [12]. Fig. 3 shows finite state machine of the Flexometer, which has 7 states (i.e. configuration parameters and control) and 7 transitions (i.e. network variables). This provides a detail description of an agent in terms of a digital

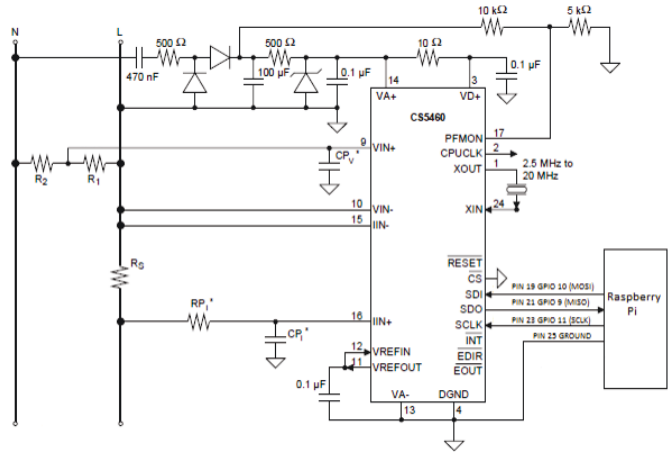

Fig. 2. A schematic diagram of Flexometer with CS5460 IC and Raspberry Pi microcontroller.

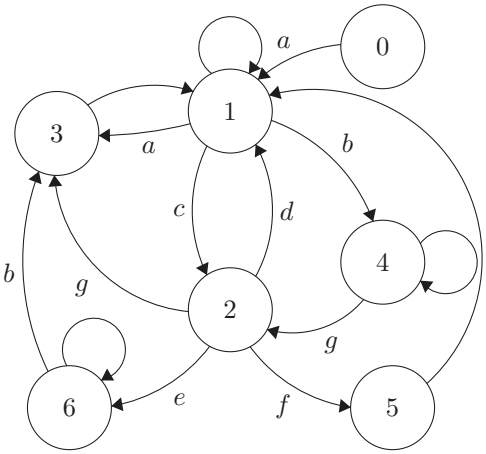

Fig. 3. Finite state machine of the Flexometer. State 0: customer preference initialization, 1: acquiring data and waiting for control signal, 2: decoding and encoding the received signal, 3: Clearing or overwriting the instant in logger, 4: generating desire control preference (e.g. bid), 5: sending, 6: performs desire action and waits till completion. Transition a: customer preference (i.e. nvParam), b: status, c: received control signal , d: wrong signal, e: decoded signal, f: encoded signal, g: generated control preference (e.g. bid).

logic circuit function at a given instant in time, to which the state circuit or program has access.

C. Knowledge base

The knowledge based ontology of the Flexometer, represents the functional relationship of all blocks within the Flexometer, is shown in Fig. 4. It contains descriptions of functional blocks and their actions, as well as reference for calculating state change when a control action (i.e. price signal) is given. Basic customer preferences (i.e. nvParam like start and stop time) are also contained in this ontology. As can be seen in Fig. 4, the logger functional block is associated with customer preference, demand response and learned value proposition.

IV. Evaluation

In this paper, a hardware-in-loop approach was adapted to conduct an experimentation for the evaluation of the Flexometer as an element that supports in the integration of TCM in EMS.

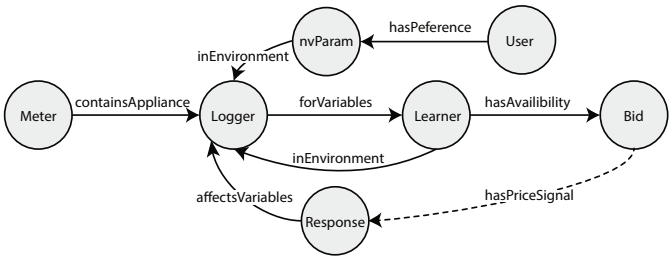

Fig. 4. Knowledge based ontology used for representing functional blocks within the Flexometer and their relationships.

A. Experiment Design

As shown in Fig. 5, the system for the experimentation was designed by implementing multi-agents. In this architectural design, as discussed in [15], multiple agents were responsible to perform their respective tasks. Herein, agents were also organized in triple layers. Agent in most upper layer was called an aggregator agent. The aggregator agent aggregated bids received from domotic agents and then adjusted an equilibrium price signal as per the objective. The most simple objective of the aggregator is to balance supply and demand, which was taken under consideration in this study. As shown in Fig. 5, herein aggregator agent simply broadcasted the price signal corresponding to nearly zero consumption as the equilibrium price signal.

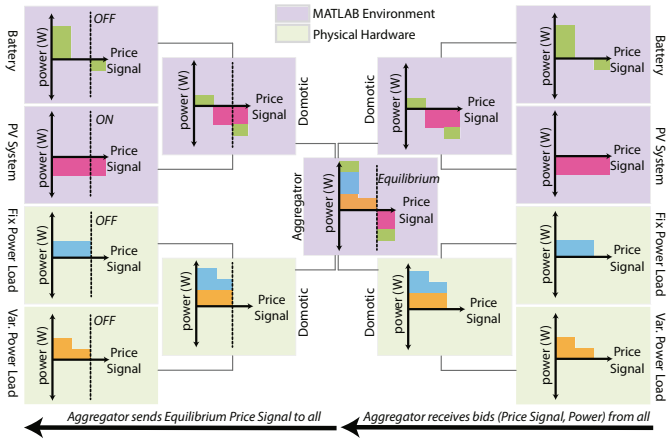

Fig. 5. Three layer multi-agent system for Transactive based control mechanism .

On the other hand, domotic agents exist in the middle layer of the organization. Herein, domotic agent worked as a transceiver of bid and price signal between the connected appliance agents and the aggregators.

In this architectural design, appliance agent were representatives of real physical load (like battery, PV system or other loads) to the domotic agent. Therefore, within this framework, “Flexometer” was an appliance agent with digital logic circuit. Therein it provided an opportunity for

the standardized integration of physical load into Transactive based control mechanism.

As mentioned, the purpose of this demonstration was to evaluate the Flexometer. So, the demonstration was planned for a time period of a week in the Smart Lab of AGH UST, Krakow - Poland [16]. Moreover, in order to simplify the analysis of data obtained during demonstration, the granularity of an hour was considered. Fig. 6 shows the illustration of lab setup for experimentation. It can be observed from Fig. 6 that an aggregator agent was entirely developed in MATLAB run-time environment. In this experimentation, two domotic agents were designed, one was MATLAB based and other was designed in Raspberry Pi. Python and C++ languages were used to implement the logic of domotic agent in Raspberry Pi.

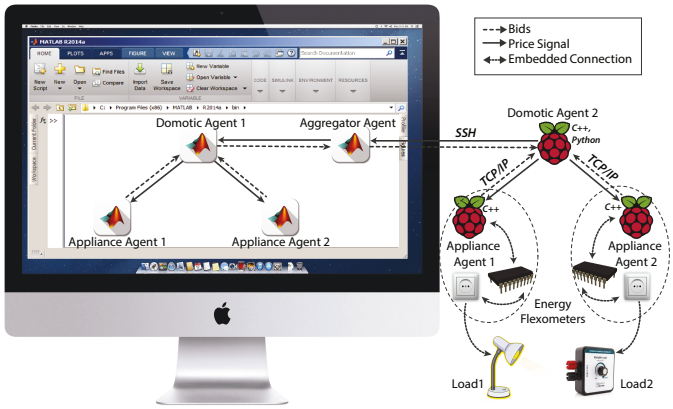

Fig. 6. Setup of multi-agent system in Lab.

Moreover, each domotic agent was equipped with two appliance agents. Appliance agents, which were connected to MATLAB based domotic agent, were also modeled in MATLAB, as shown in Fig. 6. Out of two MATLAB based appliance agents; one was modeled as a battery of maximum rated absolute power of 3kW and other was modeled as a PV system of maximum peak power of 2.6 kW. For PV system, local irradiation values of a week in June of 2012 were considered. On the other hand, two Flexometers were implemented as per the design presented in Section II. Out of two Flexometers, one was connected to fixed power dummy load of 2kW and other was connected to variable power dummy load (i.e. [min,max] = [0.5kW,4kW]). Variable power dummy load was used to generate variable power profile for a defined time duration (i.e. maximum upto 7 hours). Fig. 7 shows box diagram of the power pattern by variable load for the time period of a week. It also shows the average consumption pattern of the variable load with respect to the time.

Moreover, as two temporal preferences (i.e. nvParam) were introduced as customer preferences, namely start time and stop time. Start time is a time that refers to an hour of a day from when device can be turn on, however stop time is a time that refers an hour of a day till when device must complete its defined task. The mean stop time and start time for fixed load were from 4th hour till 19th hour of the day. On the other hand, the mean stop time and start variable for fixed load was from 2nd hour till 20th hour of the day. Keeping in mind that the day of the demonstration starts at 9.00AM.

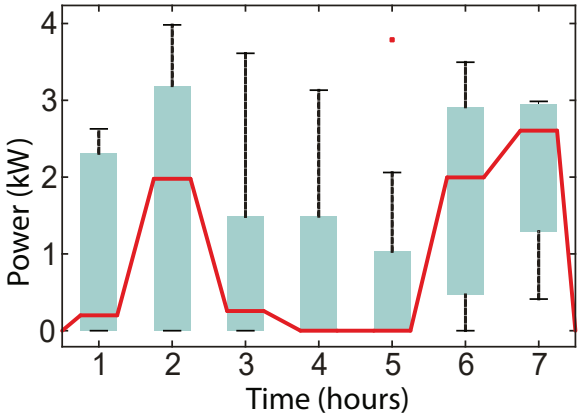

Fig. 7. Consumption pattern of variable load verses time i.e. an averaged for a week.

B. Performance Metrics

The performance matrics of Flexometer are training time taken by elasticity learner functional block and response time. When numerically calculating without nvParam for a learning task of elasticity learner programmed in Raspberry Pi 2, the algorithm that runs for 100 episodes should take 8.3s in average. However, table I shows average training time that the elasticity learner of each Flexometer takes in both situations i.e. with nvParams and without nvParams. It can be observed that time taken with nvParam is way lower than without nvParam. It provides an evidence to the fact that nvParam limits the exploration across state space during a training episode, thus allowing agent to converge faster. Moreover, the average response time, i.e. a time duration required to change the status of Flexometer, was found to be 5ms.

TABLE I
AVERAGE TRAINING TIMING WITH AND WITHOUT NVPARAM

	Without	With
Flexometer (with variable loading)	13s	7.0s
Flexometer (with fixed loading)	4.9s	1.7s

C. Results

The upper graphs in Fig. 8 and Fig. 9 show bid (i.e. power verses price signal) generated by both Flexometer (variable and fix load) during two different demonstrations i.e. with or with nvParam respectively. Similarly, the lower graphs in Fig. 8 and Fig. 9 show when both Flexometer turn ON verses the respective price signal they received from domotic agent for an action. From Fig. 8, an evident observation is that Flexometers without nvParam turn ON more strictly on time as well as react on high values of price signal. On the other hand, as shown in Fig. 9, Flexometers with nvParam turn ON to relatively lower values of price signal as well as dispersed

more on time. This provides an additional fact that elasticity learner learns more strict bidding in case of without nvParam rather then with nvParam.

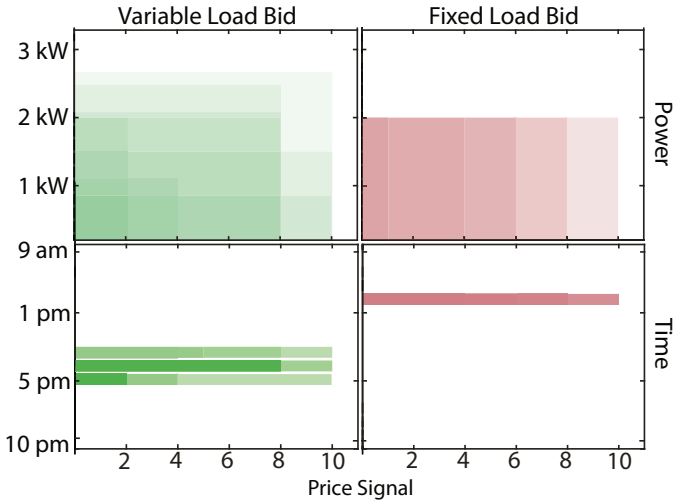

Fig. 8. Bid generated without nvParam by Flexometers and their turn ON timings during demonstration with respect to price signals.

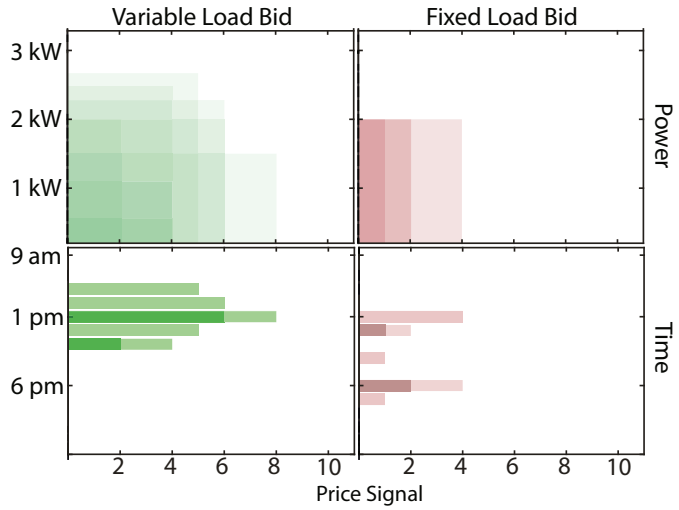

Fig. 9. Bid generated with nvParam by Flexometers and their turn ON timings during demonstration with respect to price signals.

V. Conclusion

This paper deploys successfully all six features of an Flexometer in the context of agile demand response. The investigation concludes that the proposed and discussed a logical interface of Flexometer is ready to implement in any IoT platform like multi-agent system for Transactive based control mechanism to materialize agile demand response from elemental level.

Moreover, it also indtroduces different level of data abstraction and information sharing among different agents. For an illustrative purposes, the paper only focuses on a single parameter, named nvParam. Moreover, two different options of Flexometer were compared (i.e. with and without nvParam). With nvParam in which timings for appliance operation were limited, the energy elasticity functional block learns an optimal schedule of energy and the value of price signal is lower. On the other hand, second option will increase the value of price signal and learn relatively fix time of operation as optimal schedule.

For the future work, we are going to implement the developed solution in a pilot building EMS project with Transactive based control mechanism and monitoring functions. An application of the Flexometer in prosumers micro-grids EMS is being considered as well.

References

[1] K. Kok, "The powermatcher: Smart coordination for the smart electricity grid," *TNO, The Netherlands*, pp. 241–250, 2013.

[2] K. Park, Y. Kim, S. Kim, K. Kim, W. Lee, and H. Park, "Building energy management system based on smart grid," in *Telecommunications Energy Conference (INTELEC), 2011 IEEE 33rd International*. IEEE, 2011, pp. 1–4.

[3] E. Klaassen, C. Kobus, J. Frunt, and J. Slootweg, "Responsiveness of residential electricity demand to dynamic tariffs: Experiences from a large field test in the netherlands," *Applied Energy*, vol. 183, pp. 1065–1074, 2016.

[4] J. Mahieu, "Active demand side management," *PhD Dissertation - published by Hogeschool West-Vlaanderen*, 2012.

[5] A. Haytema, "The solution to managing energy supply and demand," *White Paper by Nedap Energy Systems*.

[6] Mastervolt, "Mastervolt, innovative power systems for autonomous use," http://www.mastervolt.com/IntelliWeb/, 2017, [Online; accessed 10-April-2017].

[7] B. Biegel, P. Andersen, J. Stoustrup, M. B. Madsen, L. H. Hansen, and L. H. Rasmussen, "Aggregation and control of flexible consumers–a real life demonstration," *IFAC Proceedings Volumes*, vol. 47, no. 3, pp. 9950–9955, 2014.

[8] C. Yilmaz, S. Albayrak, and M. Lützenberger, "Smart grid architectures and the multi-agent system paradigm," *ENERGY*, pp. 90–95, 2014.

[9] M. Babar, P. Nguyen, V. Cuk, I. Kamphuis, M. Bongaerts, and Z. Hanzelka, "The evaluation of agile demand response: An applied methodology," *IEEE Transactions on Smart Grid*, 2017.

[10] M. Babar, P. Nyugen, V. Cuk, I. R. Kamphuis, M. Bongaerts, and Z. Hanzelka, "The rise of agile demand response: Enabler and foundation for change," *Renewable and Sustainable Energy Reviews*, vol. 56, pp. 686–693, 2016.

[11] A. Ożadowicz, J. Grela, and M. Babar, "Implementation of a demand elasticity model in the building energy management system," in *Event-based Control, Communication, and Signal Processing (EBCCSP), 2016 Second International Conference on*. IEEE, 2016, pp. 1–4.

[12] A. Ozadowicz and J. Grela, "An event-driven building energy management system enabling active demand side management," in *2016 International Conference on Event-based Control, Communication, and Signal Processing (EBCCSP)*, 2016, pp. 1–8.

[13] M. Babar, P. Nguyen, V. Cuk, and I. Kamphuis, "The development of demand elasticity model for demand response in the retail market environment," in *PowerTech, 2015 IEEE Eindhoven*. IEEE, 2015, pp. 1–6.

[14] A. Ożadowicz and J. Grela, "Control application for internet of things energy metera key part of integrated building energy management system," in *Emerging Technologies & Factory Automation (ETFA), 2015 IEEE 20th Conference on*. IEEE, 2015, pp. 1–4.

[15] M. Babar, P. Nguyen, V. Cuk, I. Kamphuis, and W. Kling, "Complex bid model and strategy for dispatchable loads in real time market-based demand response," in *IEEE PES Innovative Smart Grid Technologies, Europe*. IEEE, 2014, pp. 1–5.

[16] M. Noga, A. Ożadowicz, and J. Grela, "Modern, certified building automation laboratories autbudnet–put learning by doingidea into practice," *Przeglad Elektrotechniczny*, vol. 88, no. 11a, pp. 137–141, 2012.

Housing Development Building Management System (HDBMS) For Optimized Electricity Bills

Weixian Li*, Thillainathan Logenthiran†, Van-Tung Phan¶, and Wai Lok Woo‖
School of Electrical and Electronic Engineering, Newcastle University, Singapore Campus*† ‡§¶ ‖
Email: *w.li17@newcastle.ac.uk, †t.logenthiran@ncl.ac.uk, ¶,vantung.phan@ncl.ac.uk, ‖lok.woo@newcastle.ac.uk

***Abstract*—Smart Buildings is a modern building that allows residents to have sustainable comfort with high efficiency of electricity usage. These objectives could be achieved by applying appropriate, capable optimization algorithms and techniques. This paper presents a Housing Development Building Management System (HDBMS) strategy inspired by Building Energy Management System (BEMS) concept that will integrate with smart buildings using Supply Side Management (SSM) and Demand Side Management (DSM) System. HDBMS is a Multi-Agent System (MAS) based decentralized decision making system proposed by various authors. MAS based HDBMS was created using JAVA on a IEEE FIPA compliant multi-agent platform named JADE. It allows agents to communicate, interact and negotiate with energy supply and demand of the smart buildings to provide the optimal energy usage and minimal electricity costs. This results in reducing the load of the power distribution system in smart buildings which simulation studies has shown the potential of proposed HDBMS strategy to provide the optimal solution for smart building energy management.**

***Index Terms*—Power distribution system, Smart Buildings, Multi-agent system, Demand side management, Supply side management, Building energy management system, Housing development building management system, Electricity bills**

I. Introduction

Electricity has become a basic necessity for modern society and is a vital part of a socio-economic development in the world. The common challenges faced by the electricity suppliers would be systems constraints and administrative issues while supplying electricity. Additionally, past studies had shown a steady increase in annual electricity demand through the past few years due to consumers needs with respect to comfort, convenience and flexibility. In order to meet the growing demand of electricity, solutions from grid distribution to end users are required [1].

Smart grid represents a innovative next generation of power system network that delivers power from supply to demand. It uses a two-way communications which leads to enhanced reliability and energy efficiency of the grid. It has the capabilities of sensing grid situations, measure power and control appliances to electricity generations, transmission and distribution of the power grid. This increased the number of decentralised renewable energy sources due to increasing electricity demand. These issues created challenges for a stable and secure operation of power grid. Major developments were based on traditional electrical system planning and operations with information and communications technology [2]. This concept of intelligent power grid performs independent adaptations of its elements for optimal electricity consumption [3].

Important elements of a smart grid includes demand response, load management and customer engagement. The accuracy of forecasting supply and demand depends on smart meters. The stability of grid in Singapore has one of the most reliable electricity networks in the world. Singapore grid has already deployed advanced Supervisory Control and Data Acquisition (SCADA) systems with two-way communication channels. This situation creates an ideal place to bring new technologies to enhance the capability of its power grid. With the help of advanced technologies, the grid was able to respond efficiently and effectively to power disruptions [4].

Building Energy Managements System is a part of a smart grid system that control, monitor and optimize energy for buildings. BEMS play a critical role in achieving overall energy efficiency by reducing carbon footprints. As it is a key requirement for designing modern buildings and industries. Technology improvement on control systems, energy managements systems, distributed decision making and coordination for buildings contribute to better efficiency of energy usage [5].

In modern times, BEMS considered improvement on energy utilization efficiency, reduction of energy cost and integration of renewable energy technology. These improvements was meant to meet the energy demand of the buildings. To align with the zero-energy objectives and intelligent building concepts, BEMS aims to increase energy efficiency by integrating Demand Side Management and Supply Side Management. These functions decreases energy cost and sustain consumer comforts by optimizing buildings electrical distribution. It will solve complex issues through coordination and cooperation of the management systems. This is due to the system being flexible, reliable and efficient [6].

Supply Side Management (SSM) was identified as a method of optimizing the electrical supplies from various power sources. One of the key issues for future energy distribution systems, smart buildings and smart devices was the need of an intelligent management of energy distributions. The problem can be tackled from the supply sources on how electricity should be distributed. It helps to improve electrical efficiency by developing an optimal algorithm for the system. Thus, electricity can be used in an efficient manner [7], [8].

Demand Side Management (DSM) was identified as a method of optimizing energy demand consumption to achieve better efficiency and operations in an electrical system. DSM usually involves demand response and peak load scheduling. As electricity was cheaper during night time due to the whole-

sale electricity market. This encourages consumers to use more electricity during these periods, thus reducing electricity costs for end consumers [9].

Due to limitations of centralised computing capabilities on large scale power distribution system, it made decentralised and semi-centralised decision making procedures desirable in electrical distribution systems. One of the promising communication systems in solving multiple objectives during optimal period for distribution systems was the Multi-Agent Systems (MAS). MAS focuses on artificial intelligence agent interactions to solve issues and provide improvement on technologies [10].

Multi-Agent system is a system that comprises of two or more intelligent agents that cooperates, coordinates and negotiates to achieve its goal and objectives. It was designed to solve complex problems using the best solution available. Generally, an agent based system is usually formed by two agents either software or hardware. It will react to changes within its own environment. It is designed and based on its reactivity, pro-activeness and social ability in the environment. In order to ensure that agents were organized in a hierarchical structure, several agents were given authority to overwrite other agents decision in a logical manner. However, a decentralized decision system permit agents to have their own decision making unless the solution was deemed unsatisfactory [11]–[14].

Java Agent DEvelopment Framework (JADE) is a java extension based software framework available for Multi-Agent System (MAS) development. This framework complies with IEEE FIPA standards. MAS implementation through a middle ware, requires a minimum system of the JAVA (the runtime environment or the JDK) version 5 is needed to execute within a Java Virtual Machine (JVM) [15], [16].

In this paper, Housing Development Building Management System (HDBMS) using BEMS concept on residential building was developed [17].Its ability to optimize the electricity distribution and lower consumers electricity cost will be discussed. The distribution management of HDBMS uses decision-making of Multi-agent Systems for electricity distribution with the objective of decreasing electrical cost, improve energy efficiency and optimize residents comfort.

The remaining paper is organized as follows: Section II shows the information for Singapore smart building. Section III shares the methodology for the House Development Building Management System (HDBMS). Section IV explains the proposed MAS architecture for smart HDBMS. Section V provides simulation results and discussed in section VI. Finally, the paper is concluded in the section VII.

II. Information about Singapore Residential Building

A. Housing Development Board (HDB) Buildings

Fig.1 shows the percentage of how electricity is distributed in Singapore in 2014. This chart allows understanding of the amount of electricity being distributed to various sectors in Singapore [18]. Residential Buildings contributes to 15% of the total electricity consumption which was 6.936 GWh by households in Singapore.

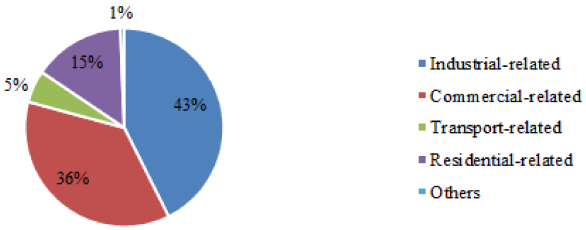

Fig. 1. Distribution of Singapore Electricity

Fig.2 shows the percentage of electricity distributed in the residential sectors for year 2014 [3]. The chart shows 60% of the electricity were distributed to public housing. It consists mainly Housing Development Board (HDB) Buildings in Singapore, therefore it is essential to find alternatives in this area to have better energy efficiency.

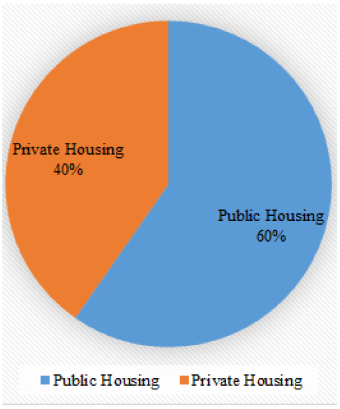

Fig. 2. Singapore residential electricity consumption in 2014

Fig.3 shows a concept of a potential Singapore smart grid concept that will be created in the future. Smart Grid concept was introduced to provide a two-way communication for consumers supply and demand of electricity. Major developments were based on traditional electrical system planning and operations with information and communications technology [4].

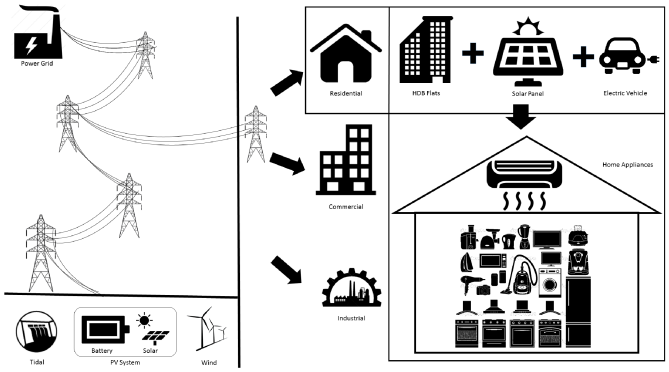

Fig. 3. Illustration of Singapore smart grid concept

Fig.4 shows the average monthly electricity consumption by public and private housing in Singapore for 2014. The average

monthly electricity consumption by public housing unit was 371 kWh [19].

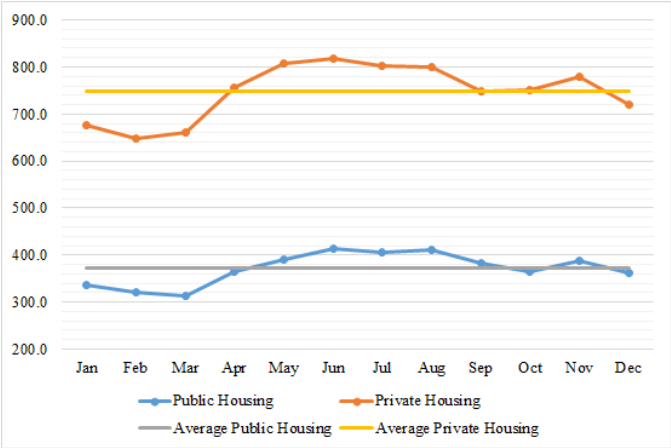

Fig. 4. Residential Average Monthly Electricity Consumption in 2014

The power utilization of frameworks, for example, regular territory lighting, lifts and water pumps of a normal HDB residential building was estimated to be 75,000 kWh a year [20].

According to a research done in 2015, the public housing buildings known as Housing and Development Board (HDB) blocks currently has 9503. This indicated that there were 980108 units of flats which averaged to 103 units per block [21]. This information builds a realistic situation for the experiment.

B. Singapore Electricity Prices

Following 2001, the Energy Market Authority (EMA) opened a retail electricity market to give consumers options to manage their energy cost through the competition of different providers. Instead of buying at regulated electricity tariff which is known as non-contestable price from SP Services Limited (SPS). Consumers were able to purchase electricity from electricity retailers or wholesale electricity market at prices that varies every half-hour which is known as contestable prices.

In order to switch to contestable prices, consumers with an average electricity consumption of 2000 kWh per month were eligible for the scheme [22].

The non-contestable consumers pricing will be 20.35 cents per kWh (with effect from 1 Oct 15 to 31 Dec 15) regardless of the time periods [23].

Data collected were used for accommodation of different pricing that allows research on whether power delivered from a contestable or non-contestable electricity source be more economical for residential building in Singapore.

Fig.5 shows the price for a Contestable consumer in a 48 period format. It represents a day where each period is half an hour from Energy Market Company (EMC) for 1 September 2015 [24].

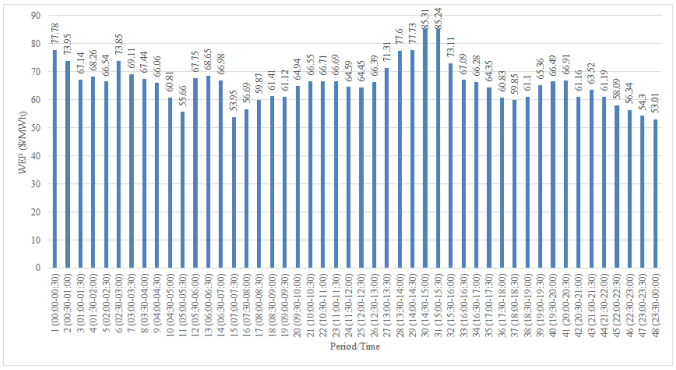

Fig. 5. Wholesale Pricing used for 48 periods

C. Singapore Photovoltaics (PV) System

The capability of PV electricity generation in Singapore depends essentially on the space and the efficiency of the PV systems. The annual electricity demand in Singapore is 42 TWh in 2011; the total installed solar PV capacity was 4MWp for both residential and non-residential installation which generates about 4.8GWh per annum [25]. The PV system was able to yield 51kWh per day between 0700-1900 hours in Singapore.

D. Singapore Electric Vehicle (EV)

Table I shows the type of chargers available in Singapore. Public Normal Chargers and Residential Normal chargers are two types of commonly used chargers.

TABLE I
SINGAPORE TYPES OF CHARGERS

Types of Charging Infrastructure	Electrical Power	Recharging Time
Public Normal Charger	3 kW	7-8 hours
Residential Normal Charger		
Quick Charger	30-50 kW	30-45 min

Public Normal Chargers are typically introduced or accessible at shopping centers, HDB car parks, and charging stations while Residential Normal Chargers were found in private properties. Both sorts of chargers have a more extended charging time of 7 to 8 hours in contrast to quick chargers.

The quick chargers are typically introduced or accessible at certain shopping centers and charging stations. It takes a quicker charging rate of 30 to 45 minutes as it will provide more electrical power.

For Electric Vehicle (EV) or hybrid car, charging stations are expected to energize the batteries for the vehicles which are about 24kW. There are presently 71 charging stations by Bosch in Singapore and buyers need to pay SGD$180 a month for unlimited charging [26].

According to the Straits time, there are a total of approximate 1.25 million households and around 45% of households in Singapore own a car. [27].

The number of electrical vehicle in a residential building can be calculated by:

$$CO_{per\ HDB\ block} = U_{per\ HDB\ block} * CO_{percentage} \quad (1)$$

Where $CO_{per\ HDB\ block}$ represents the total Car Owners in a HDB block, $CO_{percentage}$ refers to the percentage of car owners, $U_{per\ HDB\ block}$ represents the number of units in a HDB block.

The total battery storage by EV can be calculated by:

$$EVBS_{per\ HDB\ block} = CO_{per\ HDB\ block} * EVBS_{per\ car} \tag{2}$$

Where $EVBS_{per\ HDB\ block}$ represents the total EV battery storage in a HDB block and $EVBS_{per\ car}$ for one EV battery storage.

The charging/discharging rate by the total number of EV battery storage can be calculated by:

$$EVDC_{per\ HDB\ block} = CO_{per\ HDB\ block} * EVDC_{per\ car} \tag{3}$$

Where $EVDC_{per\ HDB\ block}$ represents the total charging/discharging rate for a HDB block and $EVDC_{per\ car}$ is for one EV.

III. Proposed Housing Development Building Management System (HDBMS)

Fig.6 shows the flowchart of the algorithm used for the calculation of HDBMS to provide the optimize results.

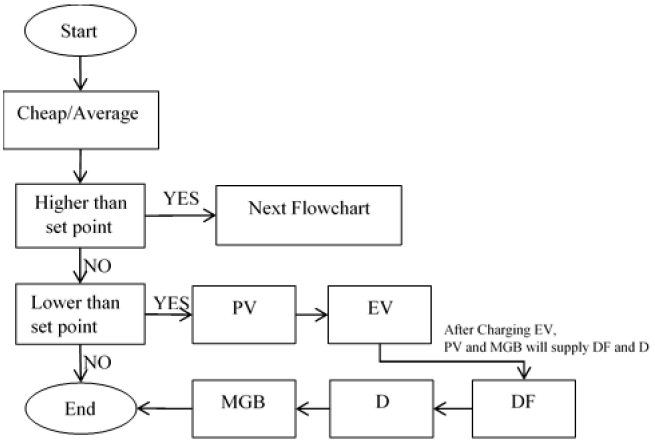

Fig. 6. Flowchart for HDBMS

There is two set points involve, one is using the average of the pricing and the other is using the cheaper range of the pricing.

When the price at that period is higher than set point, it will refer to Fig.6 to calculate the price for that period.

When the price at that period is lower than set point, it will buy the maximum charging rate of the EV batteries and the total demand for that period as the prices are lower. In this case, it is able to store the electricity at a cheaper rate and use it during the periods of higher price rate.

Fig.7 represents the flowchart when the period price is higher than the set point calculated.

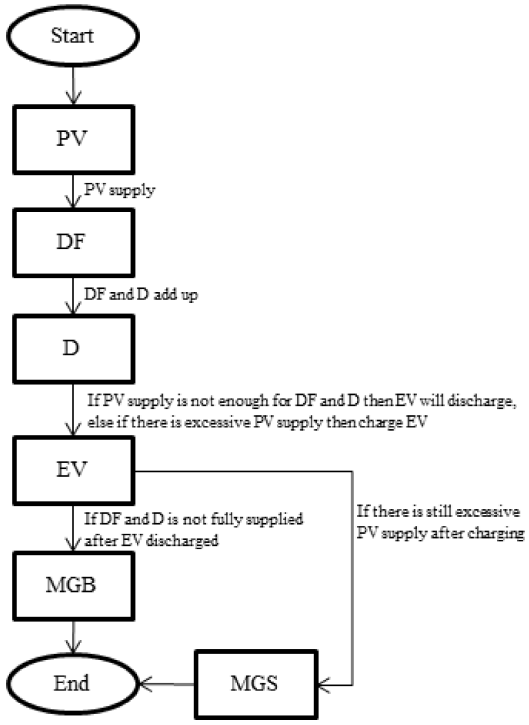

Fig. 7. Flowchart when set point is higher

The PV power will first supply to the demand of HDB building facilities like the lifts, lights and other electrical devices. It will then supply to the Demand of HDB units. After all the demand, extra PV power left will be stored in the EV batteries(Discharging, charging rate considered) and sold back to the grid.

If at any point that the PV power is not sufficient to supply the demand, it will use power from the EV batteries (Discharging, charging rate considered) and in event of insufficient power supplied, additional power will be supplies by the main grid.

Table II shows the representatives and description of Fig.6 and Fig.7. It explains the function for the following flowcharts.

TABLE II
Representative and Description for Fig.6 and Fig.7

Name	Representative	Descriptions
Block Representative		
HDB units demand	D	Total electricity demand of HDB units
HDB Building facilities demand	DF	Total electricity demand for HDB facilities
Photovoltaics System	PV	Supply of solar power
Electric Vehicle	EV	Battery storage
Main Grid Buy	MGB	Buying electricity from Main grid
Main Grid Sell	MGS	Selling electricity to Main Grid

The following formulas has been implemented in the system as show in Fig.6 and Fig.7.

The average set point calculation based on the contestable pricing can be calculated by:

$$AvgPt_{period} = (\sum_{i=1}^{48} CP_{(i)})/i \tag{4}$$

Where$AvgPt_{period}$ represents the average set point for each period, $CP_{(i)}$ represents the total contestable pricing for a period and i represent the period time.

The cheap set point calculation based on the contestable pricing can be calculated by:

$$CheapPt_{period} = CP_{i/(EVFS/EVDC/2)} \tag{5}$$

Where $CheapPt_{period}$ represents the cheap set point for each period and $EVFS$ represents the electric vehicle full battery storage.

The contestable pricing without using set point method can be calculated by:

$$CP_{day} = (\sum_{i=1}^{48} CP_{(i)} * PD_{(i)}) \tag{6}$$

Where CP_{day} represents the total contestable pricing for the day and $PD_{(i)}$ represents the total power demand for the period.

The non-contestable pricing without using set point method can be calculated by:

$$NCP_{day} = (\sum_{i=1}^{48} NCP_{(i)} * PD_{(i)}) \tag{7}$$

Where NCP_{day} represents the total non-contestable pricing for the day and $NCP_{(i)}$ for a period.

IV. Proposed Multi-Agent System

Fig.8 depicts the overall design of multi-agent system for Housing Development Building Management system (HDBMS). The functionality of SSM is to be in charge of data collection from the electrical supplies and calculate the total electricity it is able to supply. DSM function is to be in charge of collecting data from the electrical demand and calculate the total electricity required. HDBMS would then take the data from SSM and DSM to optimize the best solution for optimization of electricity prices

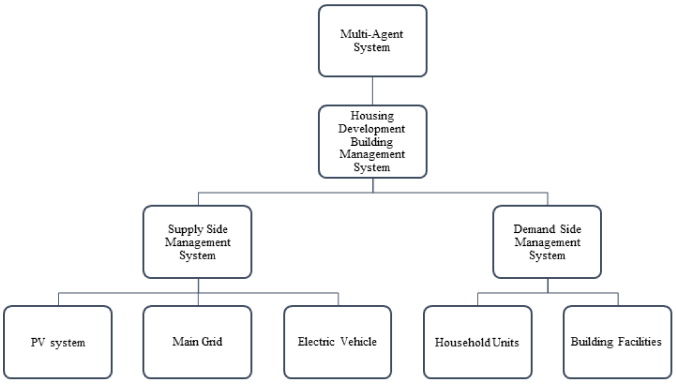

Fig. 8. Design of Multi-Agent System

Table III shows the representatives names used to program the multi-agent system. DSM manages the HDB Building demands. SSM manages the electrical supply systems. HDBMS manages the SSM and DSM requirements to make further decisions.

TABLE III
HDBMS Agents

Name	Descriptions	Agent Representative
Management System		
House Development Building Management System	HDBMS	HDBMSAgent
Demand Side Management	DSM	DSMAgent
Supply Side Management	SSM	SSMAgent
Electrical Supply System		
Solar Panel	PV	PVSystemAgent
Main Grid	MG	MGAgent
Electric Vehicle	EV	EVAgent
HDB Building demands		
HDB Unit	HDBU	HDBUAgent
HDB Facilities	HDBF	HDBFAgent

This allows the particular system to have a specific communication process or algorithms. It simplifies the coding procedures due to the hierarchy of the entire system. It benefits the control and manage programs to cater for the flexibility of altering the code due to an upgrade of the system when required.

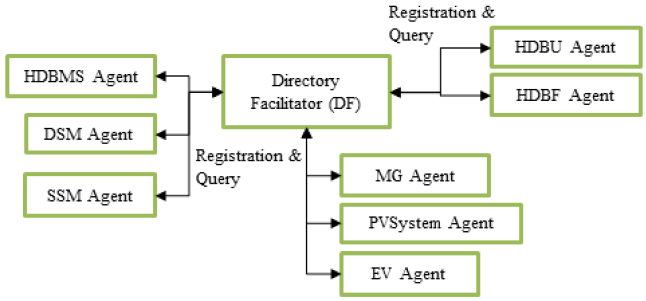

Fig. 9. Registration and query of agents

The Directory Facilitator (DF) was used to register and query the agents needed in the network as shown in Fig.9. This prevents the same agent to be recreated.

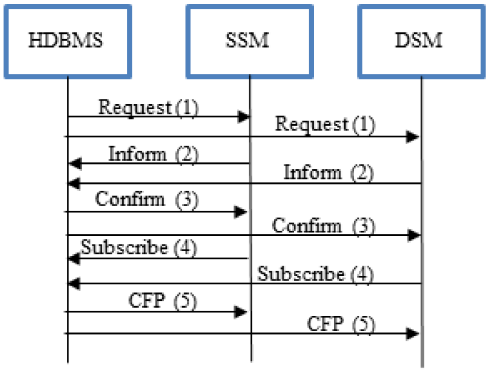

Fig. 10. HDBMS agents interactions

Fig.10 depicts the overall structure of the multi-agent system. Home Development Building Management System (HDBMS) was categorized into two parts which are the Supply

Side Management (SSM) and Demand Side Management (DSM).

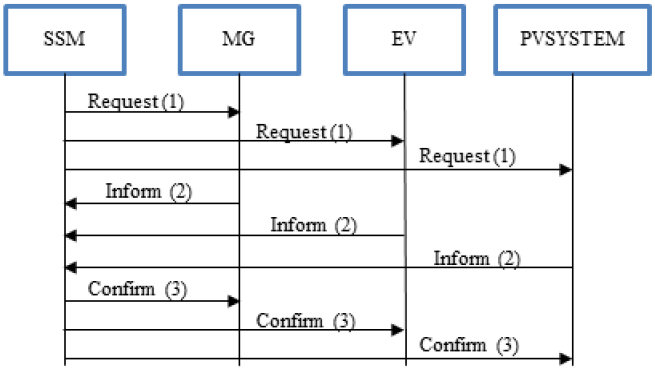

Fig. 11. SSM agents interaction

As shown in Fig.11, the functionality of SSM was in charge of data collection from the electrical supplies and calculates the total electricity supply.

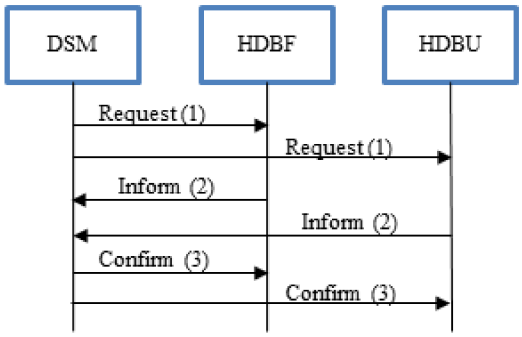

Fig. 12. DSM agents interaction

As shown in Fig.12, DSM function was in charge of collecting data from the electrical demand and calculate the total electricity required.

As multi-agent system were used to provide the communications, these figures shows the type of messages created to facilitate the communications between agents. The messages set were REQUEST, SUBSCRIBE, CONFIRM , INFORM and CFP. Each message sent provides different data messages when it is required during the process of algorithm calculations.

V. Simulation and Results

A. Housing Development Building Management System (HDBMS) results

This sections shows the algorithm implementation results for Housing Development Building Management System (HDBMS).

Table IV shows the results from different simulations based on the duration. These are the simulation results for contestable pricing with no method, non-contestable pricing with no method, average set point system pricing and cheap set point system pricing were implemented for household consumers.

TABLE IV
SIMULATION RESULTS FOR DIFFERENT METHODS

No.	HDB non-contestable price	HDB contestable price	Using Average as a set point	Using Cheap as a set point
Year				
1	$88,330.19	$28,555.82	$27,665.90	$25,135.81
Months				
1	$7,360.85	$2,379.65	$2,364.64	$2,142.51
2	$7,360.85	$2,379.65	$2,300.11	$2,101.92
3-12	$7,360.85	$2,379.65	$2,300.11	$2,089.14
Days				
1	$245.36	$79.32	$140.79	$92.08
2	$245.36	$79.32	$77.07	$70.70
3-30	$245.36	$79.32	$76.67	$70.70

Table V shows the per period results for average set point. It shows detail of the average set point pricing for each periods.

TABLE V
SIMULATION RESULTS FOR PERIODS USING AVERAGE SETPOINT

Using Average as a set point			
Period	**Day 1**	**Day 2**	**Day 3 to Day 30**
1	$2.02	$0.00	$0.00
2	$1.92	$0.00	$0.00
3	$1.75	$5.64	$0.00
4	$1.78	$0.00	$0.00
5	$1.73	$3.46	$0.00
6	$1.92	$0.00	$0.00
7	$1.80	$0.00	$0.00
8	$1.75	$0.00	$0.00
9	$1.72	$6.28	$0.00
10	$5.78	$2.13	$5.78
11	$5.29	$1.45	$5.29
12	$0.00	$0.00	$0.00
13	$0.00	$0.00	$0.00
14	$0.00	$5.11	$0.00
15	$5.03	$1.31	$5.03
16	$5.29	$1.38	$5.29
17	$5.59	$1.46	$3.51
18	$5.73	$1.49	$1.49
19	$5.70	$1.49	$1.49
20	$6.06	$1.58	$1.58
21	$0.00	$1.62	$0.00
22	$0.00	$1.62	$0.00
23	$0.00	$1.62	$0.00
24	$6.03	$1.57	$6.03
25	$6.01	$1.57	$1.82
26	$0.00	$1.61	$0.00
27	$0.00	$0.00	$0.00
28	$0.00	$0.00	$0.00
29	$0.00	$0.00	$0.00
30	$0.00	$0.00	$0.00
31	$0.00	$0.00	$0.00
32	$0.00	$0.00	$0.00
33	$0.00	$6.26	$0.00
34	$0.00	$6.18	$0.00
35	$6.00	$2.07	$6.00
36	$5.68	$1.48	$5.68
37	$5.58	$1.45	$5.58
38	$5.70	$1.48	$2.20
39	$6.21	$1.70	$1.70
40	$0.00	$1.73	$0.00
41	$0.00	$1.74	$0.00
42	$5.81	$1.59	$4.77
43	$6.03	$1.65	$1.65
44	$5.81	$1.59	$1.59
45	$5.52	$1.51	$1.51
46	$5.35	$1.47	$1.47
47	$5.16	$1.41	$1.41
48	$5.04	$1.38	$1.38

Table VI shows the per period results for cheap set point. It shows detail of the cheap set point pricing for each periods.

TABLE VI
SIMULATION RESULTS FOR PERIODS USING CHEAP SETPOINT

Using Cheap as a set point			
Period	**Day 1**	**Day 2**	**Day 3 to Day 30**
1	$2.02	$0.00	$0.00
2	$1.92	$0.00	$0.00
3	$1.75	$0.00	$0.00
4	$1.78	$0.00	$0.00
5	$1.73	$0.00	$0.00
6	$1.92	$0.00	$0.00
7	$1.80	$0.00	$0.00
8	$1.75	$0.00	$0.00
9	$1.72	$0.00	$0.00
10	$5.78	$5.78	$5.78
11	$5.29	$5.29	$5.29
12	$0.00	$0.00	$0.00
13	$0.00	$0.00	$0.00
14	$0.00	$0.00	$0.00
15	$5.03	$5.03	$5.03
16	$5.29	$5.29	$5.29
17	$5.59	$5.59	$5.59
18	$0.00	$0.00	$0.00
19	$5.70	$5.70	$5.70
20	$0.00	$0.00	$0.00
21	$0.00	$0.00	$0.00
22	$0.00	$0.00	$0.00
23	$0.00	$0.00	$0.00
24	$0.00	$0.00	$0.00
25	$0.00	$0.00	$0.00
26	$0.00	$0.00	$0.00
27	$0.00	$0.00	$0.00
28	$0.00	$0.00	$0.00
29	$0.00	$0.00	$0.00
30	$0.00	$0.00	$0.00
31	$0.00	$0.00	$0.00
32	$0.19	$0.00	$0.00
33	$1.63	$0.00	$0.00
34	$1.61	$0.00	$0.00
35	$1.56	$0.00	$0.00
36	$5.68	$5.68	$5.68
37	$5.58	$5.58	$5.58
38	$5.70	$5.70	$5.70
39	$0.00	$0.00	$0.00
40	$0.00	$0.00	$0.00
41	$0.00	$0.00	$0.00
42	$0.00	$0.00	$0.00
43	$0.00	$0.00	$0.00
44	$0.00	$0.00	$0.00
45	$5.52	$5.52	$5.52
46	$5.35	$5.35	$5.35
47	$5.16	$5.16	$5.16
48	$5.04	$5.04	$5.04

The HDB non-contestable and contestable prices were constant at $5.11 and $1.65 throughout the periods.

B. Housing Development Building Management System (HDBMS) Multi-Agent System (MAS) communications

This sections shows the Multi-Agent System (MAS) communications results for Housing Development Building Management System (HDBMS).

Fig.13 shows the integration of the Multi-Agent System (MAS) with the Housing Development Building Management System (HDBMS) calculations. This integration shows the potential of a enhanced completed system for real life application.

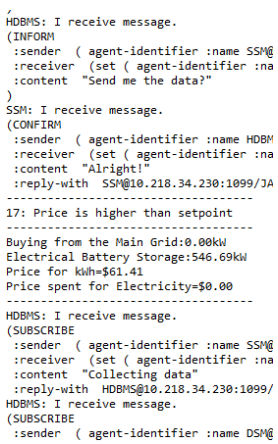

Fig. 13. MAS with HDBMS

Fig.14 shows the overall communication of the Multi-Agent System (MAS) for HDBMS using JADE. It shows the importance of the interactions in the communication based network.

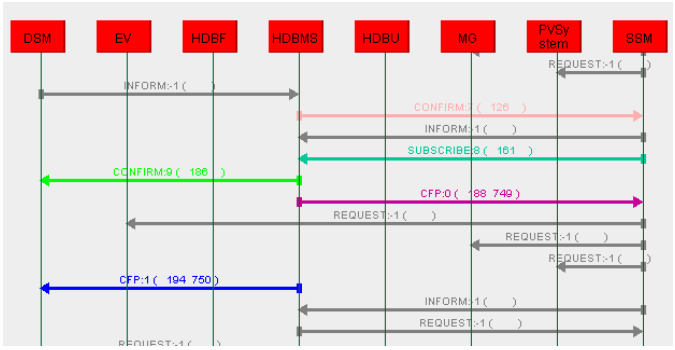

Fig. 14. Overall MAS communication

VI. DISCUSSIONS

Between contestable and non-contestable pricing, it shows significant difference of cost even when no system is implemented. After the system was implemented, it shows further reduction in cost with the set points methods. Although initially the set points method cost more but as the time increases, it shows slight difference with the average point system and a bigger difference with cheap set point by comparing the electricity cost of household.

At the same time, the per period simulations shows the system cost higher at later periods. This was due to ”off-peak” prices availiable at later timings. However, it does not affect the overall results as it is implemented and compared with different methods.

These results concluded that with the Housing Development Building Management System (HDBMS) implemention, residential buildings were able to save a significant amount of electricity bills and reduce the load of electricity generators in the grid. HDBMS provides a more cost efficient way of using electricity.

VII. Conclusions

In this paper, the development of a smart building concept was designed to optimize the electricity usage through a Housing Development Building Management System (HDBMS). This system aims to optimize the energy efficiency and electricity costs of the residential buildings. A universal idea of a HDBMS for smart buildings was introduced by integrating Demand Side Management (DSM) and Supply Side Management (SSM) system. Multi-Agent System (MAS) was used to illustrate the communication process of agents between management systems and devices for the calculation and data of energy sources. Such system has shown its capabilities to achieve the optimal use of energy efficiency and electricity bills.

Enhancements of such smart grid techniques would only benefit the power grid in terms of increased dependability and software improvement for the grid. A less costly electricity bill could also be achieved with the help of renewable energy resources and electricity market. Eventually, this methodology would genuinely be a step closer towards a reliable and decentralized decision making smart building system via effective optimization system.

References

[1] B. Asare-Bediako, P. F. Ribeiro, and W. L. Kling, "Integrated energy optimization with smart home energy management systems," in *Innovative Smart Grid Technologies (ISGT Europe), 2012 3rd IEEE PES International Conference and Exhibition on*. IEEE, 2012, pp. 1–8.

[2] J. Byun, I. Hong, B. Kang, and S. Park, "A smart energy distribution and management system for renewable energy distribution and context-aware services based on user patterns and load forecasting," *IEEE Transactions on Consumer Electronics*, vol. 57, no. 2, 2011.

[3] H.-L. Chao, C.-C. Tsai, P.-A. Hsiung, I. Chou *et al.*, "Smart grid as a service: a discussion on design issues," *The Scientific World Journal*, vol. 2014, 2014.

[4] D. D. Gross, "Spotlight on singapore: Smart grid city," 2010. [Online]. Available: http://www.cleantechinvestor.com/portal/smart-grid/5860-spotlight-on-singapore-smart-grid-city.html

[5] L. Hurtado, P. Nguyen, and W. Kling, "Agent-based control for building energy management in the smart grid framework," pp. 1–6, 2014.

[6] A. Mishra, D. Irwin, P. Shenoy, J. Kurose, and T. Zhu, "Greencharge: Managing renewableenergy in smart buildings," *IEEE Journal on Selected Areas in Communications*, vol. 31, no. 7, pp. 1281–1293, 2013.

[7] F. Corno and F. Razzak, "Intelligent energy optimization for user intelligible goals in smart home environments," *IEEE Transactions on Smart Grid*, vol. 3, no. 4, pp. 2128–2135, 2012.

[8] C. Wang, Y. Zhou, B. Jiao, Y. Wang, W. Liu, and D. Wang, "Robust optimization for load scheduling of a smart home with photovoltaic system," *Energy Conversion and Management*, vol. 102, pp. 247–257, 2015.

[9] C. Chen, K. Nagananda, G. Xiong, S. Kishore, and L. V. Snyder, "A communication-based appliance scheduling scheme for consumer-premise energy management systems," *IEEE Transactions on smart Grid*, vol. 4, no. 1, pp. 56–65, 2013.

[10] E. Mocanu, K. O. Aduda, P. H. Nguyen, G. Boxem, W. Zeiler, M. Gibescu, and W. L. Kling, "Optimizing the energy exchange between the smart grid and building systems," pp. 1–6, 2014.

[11] P. Zhao, S. Suryanarayanan, and M. G. Simões, "An energy management system for building structures using a multi-agent decision-making control methodology," *IEEE Transactions on Industry Applications*, vol. 49, no. 1, pp. 322–330, 2013.

[12] S. D. McArthur, E. M. Davidson, V. M. Catterson, A. L. Dimeas, N. D. Hatziargyriou, F. Ponci, and T. Funabashi, "Multi-agent systems for power engineering applicationspart i: Concepts, approaches, and technical challenges," pp. 1743–1752, 2007.

[13] S. D. McArthur, E. M. Davidson, V. M. Catterson, A. L. Dimeas, N. D. Hatziargyriou, F. Ponci, and T. Funabashi, "Multi-agent systems for power engineering applicationspart ii: Technologies, standards, and tools for building multi-agent systems," pp. 1753–1759, 2007.

[14] W. Li, T. Logenthiran, V.-T. Phan, and W. L. Woo, "Intelligent multi-agent system for power grid communication," in *Region 10 Conference (TENCON), 2016 IEEE*. IEEE, 2016, pp. 3386–3389.

[15] W. Li, T. Logenthiran, W. Woo, V. Phan, and D. Srinivasan, "Implementation of demand side management of a smart home using multi-agent system," in *IEEE World Congress on Computational Intelligence*. IEEE, 2016, pp. 1–8.

[16] W. Li, T. Logenthiran, and W. Woo, "Intelligent multi-agent system for smart home energy management," in *Smart Grid Technologies-Asia (ISGT ASIA), 2015 IEEE Innovative*. IEEE, 2015, pp. 1–6.

[17] W. Li, T. Logenthiran, V.-T. Phan, and W. L. Woo, "Intelligent housing development building management system (hdbms) for optimized electricity bills," in *Environment and Electrical Engineering and 2017 IEEE Industrial and Commercial Power Systems Europe (EEEIC/I&CPS Europe), 2017 IEEE International Conference on*. IEEE, 2017, pp. 1–6.

[18] B. Nee, "Singapore energy statistics 2015," 2015. [Online]. Available: https://www.ema.gov.sg/cmsmedia/Publications_and_Statistics/Publications/SES2015_Final_website_2mb.pdf

[19] E. M. Authority, "Energy consumption," 2015. [Online]. Available: https://www.ema.gov.sg/cmsmedia/Publications_and_Statistics/Publications/ses/2015/energy

[20] P. E. Centre, "Energy audit of selected hdb," 2004. [Online]. Available: http://www.siongboon.com/projects/2010-08-22%20electronic%20ballast/Energy%20Audit%20of%20selected%20HDB%20residential%20blocks%20in%20Singapore%20Aug%202004.pdf

[21] teoalida, 2015. [Online]. Available: http://www.teoalida.com/singapore/hdbstatistics/

[22] Mypower, "Overview of the singapore electricity market," 2014. [Online]. Available: https://www.mypower.com.sg/About/about.html

[23] E.M.Company, "Price information," 2015. [Online]. Available: https://www.emcsg.com/marketdata/priceinformation\#priceDataView

[24] S.P.Ltd, "Tariffs," 2014. [Online]. Available: http://www.singaporepower.com.sg/irj/servlet/prt/portal/prtroot

[25] J. LUTHER, "Solar energy technology primer: A summary," 2011.

[26] L. T. Authority, "Factsheet on electric vehicles," 2010. [Online]. Available: http://www.lta.gov.sg/data/apps/news/press/2010/EV%20Factsheet%20.pdf

[27] K. Mahbubani, "Big idea no. 1: A 'less-car' singapore," 2014. [Online]. Available: http://www.straitstimes.com/opinion/big-idea-no-1-a-less-car-singapore

An Analytical Approach For Transmission Expansion Planning with Generation Variations

Maneesh Kumar
Indian Institute of Technology, Roorkee, India

Raminder Kaur
P.E.C University of Technology, Chandigarh, India

***Abstract*—Today, the transmission expansion planning for an existing power system under different constraints, is one of the major challenge for power engineers. There are several reasons; one of the reasons is rapid growth in load and inadequate capacity addition. Hence, it is important and essential to implement an algorithm for the transmission expansion which works well and have a good feasibility under certain assumptions and available constraints. Transmission expansion planning used in proposed paper works on an analytical algorithm which has been implemented for specific load condition with variations in generation. For that purpose, an economical factor has been measured that considers economical aspects of the line to be added for expansion. The prescribed analytical approach is also implemented for its feasibility check on a practical case study system.**

Index Terms*— *Central electricity authority(CEA), Distributed generation(DG), Economic index (Ei), Power system operator (PSO), Power world simulator (PWS), Renewable energy sources (RES), Transmission expansion planning (TEP).

I. INTRODUCTION

Any power system can only work reliably, when there exists some favorable system condition and constraints for which it is designed to work upon. With increase in complexities, planning for a suitable and reliable transmission system becomes very difficult for a power engineer. Hence, there must always be a coordination between three entities i.e. generation, transmission and distribution for enhancement of overall system stability. While working upon transmission expansion planning the main consideration emphasis on the system stability and reliability.

In many developing countries the majority of power system planning comes from inefficient capacity utilization, very high line losses, unpredictable growth in electricity demand that exceeds the available capacity addition [1]. Hence, optimal solutions are needed to overcome from these problems. This will include a suitable scheduling and operation of existing capacities and detecting the bottlenecks in generation, transmission, etc. In this paper the emphasis is on an optimal solution for the transmission expansion under existing load conditions to reduce expenditures for new transmission corridors [2]. The methodology used here is based on MW-mile method under a deregulated power system environment which considered line length as well as cost associated with the line being added. The methodology is simple to implement also, convergence rate for the applied approach is fast compare to other similar approaches for transmission expansion planning. In TEP, we try to implement cost effective approaches and other measures like series compensation, re-conductoring, addition of one or more lines in the existing system and also alteration of the transmission voltage level. The responsibility of power system operators (PSO) such as utilities, is to provide suitable expansion to transmission corridor so that power transfer with in the corridor become more reliable and system stability should increase [4,11]. There is a unique effect of restructuring and deregulation of the power industry on the objectives of TEP. Therefore, there have been an increased the uncertainties in the system and also the idea behind TEP greatly influenced [5]. Due to these changes, new approaches and criteria are desirable for TEP. The expansion approach used in this paper has uniqueness in terms of its easy applicability and fast convergence unlike some other methods; also the solutions coming after iteration are more practical as seen from the case study.

II. TRANSMISSION EXPANSION PLANNING WITH RESPECT TO GENERATION CHANGE

A. Assuming a 60%t load increment in overall network

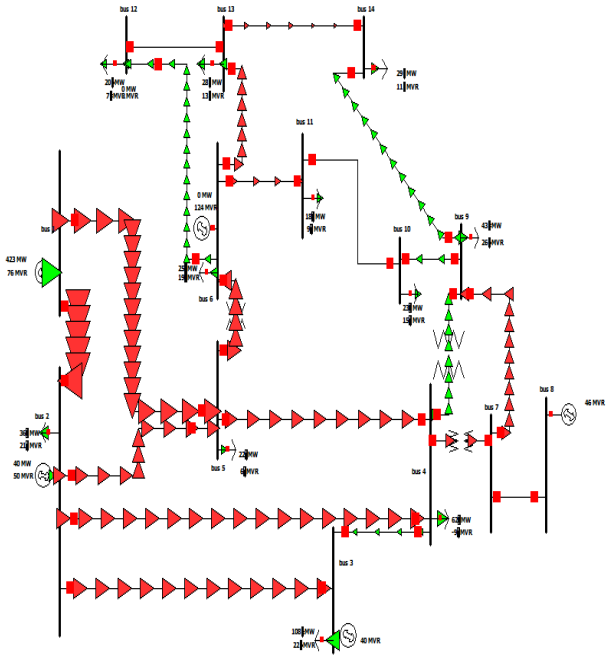

Fig1. IEEE 14 bus system with 60% uniform load increment on PWS

Here, the red arrows show the overloading in the system and hence, to overcome from this we have to add new alternate lines in the network. The system data after simulating the system on PWS with a 60% load increment is given in C. below. A60% load increment is based on 5-7 years planning

criteria of CEA [3,9,10]. Complete simulation has been done using PWS and MATLAB. Fig.1 shows the IEEE 14 bus system which is overloaded under given load conditions. E_i is obtained for each case using MATLAB through a program.

B. Assuming a solar plant of 75MW capacity at bus no. 10

We have considered a solar plant with a capacity of 75MW connected at bus 10. While working on PWS we assumed constant atmospheric conditions i.e. the output of the sources is constant to 75MW irrespective to the changes in weather conditions.

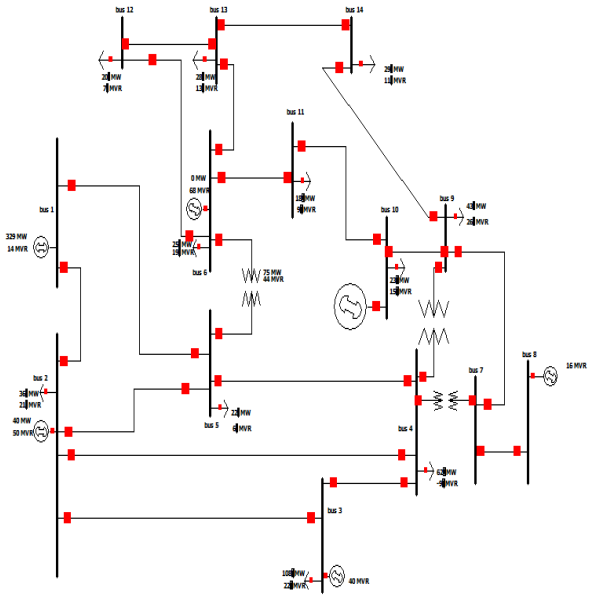

Fig 2. Distributed source added at bus no. 10

With already 60% load increment now we add a distributed source (solar farm with capacity of 75 MW) at bus 10 and check the loading of the network.Fig.2 shows a capacity addition at bus 10 as per availability.

Below is the system data in case of 60% load increment and new generation at bus 10. Here red color digits show the overloading in the network. From the system data it is observed that there are many lines in system under consideration are overloaded and hence, there is a need to remove overloading within the system.

The algorithm used here are being applied on the transmission lines only that means calculation of total number of alternate lines added or removed are only transmission lines of the system and not the transformers.

The simulation results show the different columns like bus numbers between which the lines are connected, number of circuits, status of the circuit i.e. whether they are either closed or open, connected transformers between bus no. 4-7, 4-9 and 5-6, the MW flow, MVAr flow, MVA flow also MVA limit between different line are also obtained from the simulation.

Losses occurred from power flow between different lines can also be observed from the simulation. The alternate lines needed for expansion are calculated in table 1 and will be described in later paragraphs.

C. Simulation results with 60% load increment and distributed source at bus 10

	From Number	From Name	To Number	To Name	Circuit	Status	Xfmr	From MW	From Mvar	From MVA	Lim MVA	Max Percent	MW Loss	Mvar Loss
1	1	bus 1	2	bus 2	2	Closed	No	223.3	-1.3	223.3	120.0	186.1	9.66	24.41
2	1	bus 1	5	bus 5	3	Closed	No	105.9	15.5	107.0	65.0	164.6	6.23	21.14
3	2	bus 2	3	bus 3	4	Closed	No	88.7	2.7	88.8	36.0	246.6	3.98	12.85
4	2	bus 2	4	bus 4	2	Closed	No	71.8	-1.4	71.8	65.0	110.5	3.22	6.40
5	2	bus 2	5	bus 5	1	Closed	No	57.1	1.8	57.2	50.0	114.3	2.00	3.06
6	3	bus 3	4	bus 4	1	Closed	No	-23.3	7.9	24.6	65.0	39.4	0.49	-1.75
7	4	bus 4	5	bus 5	4	Closed	No	-60.6	19.2	63.6	45.0	142.0	0.63	0.87
8	4	bus 4	7	bus 7	1	Closed	Yes	27.6	-8.4	28.9	55.0	53.6	0.00	1.92
9	4	bus 4	9	bus 9	1	Closed	Yes	15.8	-0.3	15.8	32.0	49.7	0.00	1.51
10	5	bus 5	6	bus 6	2	Closed	Yes	71.6	6.0	71.8	45.0	159.8	0.00	13.04
11	6	bus 6	11	bus 11	2	Closed	No	-5.3	11.2	12.4	18.0	68.9	0.15	0.31
12	6	bus 6	12	bus 12	1	Closed	No	19.1	10.1	21.6	32.0	67.4	0.57	1.19
13	6	bus 6	13	bus 13	3	Closed	No	32.8	21.3	39.1	32.0	122.3	1.01	1.99
14	7	bus 7	8	bus 8	1	Closed	No	0.0	-15.6	15.6	32.0	50.2	0.00	0.45
15	7	bus 7	9	bus 9	2	Closed	No	27.6	5.3	28.1	32.0	87.9	0.00	0.92
16	10	bus 10	9	bus 9	2	Closed	No	28.1	29.6	40.8	32.0	127.4	0.53	1.40
17	9	bus 9	14	bus 14	1	Closed	No	27.9	5.4	28.5	32.0	89.0	1.10	2.35
18	11	bus 11	10	bus 10	3	Closed	No	-23.5	1.9	23.5	12.0	199.6	0.47	1.10
19	12	bus 12	13	bus 13	2	Closed	No	-1.5	1.9	2.4	12.0	20.3	0.01	0.01
20	13	bus 13	14	bus 14	5	Closed	No	2.3	8.2	8.5	12.0	70.8	0.14	0.28

TABLE 1. ADDITIONAL LINES NEEDED WITH 60% LOAD INCREMENT AND DISTRIBUTION GENERATION AT BUS 10.

From bus	To bus	% loading	Total lines	Alternate lines
1	2	186.1	3	3-1=2
1	5	164.6	3	3-1=2
2	3	246.6	4	4-1=3
2	4	110.5	2	2-1=1
2	5	114.3	2	2-1=1
4	5	142	2	2-1=1
5	6	159.8	2	3-1=1 (Transformer)
6	13	122.3	2	2-1=1
9	10	127.4	2	2-1=1
10	11	199.6	3	3-1=2

Table 1 shows the number of alternate lines added in the system based on the criteria mentioned below. Here, 80% loading is considered while adding alternate line into the system. 20% margin is taken for line safety and simplicity [3]. Therefore, each line is having a maximum loading of 80%, if it is more than that existing percentage loading divided by 80% loading gives the new alternate lines. Fig.3 is obtained after adding alternating lines based on 80% loading condition as mentioned above. Approaches used for TEP should also consider different uncertainties present in the system either from load side or from generation side i.e. future generation location,

intermittency of RES production, costs of fuel, growth in load etc.) [6-7]

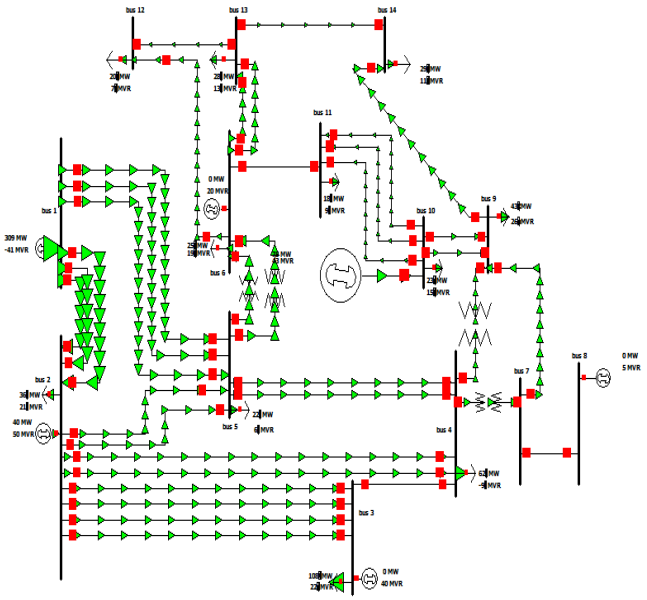

Fig3. Network with new alternate lines

III. Optimization of the Above Network Using Optimal Algorithm

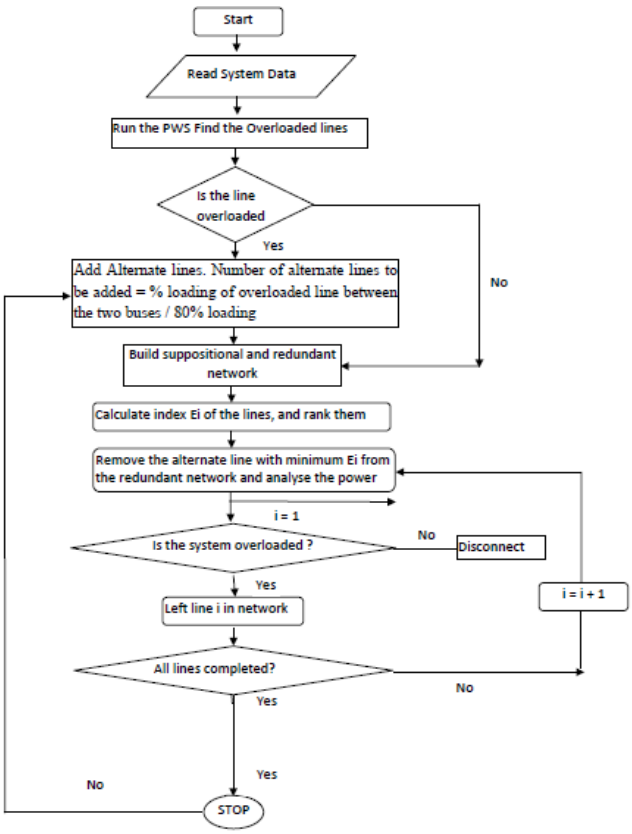

Fig. 3.1 Flowchart for Analytic algorithm for TEP

Fig.3.1 shows the algorithm used to obtain the optimization model of the network under consideration using economical factor known as economic index (Ei) described in coming section A, below. There are certain steps used under applied analytical algorithm and are described as follows:

Step 1: Run the Power world simulator to check that no route is overloaded in the network system data.

Step 2: Add another alternate line on this route in case any route is overloaded keeping the line loading limit to 80% of its capacity.

Step 3: Number of alternate lines to be added = % loading of overloaded line between the two buses divided by 80% loading.

Step 4: Build the suppositional/ redundant network by adding all the alternate lines.

Step 5: Calculate the economic index of all the transmission lines.

Step 6: Tabulate the alternate lines in the increasing order of their economic index.

Step 7: Remove the alternate line with minimum economic index from the redundant network.

Step 8: Reconnect the line which was removed in Step 5 if there is overloading in any line in the network.

Step 9: Remove the alternate line with next higher minimum economic index in the order.

Step 10: Continue the removal of alternate lines with minimum economic index fulfilling our criteria for no overloading of any line met in the process.

Step 11: Repeat the algorithm until removal of all the added alternate lines has been tested. At last we will be left with the alternate lines which reduce the percentage overloading of overloaded lines and maximizes the objective function i.e. the overall increase in the economic efficiency of system expressed as a ratio of sigma of economic index of all transmission lines and the total number of lines in the system at each step of removal of alternate line in the transmission network expansion planning algorithm. The analytical algorithm used in paper for finding out the optimal solution, is basically a set of instruction or a set of some specific steps which are used to find out overall task of optimization.

A. Economic Index (Ei)

Economic efficient lines can be obtained from a novel introduced factor which is acknowledged as Economic index (Ei) and is defined as [2]:

$$E_i = I_i / C_i = [E(P_i)^* D_i^* \rho] / C_i$$

Where,

I_i: profit prospect of alternative line **i**

C_i: Cost of alternative line **i**

P_i: Actual power flow

D_i: Length of line i

ρ: Pre-determined unit cost factor of each transmission line

If $E_i > E_j$, this implies that the line **i** is more economically efficient than line **j**.

Higher is the economic index more efficient will be the line.

Iteration 1. Without removal of any alternating line.

Fig.4 below shows the chart for E_i of network when there is no exclusion of any alternate line. Hence, summation of all E_i divided by existing number of line gives the average E_i of the network.

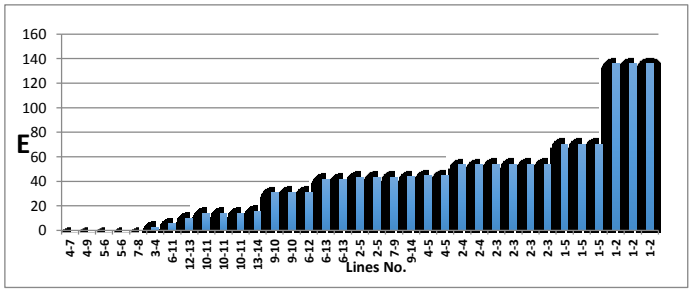

Fig4. Economic index with no exclusion of any alternate line

Average (Ei). for the existing number of lines is 1389.6/31=**43.42**

Above figure shows the lines with minimum and maximum (E_i) in ascending order i.e. minimum and maximum efficient lines. Hence, the choice of removal of lines is based on this order. The least efficient line is preferred to remove first while maintaining system stability considerations i.e. 80%loading condition should also be maintained.

TABLE 2. ROUTE THAT CAN BE REMOVED FROM SYSTEM WHILE MAINTAING 80% LOADING CONDITION

Route	Ei	Status
10-11	14	Not removed
9-10	31	Not removed
6-13	41.6	Not removed
2-5	43.2	Removed
4-5	44.8	Removed
2-4	53.6	Not removed
2-3	54	Removed
1-5	70.4	Not Removed
1-2	135.8	Not Removed

Table 2 shows the routes that can be excluded based on the 80% loading condition. It can be seen that route number 2-5, 4-5 and 2-3 can be removed from the network for the stability and loading conditions along with obtained E_i.

Iteration 2. Exclusion of route 2-5 from the network

The average E_i for existing number of lines from below figure after the exclusion of less efficient line 2-5 will be= 1425.4/30=**47.51**. Fig.5 shows the chart for E_i of network with exclusion of route 2-5.

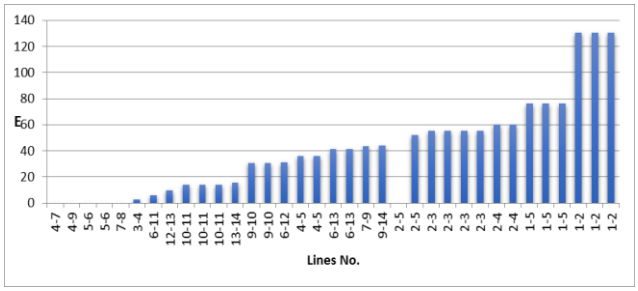

Fig5. Economic index after exclusion of less efficient line 2-5

Iteration 3: Exclusion of route 4-5

The average Ei of the system for existing number of lines from below figure after the exclusion of less efficient lines 2-5, 4-5 will be = 1419.4/29= **48.94**. Fig.6 shows the chart for E_i of network with exclusion of route 4-5 from the network.

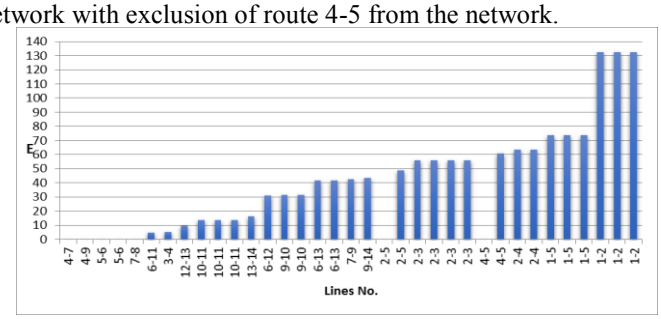

Fig6. Economic index after exclusion of inefficient line 4-5

Iteration 4: Exclusion of route 2-3

The average Ei of the system for existing number of lines from below figure after the exclusion of less efficient lines 2-5, 4-5 and 2-3 will be=1425.8/28= **50.92**= **49.1**. Fig.7 shows the chart for E_i of network with exclusion of route 2-3 from the network.

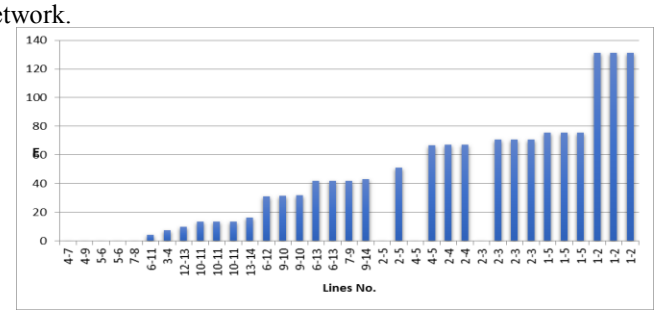

Fig7.Economic index after exclusion of less efficient line 2-3

B. Nework data corresponding to optimal system

- Total number of transmission lines (without any exclusion) = 31
- Base network transmission lines=17
- Total transformers in the network=4
- Total alternate lines added to network= 14 (excluding a transformer between bus 5-6) so that (17+14=31=total transmission lines)
- Total alternate lines left in network=11(14-3 removed lines)

- Total transmission lines left in network= 28 (31-3 removed lines)

Therefore, the optimization algorithm provides a new network that needs only 28 lines out of 31 which corresponds to the most economical and efficient network.

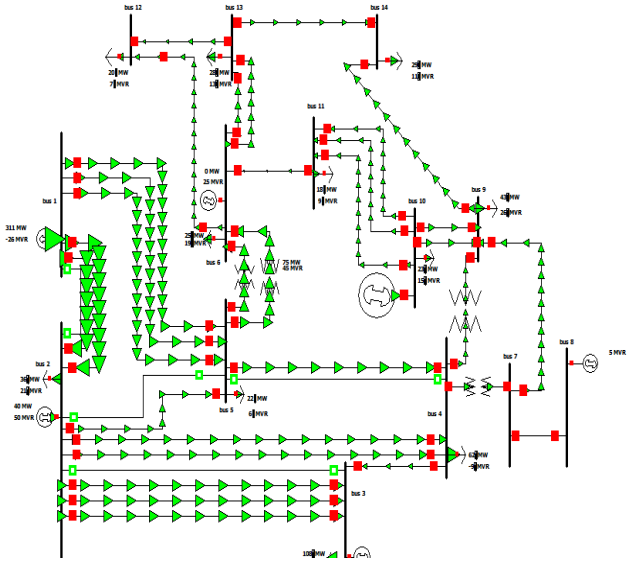

Fig8. New network after optimization

Fig.8 shows an optimized network that is obtained after applying analytical algorithm in the network. Table 3 below shows overall Ei pattern for all four iteration cases also table 4 shows overall economic index with all available routes.

TABLE 3. PATTERN FOR ECONOMIC INDEX (Ei)

S.n.	Line to be removed	Ei(overall)	Lines in network	Ei per line
1	No Removal	1389.6	31	43.42
2	2-5	1425.4	30	47.51
3	4-5	1419.4	29	48.94
4	2-3	1425.8	28	50.92

TABLE 4. OVERALL ECONOMIC INDEX (E_i) WITH ALL AVAILABLE ROUTES

S.n.	Route	Ei (%)
1	10-11	14
2	9-10	31
3	6-13	41.6
4	2-5	43.2
5	4-5	44.8
6	2-4	53.6
7	2-3	54
8	1-5	70.4
9	1-2	135.8

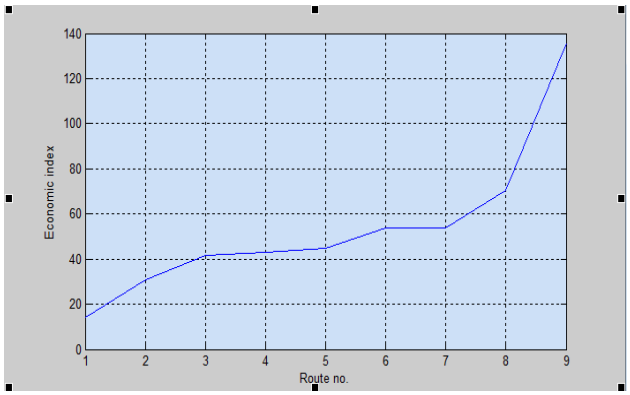

Fig 9. Graph between route and Economic index

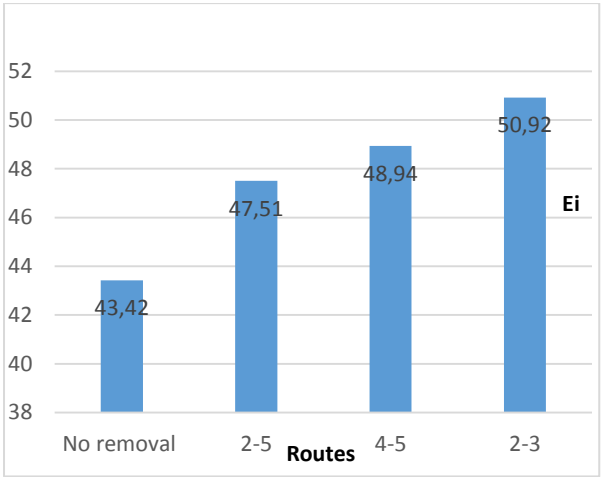

Fig10. Graph for average Economic index with removed line corresponding to E_i order.

CASE STUDY:

A practical power system of Dehradun (In Uttarakhand, an Indian state) area has been considered here to implement analytical algorithm. The overall system data for the power system under consideration is given in table 5 in 2007. There are three load buses situated at three locations known as Majra, Purkul and Bindal as shown in fig.11. There are four generator buses placed at four different locations known as khodari, dhakrani, dhalipur, and kulhal one bus at rishikes considered as slack bus. Similarly, table 6 shows the system data of 2015.

TABLE 5. BUS DATA OF DEHRADUN SYSTEM IN 2007

S. no.	Bus Name	Location
1.	Generator Bus	Khodari (60MW)
		Dhakrani(12MW)
		Dhalipur(16MW)
		Kulhal(12MW)
2.	Slack Bus	Rishikesh(70MW)
3.	Load Bus	Majra (80MW)
		Purkul (35MW)
		Bindal(50MW)

Table 6. BUS DATA OF DEHRADUN SYSTEM IN 2015

S. no.	Bus Name	Location
1.	Generator Bus	Khodari (60MW)
		Dhakrani(12MW)
		Dhalipur(16MW)
		Kulhal(12MW)
2.	Slack Bus	Rishikesh(70MW)
3.	Load Bus	Majra (96MW)
		Purkul (69MW)
		Bindal(81MW)

Iteration 1a: The power system network data of 2007 and 2015 are taken with corresponding increase in load in the duration from 2007-2015 as shown in fig.11. The below network is obtained after first iteration with an increment in load between 2007 to 2015. The line length data and type of conductor used are obtained from the manual and power map available at Power Transmission Corporation of Uttarakhand state website [12]. It is observed from table 6 that in 2015, the load has increased on all the three load buses in the areas of Majra from 80 MW to 96 MW, Purukul from 35 MW to 69 MW and Bindal from 50 MW to 81 MW.

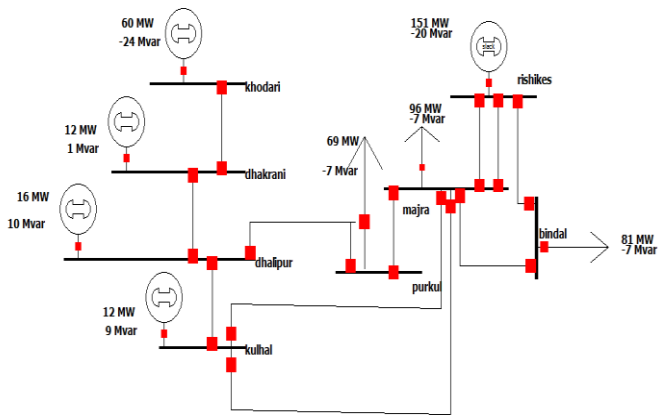

Fig.11 Dehradun area power system on PWS (with 2007-2015 load change)

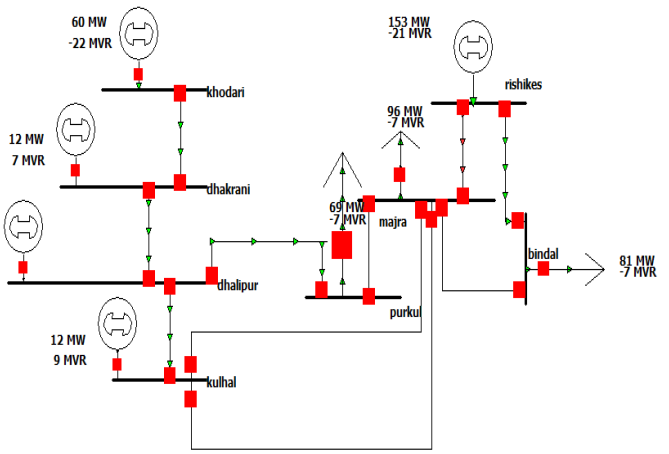

Fig.12 Overloaded system after first iteration

From fig. 12 is observed that there is overloading in the bus between Majra and Rishikesh. The algorithm when applied to the network along with the loading condition of the lines shows one more line is required in the areas between Majra and Rishikesh.

TABLE.7 ADDITIONAL LINES REQUIRED AFTER LOAD INCREMENT

From bus	To bus	% loading	Total lines	Alternate lines
Rishikesh	Majra	159	2	2-1=1

From table 7 it is observed that there is only one additional line is needed between Rishikesh and Majra for removing the system overloading and hence to obtain optimized network as there is no scope to remove any additional line from the system from the view point to system loading corresponding to 80% as considered throughout the system. Hence, system in fig. 13 below, is the optimized system which is also the actual or practical system present in Dehradun. fig.13 shows the optimal network.

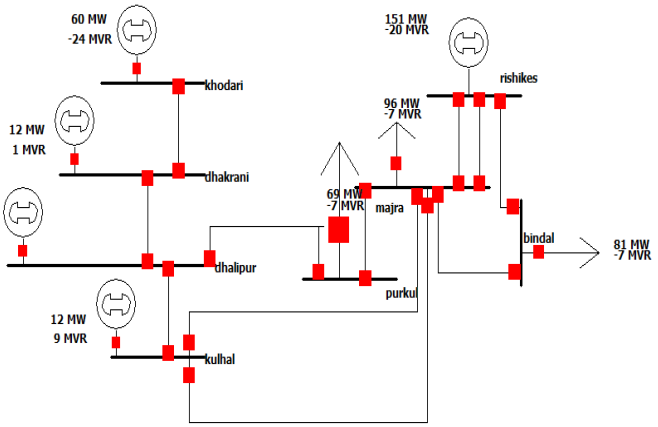

Fig.13 Optimized power system of Dehradun (2015) after addition of only one line

TABLE. 8 Ei OF THE SYSTEM WITH NO RES

From Bus	To Bus	Ei
5.0	6.0	50.8
4.0	6.0	52.4
4.0	6.0	55.4
6.0	8.0	74.6
6.0	7.0	81.2
6.0	7.0	81.2
3.0	4.0	85.4
3.0	5.0	89.2
7.0	8.0	97.6
1.0	2.0	120.0
2.0	3.0	143.4

Table.8 shows the Ei of the Dehradun system when there is no RES in system. Bus numbering is obtained as per table 9. Table also gives require data like MW flow etc.

From the above table average Ei = 931.2305/11 = **84.685.**

TABLE. 9 SYSTEM DATA OBTAINED FROM PWS AFTER FIRST ITERATION.

	From Name	To Number	To Name	Circuit	Status	Branch Device Type	Xfrmr	MW From	Mvar From	MVA From	Lim MVA	% of MVA Limit (Max)	MW Loss	Mvar Loss
1	khodari	2	dhakrani	1	Closed	Line	NO	60.0	-24.0	64.6	100.0	64.6	0.34	0.37
2	dhakrani	3	dhalipur	1	Closed	Line	NO	71.7	-23.4	75.4	100.0	75.4	0.30	0.41
3	dhalipur	4	kulhal	1	Closed	Line	NO	42.6	-10.3	43.9	100.0	43.9	0.10	-0.05
4	dhalipur	5	purkul	1	Closed	Line	NO	44.7	-3.5	44.9	100.0	44.9	0.83	-0.25
5	majra	4	kulhal	1	Closed	Line	NO	-27.8	-0.8	27.8	100.0	28.1	0.31	-1.37
6	majra	4	kulhal	2	Closed	Line	NO	-26.2	-0.8	26.2	100.0	26.5	0.29	-1.54
7	majra	5	purkul	1	Closed	Line	NO	25.2	-4.6	25.6	100.0	25.6	0.14	-0.79
8	rishikes	6	majra	3	Closed	Line	NO	49.8	-6.7	50.2	50.0	100.4	0.96	0.21
9	rishikes	6	majra	4	Closed	Line	NO	49.8	-6.7	50.2	50.0	100.4	0.96	0.21
10	majra	8	bindal	1	Closed	Line	NO	30.3	-0.6	30.3	100.0	30.3	0.07	-0.25
11	rishikes	8	bindal	2	Closed	Line	NO	51.9	-6.2	52.3	100.0	52.3	1.13	0.45

Iteration 1b: Considering one RES of 25MW capacity at heavily loaded bus of Majara. The consideration behind capacity addition is as per "24x7 power for all Uttarakhand" a joint initiative by Government of India and Government of Uttarakhand, manual. There is a proposal of a capacity addition of renewable energy sources into existing system. The addition of solar power (grid connected as well as off grid) for the year 2016-17, has an average of approximately 24 MW (32.1 MW for 2016; 15.4 MW for 2017) [9-10]. So, a solar capacity addition of 25 MW is taken in our case study.

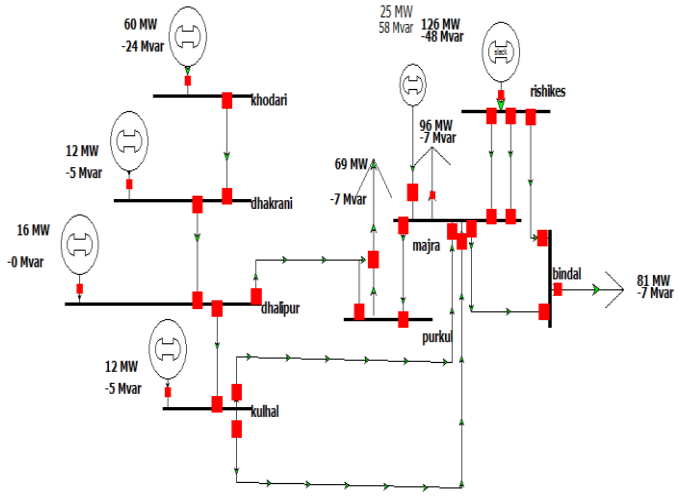

Fig.14 Dehradun system with one RES of 25MW at Majra bus

TABLE. 10 Ei OF THE SYSTEM WITH ONE RES

From Bus	To Bus	E.I
4.0	6.0	51.0
4.0	6.0	54.0
5.0	6.0	59.8
3.0	4.0	82.2
6.0	7.0	82.4
6.0	7.0	82.4
6.0	8.0	82.4
7.0	8.0	87.6
3.0	5.0	92.4
1.0	2.0	120.0
2.0	3.0	143.4

From table 10 above, the average E_i of the system is 937.5835/11 = **85.23.** Hence, from the above two iterative cases it is concluded that with an additional RES at bus 6 the overall E_i of the system improved and the overall system loading is enhanced.

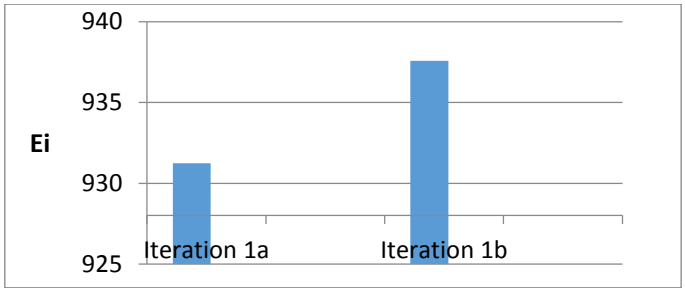

Fig.15 Graph for Economic Index with and without RES

Figure 15 above shows the increase in average E_i of the system after applying analytical algorithm.

VI. CONCLUSION AND FUTURE SCOPE

There are several approaches available for power system expansion planning with different available constraints. The approach given in this paper is based upon MW-Mile method comprises for deregulated power systems. The approach is simple and easy to implement for different configurations of power system e.g. load variations, generation variations, any available contingency in the system or other. Proposed methodology is applied to a practical power system which shows its ease of implementation and importance. Based on different scenarios, the given approach can be implemented in future on the following described areas.

1. The proposed methodologies in future can also be applied on GARVER's 6 bus, IEEE-9 and IEEE-30 etc. bus systems and also on practical systems to see the responses against various transmission system constraints.
2. The prescribed system can also be used as stand-alone system with storage system.
3. The cost analysis of the system under consideration can also be done.
4. Transmission losses and their reduction could be part of the planning process.

5. The load end can be used as input (predefined) in order to identify transmission plans. The consideration of transmission constraints in the generation planning process would be also a possible subject for future work.
6. In addition to this other software like ETAP, MATPOWER, etc. can also be used.

REFERENCES

[1] Junhua Zhao and John Foster, "Flexible Transmission Network Planning Considering the Impacts of Distributed Generation", Energy economics and managenent group, School of economics, Queensland university. Availableat: http://eemg.uq.edu.au/filething/get/194/01.pdf

[2] Xinsong Zhang, Yue Yuan, Boweng WU, Qiang Li, "A Novel Algorithm for Power System Planning Associated with Large-scale Wind Farms in Deregulated Environment" *IEEE 4th International conference* on electric utility deregulation and restructuring and power technologies (DRPT), 2011, China

[3] Kaur Raminder, Kaur Tarlochan, Kumar Maneesh, Verma Shilpa, "Optimal transmission expansion planning under deregulated environment: An analytical approach" *IEEE 1st International Conf.* on Power Electronics, Intelligent Control and EnergySystems (ICPEICES) 2016 India.

[4] Rajeev Kumar Gajbhiye,, Devang Naik, Sanjay Dambhare, and S. A. Soman, "An Expert System Approach for Multi-YearShort-Term Transmission System ExpansionPlanning: An Indian Experience" *IEEE Trans. on Power Systems*, VOL. 23, NO. 1, February 2008

[5] M. Oloomi, H. M. Shanechi, G. Balzer and M. Shahidehpour, "Transmission planning approaches in restructured power systems," in *Proc. IEEE/Power Eng. Soc. Power Tech. Conf.*,Bologna, Italy, vol.2, 2003.

[6] I. I. Skoteinos, G. A. Orfanos, P. S. Georgilakis and N. D.Hatziargyriou "Methodology for Assessing Transmission Investments in Deregulated Electricity Markets*", IEEE Trondheim PowerTech*,2011

[7] Risheng Fang and David J. Hill, "A New Strategy for Transmission Expansion in Competitive Electricity Markets", *IEEE Transactions* on *power systems*, VOL. 18, NO. 1, February 2003

[8] V. S. K. Murthy Balijepalli, and S. A. Khaparde, "Novel Approaches for Transmission System Expansion Planning Including Coordination Issues" *IEEE Power and Energy Society General Meeting,* July 2010

[9] CEA General Guidelines for Substation, New Delhi, India, June 2012

[10] Manual on transmission planning criteria, New Delhi, India January 2013

[11] T. Tachikawa,Hiroyuki Kita, Hideharu Sugihara, Ken-ichi Nishiya and Jun Hasegawa "A study of transmission planning under a deregulated environment in in power system," in *Proc. IEEE Int.* Conf. Electric Utility Deregulation and Restructuring, pp. 649–654,2000

[12] Power transmission corporation of uttarakhand ltd. website available: www.ptcul.org

Maneesh Kumar (M'15–S'16) was born in Haridwar district of Uttarakhand state in Indian on Feb. 1987. He received his Bachelor degree in Electrical engineering from College of Technology, G.B. Pant University of Agriculture and Technology Pantnagar, Uttarakhand in 2009. He received his Master's degree in Electrical engineering from P.E.C University of Technology, Chandigarh, India in 2015 currently he is pursuing his PhD. degree from Indian Institute of Technology, Roorkee, India, since Dec. 2015. He also worked as a lecturer for more than 3 years (from 2009 to 2013) and also assistant professor for 6 months (from July 2015 to Dec. 2015). His major research area includes power system. renewable energy systems, microgrids etc.

Raminder Kaur has received her Bachelor degree from P.E.C Chandigarh, India in 1984 and also her master's degree from the same institute in 1991. She has submitted her PhD. thesis in 2017 and currently she is working as an assistant professor in P.E.C university of technology Chandigarh, India. She has more than 30 years of teaching experience. Her area of interest is power system planning, distributed generation, renewable energy systems etc.

Investigation of Supra-Harmonics through Signal Processing Methods in Smart Grids

Turgay Yalcin[1], Muammer Ozdemir[1]

[1]Ondokuz Mayis University, Electrical&Electronic Engineering Faculty, Samsun, TURKEY
turgay.yalcin@omu.edu.tr , ozdemirm@omu.edu.tr

Pawel Kostyla[2], Zbigniew Leonowicz[2]

[2]Wroclaw University of Technology
Faculty of Electrical Engineering, Wroclaw, Poland
pawel.kostyla@pwr.wroc.pl, leonowicz@ieee.org

***Abstract*— Nowadays supra-harmonic distortion studies are gaining attention day by day in power quality research area. When handling communication systems especially Power Line Carrier (PLC) systems in frequency range 2- 150 kHz, they are suitable for causing electromagnetic interference (EMI) to other systems. This study shows results of analysis employing advanced method called ensemble empirical mode decomposition (EEMD) to describe supra-harmonic distortion. Unlike the traditional method (short time fourier transform- STFT), EEMD gives extensive representation for supra-harmonic components**

Index Terms—ensemble empirical mode decomposition; power quality; short time fourier analysis; supra-harmonics;

I. INTRODUCTION

A novel and significance increasing day by day hazardous risk to smart grid systems called supra - harmonics or emissions in 2 kHz -150 kHz frequency band. This threat can affect capacitors, lose communication contacts with smart meters. The important single fault source operations from photovoltaic inverters (PVs). Naturally fuel cells, battery chargers also wind turbines, can produce this serious threat [1, 2, 3]. Supra-harmonics also disturb domestic appliances, semi-conductor manufacturing devices, medical equipments, security systems even transportation controls. PLC produces low-impedance for emissions in subharmonics frequency range. The highest levels are commonly by virtue of PLC. As a result, power grids are worked out to transfer power at 50 Hz however, line also carries 2 kHz- 150 kHz electromagnetic components [4, 5, 6, 7, 17]. In this study, National Instruments PWr cRIO Data Recorder was used to acquire distortions in power systems. Sampling frequency was selected 1 MHz for measurements. Table I. gives the information of PV systems components properties. Fig 1 shows PV System at the Faculty of Electrical Engineering Wroclaw University of Technology.

TABLE I. PV SYSTEM COMPONENTS PROPERTIES

	Monocrystalline c-Si	Polycrystalline p-Si	The panel thin-film CIGS
Efficiency	14,90%	15,50%	11,80%
Maximum power	190W	240W	90W
Maximum voltage	36,5V	30V	60,8V
Maximum current	5,2A	8A	1,48A
Dimensions	1580 × 808 × 35mm	1680 × 1040 × 35mm	1196 × 636 × 36mm
Weight	17,2 kg	20 kg	14,5 kg

The angle of inclination to the horizontal	β =40^0	β = 40^0	β =40^0
Azimuth	γ =135^0	γ =225^0	γ =135^0

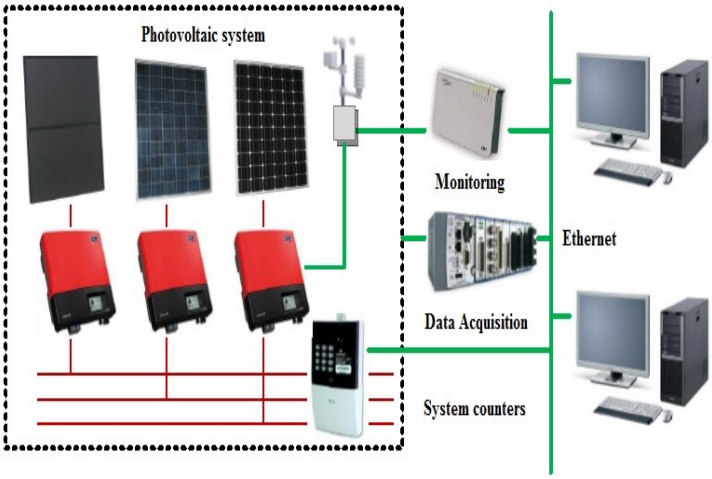

Fig 1. Photovoltaic System at the Faculty of Electrical Engineering Wroclaw University of Technology

II. SIGNAL PROCESSING METHODS

A. Short Time Fourier Transform

Traditionally STFT is applied to measured data from domestic appliances and Sunny Mini Central PV inverter. The results from the STFT are presented in a spectrogram. Spectrograms used for signal processing owing to show supra-harmonics. STFT has drawbacks about representation magnitude and frequency bands [8]. In algorithm we used STFT with hamming sliding window (5 ms) for decompositon. . Respectively fig 2 and 5 shows STFT spectrograms and 2 Hz - 120 kHz frequency band for current signals of domestic appliances LCD TV and Laser Printer.

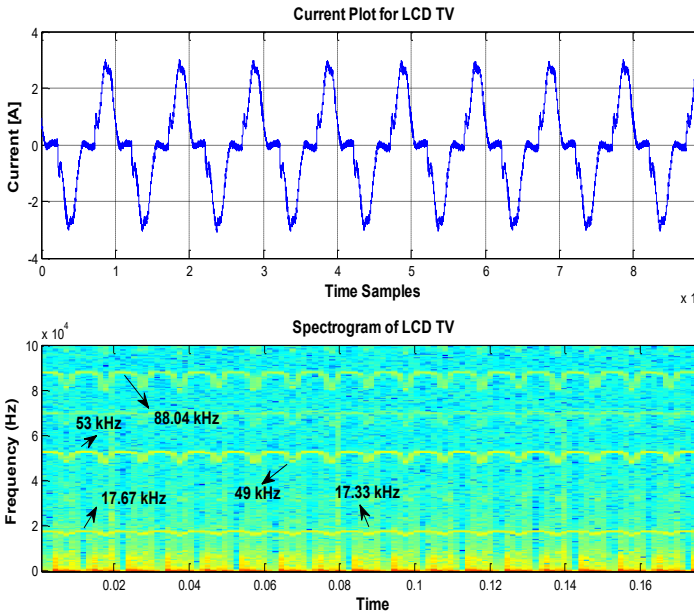

Fig 2. Spectrogram of the current LCD TV

In figure 2 is illustrated constant or continuous frequency emissions at 17. 6 kHz, 53 kHz and 88 kHz bands.

B. Ensemble Emprical Mode Decomposition (EEMD)

EMD has been profitably performed for non-stationary signal processing. The EMD could decompose the complicated signal function into a number of Intrinsic Mode Functions (IMFs)[9,10,11]. The algorithm has major drawbacks of mode mixing, end effects and etc[12,13,14,15,16]. Therefore, in this work we performed EEMD method for generating IMFs in order to analyze supra-harmonics. We focused on pattern frequency band which is dominated in power grid.

The mathematical background of EEMD algorithm (Fig 3):

i. Add noise, $wn(t)$, to target signal $s_1(t)$. $s_2(t)=s_1(t)+wn(t)$.
ii. Used EMD [9, 10, 11, 12, 16] algorithm for decomposing the final signal $s_2(t)$.
iii. Continue steps (i) and (ii) till the trial numbers. When new imf combination $C_{ij}(t)$ is succeeded, predict the ensemble mean of the last intrinsic mode function (IMF). (Selected Nstd: 0 and Number of Ensemble: 1 we used EEMD like EMD.)
The aimed output:

$$EEMD[c_j(t)] = \sum_{i=1}^{tn} c_{ij}(t) \qquad (1)$$

tn: trial numbers, *i:* iteration number and *j:* imf scale [13, 14, 15].

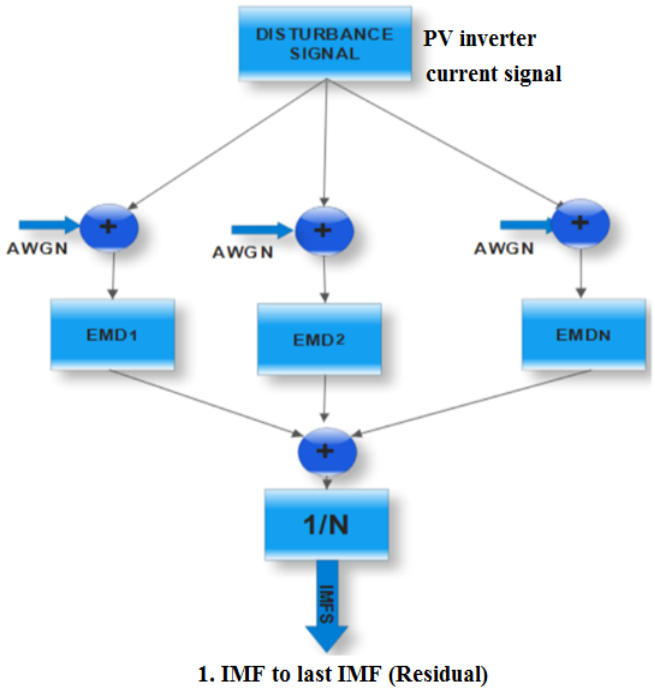

Fig. 3. The representation of the EEMD algorithm[16]

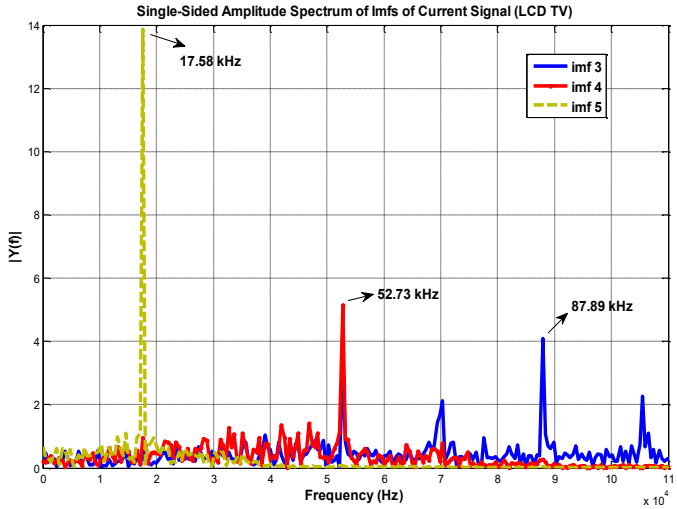

Fig 4. Frequency IMFs components for current of LCD TV

Figure 4 shows the frequency spectrum of IMF 3- IMF 5. When we look for the spectrum it is clearly illustrated that IMF 3 represents the frequency component (17.58 kHz). Moreover, IMF 4 also shows frequency (52.73 kHz) band.

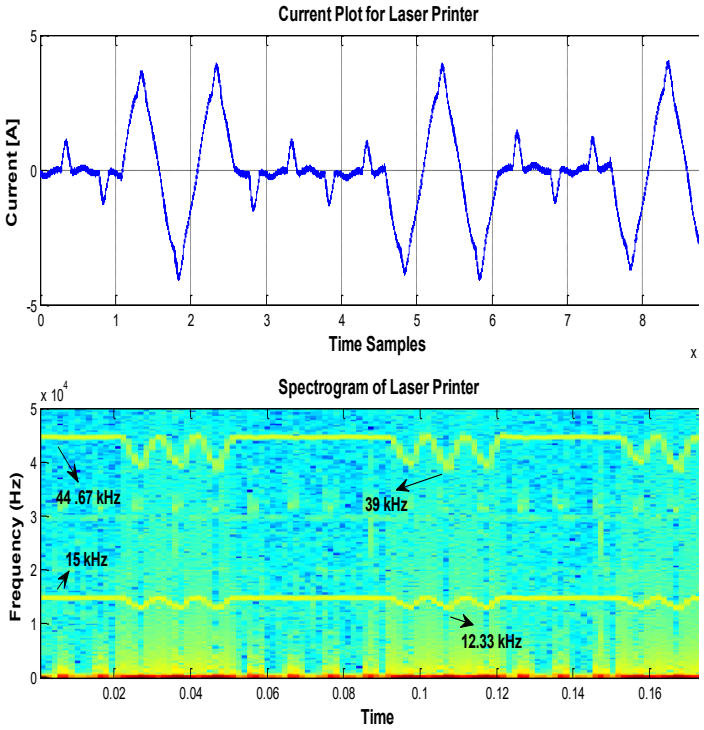

Fig 5. Spectrogram of the current Laser Printer

In figure 5 is illustrated continuous and fluctuant frequency emission at 15 kHz and 44.67 kHz bands. Figure 6 shows the frequency spectrum of IMF 3- IMF 5. When considering the spectrum it is comprehensively shown that IMF 3 represents the frequency component (15.14 kHz). Furthermore, IMF 4 also shows frequency (44.92 kHz) band.

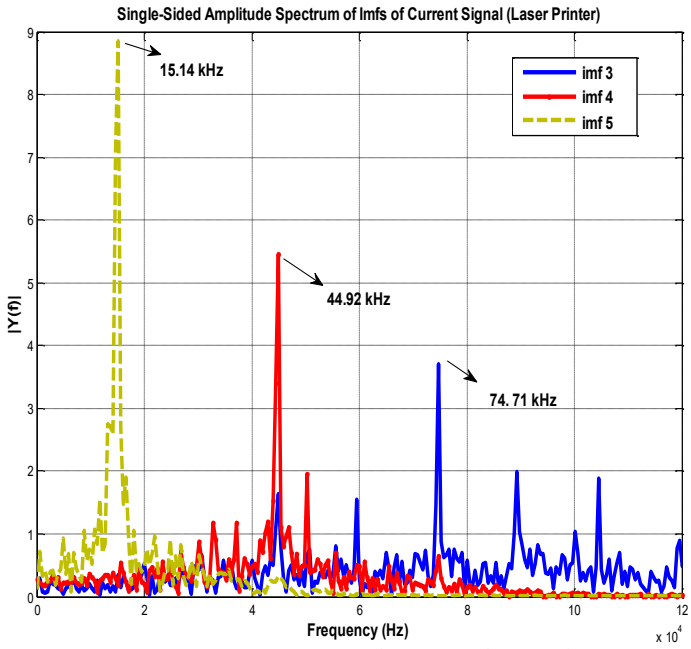

Fig 6. Frequency IMFs components for current of Laser Printer

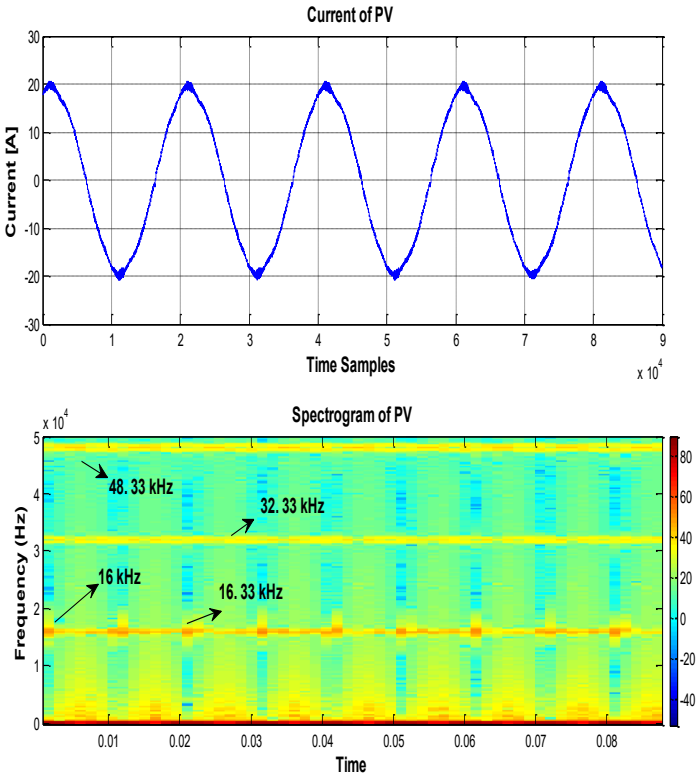

Fig 7. Spectrogram of the current power line with PV (Sampling Frequency: 1 MHz)

In figure 7 is illustrated Continuous and fluctuant frequency emissions at 16 kHz output PLC frequency and Daylight emission at 32 kHz PV inverter signature bands.

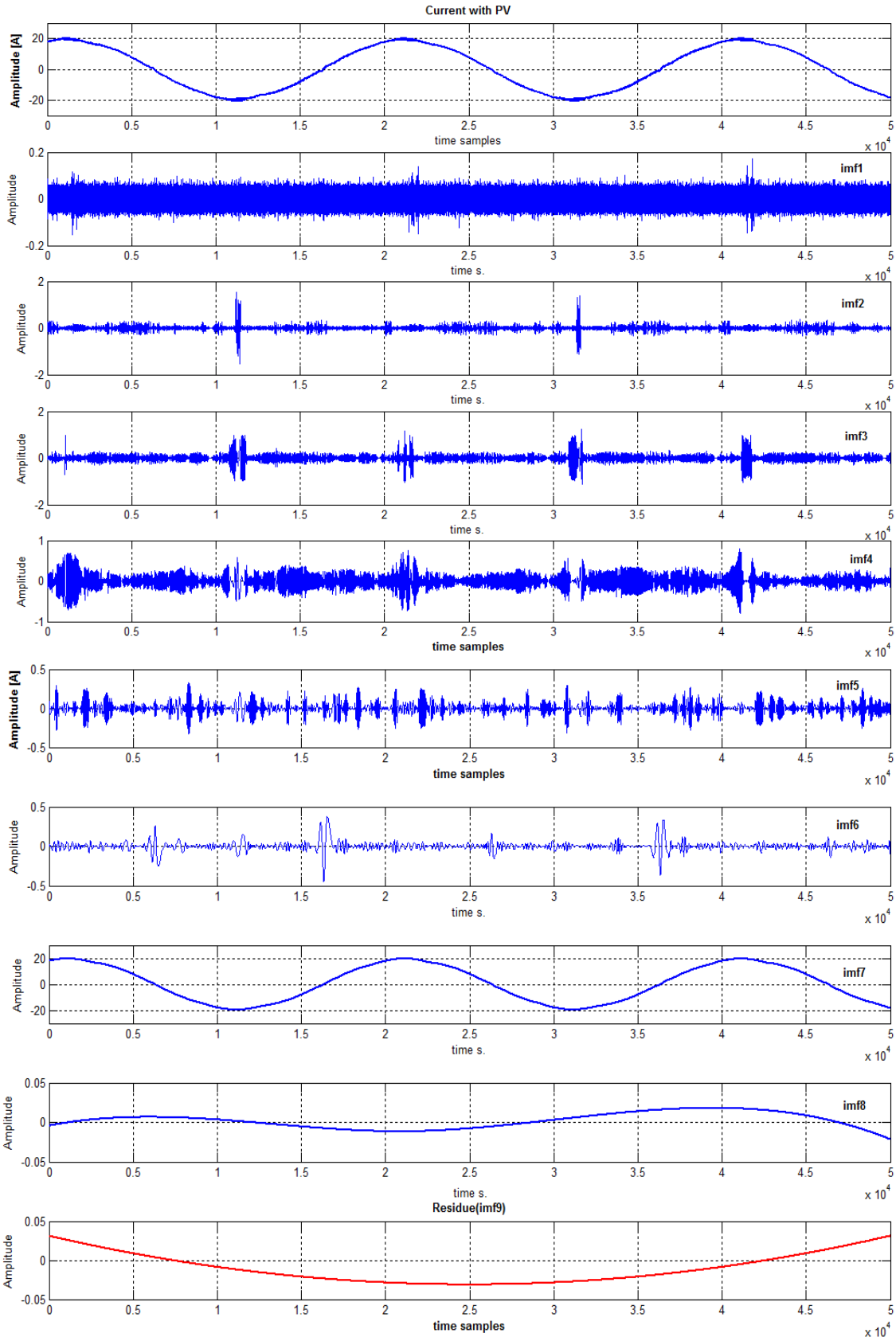

Fig 8. IMF components of PV current signal

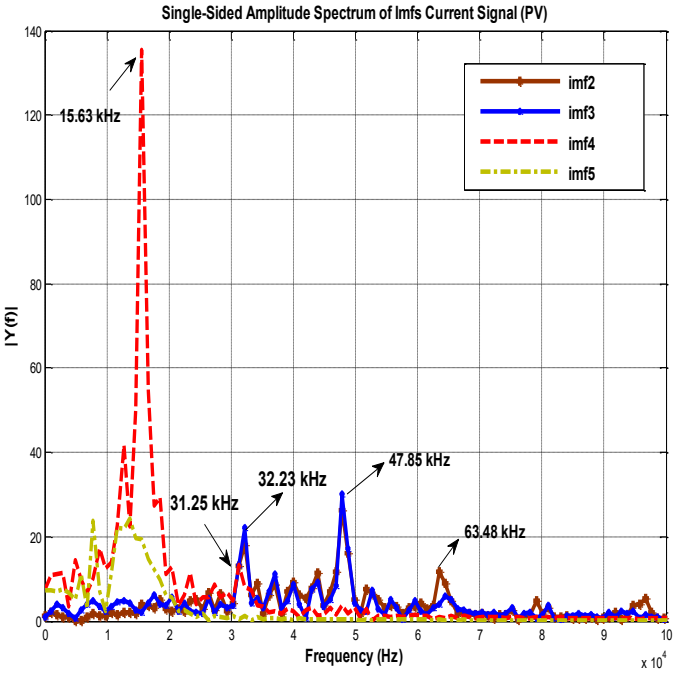

Fig 9. Frequency components of IMFs

Figure 8 shows the IMF components of PV signal. For measurements for PV, fig 9 shows frequency spectrum of IMF 2- IMF 5. When we look for the spectrum it is clearly illustrated that IMF 3 has PLC frequency component (15.63 kHz). Moreover, IMF 4 also shows PV converter frequency (32.23 kHz) band.

Table II. shows the relationship between signal and the IMFs components. IMFs are sorted from higher frequency to lower. Algorithm routine stops till the end of getting monotonic function IMF 9 called residual IMF 7 (R=0.9998) strongly related with the signal.

TABLE II. CORRELATION COEFFICIENT BETWEEN SIGNAL AND IMFS

	R (correlation coefficient)
signal,imf1	0,0006
signal,imf2	-0,0014
signal,imf3	-0,0005
signal,imf4	0,0087
signal,imf5	0,0049
signal,imf6	0,0079
signal,imf7	**0,9998**
signal,imf8	0,0511
signal,imf9	0,1524

III. CONCLUSIONS

Instead of traditional methods such as STFT, EEMD gives more accurate results, determining the PV inverter and PLC frequency bands with high exactitude. It was shown that EEMD method can be used for spectral analysis of supra- harmonics and can be also applied for pattern recognition of supra-harmonics in smart grids with PV systems. With the help of the proposed method supra-harmonic analysis and pattern detection of them easily inquire into.

For future study, this results will discuss with another signal processing methods. Filter design for measuring supra-harmonics in smart grids will be investigated in the light of the analysis.

REFERENCES

[1] E.O.A. Larsson, M.H.J. Bollen, M.G. Wahlberg, C.M. Lundmark, and S.K. Rönnberg, Measurements of high-frequency (2–150 kHz) distortion in low-voltage networks, IEEE Transactions on Power Delivery, Vol.25, No.3 (July 2010), pp.1749-1757.

[2] S.K. Rönnberg, M.H.J. Bollen, M. Wahlberg, Interaction between narrowband power-line communication and end-user equipment, IEEE Transactions on Power Delivery, Vol.26, No.3 (July 2011), pp.2034-2039.

[3] M. Bollen, M. Olofsson, A. Larsson, S. Rönnberg and M. Lundmark, Standards for supraharmonics (2 to 150 kHz), IEEE EMC Magazine, Vol.3 (2014), quarter 1, pp.114-119.

[4] S. Rönnberg, M. Wahlberg, M. Bollen, Conducted emission from a domestic customer in the frequency range 2 to 150 kHz with different types of lighting, Int. Conf. Electricity Distribution (CIRED), Frankfurt, June 2011.

[5] A. Gil-de-Castro, S. K. Rönnberg and M. H. J. Bollen, "Harmonic interaction between an electric vehicle and different domestic equipment," in International Symposium on Electromagnetic Compatibility, Gothenburg, 2014, pp. 991-996.

[6] S. Rönnberg, M. Bollen, A. Larsson, Grid impact from PV-installations in northern Scandinavia, Int. Conf. Electricity Distribution (CIRED), Stockholm, June 2013.

[7] Conducted emissions in the 2kHz - 150kHz band Supra-harmonics, PQube®ApplicationNotev3.0, http://www.powersensorsltd.com/Download/AppNotes/

[8] M. Bollen, H. Hooshyar, S. Rönnberg, Spread of high frequency current emission, Int. Conf. Electricity Distribution (CIRED), Stockholm, June 2013.

[9] K.-M. Chang,"Arrhythmia ECG Noise Reduction by Ensemble Empirical Mode Decomposition", *Sensors*, *10*, 2010, pp. 6063 - 6080.

[10] N.E. Huang, Z. Shen., S.R. Long, M.L. Wu, H.H. Shih, Q. Zheng, N.C. Yen, C.C. Tung, H.H. Liu, "The empirical mode decomposition and Hilbert spectrum for nonlinear and non-stationary time series analysis", Proc. Roy. Soc. London A, Vol. 454, 1998, pp. 903–995.

[11] Z. Wu, N.E. Huang, "A study of the characteristics of white noise using the Empirical Mode Decomposition method," Proc. Roy. Soc. London A, 2002.

[12] T.Yalcin, O.Ozgonenel, “Feature vector extraction by using empirical mode decomposition from power quality disturbances”, IEEE SIU, Fethiye, Mugla, 2012.

[13] O.Ozgonenel, T. Yalcin, I. Guney, U. Kurt, “A New Classification for Power Quality Events in Distribution System”, Electric Power System Research (EPSR), 95, 2013, pp. 192-199.

[14] Z.Wu, N.E. Huang, “Ensemble empirical mode decomposition: a noise-assisted data analysis method”, *Adv. Adapt. Data. Anal.*, 1, 2009, pp.1–41.

[15] Z. Wang, Q. Zhu, J. Kiely, R. Luxton, “Hilbert Huang transform impedance measurement data for cellular toxicity monitoring” *International Conference on Networking, Sensing and Control*, 2009, pp. 767-772.

[16] ,T Yalcin, M Ozdemir, “An Implementation of Exploratory Start for Power Quality Disturbance Pattern Recognition”, TRANSACTIONS ON ENVIRONMENT AND ELECTRICAL ENGINEERING, Vol 1, No 3, 2016, pp 86-93.

[17] T. Yalcin, M Ozdemir, P. Kostyla, Z Leonowicz, “Analysis of Supra-Harmonics in Smart Grids”, EEEIC 2017., 6-9 June 2017 . **DOI:** 10.1109/EEEIC.2017.7977812

About the Authors

Turgay YALCIN received the B.Sc. Erciyes University (ERU), Kayseri, Turkey in 2006 and M.Sc. degrees in electrical engineering from Ondokuz Mayıs University (OMU), Samsun, Turkey, in 2010 and he is currently pursuing the Ph.D. degree in electrical engineering from Ondokuz Mayıs University (OMU). His areas of interest are Identification of Power Quality Disturbances, Signal Processing Methods and Machine Learning Algorithms.

Muammer OZDEMIR received the B.Sc. and M.Sc. degrees in electrical engineering from Black Sea Technical University (KTÜ), Trabzon, Turkey, in 1988 and 1991, respectively, and the Ph.D. degree in electrical engineering from The University of Texas at Austin (UT), Austin, TX, USA, in 2002.Currently, he is an Assistant Professor with the Department of Electrical and Electronics Engineering, Ondokuz Mayıs University (OMU), Samsun, Turkey. His areas of interest are power systems harmonics, power quality, and power system analysis.

Pawel Kostyla in 1998 was awarded the title of Doctor of Science at the Wroclaw University of Science and Technology. From 1999 until now he has been working as an Assistant Professor at the Department of Electrical Engineering. He holds the position of Laboratory Manager of the Theoretical Electrical Engineering. Author and coauthor of publications from the author's interest areas such as artificial neural networks and methods of digital signal processing in automation and electrical engineering, algorithms of digital signal processing and electrical measurements, development and testing of new methods of measuring electrical parameters, quality of electricity.

Zbigniew Leonowicz (IEEE M’03–SM’12) became a Member (M) of IEEE in 2003 and a Senior Member (SM) in 2012. He received the M.Sc., Ph.D. and Habilitate Doctorate (Dr Sc.) degrees, all in Electrical Engineering, in 1997, 2001, and 2012, respectively. He has been with the Department of Electrical Engineering, Wroclaw University of Technology, since 1997 where he currently holds position of Associate Professor. His current research interests are in the areas of power quality, control and protection of power systems, renewables, industrial ecology and applications of signal processing methods in power systems.

System Identification and Tuning of Wireless Power Transfer Systems with Multiple Magnetically Coupled Resonators

Johan Winges, Thomas Rylander, Carl Petersson, Christian Ekman, Lars-Åke Johansson and Tomas McKelvey

***Abstract*—We present a procedure for system identification and tuning of a wireless power transfer (WPT) system with four magnetically coupled resonators, where each resonator consists of a coil and a capacitor bank. The system-identification procedure involves three main steps: 1) individual measurement of the capacitor banks in the system; 2) measurement of the frequency-dependent two-port impedance matrix of the magnetically coupled resonators; and 3) determining the inductance of all coils and their corresponding coupling coefficients using a Bayesian approach. The Bayesian approach involves solving an optimization problem where we minimize the mismatch between the measured and simulated impedance matrix together with a penalization term that incorporates information from a direct measurement procedure of the inductance and losses of the coils. This identification procedure yields an accurate system model which we use to tune the four capacitance values to recover high system-performance and account for, e.g., manufacturing tolerances and coil displacement. For a prototype WPT system, we achieve 3.3 kW power transfer with 91% system efficiency over an air-gap distance of approximately 20 cm.**

***Index Terms*—Bayesian estimation, charging electric vehicles, impedance matching, magnetically coupled resonators, system identification, tuning, wireless power transfer (WPT).**

I. Introduction

Magnetically coupled resonators are becoming increasingly popular for mid-range wireless power transfer (WPT) that is suitable for charging electric vehicles [1], [2], [3]. Given the low magnetic coupling that is typical in such WPT systems, resonant circuits with low losses are used to achieve high power transfer at high efficiency. However, it is crucial that such resonators are tuned in order to achieve satisfactory system performance, as the power transfer and efficiency rapidly decays should the system become de-tuned [4], [5].

Aldhaher et al. [6] studied a WPT system with two resonators, where they mitigated de-tuning issues associated with coil misalignment and displacement by means of a current-controlled inductor and a variable switching frequency. However, in automotive applications, it may not be possible to change the switching frequency due to regulations and standards [7]. Beh et al. [8] considered a WPT system that operates at a fixed frequency (13.56 MHz), where they used an automatized impedance matching system with three extra components (an L-match network) to tune the resonance frequency of the resonator pair to that of the power source. Similarly, Li et al. [9] used four tunable components for a WPT system with two resonators, which allows for some advantages, such as making the resonant network inductive and achieving zero-voltage switching. Halpern et al. [10] analyzed the limits of capacitor tuning for a WPT system with two resonators and present the optimal selection of the capacitance values with respect to maximizing a weighted sum of both system efficiency and power transfer.

In an effort to increase the power transfer distance and efficiency, WPT systems with more than two magnetically coupled resonators have been considered in the literature [11], [12], [13]. Zhong et al. [14] presents a wide variety of so-called domino WPT systems where a large number of magnetic resonators are placed in a domino pattern to increase the power transfer range. Liu et al. [15] show how two additional resonant circuits can be located at an off-center location about midway between the primary and secondary resonators to increase the range and performance of a WPT system. However, the total size of such domino-like WPT systems may be unpractical for some mid-range high power transfer applications such as electric vehicle charging. Lin et al. [16] show how it is possible to identify the capacitance values and inter coil distances for a 3-coil domino system from measurements of the input voltage

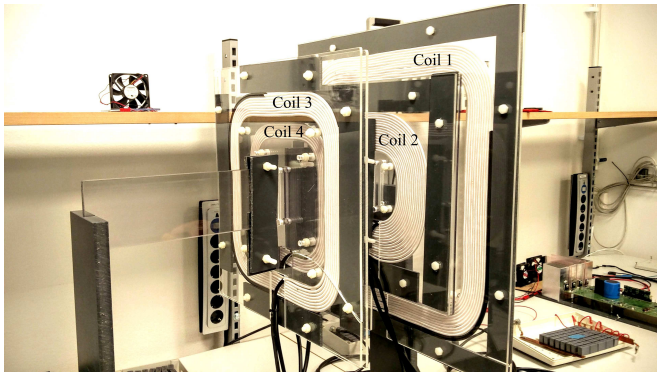

Fig. 1. Photo of the air-wound coils used in the WPT system prototype with four magnetically coupled resonators.

Manuscript accepted Januari 12, 2018. This work was funded by the Swedish Energy Agency in the project "Säker induktiv energiöverföring för elfordon – Safe Wireless Energy (SAWE)", which has the project number 38577-1.

J. Winges, T. Rylander and T. McKelvey are with the Department of Electrical Engineering, Chalmers University of Technology, Göteborg, 41296 Sweden (e-mail: winges@chalmers.se; rylander@chalmers.se).

C. Petersson, C. Ekman and L.-Å. Johansson are with QRTECH AB, Flöjelbergsgatan 1c, Mölndal, 43135 Sweden.

and current over a frequency band using a genetic optimization algorithm. However, in their work they assume that the coil losses and inductance can be accurately calculated, which is not necessarily the case for more involved coil designs.

In this extended article based on the conference submission [17], we present a system identification procedure combined with tuning for a WPT system with four magnetically coupled resonators, where two resonators are located at the primary side and two on the secondary side. Here, the four resonators can improve the efficiency and power transfer for applications with low magnetic coupling between the primary and secondary side [11], [12]. Moreover, the extra resonant circuits yields additional degrees of freedom in the WPT system design, and we show that that the capacitance values can be used for system tuning. In the system identification step, we estimate the coil inductances, mutual couplings and losses using a Bayesian approach [18], where we minimize the weighted sum of two terms: 1) the mismatch between the coil parameters and an approximate measurement of these parameters; and 2) the mismatch between the simulated and measured impedance matrix for the magnetically coupled resonators over a frequency band. Here, the system identifications is used to find deviations from a nominal system design due to e.g. manufacturing tolerances and coil misalignment. Furthermore, we demonstrate that high power transfer and efficiency can be recovered for an experimentally realized (non-nominal) design at a fixed operating frequency using only one tunable capacitor per resonant circuit, where the capacitance of each capacitor can be adjusted in a few discrete steps. In addition, the realized design complies with a set of circuit constraints which prevent over-heating or voltage breakdown of the components in the WPT system.

II. WPT SYSTEM DESIGN

A WPT system consisting of four magnetically coupled resonators is considered and Fig. 1 shows a photograph of the coils in a WPT system prototype. The coil geometry of the prototype is described in Table I in terms of the number of turns N_m, the side length s_m and the placement along the z-axis, which is perpendicular to the plane of each coil and coincides with their respective centers. Here, the air gap between the two groups of coils is 18.5 cm. We use Litz wire with an outer diameter of 10 mm, consisting of 1080 copper strands with a diameter of 0.1 mm. For all coils, the minimum inner bend radius is 4.5 cm. The different coil sizes in the prototype system were chosen to illustrate that different geometrical constraints may be applicable to the primary and secondary side in a WPT system depending on the application. Further, the small additional coils may in theory be incorporated into the same plane as the large coils, which yields a WPT system that is relatively thin, which is important for e.g. charging electric vehicles.

We use *COMSOL Multiphysics*® [19] to compute the self-inductance L_m of each coil and the mutual coupling coefficient k_{mn} between each coil, and the results are presented in Table I. The individual Litz wires of the coils are not explicitly modeled in the *COMSOL* model, which instead uses a multi-turn coil domain applied to a simplified coil geometry where we approximate the coil cross-section as a rectangle of height equal to the wire diameter and length equal to the number of turns times the wire diameter.

TABLE I
GEOMETRY DESCRIPTION WITH NUMBER OF TURNS N_m OF LITZ WIRE ($\oslash = 10$ mm), OUTER SIDE LENGTH s_m AND AXIAL POSITION z_m OF THE COILS SHOWN IN FIG. 1 ENUMERATED BY $m = 1, \ldots, 4$ AND CORRESPONDING INDUCTANCE AND COUPLING COEFFICIENTS COMPUTED USING A *COMSOL* MODEL

Coil m	1	2	3	4
N_m (-)	11	16	8	6
s_m (cm)	51.0	29.0	34.0	25.0
z_m (cm)	0	2.50	24.5	22.0
L_m (μH)	120	66.4	41.3	15.6
k_{1m} (%)	-	21.3	9.09	6.87
k_{2m} (%)	21.3	-	6.99	6.77
k_{3m} (%)	9.09	6.99	-	37.9

A. Circuit model

A circuit diagram model of the magnetically coupled resonators are shown in Fig. 2, which also includes capacitor banks and series resistances that model losses in the system. Our nominal system design for the prototype is described by the component values in Table I and the capacitance values $C_1 = 27.0$ nF, $C_2 = 42.7$ nF, $C_3 = 67.7$ nF and $C_4 = 140$ nF.

At the terminals A_1-A_2, the magnetically coupled resonators are fed by a power inverter, which is modeled by a square-wave voltage source $u_{\rm in}(t) = U_0 \,\mathrm{sgn}[\cos(\omega_{\rm p} t)]$ in series with an internal resistance $R_{\rm G}$ = 0.25 Ω. It operates at the frequency $f_{\rm p}$ = 85 kHz with a maximum output voltage of $U_0^{\max}$ = 450 V. At the terminals B_1-B_2, the magnetically coupled resonators are loaded by a rectifier, smoothing filter and resistive load $R_{\rm L} = 27$ Ω as shown in Fig. 3. The current-voltage curve of the diodes is modeled as piece-wise linear with a forward voltage drop of 1.3 V and a forward resistance of 0.08 Ω. We define the efficiency η of the system as the power $p_{\rm load}$ transferred to the load $R_{\rm L}$ divided by the input power $p_{\rm in}$ supplied by the generator. The power levels are found after the system has reached steady-state operation, and are time-averaged over one period. The complete circuit is simulated in time-domain using the circuit simulation software *LTspice* and an in-house circuit simulation implementation in *MATLAB*.

III. SYSTEM IDENTIFICATION

In simulation, the nominal system design presented in Section II achieves both high power transfer and efficiency. However, our experimental realization suffers from various manufacturing tolerances and, consequently, the actual component values of the magnetically coupled resonators differ from the nominal design. Such deviations are common in practical situations where misalignment and incorrect distance between

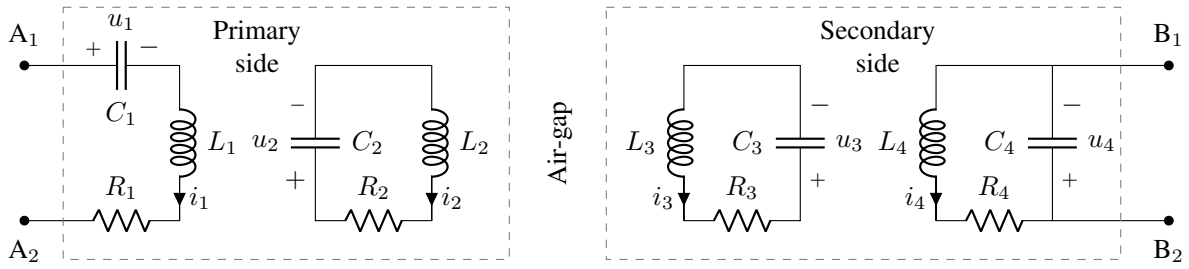

Fig. 2. Circuit diagram for the magnetically coupled resonators with four coils and capacitors.

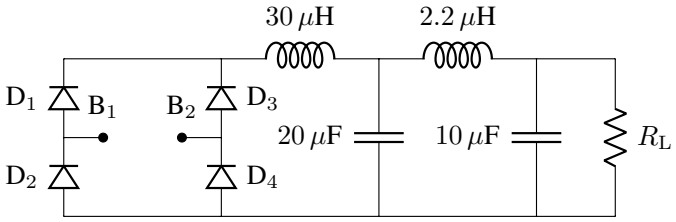

Fig. 3. Circuit diagram for rectifier, filter and load resistance.

the primary and secondary side are typical disturbances. Thus, we propose the following procedure for identifying the component parameters of WPT systems.

First, the capacitance of the capacitor banks is measured to high accuracy when they are disconnected from the rest of the circuit. Here, the capacitor banks are assumed to be tunable to a few discrete values, where we measure each discrete capacitance value to high accuracy.

Next, the realized system parameters $\mathbf{p} = [L_1, \ldots, L_4, k_{12}, \ldots, k_{34}, R_1, \ldots, R_4]$ of the magnetically coupled resonators are identified. Initially, the coil inductance, coupling coefficients and losses are measured approximately using a direct procedure where we disconnect the individual coils from the rest of the circuit. The approximate measurement result is denoted $\mathbf{p}_0$. Next, we connect the capacitor banks (which are set to known values) to form the system of the magnetically coupled resonators. The corresponding model is shown in Fig. 2 and we introduce the two-port impedance matrix

$$\mathbf{Z} = \begin{bmatrix} Z_{AA} & Z_{AB} \\ Z_{BA} & Z_{BB} \end{bmatrix}, \tag{1}$$

where the index A corresponds to the terminals A_1-A_2 and the index B corresponds to the terminals B_1-B_2 and, due to reciprocity, we have $Z_{BA} = Z_{AB}$. The impedance matrix $\overline{\mathbf{Z}}(f_\nu)$ is then measured for N_ν frequency points in a frequency band around the operating frequency of the WPT system. To simplify the notation, we vectorize the three unique elements of the impedance matrix with respect to frequency, i.e. $\overline{\mathbf{z}} = \text{vec}\{\overline{Z}_{AA}(f_\nu), \overline{Z}_{AB}(f_\nu), \overline{Z}_{BB}(f_\nu)\}$. (Here the bar notation indicates that the quantity is measured.)

To identify the system parameters $\mathbf{p}$, we use a Bayesian approach [18] to formulate a weighted maximum a posteriori estimator that combines: 1) the mismatch between the measured impedance matrix $\overline{\mathbf{z}}$ and the simulated impedance matrix $\mathbf{z}(\mathbf{p}) = \text{vec}\{Z_{AA}(f_\nu, \mathbf{p}),\ Z_{AB}(f_\nu, \mathbf{p}),\ Z_{BB}(f_\nu, \mathbf{p})\}$; and 2) a penalization term that corresponds to the deviation between the parameters $\mathbf{p}$ subject to optimization and the measured parameters $\mathbf{p}_0$ from the direct procedure. This gives the minimization problem

$$\min_{\mathbf{p}} \frac{1}{N_z} \left\| \mathbf{z}(\mathbf{p}) - \overline{\mathbf{z}} \right\|_{\mathbf{P}}^2 + \frac{\gamma}{N_p} \left\| \mathbf{p} - \mathbf{p}_0 \right\|_{\mathbf{Q}}^2 . \tag{2}$$

We assume independent Gaussian distributions for the measurement errors and compute the norms with respect to the diagonal matrices $P_{kk} = 1/|\delta_{z_k} \overline{z}_k|^2$ and $Q_{ll} = 1/(\delta_{p_l} \overline{p}_l)^2$, where δ_{z_k} and δ_{p_l} are estimates of the relative standard deviation of the respective measurement uncertainties. In this work, we use $\delta_{z_k} = 1/3\,\%$ for $\overline{\mathbf{z}}$, and for the optimization parameters we use $\delta_{p_l} = 1/3\,\%$ for L_m, $\delta_{p_l} = 2\%$ for k_{mn} and $\delta_{p_l} = 5\%$ for R_m. Furthermore, $N_z = 3N_\nu$ and $N_p = 10$ are the number of elements in the vectors $\mathbf{z}$ and $\mathbf{p}$, respectively. From (2), we can interpret that the regularization parameter γ penalizes deviation of the estimate $\mathbf{p}$ from the measurement $\mathbf{p}_0$, weighted by the corresponding measurement uncertainties of the direct measurement procedure.

We solve the minimization problem (2) using the gradient-based optimization algorithm *fmincon* implemented in *MATLAB* [20] with the initial guess $\mathbf{p}_0$, and an optimum is typically found in less than 70 iterations. An important feature of the proposed optimization problem (2) is that the impedance matrix model only involves linear components and can be solved efficiently in frequency domain. Consequently, the objective function is associated with a relatively low computational cost per frequency point and it is therefore feasible to resolve rapid frequency variations over a relatively large frequency band, which is beneficial for real-time applications.

IV. Tuning

The system identification procedure in Section III yields accurate estimates of the circuit parameters, shown in Fig. 2, that deviate from the nominal design due to manufacturing tolerances and coil misalignment. Consequently, the realized system performance may have deteriorated considerably when compared to the nominal system. However, by tuning the four capacitance values, we can recover high power transfer and efficiency for rather significant perturbations due to, e.g., coil misalignment.

To recover high performance, we simulate the WPT system for a large set of different combinations of the discrete values of the capacitor banks and compare the final power transfer and

TABLE II
CONSTRAINTS ON RMS VALUES OF THE CURRENTS AND VOLTAGES, WHICH ARE ENFORCED FOR THE COMPONENTS LISTED WITHIN THE PARENTHESES FOR $m = 1, \ldots, 4$

Component	Quantity	unit	max
Coil (L_m, R_m)	i	A	60
Capacitor (C_m)	u	kV	5
	i	A	40
	$u \times i$	kVA	50
Power inverter (R_G)	i	A	30
Rectifier (D_m)	u	V	850
	i	A	15

efficiency after the system has reached steady-state operation. For each of these solutions, we limit the generator voltage U_0 such that none of the constraints listed in Table II are violated. These constraints prevent over-heating or voltage breakdown for the particular components in the realized WPT prototype system. Here, we require that the power inverter is connected to an inductive load $Z_{\mathrm{AA}}^{\mathrm{loaded}}$ when the terminals B_1-B_2 of the magnetically coupled resonators are connected to the load circuit shown in Fig. 3. Thus, we require that $0° < \angle Z_{\mathrm{AA}}^{\mathrm{loaded}} < 90°$ for the operational frequency f_p and remove all solutions that yield a non-inductive load.

The remaining solutions are sorted with respect to power transferred to the load R_L and a suitable candidate is selected.

V. RESULTS

We present results for the system identification and tuning of the WPT system shown in Fig. 1, which is a prototype system intended to transfer 3.3 kW power over a 20 cm air-gap at high efficiency. Prior to assembly, we measure all components with an *OMICRON LAB Bode100* network analyzer using a direct procedure where each component is disconnected from the rest of circuit and measured. A rather limited set of discrete capacitance values for the capacitor banks are realized for the prototype system and the measured results are shown in Table III. The different capacitance values are implemented by a set of discrete low loss capacitors (*Kemet R73 series*) in a parallel configuration connected by switches.

TABLE III
DISCRETE VALUES FOR EACH C_m IN CAPACITOR BANKS

Parameter	Values
C_1 (nF)	17.6, **21.7**, 26.4, 30.8, 35.2
C_2 (nF)	23.5, 31.1, **39.2**, 47.0, 54.8, 62.7
C_3 (nF)	47.0, 53.7, **62.0**, 66.4, 73.9, 80.6
C_4 (nF)	110, 122, 130, **139**, 145, 152

Next, the coils and capacitors are assembled with the discrete values marked in bold in Table III to form the system of magnetically coupled resonators. We measure the impedance matrix $\overline{\mathbf{Z}}(f_\nu)$ for $N_\nu = 600$ uniformly distributed frequency points f_ν from 50 kHz to 170 kHz. In Fig. 4, we show the absolute value and phase of the measured impedance matrix $\overline{Z}_{pq}(f_\nu)$ with solid curves and the computed result using the coil parameters from the direct procedure, i.e. $Z_{pq}(f_\nu, \mathbf{p}_0)$, with dashed curves. It should be noted that there are substantial differences between the measured and computed results in Fig. 4, with an average relative error of about 40%. This error indicates that we have an unsatisfactory identification of the component values in our system of magnetically coupled resonators. Here, this deviation is in part due to the measurement uncertainty of the direct measurement procedure in combination with incorrect inter-coil spacing which may occur as the WPT system is assembled prior to the impedance matrix measurement. It should be noted that the resonant behavior of the magnetically coupled resonators results in that the WPT system is relatively sensitive to rather small perturbations of the circuit parameters.

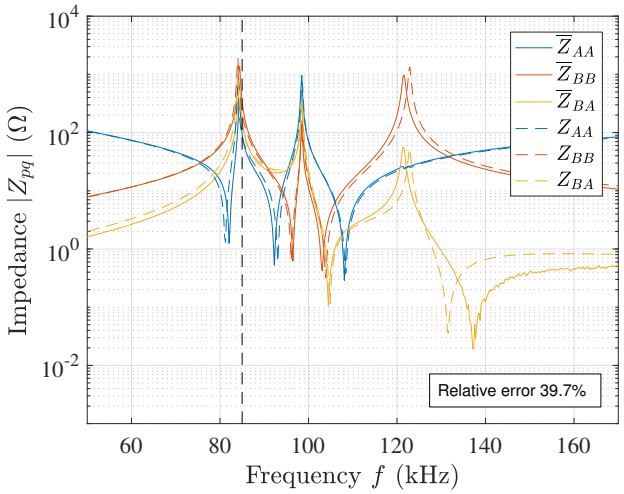

(a) Magnitude

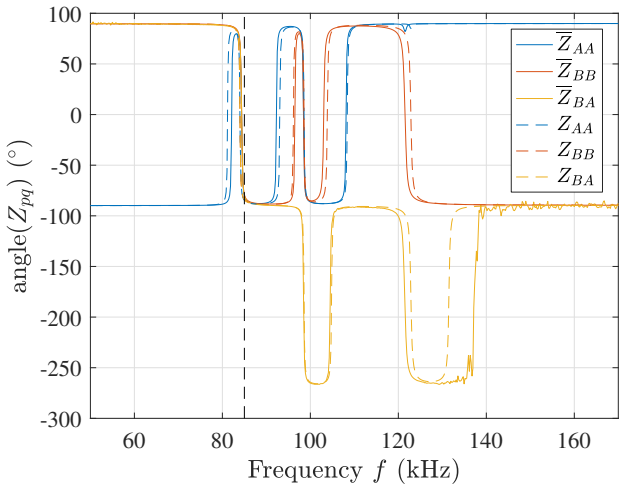

(b) Phase

Fig. 4. Magnitude and phase of impedance matrix entries as a function of frequency: 1) solid curves – measurements $\overline{Z}_{pq}(f_\nu)$; and 2) dashed curves – model $Z_{pq}(f_\nu, \mathbf{p}_0)$ for the initial parameter vector $\mathbf{p}_0$. The vertical dashed line show the operating frequency 85 kHz.

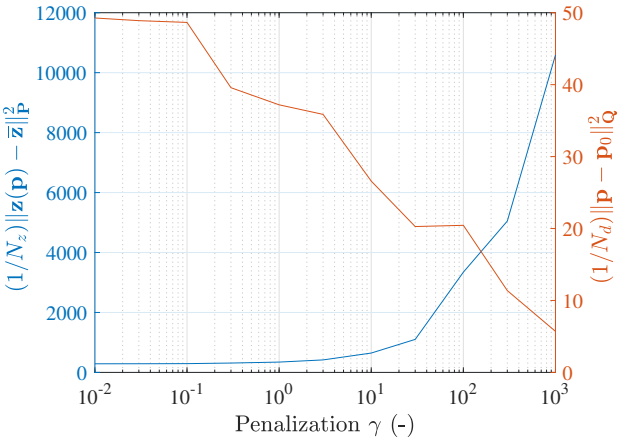

Fig. 5. Magnitude of the two different norms in the minimization problem (2) versus penalization.

We solve the optimization problem (2) for $10^{-2} \leq \gamma \leq 10^{3}$. Fig. 5 shows the corresponding magnitude of the two norms in (2) as a function of the penalization parameter γ. We note that the impedance matrix norm increases significantly for $\gamma > 30$, which indicates that $\gamma = 30$ is a suitable penalization value that achieves good model agreement, with low deviation between the optimization parameters and the measured parameters. Selecting the result with $\gamma = 30$ yields the optimized parameter vector $\mathbf{p}^*$ and the corresponding impedance matrix entries $Z_{pq}(f_\nu, \mathbf{p}^*)$ which are shown with dashed curves in Fig. 6. For reference, we also show $\overline{Z}_{pq}(f_\nu)$ with solid curves in Fig. 6. It should be noted that the agreement is excellent after the system identification and that the average relative error is less than 4%.

Table IV shows the initial parameter vector $\mathbf{p}_0$ and the optimized result $\mathbf{p}^*$. Here, we note a rather large reduction in the coupling coefficients associated with the air-gap when we compare the initial and optimized results. These results indicate that the distance between the primary and secondary side may have been increased by approximately 5-10 mm when the system was reassembled after the direct measurement of the individual components.

In realistic usage scenarios of WPT systems, air-gap deviations on the order of at least 10-20 mm are expected due to, among other factors, parking misalignment, variations in the ground clearance between different car models and installation differences between different charging stations. It is reassuring that the system identification procedure presented here significantly reduces the deviation between the model and the measurement. Thus, the complete WPT model presented in Section II can be used for accurate system simulation, which in turn can be used to tune the WPT system for high power transmission and efficiency.

Given the identified model parameters, we tune the four capacitor banks by comparing the simulated performance of the 1080 different discrete capacitance combinations given by Table III using an exhaustive search. For each combination in the exhaustive search, the generator voltage is reduced from $U_0^{\max} = 450$ V until all constraints in Table II hold and, consequently, the maximum power transfer can vary

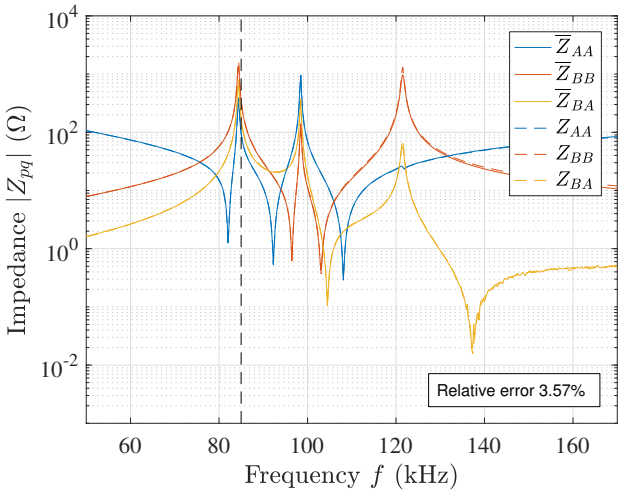

(a) Magnitude

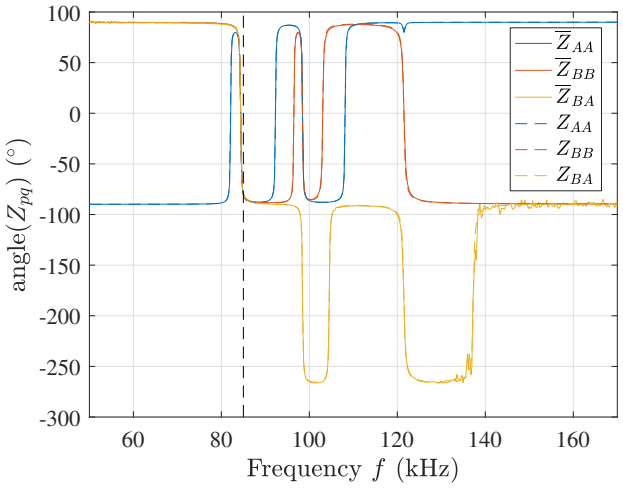

(b) Phase

Fig. 6. Magnitude and phase of impedance matrix entries as a function of frequency: 1) solid curves – measurements $\overline{Z}_{pq}(f_\nu)$; and 2) dashed curves – model $Z_{pq}(f_\nu, \mathbf{p}^*)$ for the optimized parameter vector $\mathbf{p}^*$.

significantly between different realizations. In the search, we also identify and disregard capacitance combinations which yield non-inductive loading of the power inverter. For the prototype, more than 100 different capacitance combinations yielded a power transfer of at least 3.0 kW with system efficiency of above 87 % in simulation. The top ten capacitance combinations with respect to maximum power transfer are presented in Table V.

The capacitance combination $C_1 = 26.4$ nF, $C_2 = 39.2$ nF, $C_3 = 62.0$ nF and $C_4 = 139$ nF marked in bold in Table V is selected as an appropriate tuning for the prototype system as it has good performance and only required that the first capacitance bank was switched from the previously used value of $C_1 = 21.7$ nF. In an experiment that aim at a power transfer of 3.3 kW, our prototype system transfers 3.35 kW at 91.4% efficiency with this capacitance selection. This results compares well with the expected power transfer of 3.49 kW at 91.1% efficiency predicted by the model at the lower generator input power used in the experiment.

TABLE IV
INITIAL COMPONENT VALUES WHEN MEASURED INDIVIDUALLY FOR EACH COMPONENT BY A DIRECT PROCEDURE AND OPTIMIZED PARAMETER VALUES USING SYSTEM IDENTIFICATION PROCEDURE FOR WPT SYSTEM SHOWN IN FIG. 1 AFTER REASSEMBLY

Parameter	Initial $\mathbf{p}_0$	Optimized $\mathbf{p}^*$	Change (%)
L_1 (μH)	126.	126.	0.079
L_2 (μH)	68.9	68.6	-0.38
L_3 (μH)	45.3	45.4	0.21
L_4 (μH)	17.8	17.9	0.67
k_{12} (%)	20.5	20.1	-2.2
k_{13} (%)	9.90	8.12	-18.
k_{14} (%)	8.18	6.40	-22.
k_{23} (%)	7.72	6.67	-14.
k_{24} (%)	7.59	7.13	-6.1
k_{34} (%)	34.7	33.6	-3.4
R_1 (mΩ)	142.	142.	0.31
R_2 (mΩ)	81.3	82.9	2.0
R_3 (mΩ)	66.1	71.7	8.4
R_4 (mΩ)	43.6	46.2	5.9

TABLE V
TIME AVERAGED MAXIMUM POWER TRANSFER AND EFFICIENCY FOR THE TOP TEN CAPACITANCE COMBINATIONS OF THE CAPACITOR BANKS

p_{load} kW	η %	C_1	C_2	C_3	C_4
			– nF –		
6.51	92.3	26.4	39.2	67.1	145
6.48	92.2	26.4	39.2	67.1	152
6.11	92.4	26.4	39.2	67.1	139
5.93	92.3	30.8	39.2	67.1	152
5.91	91.3	30.8	31.3	67.1	139
5.84	91.8	26.4	39.2	62	152
5.75	91.6	26.4	39.2	62	145
5.74	91.3	30.8	31.3	67.1	145
5.57	**91.3**	**26.4**	**39.2**	**62**	**139**
5.54	92.3	26.4	39.2	67.1	130

VI. CONCLUSION

We have presented a system identification and tuning procedure for a wireless power transfer (WPT) system that consists of four magnetically coupled resonators. In the system identification procedure, we employ a Bayesian approach to estimate the self-inductance and losses of the four coils in combination with their magnetic coupling. After the system identification procedure, the WPT model is used to predict appropriate capacitance values for the four capacitor banks to recover high system performance, where the generator voltage is limited by a set of circuit state constraints that prevent component overheating and breakdown. We find that the system identification procedure combined with the four tunable capacitors can account for and take care of rather significant perturbations due to, e.g., manufacturing tolerances and coil displacement. Further, a large set of different capacitance selections for the four tunable capacitor banks achieved high system performance for an experimentally realized WPT system design with magnetic coupling coefficients on the order of 6% to 8% between the primary and secondary side. This feature may be of key importance for future high performance WPT systems in applications where rather low magnetic coupling in combination with large variations in coil positions are expected, such as for electric vehicle charging.

REFERENCES

[1] S. Li and C. C. Mi, "Wireless Power Transfer for Electric Vehicle Applications," *IEEE J. Emerg. Sel. Top. Power Electron.*, vol. 3, no. 1, pp. 4–17, Mar 2015. [Online]. Available: http://ieeexplore.ieee.org/document/6804648/

[2] F. Musavi and W. Eberle, "Overview of wireless power transfer technologies for electric vehicle battery charging," *IET Power Electron.*, vol. 7, no. 1, pp. 60–66, Jan 2014. [Online]. Available: http://ieeexplore.ieee.org/document/6715805/

[3] B. Esteban, M. Sid-Ahmed, and N. C. Kar, "A Comparative Study of Power Supply Architectures in Wireless EV Charging Systems," *IEEE Trans. Power Electron.*, vol. 30, no. 11, pp. 6408–6422, Nov 2015. [Online]. Available: http://ieeexplore.ieee.org/document/7119591/

[4] A. Kurs, A. Karalis, R. Moffatt, J. D. Joannopoulos, P. Fisher, and M. Soljacic, "Wireless Power Transfer via Strongly Coupled Magnetic Resonances," *Science*, vol. 317, no. 5834, pp. 83–86, Jul 2007. [Online]. Available: http://www.sciencemag.org/cgi/doi/10.1126/science.1143254

[5] A. P. Sample, D. A. Meyer, and J. R. Smith, "Analysis, Experimental Results, and Range Adaptation of Magnetically Coupled Resonators for Wireless Power Transfer," *IEEE Trans. Ind. Electron.*, vol. 58, no. 2, pp. 544–554, Feb 2011. [Online]. Available: http://ieeexplore.ieee.org/document/5437250/

[6] S. Aldhaher, P. C.-K. Luk, and J. F. Whidborne, "Electronic tuning of misaligned coils in wireless power transfer systems," *IEEE Trans. Power Electron.*, vol. 29, no. 11, pp. 5975–5982, Jan 2014. [Online]. Available: http://ieeexplore.ieee.org/document/6702433/

[7] SAE Standard, "J2954, Wireless Power Transfer for Light-Duty Plug-In/Electric Vehicles and Alignment Methodology," 2016. [Online]. Available: http://standards.sae.org/j2954_201605/

[8] T. C. Beh, M. Kato, T. Imura, S. Oh, and Y. Hori, "Automated impedance matching system for robust wireless power transfer via magnetic resonance coupling," *IEEE Trans. Ind. Electron.*, vol. 60, no. 9, pp. 3689–3698, Sep 2013. [Online]. Available: http://ieeexplore.ieee.org/document/6226848/

[9] S. Li, W. Li, J. Deng, T. D. Nguyen, and C. C. Mi, "A double-sided LCC compensation network and its tuning method for wireless power transfer," *IEEE Trans. Veh. Technol.*, vol. 64, no. 6, pp. 2261–2273, Jun 2015. [Online]. Available: http://ieeexplore.ieee.org/document/6876154/

[10] M. E. Halpern and D. C. Ng, "Optimal tuning of inductive wireless power links: Limits of performance," *IEEE Trans. Circuits Syst. I Regul. Pap.*, vol. 62, no. 3, pp. 725–732, Jan 2015. [Online]. Available: http://ieeexplore.ieee.org/document/7024943/

[11] M. Kiani and M. Ghovanloo, "The Circuit Theory Behind Coupled-Mode Magnetic Resonance-Based Wireless Power Transmission," *IEEE Trans. Circuits Syst. I Regul. Pap.*, vol. 59, no. 9, pp. 2065–2074, Sep 2012. [Online]. Available: http://ieeexplore.ieee.org/document/6138883/

[12] S. Y. R. Hui, W. Zhong, and C. K. Lee, "A Critical Review of Recent Progress in Mid-Range Wireless Power Transfer," *IEEE Trans. Power Electron.*, vol. 29, no. 9, pp. 4500–4511, Sep 2014. [Online]. Available: http://ieeexplore.ieee.org/document/6472081/

[13] K. Lee and S. H. Chae, "Power Transfer Efficiency Analysis of Intermediate-Resonator for Wireless Power Transfer," *IEEE Trans. Power Electron.*, vol. 8993, no. c, pp. 1–1, Apr 2017. [Online]. Available: http://ieeexplore.ieee.org/document/7913710/

[14] W. Zhong, C. K. Lee, and S. Y. Ron Hui, "General analysis on the use of tesla's resonators in domino forms for wireless power transfer," *IEEE Trans. Ind. Electron.*, vol. 60, no. 1, pp. 261–270, Oct 2013. [Online]. Available: http://ieeexplore.ieee.org/document/6041026/

[15] X. Liu and G. Wang, "A Novel Wireless Power Transfer System with Double Intermediate Resonant Coils," *IEEE Trans. Ind. Electron.*, vol. 63, no. 4, pp. 2174–2180, Dec 2016. [Online]. Available: http://ieeexplore.ieee.org/document/7362019/

[16] D. Lin, J. Yin, and S. Y. R. Hui, "Parameter identification of wireless power transfer systems using input voltage and current," *Energy Convers. Congr. Expo. (ECCE), 2014 IEEE*, pp. 832–836, Nov 2014. [Online]. Available: http://ieeexplore.ieee.org/document/6953483/

[17] J. Winges, T. Rylander, T. McKelvey, C. Petersson, C. Ekman, and L. Å. Johansson, "System identification and tuning of wpt systems," in *Proc. EEEIC/I&CPS Conf.*, Jun 2017, pp. 1–5. [Online]. Available: http://ieeexplore.ieee.org/document/7977544/

[18] S. M. Kay and M. K. Steven, *Fundamentals of Statistical Signal Processing: Estimation Theory*. Englewood Cliffs, NJ, USA: Prentice-Hall, Inc., 1993.

[19] COMSOL AB, "COMSOL Multiphysics® v. 5.2," Stockholm, Sweden, 2016. [Online]. Available: www.comsol.com

[20] The MathWorks Inc., "Matlab®," Natick, Massachusetts, United States, 2017. [Online]. Available: www.mathworks.com

Johan Winges received the B.S. degree in engineering physics from Chalmers University of technology, Gothenburg, Sweden, in 2009, the M.S. degree in applied physics from Chalmers University of Technology in 2011, and the Ph.D. degree in electrical engineering from Chalmers University of Technology in 2016.

He is currently a researcher at Chalmers University of Technology in the Signal processing group at the Department of Electrical Engineering. His research interests are computational electromagnetics, inverse scattering problems and wireless power transfer.

Thomas Rylander received the M.S. degree in electrical engineering from the KTH Royal Institute of Technology, Stockholm, Sweden, in 1997, and the Ph.D. degree in electrical engineering from Chalmers University of Technology, Göteborg, Sweden, in 2002.

He was a Post-Doctoral Associate with the Center for Computational Electromagnetics, University of Illinois at Urbana-Champaign, Champaign, IL, USA, from 2002 to 2004. He was an Assistant Professor and an Associate Professor with Chalmers University of Technology in 2004 and 2007, respectively. His research interests are electromagnetic field theory with a broad range of applications. In particular, his research is based on computational electromagnetics with a focus on finite-element-based methods.

Tomas McKelvey received the M.S. degree in electrical engineering from Lund University, Lund, Sweden, in 1991, and the Ph.D. degree in automatic control from Linköping University, Linköping, Sweden, in 1995.

He has held research and teaching positions with Linköping University from 1995 to 1999, where he became a Docent in 1999. From 1999 to 2000, he was a Visiting Researcher with The University of Newcastle, Newcastle, NSW, Australia. Since 2000, he has been with the Chalmers University of Technology, Gothenburg, Sweden, where he has been a Full Professor since 2006. He has been the Head of the Signal Processing Group, Chalmers University of Technology, since 2011. His current research interests include model-based and statistical signal processing, system identification, machine learning, image processing and control with applications to biomedical engineering, and combustion engines.